UNIVERSITÀ DEGLI STUDI DI CATANIA

DIPARTIMENTO DI SCIENZE BIOLOGICHE GEOLOGICHE E AMBIENTALI

DOTTORATO DI RICERCA IN SCIENZE DELLA TERRA E DELL'AMBIENTE

XXXIV CICLO

INVESTIGATING SEISMO-VOLCANIC ACTIVITY AT MT. ETNA THROUGH ARRAY TECHNIQUES

Vittorio Minio

PhD coordinator:
Prof. Agata Di Stefano

Supervisor:

Prof. Andrea Cannata

Tutors:

Dr. Luciano Zuccarello (INGV)

Dr. Giuseppe Di Grazia (INGV)

FEBBRAIO 2022

TABLE OF CONTENTS

SINTESI IN ITALIANO

STUDIO DELL'ATTIVITÀ SISMO-VULCANICA DEL MT. ETNA MEDIANTE TECNICHE D'ARRAY

ABSTRACT

I vulcani mostrano una grande varietà di segnali sismici che solitamente si originano grazie alle interazioni dinamiche tra il magma e i fenomeni di degassamento e pressurizzazione del sistema di alimentazione. Le caratteristiche di tali segnali spesso forniscono informazioni sui meccanismi di trasporto del magma e sui processi eruttivi. Infatti, la localizzazione e l'analisi dei segnali sismo-vulcanici giocano un ruolo fondamentale nello studio delle dinamiche che interessano un vulcano. Tuttavia, a causa delle caratteristiche dei segnali sismo-vulcanici, tali studi richiedono l'utilizzo di specifiche tecniche d'analisi e/o di particolari geometrie delle reti di acquisizione dati. Negli ultimi decenni, gli array sismici sono diventati uno strumento molto affidabile per la localizzazione della sorgente dei segnali sismici registrati in aree vulcaniche. Le cosiddette tecniche d'array, basate sulla stima del vettore "*slowness*", hanno ricevuto una notevole attenzione soprattutto per scopi di ricerca; tuttavia, tali tecniche ancora non sono utilizzate di routine per il monitoraggio sismico nelle aree vulcaniche. Con lo scopo di affrontare queste problematiche, sono stati analizzati i segnali sismici del tremore vulcanico e degli eventi a lungo ("*Long Period*"; LP) e a lunghissimo periodo ("*Very Long period*"; VLP) registrati all'Etna durante il periodo 2010-2011, utilizzando le tecniche d'array. Il lavoro di questa tesi è stato articolato in tre fasi: (*i*) analisi delle proprietà dei segnali sismici, per determinare le loro caratteristiche principali e per valutare un intervallo di frequenza ottimale per l'analisi in tecnica d'array; (*ii*) localizzazione della sorgente dei segnali sismici, per ricostruire porzioni del sistema di alimentazione dell'Etna; (*iii*) implementazione di un software con interfaccia grafica in ambiente Matlab, per fornire uno strumento "*user-friendly*" utile per le routine d'analisi presso le sedi di monitoraggio sismico e vulcanico. Per queste attività di studio, sono stati utilizzati i dati acquisiti durante alcuni esperimenti sismici condotti all'Etna durante il 2010 e il 2011, i quali prevedevano l'installazione di array sismici nei pressi dell'area sommitale etnea. Allo stesso tempo, questi dati sono stati integrati con quelli registrati dalla rete permanente di stazioni sismiche gestita dall'Istituto Nazionale di Geofisica e Vulcanologia, Osservatorio Etneo. Dai risultati ottenuti in questi studi, è

possibile dedurre che, durante l'attività eruttiva all'Etna, le proprietà e le sorgenti dei segnali sismo-vulcanici sono correlate temporalmente con i fenomeni di pressurizzazione e depressurizzazione che interessano il sistema di alimentazione del vulcano. Inoltre, le analisi condotte in questi studi potrebbero essere uno strumento valido ai fini della valutazione della pericolosità vulcanica e dello sviluppo di sistemi d'allerta in vulcani attivi.

CAPITOLO 1

Il primo capitolo di questa tesi espone gli argomenti relativi alle conoscenze di base necessarie per lo studio del tremore vulcanico e degli eventi LP e VLP. Nello specifico, si compone di tre sezioni: la prima sezione introduce brevemente la sismicità vulcanica; la seconda sezione descrive il vulcano Etna; la terza sezione è dedicata ad una descrizione dei metodi d'analisi utilizzati per lo studio dei segnali sismici registrati al vulcano Etna.

L'introduzione alla sismicità vulcanica, oggetto della prima sezione, descrive le diverse tipologie di segnali sismici che è possibile osservare nei pressi di un vulcano attivo. Sulla base degli studi più recenti, è stata effettuata una descrizione dei segnali sismo-vulcanici, tra cui il tremore vulcanico e gli eventi LP e VLP.

La descrizione del vulcano Etna, oggetto della seconda sezione, è stata effettuata prendendo in esame i più recenti studi al fine di mostrarne le principali caratteristiche geologiche, strutturali e geodinamiche. Particolare attenzione, inoltre, è stata dedicata sia alla descrizione delle caratteristiche dei segnali sismo-vulcanici, sia alla descrizione della recente attività, specie per quanto riguarda l'attività eruttiva osservata tra il 2010 ed il 2011.

Infine, la terza sezione è stata dedicata alla descrizione dei concetti base necessari per effettuare l'analisi in tecnica d'array. Allo stesso tempo, particolare attenzione è stata posta alla descrizione dei metodi d'analisi necessari per la caratterizzazione dei segnali sismici, come contenuto spettrale, ampiezza, polarizzazione e localizzazione della sorgente, e per l'individuazione di segnali transienti come gli eventi LP e VLP.

CAPITOLO 2

Il secondo capitolo di questa tesi è dedicato all'analisi delle caratteristiche del tremore vulcanico e degli eventi LP e VLP registrati al vulcano Etna durante il periodo 2010-2011. A tale scopo, il capitolo è stato suddiviso in diverse parti.

In primo luogo, dopo una breve descrizione della letteratura concernente diversi casi studio, sono state descritte le modalità di acquisizione dei segnali sismici e la copertura temporale dei dati acquisiti. In particolare, sono stati utilizzati i dati registrati durante una campagna di acquisizione condotta tra il 2010 e il 2011 dai ricercatori dell'Istituto Nazionale di Geofisica e Vulcanologia (INGV), che ha previsto l'installazione di array sismici nei pressi dell'area sommitale etnea. Questi dati sono stati integrati con quelli registrati dalla rete sismica permanente gestita dall'INGV. Per lo studio del tremore vulcanico e degli eventi LP e VLP, ci si è focalizzati su diversi intervalli temporali, sulla base di: (*i*) periodo di funzionamento delle stazioni che costituiscono gli array e della rete sismica permanente; (*ii*) attività eruttiva dell'Etna, con particolare attenzione alla sequenza esplosiva osservata durante l'estate del 2010 alla Bocca Nuova (BN) e ai 18 episodi parossistici verificatosi al Nuovo Cratere di Sud-Est (NSEC) durante il 2011.

Successivamente, sono state descritte le modalità d'analisi e i risultati ottenuti per la caratterizzazione del tremore e degli eventi LP e VLP durante i periodi oggetto di studio. In generale, particolare attenzione è stata dedicata alla variazione delle caratteristiche dei segnali in concomitanza con le variazioni dell'attività vulcanica. Per quanto riguarda il tremore, è stata affrontata una prima indagine mirata ad individuare l'intervallo in frequenza ideale per l'analisi in tecnica d'array, sulla base delle capacità degli array di registrare un campo d'onda coerente. In un secondo momento, è stata eseguita una serie di analisi per la caratterizzazione del tremore in termini di ampiezza, contenuto in frequenza e polarizzazione del segnale. Per quanto riguarda gli eventi LP e VLP, oltre alla determinazione delle loro caratteristiche principali, è stata effettuata un'analisi mirata alla individuazione e classificazione in base alla loro forma d'onda.

Infine, oltre a riassumere i principali risultati ottenuti, sono state esposte varie considerazioni e suggerimenti per eventuali lavori futuri concernenti studi analoghi.

CAPITOLO 3

Il terzo capitolo di questa tesi è dedicato alla localizzazione di sorgente del tremore vulcanico e degli eventi LP e VLP registrati al vulcano Etna durante l'attività del 2010 e del 2011. Anche in questo caso il capitolo è stato suddiviso in sezioni, con una struttura simile ai capitoli precedenti. In una prima parte introduttiva, è stata descritta brevemente la letteratura concernente lo stato dell'arte in materia di analisi in tecniche d'array. In seguito, ci si è focalizzati sulla descrizione delle modalità di esecuzione delle analisi in tecnica d'array e sui risultati ottenuti per il tremore e gli eventi LP e VLP. Nelle sezioni finali, è stata esposta, invece, l'interpretazione delle sorgenti sismiche in relazione alle dinamiche eruttive osservate durante i periodi d'investigazione, nonché sono stati elencati alcuni suggerimenti per eventuali lavori futuri.

Per la localizzazione del tremore vulcanico, è stata applicata una tecnica basata sulla stima delle componenti del vettore "*slowness*". A tal proposito, sono stati utilizzati esclusivamente i dati sismici registrati dagli array durante il 2010 e il 2011. Per gli eventi LP e VLP, la localizzazione di sorgente è stata effettuata mediante due approcci differenti. Il primo si basa sullo stesso metodo d'analisi che è stato utilizzato per il tremore; il secondo, invece, sulla determinazione della posizione della sorgente mediante metodi che prevedono una ricerca su griglia. In questo caso, sono stati utilizzati sia i dati sismici degli array che quelli acquisiti dalla rete permanente etnea dell'INGV durante i periodi oggetti di studio. Inoltre, sono state valutate le performance di alcune tecniche d'analisi mediante una serie di segnali sintetici di eventi LP e VLP, cercando di emulare il più possibile le loro caratteristiche. In tutti questi approcci, è stata comunque eseguita una valutazione degli errori mediante un metodo statistico basato su ricampionamenti sequenziali.

Particolare attenzione è stata dedicata anche alle variazioni della posizione della sorgente dei segnali sismici in relazione all'attività esplosiva del 2010 e del 2011. Tenendo anche conto dei risultati ottenuti nel Capitolo 2, si è tentato di schematizzare pattern caratteristici di episodi eruttivi come quelli delle fontane di lava o delle esplosioni minori. Dai risultati ottenuti, sono state individuate alcune evidenze preeruttive relative allo stato di unrest del vulcano Etna, specialmente per quanto riguarda lo sviluppo dell'attività parossistica. In particolare, alcune ore prima dell'attività eruttiva, è stato osservato che: (*i*) la frequenza del tremore vulcanico si focalizza attorno a 1 Hz; (*ii*) l'ampiezza del tremore vulcanico e degli eventi LP e VLP aumenta gradualmente con la ripresa dell'attività eruttiva; (*iii*) la sorgente di questi segnali sismici migra verticalmente e/o lateralmente, spostandosi verso la

porzione più superficiale del sistema di alimentazione del vulcano; (*iv*) la sorgente di questi segnali sismici genera onde P e SH-Rayleigh.

CAPITOLO 4

Il capitolo 4 rappresenta l'ultimo capitolo di questa tesi. Oltre a riassumere i principali risultati ottenuti nei precedenti capitoli, espone una serie di considerazioni e suggerimenti per eventuali lavori futuri concernenti studi analoghi. Dai risultati ottenuti, è possibile dedurre che le proprietà e le sorgenti dei segnali sismo-vulcanici sono temporalmente correlate con i fenomeni di pressurizzazione e depressurizzazione che interessano il sistema di alimentazione del vulcano. Variazioni nel tempo delle proprietà e della posizione sorgente dei segnali sismici, alcune ore prima lo sviluppo dell'attività eruttiva, potrebbero fornire informazioni sullo stato di attività del vulcano sul breve periodo, specialmente per episodi eruttivi come i parossismi. MISARA, software con interfaccia grafica in ambiente Matlab (vedi Appendice A), potrebbe essere uno strumento valido ai fini della ricerca scientifica e del monitoraggio vulcanico. Pertanto, questi risultati potrebbero contribuire allo sviluppo di strategie per la valutazione della pericolosità vulcanica e dei sistemi d'allerta presso aree vulcaniche.

APPENDICE A-MISARA

In questa appendice sono illustrati l'implementazione e il funzionamento di MISARA (*Matlab Interface for the Seismo-acoustic ARary Analysis*), un software con interfaccia grafica in ambiente Matlab, sviluppato per la visualizzazione, caratterizzazione, individuazione e localizzazione di segnali sismo-acustici. In particolar modo, ci si è focalizzati sulla struttura e sulle metodologie sui cui si fonda il software, prestando attenzione ai vantaggi e alle limitazioni nel suo utilizzo, nonché alle possibili implementazioni future.

ABSTRACT

Volcanoes exhibit a large variety of seismic signals involved in dynamic interactions between magma movements, degassing and pressurized conditions. Their characteristics often provide important clues on the transport mechanisms and eruption processes. The source localization and analysis of these signals play a key role in the study of volcano dynamics, but they require specific techniques and/or networks geometries due to their unique features. In the last decades, small aperture seismic arrays have become a reliable and useful tool for tracking the seismic sources in volcanic areas. New methods of source localization, based on estimations of back-azimuth and apparent velocity of seismo-volcanic sources, have received considerable attention in volcano research, but were not often used as operational routines for volcano monitoring. In order to address these challenges, volcanic tremor, Long Period and Very Long Period events recorded at Mt. Etna during eruptive activity in 2010-2011 were analysed through array techniques. In this thesis, the research work was mainly divided into three different phases: (*i*) analysis of the features of seismic signals, to determine their wavefield properties and the frequency range of analysis reliable for the array processing; (*ii*) source location of the seismic signals, to image the plumbing system of the volcano; (*iii*) implementation of a Matlab Graphic User Interface, to provide a useful and user-friendly tool for analytical routines at volcanological observatories. For these studies, we used the data archived during seismic array experiments performed in the 2010-2011 period, integrated with those recorded by seismic permanent network managed by Istituto Nazionale di Geofisica e Vulcanologia, Osservatore Etneo. From the results obtained in these studies, we infer that variation of the features of signals and source locations are time-related to pressurization and depressurization dynamics of the plumbing system of Mt. Etna during the different phases of eruptive activity. In addition, we argue that arrays methods could be considered as additional and powerful tools in the hazard assessment and in the development of early-warning systems of a volcano.

Keywords: seismology, Mt. Etna volcano, volcanic tremor, Long Period events, Very Long Period events, lava fountains, array techniques, Matlab software with interface.

INTRODUCTION

Volcanoes are striking manifestations of magma rising from the depths of the Earth's crust. Human activity takes place near many volcanoes, which can produce violent explosive eruptions, including ash and pyroclastic fragments. These eruptive events can certainly have a catastrophic impact on society. However, eruptions are frequently preceded and followed by volcanic and seismic phenomena, indicating strong variations in the dynamic process caused by internal forces. Such pre-, syn- and post- eruptive indicators can be measured by seismometers, providing very valuable tools for the monitoring of volcanic areas. For this reason, volcanologists deal with a large variety of seismic signal involved in dynamic interactions between magma movements, degassing and pressurized conditions. Source localization and analysis of these signals can lead to a better knowledge of magma transport mechanisms and eruption processes. In fact, the upward movement of magma towards the volcano's crater frequently breaks rocks and hence leads to propagation of seismic waves (Dingwell, 1996; McNutt, 2005; Sparks, 2000). At surface, physical and chemical properties of magma change and cause different processes that explain the diversity of seismic signals recorded at volcanoes around the world. A fundamental goal of volcano seismology consists of a better understanding of these mechanisms.

In the last two decades, improvements in digital data acquisition, seismic signal processing and more precise and higher quality data, have allowed to improve the knowledge about the structures and dynamics that characterized active volcanoes, such as Piton de la Fournaise (Réunion island, France), Kilauea (Hawaiian, USA), St. Helens (Washington, USA), Sakurajima (Japan), etc. Results obtained from these different sites show that the magma dynamics in the plumbing system are reflected in the pattern of geophys-ical data series, such as seismicity. The determination of the seismic source is very important, since changes of wavefield properties or source position of seismo-volcanic signals are frequently one of the first signs of volcanic unrest. For this reason, hundreds of volcanoes are currently seismically monitored.

Recently, the use of broadband three component seismometers has significantly improved the resolution and range of signals detectable at volcanoes, leading to the development of new strategies for the interpretation and analysis of seismo-volcanic phenomena (Chouet, 2003; Wassermann, 2012). A great variety of seismic signals can be generally recorded on active volcanoes. On the basis of their waveform features and frequency content, these signals can broadly be classified into different groups (Chouet, 1996a,b; Neuberg et al.,

2006; Wassermann, 2012), including volcanic tremor and Long Period (LP) and Very Long Period (VLP) events.

Seismo-volcanic signals such as volcanic tremor and LP and VLP events show sustained or emergent nature and ambiguous seismic P- and S-phases. Due to lack of clear body-waves phases, volcanic tremor cannot be located precisely using classical earthquake hypocenter tools (Chouet et al., 2003). Localization of the source of LP/VLP events using travel time inversion is possible, but the uncertainty of location is very large due to lack of distinct S-phases and large error in first arrival picking. Because sources of these seismo-volcanic signals are different from those of tectonic earthquakes, analysis techniques and equipment configuration must be adapted to operate on these types of signals. For instance, small aperture seismic arrays have become a reliable and useful tool for tracking the seismic sources in volcanic areas (Rost and Thomas, 2002). For this reason, new methods of source localization were developed in last decades, based on estimations of back-azimuth and apparent velocity of seismo-volcanic sources. In the literature, most methods using seismic sensor arrays have received considerable attention in volcano research (e.g. Métaxian et al., 1997; Saccorotti et al., 2001; La Rocca et al., 2004; Almendros et al., 2004; Di Lieto et al., 2007). In fact, an advantage of array methods is the ability to improve the signal-to-noise ratio (SNR), allowing to estimate lateral and vertical migration of signal sources. However, arrays are not often used as an operational tool for volcano monitoring, excepts in some cases (e.g. Coombs et al., 2018).

Mt. Etna volcano (Sicily, Italy) is one of the most active and monitored volcanoes in the world, characterized by the continuous acquisition of different geophysical data. The rapid evolution of the eruptive dynamics that characterizes this volcano and the multiparametric monitoring network, managed by the "Istituto Nazionale di Geofisica e Vulcanologia (INGV)", allow us to consider Mt. Etna as a natural laboratory.

The aim of this thesis is the study of seismic signals, generated by Mt. Etna volcano, through array techniques, in order to provide both useful information about magma dynamics in the plumbing system of the volcano and efficient tools for monitoring purposes at volcanological observatories. In the chapters of this thesis the results, obtained by the study of the activity that occurred at Mt. Etna during the 2010-2011 period, will be presented. These years were characterized by an intense eruptive activity showing more than 30 minor explosive events at Bocca Nuova crater (BN) and 18 paroxysmal episodes at the New South East Crater (NSEC).

This study concerned the investigation of seismic signals recorded during the considered period, focusing the attention on the features of volcanic tremor, LP and VLP events (frequency content, amplitude, polarization attributes, source location). The following work, was articulated in three different phases: (*i*) analysis of the features of seismic signals recorded at Mt. Etna during 2010-2011 period, to define their wavefield properties in time and a frequency range of analysis reliable for the array processing; (*ii*) source location of the seismic signals recorded at Mt. Etna during 2010-2011 period, in order to localize the source of the seismic signals and describe its mechanisms related to dynamics of injection and transport of magma; (*iii*) implementation of a Matlab GUI (Graphic User Interface), based on the techniques used in (*i*) and (*ii*), in order to provide an useful tool for analytical routines at volcanological observatories. For these phases, we used the data archived during seismic array experiments performed in the 2010-2011 period, integrated with those recorded by INGV seismic permanent network. In particular, in the Chapter 1 of this thesis the fundamentals regarding volcano seismicity, geological features and recent activity of Mount Etna, as well as the principal analyses routinely performed on Etna seismo-volcanic signals, have been briefly described. In Chapter 2 and Chapter 3, the features and the source location of seismic signals, were described. Specifically, each of the two chapters was divided into sections concerning general introduction, description of the results, discussion and conclusions. Then, the Chapter 4 summarized the main results obtained with the studies carried out in this thesis, providing some perspectives for possible future studies. Finally, in the Appendix A, the main features of the Matlab GUI and its functionalities were illustrated, discussing on the advantages and limitations of the software.

CHAPTER 1 - BACKGROUND AND STATE OF ART

1.1 VOLCANO SEISMOLOGY

Active volcanic areas generate several types of seismic signals, characterized by well-defined features. Volcano seismology studies these signals, in order to understand the nature and dynamics of the injection and transport of magma and related to hydrothermal fluids (Chouet, 2003). They are traditionally classified based on waveform features and frequency content. The commonly adopted classification schemes (e.g. Lahr et al., 1994; Chouet, 2003; Wassermann, 2012; McNutt et al., 2015) distinguish different groups of signals, depending on their frequency content. These are: high-frequency (HF) and low-frequency (LF) earthquakes, volcanic tremor, hybrid events and volcanic explosions (Fig. 1.1).

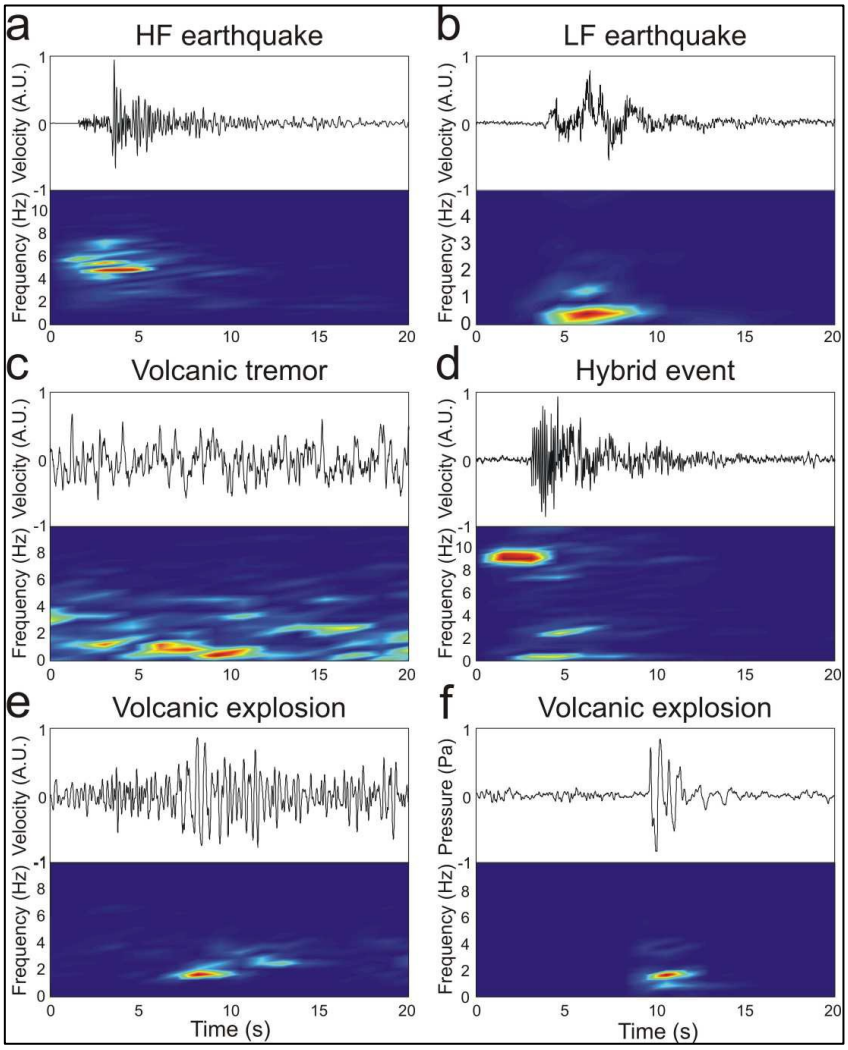

Figure 1.1. Waveforms and spectrograms of (a) HF earthquake, (b) LF earthquake, (c) volcanic tremor, (d) hybrid event, and (e)-(f) volcanic explosions at Mt. Etna (From Patané et al., 2008).

1.1.1 HF EARTHQUAKES

HF earthquakes (Fig. 1.1a), also known as Volcano-Tectonic (VT) or A-type earthquakes, are characterized by clear P-S wave phases and dominant frequencies spanning from 2 to 20 Hz. These types of events are similar to pure tectonic ones, except for the occurrence patterns which are in swarms rather than the usual mainshock-aftershock sequences (McNutt, 2002).

HF events are thought to be related to regional tectonic forces, gravitational loading, pore pressure effects and hydrofracturing, thermal and volumetric forces associated with magma intrusion, withdrawal, cooling or some combinations of any or all of these (McNutt, 2005). In a volcano, HF seismicity can be generated by the propagation of the ascent of magma and rock breaking. For this reason, variations in volcano tectonic seismicity can often represent the earliest detectable precursors to volcanic eruptions (e. g. Roman and Cashman, 2006).

One of the main progresses in the investigation of VT events is represented by implementation of a suite of techniques used to improve locations. These techniques allowed to define many faults that are not discernible in usual locations (e.g. Prejean et al., 2002; McNutt, 2005). Another technique of research is high-resolution tomography developed to image subsurface volcanic velocity structures at scales of a few hundred meters (e.g. Dawson et al., 1999; Patanè et al., 2006). In addition, these events allow to determine stress orientations via study of focal mechanisms and stress tensor inversion (e.g. Barberi et al., 2000; Waite and Smith, 2004).

1.1.2 LF EARTHQUAKES

LF earthquakes (Fig. 1.1b) are also called Long Period (LP) events or B-type earthquakes. With frequencies ranging between 0.5 and 5 Hz, these events are usually interpreted as precursors to an eruption (Chouet, 1996a), because volcano activity is often preceded and accompanied by them.

Although their source processes are still not well understood, LF events may be attributed to internal volcanic activities associated with fluid movement, heat and gas supply from magma, and interaction between magma and underground water. The main model invokes the resonance within a pressurized fluid-filled crack (e. g. Chouet, 1986), that is controlled by the geometry/dimension of the crack and the impedance contrast between the fluid and

the host rock and the crack stiffness. Even if this model explains how the characteristics of LP events could be produced, the trigger mechanism is still unknown and many volcanic processes could be involved (e.g. Chouet and Matoza, 2013).

Magmatic-hydrothermal fluids interactions are one of the first trigger mechanisms proposed for LP events generation (Chouet, 1986). LP seismicity could be generated via boiling and depressurization of ground water (Leet, 1988; Matoza and Chouet, 2010), cyclic collapse and recharge of pressurized hydrothermal cracks (Arciniega-Ceballos et al., 2012; Matoza and Chouet, 2010; Matoza et al., 2009; Nakano, 2005; Ohminato et al., 2006; Waite et al., 2008) or unsteady chocking of a supersonic flow of magmatic steam (Chouet et al., 1994; Morrissey and Chouet, 1997).

Magmatic degassing has been recognized as trigger mechanism of LP events that is based on the oscillation of the terminal part of the conduit system induced either by the chocking of the flow or the explosive jet recoil (e.g. Ohminato et al., 1998; Chouet, 2003; Davi et al., 2012).

Experimental and numerical studies have recently showed that highly viscous melts can exhibit solid–like brittle behavior (Webb and Dingwell, 1990; Alidibirov and Dingwell, 1996; Dingwell, 1996; Ichihara and Rubin, 2010;) in conditions realizable in magma conduits (Papale, 1999; Collier and Neuberg, 2006; Gonnermann and Manga, 2007; Hale, 2007; Thomas and Neuberg, 2012). The process is related to non-Newtonian behavior of different melt compositions which could experience a transition from viscous-fluid-like to solid-like mechanical behavior (Webb and Dingwell, 1990). The brittle behavior of part of melt and crystals could result in shear-failure and trigger the resonance of the fluid filled crack generating the LP signal (Neuberg et al., 2006).

Solid lava dome extrusion is another trigger mechanism proposed for the LP events generation (e.g. Iverson et al., 2006; Moran et al., 2008). It is based on the existence of a solid plug pulled upward by a constant flux of molten (bubbly) magma at depth in a conduit. Each LP event would correspond to stick-slip motion of the lava plug. This stick-slip motion would occur on the margins of the lava plug where extrusion is resisted by friction forces.

Recently, Bean et al., (2014) proposed a new model for explaining shallow LP seismicity. They attributed the apparent resonance of these low-frequency seismic events caused by propagation effects and not being source related. Their model hypothesizes that these LP events are consequence of failure in materials close to the brittle-ductile transition. The

brittle-ductile transition in shallow volcanic material is not supposed to be related to high temperature and pressure, but to the low friction angles of the unconsolidated shallow volcanic deposits.

In the last decades, the widespread use of broadband stations has allowed to observe a new type of LF signals, known also as Very Long Period (VLP) events, at many volcanoes around the world, such as Aso (Legrand et al., 2000), Merapi (Hidayat et al., 2000), Stromboli (Neuberg et al., 1994; Chouet et al., 2003), Popocatépetl (Chouet et al., 2005), Kilauea (Ohminato et al., 1998) and Etna (Cannata et al., 2009a; Zuccarello et al., 2013). These events usually show a period spanning between 2 and 100 seconds (Neuberg et al., 1994; Ohminato et al., 1998).

VLP events may provide important information about the geometry of the shallow portion of the plumbing system and the temporal variations of the physical characteristics of magma (e.g. Chouet et al., 2003). In fact, changes in their spectral, amplitude and waveform properties could be associated to pressure variations within conduits, constituting a potentially useful element to forecast eruptive activity (e.g. Saccorotti et al., 2007; Patané et al., 2008; Cannata et al., 2009a; Chouet et al., 2010; Patanè et al., 2013; Zuccarello et al., 2013; Chouet and Matoza, 2013).

VLP signals are generally attributed to the elastic response of the volcano's plumbing system resulting from transient volumetric changes accompanying the transport of magma and gases through the conduits or dikes-sills (e.g. Uhira and Takeo, 1994; Kaneshima et al., 1996; Chouet and Matoza, 2013). Inversions of VLP waveforms have imaged crack geometries in the form of dikes or sills (Ohminato et al., 1998; Yamamoto et al., 1999; Chouet et al., 2003; Kumagai et al., 2003), as well as more complicated geometrical configurations involving sill-dike composites (Chouet et al., 2005; Dawson et al., 2011; Haney et al., 2012), composites of intersecting dikes (Chouet et al., 2008; Chouet and Dawson, 2011), or two chambers connected to each other by a narrow channel (Nishimura et al., 2000).

Some authors use also the term Ultra Long Period event (ULP) to refer events with period longer than 100 s (e.g. Ohminato et al., 1998). These events are identified as precursor of volcanic activity and, generally, they are interpreted as consequence of a tilt responding to the volcano deformation during magma ascent and ejection (e.g. D'Auria et al., 2006; Cesca et al., 2007; Sanderson et al., 2010).

The source localization of LF signals can greatly improve knowledge about the source mechanisms and geometry of the plumbing system of a volcano. Since LF signals show emergent P-waves and not detectable S-waves, classical travel-time inversion methods cannot usually be applied to determine their source position, but it necessary to use other techniques. For this purpose, several methods have been implemented, such as (*i*) Semblance algorithm (e.g. Cannata et al., 2013), (*ii*) array analysis (Metaxian et al., 2002; Inza et al., 2011, Almendros et al., 2014), amplitude decay (Battaglia et al., 2003) method, (*iii*) coupled inversion location and moment tensor (Kumagai et al., 2002), (*iv*) cross-correlation location (De Barros et al., 2009) and (*v*) time reversal method (O'Brien et al., 2011).

1.1.3 VOLCANIC TREMOR

Volcanic tremor (Fig. 1.1c) is a sustained seismic signal and it has been widely observed at volcanoes throughout the world (Kostantinou and Sclindwein, 2002; McNutt, 2011). It can be recognized as a common precursor of volcanic eruptions (e.g. Balmforth et al., 2005). In several volcanos, the spectral content of tremor is usually focused on frequency band ranging from 0.1 to 10 Hz through one or more dominant sharp peaks associated with source effects (e.g. Fehler, 1983; Almendros et al., 1997; Hagerty et al., 2000). Generally, the origin of volcanic tremor is related to the complex interplay between magmatic-hydrothermal fluids and their host rocks (e.g. Chouet, 1986; Julian, 1994). Several models have been proposed in order to account for tremor generation including free oscillations of fluid filled cavities (Crosson and Bame, 1985; Fujita et al., 1995), jerky crack propagation (Aki et al., 1977), flow-induced oscillations of volcanic conduits (Julian, 1994; Hellweg, 2000), and the resonance of fluid filled cracks and conduits (Chouet, 1986; Benoit and McNutt, 1997; Garces and McNutt 1997).

Earlier models of tremor, based on the free oscillations of magma chambers, were able to reproduce peaked harmonic spectra but often relied on unrealistic dimensions of the resonating volumes (De Angelis and McNutt, 2007). Most recently, the study of tremor has received increasing attention by volcano seismologists because of its potential as a monitoring and forecasting tool for unrest at volcanoes, and more refined models have been proposed. Aki et al. (1977) proposed that tremor is generated by the pressure driven motion of fluids through a chain of cracks connected by narrow channels; the characteristics of tremor are controlled by parameters such as the length of the cracks and the fluid pressure. Chouet (1986) suggested that the resonance modes of a fluid-filled rectangular crack,

triggered by a localized pressure disturbance acting on the crack walls, correspond to the peaks observed in the spectra of volcanic tremor. The predicted wavefield depends on parameters that include the crack dimensions, the position and intensity of the pressure disturbance and the impedance contrast between the fluid and the surrounding rocks. Julian (1994) proposed that tremor results from the oscillations of slot-like channels with movable elastic (damped) walls, induced by the flow of a viscous incompressible fluid. This model is described by a third-order system of non-linear differential equations whose solutions are controlled by the fluid flow pressure; increasing values of this parameter account for steady flow without oscillations, short-lasting oscillations, sustained oscillations, period-doubling cascades, and chaotic oscillations controlled by non-linear attractors. More recently, Jellinek and Bercovici (2011) proposed a model for generation of volcanic tremor based on magma-wagging. This model suggests that, in silicic systems, magma rises as a relatively stiff column surrounded by a gas-rich annulus (Okumura et al., 2006, 2008; Gonnermann and Manga, 2007). Specifically, lateral displacements of the magma column from its central resting position compress or dilate the annulus, which acts as a semi-permeable springy foam that restores the magma column to its resting state. The column's inertia causes an over-shoot of this resting position, leading to a wagging oscillation, whose impulse is imparted to the conduit walls to cause tremor.

Harmonic tremor and spasmodic tremor represent two particular cases of general volcanic tremor. The former is a low-frequency, often monotonic sinusoid with smoothly varying amplitude, while the latter is a higher-frequency, pulsating, irregular signal (McNutt, 1996). There is also another type of volcanic tremor called banded tremor. Characterized by regular cyclic increases of amplitude, it has widely been recorded during hydrothermal activity (McNutt, 1992; Cannata et al., 2010), and its source processes have been modelled (Fujita, 2008).

In many volcanoes, tremor shares the same frequency band and source processes with LP events, although it is characterized by different duration: similar to that of earthquakes for the LP events; minutes to longer than months for volcanic tremor. On the base of it, many authors have concluded that tremor consists of a series of LF events occurring at intervals of few seconds (Chouet, 1992).

The quantitative analysis of this kind of seismicity is very important for understanding and distinguishing the different source processes. Other seismic signals with similar properties to volcanic tremor can be also generated by several other processes such as subglacial flooding (Eibl et al., 2020), lahars (Kumagai et al., 2009) or other surficial mass flows

(Allstadt et al., 2018) and deeper slow slip earthquakes in subduction zones (Beroza and Ide, 2011). Therefore, it is very important to determine the features and source location of tremor to distinguish the processes underlying tremor generation. Owing to its emergent and sustained nature and lack of clear body-wave phases, volcanic tremor cannot be located through techniques based on travel time inversion, but it is necessary to use alternative methods such as amplitude-based techniques (Battaglia et al., 2005; Cannata et al., 2015; Morioka et al., 2017) or seismic array analysis (Almendros et al., 1997; Di Lieto et al., 2007; Eibl et al., 2017a,b).

1.1.4 HYBRID EVENTS

Hybrid events (Fig. 1.1d) share signal and frequency characteristics of LF and HF events. The spectral analysis of these signals reveals two distinct phases. The initial high-frequency segment reaches frequency up to 40 Hz, while the low-frequency portion is very similar to a LP event and peaks around 1-6 Hz. Before eruption o during phases of lava extrusion, hybrid events can be generated as seismic warms (Lahr et al., 1994; Miller et al., 1998).

This kind of signals may be attributed a possible combination of source mechanisms from both event types and additionally may reflect possible path effect (Harrington and Brodsky, 2007). However, the repetitive nature of hybrid events suggests also a spatially stable source linked to the interaction between a plug of magma and the conduit walls (Iverson, 2006; Kendrick et al., 2014).

1.1.5 VOLCANIC EXPLOSIONS

Volcanic explosions (Fig. 1.1e-f) or explosion-quakes accompany explosive activity and many of them are composed by air-shock phase in the seismic record (McNutt et al., 2015). In the recent years, they have been largely investigated through the use of infrasonic pressure sensors. The infrasonic signal consists of acoustic waves travelling in atmosphere at frequency lower than the audible component of sound (<20 Hz). During the propagation, especially in case of short paths, this kind of signal keeps its characteristics almost unchanged, because the acoustic waves travel in an almost homogenous medium with no structures that might scatter, attenuate or reflect them. Therefore, unlike the seismic signal, acoustic wavefield is not strongly affected by topography and path effects, allowing to acquire information on source location.

The source mechanism of this kind of signal may be attributed to different phenomena, such as (*i*) the acoustic resonance of magma in the conduit, triggered by explosive sources, (Buckingham and Garces, 1996; Garces and McNutt, 1997; Hagerty et al., 2000), (*ii*) local bubbles coalescence within a foam (Vergniolle and Caplan-Auerbach, 2004), and (*iii*) Strombolian bubble vibration (Vergniolle and Brandeis, 1994, 1996; Vergniolle et al., 1996, 2004). Methods for determining the relative acoustic and seismic contributions during explosive eruptions were developed (Johnson and Aster, 2005; Andronico et al., 2013).

1.2 MT. ETNA VOLCANO

Situated in Eastern Sicily (Italy), Mt. Etna (Fig. 1.2) is one of the most active volcanoes in the world. With a total area of 1250 km^2, it is characterized by roughly elliptical base (38 × 47 km) and maximum elevation of about 3350 m a.s.l. (Branca et al., 2004). The summit portion of the volcano currently consists of five main active craters: Bocca Nuova (BN), North-East Crater (NEC), Voragine (VOR), South-East Crater (SEC) and New South-East Crater (NSEC). In addition, about 350 crater or minor vents are situated in the flank of the volcano, each of which erupted once.

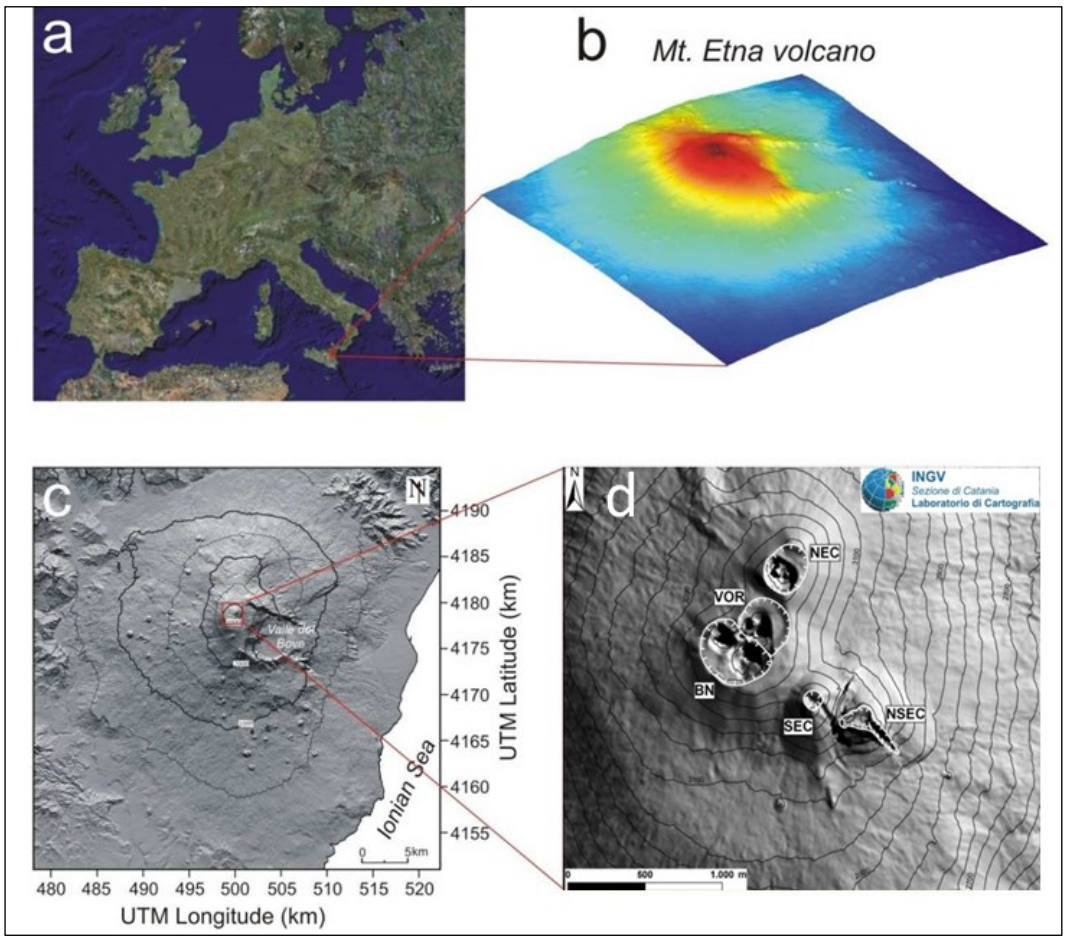

Figure 1.2. a) Map of Europe (From Google Earth). b) 3D elevation model of Etna. c) Map of Etna (redrawn from Aiuppa et al., 2015). d) zoom on the summit area of the volcano (from https://www.ct.ingv.it).

1.2.1 GEOLOGICAL FRAMEWORK

According to recent geological investigation (Branca et al. 2004, 2008, 2011) and geochronological data (De Beni et al., 2011), the geological history of Mt. Etna can be divided in four main phases (Fig. 1.3): (*i*) the Basal Tholeiitic phase, (*ii*) the Timpe phase, (*iii*) the Valle del Bove centers and (*iv*) the Stratovolcano phase.

(*i*) The Basal Tholeiitic phase (Fig. 1.3a) began in the middle of Pleistocene, about 500 ka ago (Branca et al., 2008), through fissure-type submarine eruptions within the Gela-Catania foredeep basin. The products of these eruptions are situated in the area of Aci Castello (Corsaro and Cristofolini, 2000) and they are composed of subalkaline pillow lavas, hyaloclastic breccias and tholeiitic shallow intrusions (Branca et al., 2004). About 330 ka ago, the first subaerial products of Mt. Etna were erupted from scattered fissure-type eruptions in Simeto paleovalley (De Beni et al., 2011), because of uplifting of the area. During this geological period, the main eruptive products were represented by tholeiitic basalts (Branca et al., 2008).

(*ii*) The Timpe phase (Fig. 1.3b) took place between 220 ka and 129 ka ago (De Beni et al., 2011) through repetitive effusive eruptions along Timpe fault system (Branca et al., 2011). The main products of this period are attributed to a first primitive volcano structure, whose evidences are exposed as a lava shield elongated 22 km on an NNW-SSE basis in correspondence of the actual Acireale scarps on the east flank of the volcano (Branca et al., 2008, 2011b). Volcanism was characterised by a transition from sub-alkaline to alkaline-Na affinity (Corsaro and Pompilio, 2004; Branca et al., 2008).

(*iii*) During the Valle del Bove phase (110-65 ka ago-Fig. 1.3c), the volcanism was focused on the actual Valle del Bove area, shifting from sporadic fissure eruptions to central-type magma uprising mechanism with formation of several small polygenic volcanic centres (De Beni et al., 2011). During this phase, the plumbing system started the construction of the first stratovolcano edifice, reaching a maximal elevation of about 2600 m (Branca et al., 2011). The main activity was associated to Trifoglietto centre (~107 – 99 ka ago) on the southern flank of Valle del Bove. Its activity consisted of effusive lava flows and explosive activity, which ended with a Plinian eruption which generated a thick sequence of pumice and flow deposits (Branca et al., 2011). In general, volcanism of this period varies from hawaiitic to benmoreitic composition (Corsaro et Pompilio, 2004).

(*iv*) In the Stratovolcano phase (Fig. 1.3d), the volcanism shifted 4 km NNW from previous eruptive centres, marking the building of Ellittico crater (Coltelli et al., 2000) about 57 ka

ago. Its activity was mainly characterized by explosive and effusive events from summit vents and flank fissures, allowing the expansion of its flanks until it reached the actual boarders of volcano (Branca and Ferrara, 2013) and a maximal elevation of about 3600 m a.s.l. (De Beni et al., 2011). About 15.5-15 ka ago, the Ellettico activity ended with the collapse of the summit area through four plinian eruptions, generating the Ellitico caldera (Coltelli et al., 2000). Since 15 ka ago, the volcanic activity consisted of effusive summit eruptions, that gradually filled the Ellittico caldera, and flank eruptions, that covered the previous morphology (Calvari et al., 1994). This kind of volcanism contributed to the construction of the actual morphological setting of Mt. Etna, called Mongibello volcano. About 10 ka ago, the eastern flank of the volcano was involved in a collapse that generated the depression of the Valle del Bove (Calvari et al., 2004). In the Holocene, explosive activity of Mongibello led to the formation of the Cratere del Piano caldera (Branca et al., 2011). In the last 2 ka, the effusive activity of the volcano allowed to fill the previous caldera and to build the present summit area.

The current volcanism may be divided into persistent activity and flank eruptions. The first one is linked to the summit craters, while the second ones are associated to fissures and magmatic intrusions. The summit activity of the volcano is various and can involve different types, such as degassing, strombolian or hydromagmatic explosions, lava filling or collapses and low rate lava emissions (Cristofolini et al., 1988). Flank eruptions are generally accompanied by lava flows (Harris et al., 2000) and explosion activity (Behncke and Neri, 2003; Andronico et al., 2005). In the last decades, Mt. Etna was characterized by a high level of activity, with a marked increase in effusive rates and in the frequency of summit and flank eruptions (e.g. Tanguy et al., 1996; Behncke and Neri, 2003; Allard et al., 2006; Di Grazia et al., 2006; Andronico et al., 2008; Bonaccorso et al., 2011; Behncke et al., 2014, Cannavò et al., 2017).

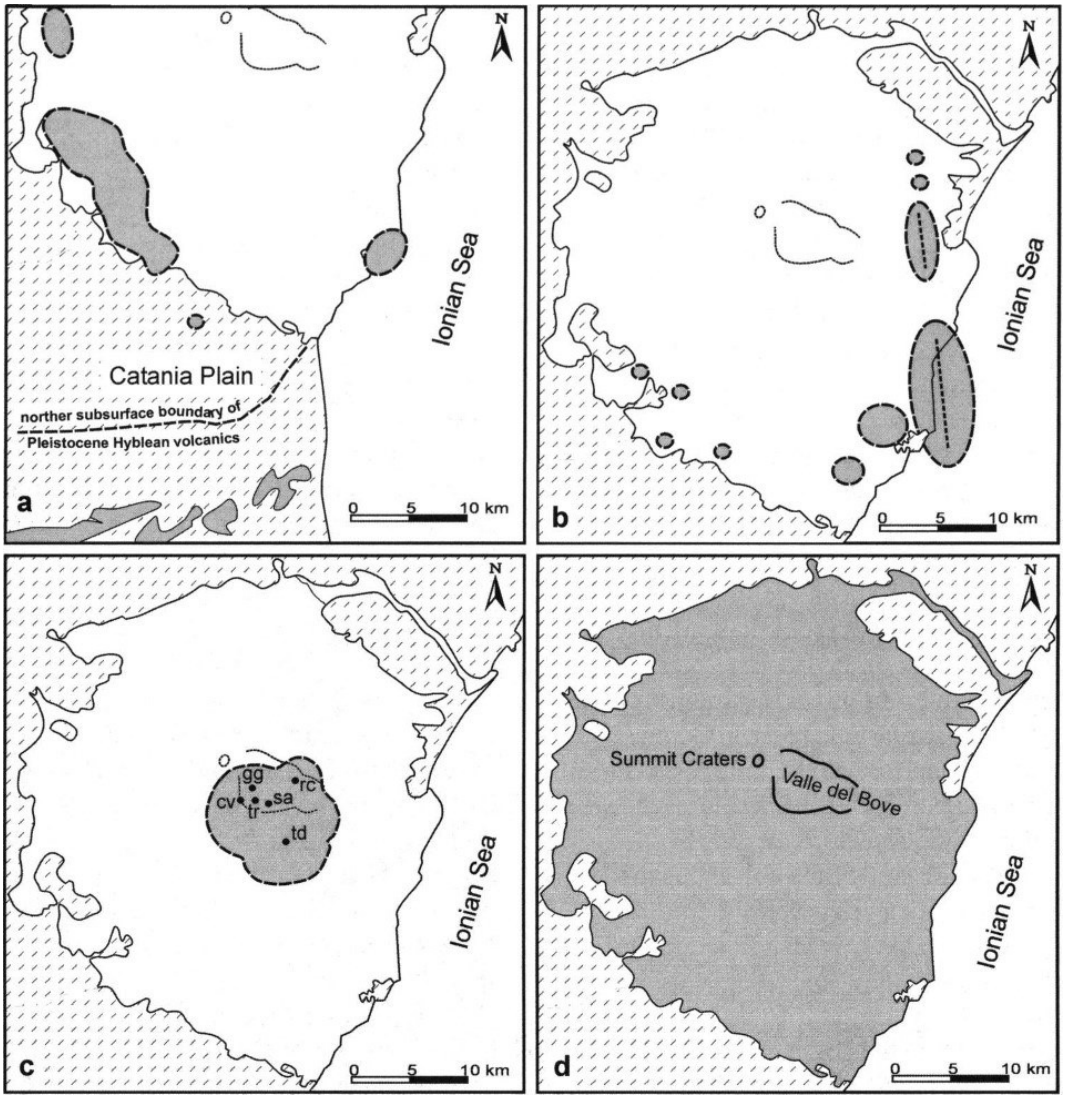

Figure 1.3. Schematic representation of Etna volcano evolutionary phases: a) Basal Tholeiitic phase; b) Timpe phase; c) Valle del Bove Centers phase, circle indicate the location of the volcanoes: td=Tarderia, rc=Rocche, tr=Trifoglietto, gg=Giannicola; sa=Salifizio, cv=Cuvigghiuni; d) Stratovolcano phase (from Branca et al., 2004).

1.2.2 GEODYNAMIC AND STRUCTURAL FRAMEWORK

Mt. Etna is situated in a complex structural area in which there are different domains (Fig. 1.4). It is characterized by a N-S maximum compression and an E-W maximum extension, due to the Euroasia-Africa plates collision and the development of the Malta Escarpment (Bousquet and Lanzafame, 2004), respectively. In particular, the volcano belongs to structural domain of Catania-Gela foredeep basin and it borders with three geostructural units: (*i*) the Appenine-Maghrebian chain at Nord and West; (*ii*) the Iblean foreland at South, belonging to the Pelagian block, the northrmost part of the African plate (Lentini et al., 2006); (*iii*) the Ionian basin at East, that represents an ocean basin developed between the middle-late Mesozoic and the Tertiary (Catalano et al., 2001). The Aeolian Maltese fault system ca be considered as the edge of two different crustal domains. This system extends from Malta Escarpment to Tyrrhenian Sea (Fig. 1.4), crossing the south-eastern coast of the Ionian Sea, the eastern portion of Etna (Timpe faults), the north-eastern Sicily and the Vulcano-Lipari-Salina alignment. The Aeolian-Maltese fault system divides also the Calabrian-Sicilian arc into two different sectors (Bousquet and Lanzafame, 2004): (*i*) the eastern portion, characterized by the subduction of the Ionian basin under Calabria; (*ii*) the western portion, in which there is a collisional regime.

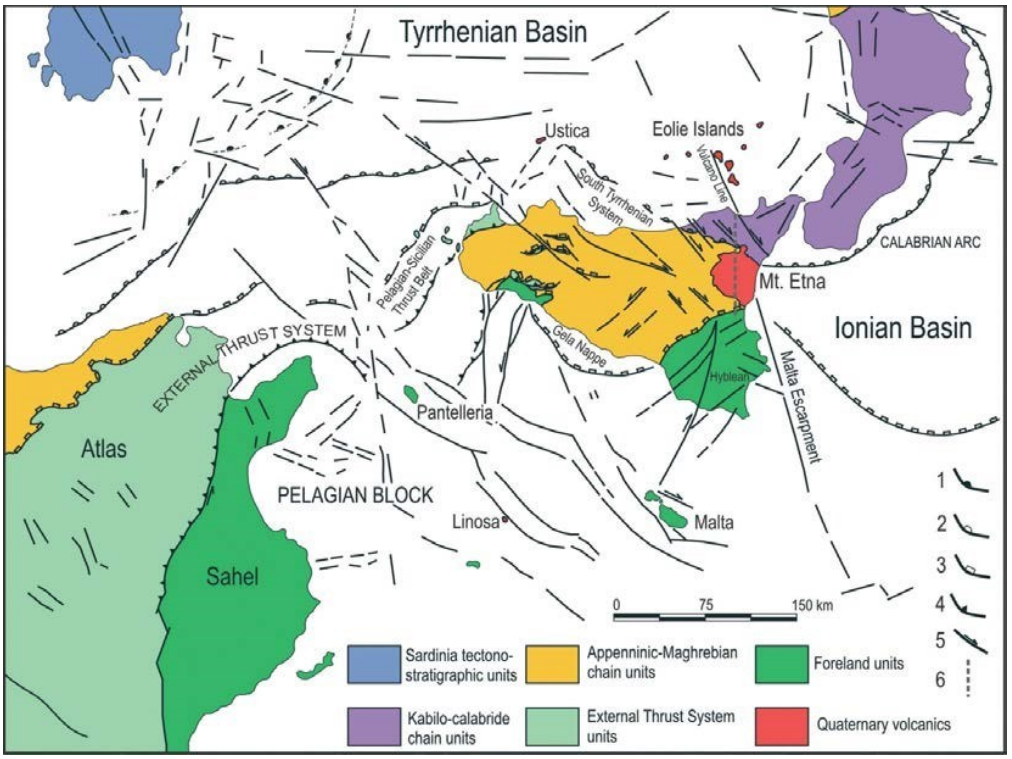

Figure 1.4. Structural setting of central Mediterranean Sea and location of Mt Etna (from Lentini et al.,2006).

The structural framework of Mt. Etna is very complex and results from the interaction between regional tectonic, flank instability and basement geometry (e.g. Bousquet and Lanzafame, 2004; Norini and Acocella, 2011; Azzaro et al., 2013). The Etnean area can be dismembered into different structural blocks that show homogeneous kinematic properties (Bonforte et al., 2011). The main structural lineaments of the unstable flanks of Mt. Etna are (Fig. 1.5): (*i*) Timpe fault system, (*ii*) Pernicana fault system, (*iii*) Mascalucia-Trecastagni fault system, (*iv*) Ragalna fault system, (*v*) NE rift, (*vi*) NNW-SSE fissure system, (*vii*) N-S fissure system, (*viii*) Other structures and volcanic alignments.

(*i*) Timpe fault system consists of normal faults that dip towards the Ionian Sea. This system trends SSW-NNE direction on the north-eastern area of the volcano, bending towards the south-eastern flank with a right-lateral component of motion (Azzaro et al., 2012). Most faults show steep escarpments, called Timpe and are associated with frequent shallow-depth seismicity (Azzaro et al., 2000). The fault system trends also towards North, uplifting the Ionian on-shore and reaching the Strait of Messina (Catalano and De Guidi, 2003). This structural line divides the area into two different tectonic domains, which are characterized by distinct seismogenic features: the eastern domain, seismically active, and the western domain, related to very shallow seismic activity (Falsaperla, 1999). This system extends also towards the base of Malta Escarpment (Bianca et al., 1999), dividing the relict Mesozoic Ionian basin from the Western Sicily.

(*ii*) Pernicana fault system extends towards East from the NE rift to the coastline over a distance of about 18 km (Neri et al., 2004). It represents the most active fault system in the region (Neri et al., 2004; Bonforte et al., 2011). In general, Pernicana fault system can be divided into two main domains, which show different mechanisms and seismic activity (Azzaro et al., 1998; Neri et al., 2004). The first part develops from NE rift to Presa and is characterized by normal dip-slip motion and shallow moderate seismic activity. The second one, rather, trends from Presa to the coastline, with left strike-slip motion and absence of seismic activity. Probably, these different deformation styles may be attributed to different rheological properties of their substratum (Neri et al., 2004). Recently, some authors (Cannata et al., 2021) identify four distinct domains of the fault, which show different behaviour in terms of seismicity, repeating earthquakes and ground deformation. According these authors, these different portions could be related to a segmentation of the fault plane at depth, suggesting an episodic triggering mechanism on the basis of the recurrence intervals of repeating earthquakes.

(*iii*) Mascalucia-Trecastagni fault system consists of NNW-SSE-oriented faults, deployed on the south-eastern flank of the Mt. Etna. The deformation mechanism is characterized by shallow seismicity and strike-slip motion (Lo Giudice and Rasà, 1992).

(*iv*) Ragalna fault system trends in the lower south-western flank of the volcano and it is composed by N-S striking faults (Azzaro et al., 2012). This system can be interpreted as the western boundary of the unstable south flank (Neri et., al 2007).

(*v*) NE rift is located on the north-eastern side of summit area of the volcano. The main structures of this system form a 5-km-long and 1-km-wide ridge across lavas and pyroclastics. These fissures have generally a gradual clockwise rotation along the rift towards NE (Tibaldi and Groppelli, 2002).

(*vi*) NNW-SSE fissure system trends S-SE direction on the south-western rim of the Valle del Bove. The upper portion of this structure is formed by closely spaced normal faults. The overall mechanism of the NNW-SSE system is associated to a right-lateral component of motion (Monaco et al., 2005).

(*vii*) N-S fissure system extends on the southern slope of the volcano through a set of N-S or SSW-NNE striking faults, covering a distance of about 10 km between the Montagnola Area and Nicolosi. Generally, these structures are about 1-2 km long and they are characterized by aligned cones or volcanic ridges (Monaco et al., 2005).

(*viii*) Other structures and volcanic alignments are radially distributed on the western flank of the volcano. Their characteristics suggest that they are related to a local deformation field affected by hydraulic load of the magmatic column in the central conduit (Villari et al., 1988).

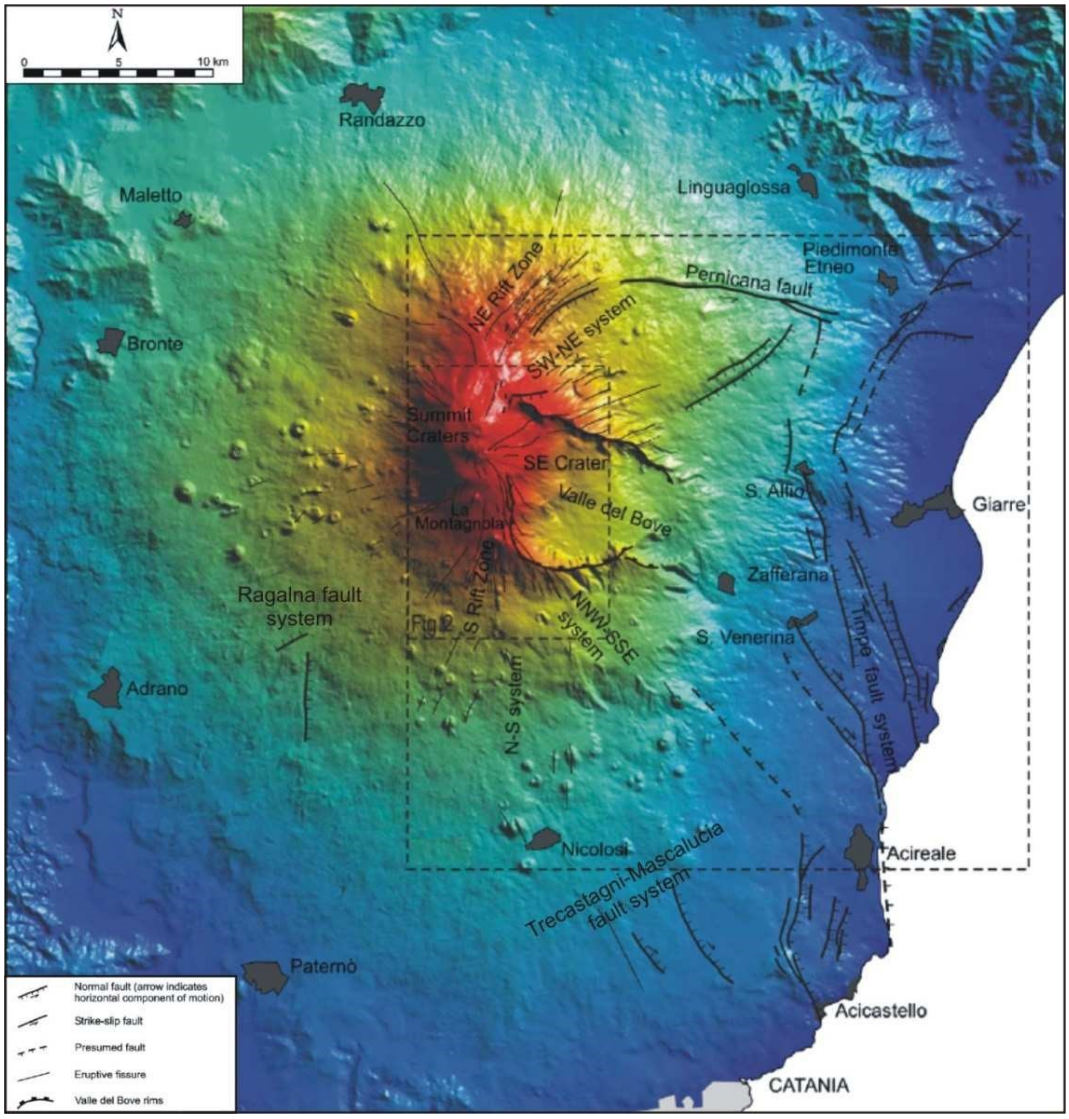

Figure 1.5. Map of active tectonics of Mt. Etna (redrawn from Monaco et al., 2005).

The complex geodynamic and structural features of Mt. Etna have led to elaborate a great number of models depicting its origin:

(i) According to some authors (Ritmann, 1973; Cristofolini et al., 1979; Lo Giudice et al., 1982), the intersection of three main faults system, extending E-NE, N-NW and W-NW, generate a weakness zone of magma uprising (Fig. 1.6a)

(ii) The entire volcanism of volcano is fed by a limited and continuous differentiation of the magma accumulated near the mantle-crust interface, in response to the asthenospheric upwelling and the melting of a mantle diaper (Tanguy et al., 1997-Fig. 1.6b).

(iii) The magmatism of Mt. Etna can be related to the rollback of the Ionian slab underneath the Calabrian Arc (Gvirtzman and Nur, 1999-Fig. 1.6c). This leads to the opening of a gap between the Ionian lithosphere and the African plate, which is filled through the melting of asthenospheric material. According to other authors (Doglioni et al., 2001), the rollback process, rather, is affected by the transtesional mechanism of the Malta escarpment, creating a zone of magma ascent between the Sicilian and Ionian segments of Appennines slab.

(iv) On the basis of structural, seismological and volcanological studies (Monaco et al., 1997; Monaco et al., 2005), the conditions of magma uprising are heavily related to the dilatational strain on the normal fault system located on the Ionian shore (Fig. 1.6d).

(v) The ascent of magma is attributed to the instability of the eastern flank of the volcano (Fig 1.6e). Considering seismic and geodetical data in agreement with high deformation rate measured on the eastern or south-eastern slope of the volcano, the eastern sector of Mt. Etna highlights a high dynamism (Bonaccorso et al., 2006; Bonforte et al., 2011; Azzaro et al., 2013). In particular, this unstable sector is bounded northward by the Pernicana fault, westward by the North-East Rift and the South Rift, and southward by the Mascalucia- Trecastagni fault system. These structures join with a displacement plane located at a depth of about 1.4-4 km (Palano et al., 2008), which corresponds to the maximum depth of the earthquakes recorded along the Pernicana fault (Alparone et al., 2013). The sliding movement of this plane is thought to reproduce the eastward motion of the eastern slope towards the sea, facilitating the decompression of the plumbing system and the uprise of magma to the surface (Neri et al., 2004; Privitera et al., 2012).

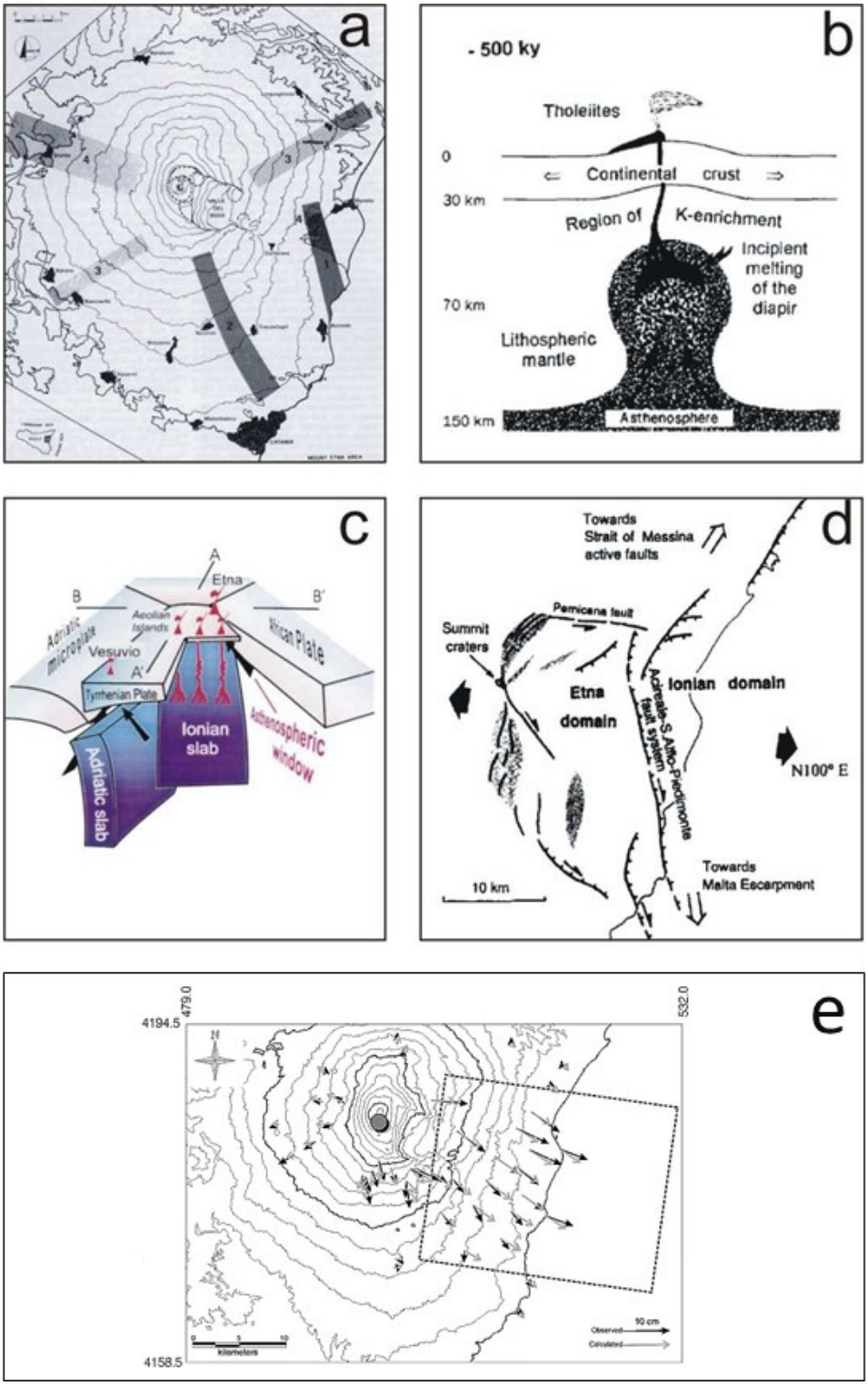

Figure 1.6. a) Main sheaves of tectonic linear elements in the Etnean area (from Lo Giudice et al., 1982). b) Schematic representation of Mt. Etna in Tanguy et al. (1997). c) Three-dimensional sketch of the south Tyrrhenian subduction zone (from Gvirtzman and Nur, 1999). Red lines represent magma rising. Black arrows represent local patterns of mantle flow driven by slab motion. d) Cartoon showing the kinematic interpretation of major structures of Mt. Etna (from Monaco et al., 1997). e) Models of flank instability at Etna proposed by Bonaccorso et al. (2006).

1.2.3 VOLCANIC TREMOR AT MT. ETNA

Volcanic tremor is a seismic signal that is generally observed at volcanoes around the world, such as Mt. Etna. It is frequently used to study volcanic activity, due to its close relationships with magmatic and hydrothermal activity in the volcano's plumbing system (e.g. Kostantinou and Schlindwein, 2002). Several models have been developed to explain the source mechanism of volcanic tremor, although most part of authors concord to attribute its origin to the complex interplay among the magmatic-hydrothermal fluids and their host rock (Chouet, 1986; Julian, 1994; McNutt, 1996; Fujita, 2008).

At Mt. Etna, the first instrumental observations of volcanic tremor were performed by Schick and Riuscetti (1973). Successively, many different studies led to constrain conclusion about its source mechanism, highlighting the complexity of the problem. One characteristic aspect of this signal at Mt. Etna is its persistency in time, as observed at many other basaltic volcanoes with persistent activity such as Stromboli (e.g. Langer and Falsaperla, 1996). This type of volcanic tremor, defined as *ordinary tremor*, may be accompanied or substituted by *banded tremor*, as occurred during March-May 1987 (Gresta et al., 1996) and in August-October 2008 (Cannata et al., 2010). According to these authors, this kind of tremor showed different frequency content and source location compared to the *ordinary tremor*, suggesting different sources for the two types of signals. In particular, the banded tremor generation may be attributed to the action of the hydrothermal fluids, while magma passively affects the phenomena, such as a heat source.

In general, volcanic tremor has always been observed in concomitance with degassing, explosive and effusive activity from the summit or flank craters (e.g. Del Pezzo et al., 1993; Falsaperla et al., 1994; Alparone et al., 2003; Privitera et al., 2003). Variations in amplitude, frequency content, wavefield features and source locations occurred concurrently with changes in volcanic activity (Di Grazia et al., 2006, 2009; Alparone et al., 2007; Carbone et al., 2008; Patanè et al., 2008; Cannata et al., 2009b; Viccaro et al., 2014; Cannata et al., 2013,2015). In particular, during paroxysmal events, tremor amplitude is correlated well with the height and duration of lava fountains (Alparone et al., 2003; Privitera et al., 2003; Carbone et al., 2006; Patanè et al., 2013), while its source position undergoes both vertical and lateral migration on the basis of the changes in paroxysmal activity (Patanè et al., 2013; Viccaro et al., 2014; Cannata et al., 2013, 2015). In addition, the spatial distribution of seismic amplitudes and polarization attributes of tremor also highlighted a contribution from deeper sources (Alparone et al., 2003; Privitera et al., 2003; Di Grazia et al., 2006, 2009).

1.2.4 LP AND VLP EVENTS AT MT. ETNA

Since 2003, the installation of the first permanent three component broad-band stations allowed a better evaluation of the low frequency seismic activity, making LP and VLP events as the most common signatures at Mt. Etna (Farsaperla et al., 2002; Saccorotti et al., 2007; Lokmer et al., 2007, 2008; Zuccarello et al. 2013; Cannata et al., 2013,2015). Generally, they develop in swarms or as independent events and they also occur during both eruptive and non-eruptive periods of the volcano (Patanè et al., 2008; Cannata et al., 2009a; Patanè et al., 2013 Cauchie et al., 2015; Cannata et al., 2015). On the basis of their waveform similarities, low frequency events can be classified into families (e.g Falsaperla 2002; De Barros 2009, 2011; Zuccarello et al., 2013).

According to some authors, LP and VLP events were also characterized by almost constant spectral and waveform properties in the long term, which were associated to a repetitive non-destructive source mechanism (Farsaperla et al., 2002; Saccorotti et al., 2007; Lokmer et al., 2007, 2008; Cannata et al., 2009a; De Barros et al., 2009; Cannata et al., 2013,2015). Some of these authors have also found the LP and VLP sources in a volume located above the shallow magma storage zone, over 2500-3000 and 2000-2500 metres above sea level, respectively for LP and VLP events.

Due to their low frequencies, LP and VLP has allowed to perform a moment tensor inversion of the seismic source at Mt. Etna, proving information about magma dynamics and geometry of the shallower portion of the plumbing system (Lokmer et al., 2008, Cannata et al., 2009a; De Barros et al., 2011,2013; Zuccarello et al., 2013; Trovato et al., 2016). Therefore, for Mt. Etna., several models have been proposed to explain their source mechanisms.

The generation of LP was generally attributed to one or more resonant fluid filled cracks at relatively shallow depths (Falsaperla et al., 2002; Saccorotti et al., 2007; Lokmer et al., 2008; De Barros et al., 2011). However, recently, Bean et al., (2014) have proposed a new source model based on the deformation of weak, compliant material of the shallow portion of the Etnean volcanic edifice. This interpretation was implicitly consistent with the recent work of Cauchie et al. (2015), who imagined that stress changes associated to degassing pulse could indirectly generate LP events.

The source processes involved in VLP events were thought to be related to magma transport, gas slug ascent or dike resonance initiated by a fluid driven process (Aiuppa et al., 2010; Patanè et al., 2008). According to these authors, VLP events could be triggered

by gas bubbles released from the aforementioned magma storage zone, exciting a crack or system of cracks located in the upper portion of the shallow plumbing system of Mt. Etna. Therefore, variations in the frequency, amplitude, and waveform characteristics of these signals could be interpreted as pressure changes within the magmatic system (e.g. Saccorotti et al., 2007; Patané et al., 2008; Cannata et al., 2009a; Patanè et al., 2013, Zuccarello et al., 2013).

Sometimes, LP and VLP seismicity are interlinked, although these relationships are not systematic. Indeed, different authors recognized relationships between the shallower LP and the deeper VLP, suggesting the presence of a common system of shallow cracks in which both LP and VLP oscillation were originated (Patanè et al., 2008; Cannata et al., 2009a). Other authors, rather, argued that the source trigger of VLP events was related to mass transfer, while the subsequent mass injection in overlying cavities could have driven the LP resonance in a reservoir filled of hydrothermal fluids (Saccorotti et al., 2007).

1.2.5 VOLCANIC FRAMEWORK DURING 2010-2012 ACTIVITY

In the early months of 2010, the summit area of Mt. Etna was relatively quiescent. The resumption of volcanic activity began in March, through high-temperature degassing at SEC (Andronico et al., 2013). Subsequently, in the remainder of year, more than 30 minor explosive events occurred mainly at BN and secondarily at SEC (Table 1). These events consisted of single explosions or series of explosions, developed within a few second of each other and accompanied by minor and/or intense ash emissions. Comparing to the previous similar periods of volcanic activity, this year was distinguished from others by the high occurrence frequency of explosions. Most of these explosions were directly observed by camera records or visual field observations, but, in some cases, they have been observed through the ash fallout collection or the seismo-acoustic recordings (Andronico et al., 2013). In particular, three of these events (8 April at SEC and 25 August and 22 December at BN) were more intense than the others in terms of duration, height of eruptive column and amount of tephra. Moreover, some of the events, that occurred on 14-15 November at NEC, were characterized by continuous but low ash emissions and vigorous steam releases, creating a weak eruption column above the volcano.

From January 2011 to the end of April 2012, Mt. Etna was characterized by intensification of eruptive activity in the summit area, focused at NSEC through a series of brief episodes of vigorous lava fountaining, ash emissions and generation of lava flows (paroxysms).

Since the early days of January 2011, the increment of volcanic activity began with Strombolian activity at the pit crater near SEC, culminating with a paroxysmal episode on 12 January at the same crater. Starting with first event, other 24 episodes occurred, producing significant morphological changes in the summit portion of the volcano such as the growth of the NSEC cone (Behncke et al., 2014).

During this period, these 25 paroxysms did not take place with a constant rate, but they were characterized by different number and duration of episodes and frequency of occurrence (Behncke et al., 2014; Table 2). In fact, the intervals between paroxysmal episodes varied strongly, from a minimum of 5.5 days to a maximum of 58 days. In particular, from January to May 2011, only 4 episodes of lava fountaining occurred. The intensification of the occurrence of paroxysmal activity, rather, was observed between July and November 2011, with the development of 14 episodes. After a period of relative quiet, the volcanic activity culminated with 7 paroxysmal episodes during the early months of 2012 (January-April 2012).

Most part of these events ware characterized by similar dynamics or a common succession of volcanic phases (Behncke et al., 2014; Viccaro et al., 2014): (*i*) *reactivation phase*, which consisted of minor explosive activity and ash emissions; (*ii*) *Strombolian activity*, with duration from a few hours to many days; (*iii*) *lava emission*, preceding the onset of lava fountaining from a few tens of minutes to several hours; (*iv*) progressive intensification of Strombolian activity until the development of *lava fountaining*, with duration from a few tens of minutes to many hours; (*v*) *end of episode*, characterized by gradual decrease of the lava fountaining intensity replaced by a weak Strombolian activity, ash emission and draining of lava flow from the main channel. However, significant differences from this main sequence can be found in the initial stages of some events. In fact, some episodes were characterized by different paroxysmal schemes, in which the extrusion of lava preceded the onset of the Strombolian explosions (15 November 2011) or started a few minutes after the onset of lava fountaining (19 July 2011) or developed without any explosive activity (23 April 2012).

During the same time interval, the other summit craters were interested only by persistent degassing activity, except for the BN crater. From June to July 2011, this crater also showed explosive activity, ash emissions, intra-crater Strombolian activity and emission of lava flow (Behncke et al., 2014; Viccaro et al., 2014). The same kind of activity occurred at BN craters during 2012, in the periods between June-August and October-November (Aiuppa

et al., 2016). A schematic review of the activity recorded at Mt. Etna during 2011-2012 can be observed in the Fig. 1.7.

Explosive events	Failure Events	Glowing episodes	Date	Time (GMT)	SEC	BN	NEC
1			08-apr	16:28	**XXX**		
2			7 May	11:04	x		
3			19 June	06:22–06:52	x		
		1	29 June	13:15	glow		
4			5 July	05:01		X	
			8 August	10:01		X	
5			25 August	13:09		**XXX**	
6			25 August	17:28		X	
7			25 August	23:25		X	
		2	26 August	22:20	glow		
8			26 August	02:08		X	
9			27 August	09:28		X	
10			27 August	16:00		X	
11			28 August	09:14		X	
12			28 August	14:18		X	
13			29 August	01:00–01:17		X	
14			29 August	05:39		X	
15			29 August	07:31		X	
16			30 August	07:28		X	
17			3 September	/		X	
18			4 September	13:01		X	
19			6 September	22:42		X	
20			10 September	10:42		X	
21			12 September	11:13		X	
22			13 September	07:04		X	
23			17 September	07:57		X	
	1		18 September	/	X		
24			24 September	12:46		X	
25			30 September	10:02		X	
26			7 October	09:27			
27			8–9 October	23:44		X	
28			9 October	00:35		X	
29			22 October	16:23		X	
	2		31 October	15:33		X	
30			1 November	02:08		X	
31			1–2 November	02:22		X	
	3		2–4 November	/	X		
	4		12 November	/	X		
32			14–15 November	05:25			**XX**
33			7 December	14:30			
34			22 December	04:46		**XXX**	
35			29–30 December	16:28	X + Str. Act.		

Table 1. List of the explosive events observed in 2010, subdivided into related to explosive activity and related to the source vent (data from Andronico at al., 2013). Abbreviations: SEC, Southeast Crater; BN, Bocca Nuova; NEC, Northeast Crater; X, minor ash emission; XX, prolonged ash emission; XXX, intense ash emission.

Episode	Start Reactivation	Start Strombolian	Start lava emission	Start fountaining	End fountaining	End episode	Episode duration (hh:mm:ss)	Lava fountaining Duration (hh:mm:ss)
1	2/1/11 16.00	11/1/11 8.00	12/1/11 20.10	12/1/11 21.50	12/1/11 23.50	13/1/11 2.00	42:00:00	2:00:00
2	18/2/11 1.00	18/2/11 1.45	18/2/11 12.00	18/2/11 3.30	18/2/11 12.30	18/2/11 13.17	12:20:00	9:00:00
3	29/3/11 8.00	8/4/11 6.00	9/4/11 17.55	10/4/11 8.05	10/4/11 13.30	10/4/11 14.03	56:00:00	5:25:00
4	8/5/11 6.00	11/5/11 17.00	11/5/11 20.30	12/5/11 3.20	12/5/11 5.00	12/5/11 5.55	96:00:00	1:40:00
5	4/7/11 7.00	7/7/11 20.00	9/7/11 12.05	9/7/11 13.45	9/7/11 14.45	9/7/11 15.30	128:30:00	1:00:00
6	16/7/11 8.00	18/7/11 17.00	19/7/11 0.00	19/7/11 0.05	19/7/11 1.30	19/7/11 3.00	67:00:00	1:25:00
7	24/7/11 16.00	24/7/11 18.00	25/7/11 1.30	25/7/11 3.00	25/7/11 5.00	25/7/11 5.30	13:30:00	2:00:00
8	28/7/11 20.00	30/7/11 7.50	30/7/11 17.30	30/7/11 19.35	30/7/11 21.35	30/7/11 22.00	50:00:00	2:00:00
9	5/8/11 16.00	5/8/11 17.00	5/8/11 20.15	5/8/11 21.00	5/8/11 23.00	6/8/11 0.15	8:15:00	2:00:00
10	11/8/11 3.30	12/8/11 5.30	12/8/11 7.50	12/8/11 8.30	12/8/11 10.00	12/8/11 11.00	31:30:00	1:30:00
11	19/8/11 3.36	20/8/11 2.00	20/8/11 2.55	20/8/11 7.00	20/8/11 7.30	20/8/11 7.50	28:15:00	0:30:00
12	28/8/11 0.52	28/8/11 18.00	29/8/11 3.15	29/8/11 4.05	29/8/11 4.40	29/8/11 5.15	28:30:00	0:35:00
13	6/9/11 12.00	8/9/11 5.30	8/9/11 6.50	8/9/11 6.30	8/9/11 8.30	8/9/11 8.45	45:15:00	2:00:00
14	16/9/11 10.27	19/9/11 2.00	19/9/11 6.30	19/9/11 12.20	19/9/11 13.00	19/9/11 13.10	74:30:00	0:40:00
15	28/9/11 8.00	28/9/11 17.30	28/9/11 19.15	28/9/11 19.31	28/9/11 19.55	28/9/11 20.10	12:10:00	0:24:00
16	8/10/11 11.00	8/10/11 11.24	8/10/11 13.30	8/10/11 14.30	8/10/11 14.50	8/10/11 17.45	6:45:00	0:20:00
17	23/10/11 17.13	23/10/11 17.40	23/10/11 18.07	23/10/11 18.30	23/10/11 20.30	23/10/11 21.15	4:00:00	2:00:00
18	15/11/11 6.00	15/11/11 8.00	15/11/11 6.00	15/11/11 11.00	15/11/11 12.29	15/11/11 13.00	7:00:00	1:29:00
19	4/1/12 8.00	4/1/12 16.00	5/1/12 2.45	5/1/12 5.00	5/1/12 6.50	5/1/12 8.30	24:30:00	1:50:00
20	27/1/12 11.24	27/1/12 21.40	8/2/12 19.00	9/2/12 0.00	9/2/12 5.30	9/2/12 9.00	309:30:00	5:30:00
21	16/2/12 0.00	16/2/12 20.00	4/3/12 6.00	4/3/12 7.30	4/3/12 9.32	4/3/12 9.32	417:30:00	2:02:00
22	16/3/12 0.00	17/3/12 20.00	18/3/12 5.55	18/3/12 8.00	18/3/12 9.45	18/3/12 10.10	58:10:00	1:45:00
23	26/3/12 0.00	30/3/12 18.30	1/4/12 1.00	1/4/12 2.00	1/4/12 3.30	1/4/12 4.30	154:10:00	1:30:00
24	10/4/12 17.50	11/4/12 19.00	12/4/12 12.25	12/4/12 14.30	12/4/12 15.15	12/4/12 16.00	46:10:00	0:45:00
25	21/4/12 10.00	23/4/12 17.00	23/4/12 0.00	24/4/12 1.30	24/4/12 2.20	24/4/12 2.40	64:20:00	0:50:00

Table 2. Timing of the various phases recognized for each episode and duration both of the lava fountaining phases and the full episodes (Data from Behncke et al., 2014).

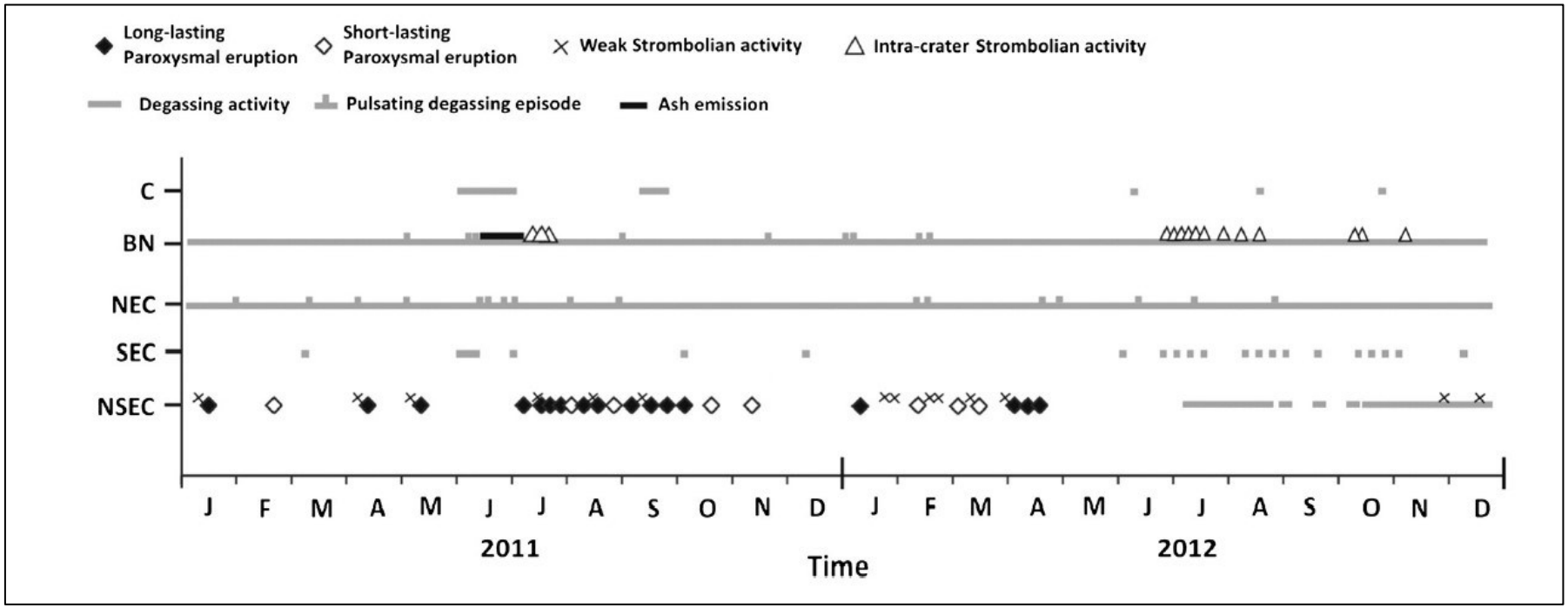

Figure 1.7. Plot summarizing the eruptive activity during 2011-2012 at Voragine (VOR), Bocca Nuova (BN), North East Crater (NEC), South East Crater (SEC) and New South East Crater (NSEC). (from Viccaro et al., 2014).

1.3 SEISMIC ARRAYS AND METHODS OF ANALYSIS

An array consists of multiple, tightly clustered sensors arranged in a well-defined geometric configuration and deployed outside the source area. The sensors have the same response curve and they are time synchronized, in order to obtain a coherent spatial sampling of the wavefield in time (Havskov, 2016).

They are used in geophysics in many fields of application. The deployment of the first seismic arrays dates back to the beginning of the 1960s, when it was necessary to improve the detection threshold of worldwide underground nuclear tests and to discriminate between them and global natural earthquakes (e.g. Douglas et al., 1999, 2002). Since then, thanks to their powerful potentiality, seismic arrays were also used for other scientific purposes, such as estimation of the seismic phases vectors (e.g. Shyh-Jeng et al., 1993), signal extractions and polarization analysis (e.g. Jurkevics, 1988; De Meersman et al., 2006), characterization of a rupture propagation during an earthquake (Goldstein and Archuleta., 1991), refining small scale structures in the Earth's interior (e.g. Weber and Wicks, 1996) or high resolution tomographic images on regional scales (e.g. Arlitt et al., 1999).

In recent years, another application field has been represented by the array surveys performed in volcanic areas, where conventional networks are difficult to use. Several of these studies have provided insight into the nature of the seismo-volcanic sources, the structures and the magmatic processes at different volcanoes in the world. One of the earliest investigations dated back to the work of Furumoto et al. (1990), that characterized the source of tremors recorded by a seismic array located near the caldera of Izu-Ochima volcano, Japan. They observed post eruption activity by a 24 sensors seismic array, revealing frequency features of the source tremor. Almendros et al. (2001a,b) located source areas of LP and volcanic tremor seismicity observed at Kilauea, Hawaii (USA). This seismicity was recorded in 1997 during a campaign through three seismic antennas composed of one component seismometers. La Rocca et al. (2004) applied dense one-component array techniques to locate explosive activity at Stromboli. Di Lieto et al. (2007) used two dense one-component arrays of short period seismometers to track volcanic tremor at Mt. Etna. Inza et al. (2011, 2014) analysed a series of 16 vulcanian explosions occurred at Ubinas volcano (Perù) by using three component seismic arrays. Zuccarello et al. (2016) recorded the seismic noise by using a temporary array installed around Pozzo Pitarrone, NE flank of Mt. Etna. They investigated the local shallow structure, producing a reliable shear wave velocity model of the area. Eibl et al. (2017a,b) estimated the vertical

and lateral migration of source tremor recorded at Bárdarbunga volcano (Iceland) through a seismic array.

A seismic array differs from a sparse network of stations mainly by the techniques used for data analysis. In a network, arrival times are determined at each station, while, in an array, all sensors are processed together on the basis of the common waveform model (Aki e Richards, 1980). The waveform at a given sensor depends on the source, path and site effects. Considering a seismic array, the records share very similar waveforms, except for time delay due to the different source-receiver distances across the array. In fact, path effects, at least the frequencies/wavelengths of volcanic tremor and/or LP and VLP events, are pretty much the same when sensors are separated by only tens of meters, and, therefore, the array records share very similar waveforms. Slight differences in waveforms generally appear at higher frequencies, mostly due to small differences in the installation of each individual sensor within the array (e.g. Almendros et al., 2012). The use of array allows to improve the signal-to-noise ratio (SNR) by time-shifting and summing all records, so that the signal of interest is in phase across all channels of array. Even if there is the presence of a non-local correlated noise, such as ocean generated noise, the time delay is not the same for signal and noise, because of their different wavefield properties. This method can be described by the same mathematical principles used in radioastronomy or radar science (Harjes and Henger, 1973).

In array processing, ray spatial coherency is assumed, so that each wavefront keeps its shape during the propagation across the array. For each spectral component, the phase relation among points along the ray path is only related to their reciprocal distances. This makes the size of any array as a function of the area homogeneity and the wavelengths of interest, because earth heterogeneities destroy the wavefield coherency through wave scattering and diffraction. In particular, the waveform similarity is wavelength-dependent and the records are very coherent only for inter-station distances shorter than a few wavelengths. Therefore, size, spacing and geometry of the array are decided based on the wavelength range of interest. In addition, it is important not to neglect “spatial aliasing”, that is the distortion or artifact that results when a signal reconstructed from samples is different from the original continuous signal (Haldorsen, 2021). To avoid spatial aliasing, the sensors of array must be separated by less than half of the shortest wavelength in the signal of interest (Asten and Henstridge, 1984). According to Aster and Scott (1993), the maximum reciprocal distance among array sensors should be about a quarter of signal wavelength that we want to analyze. In particular, the best waveform coherence is achieved

when the wavelength of interest ranges from two times the minimum array aperture to three times the array maximum aperture (Tokimatsu, 1997). Most array methods assume a plane wave arriving at array, representing a good approximation for far field investigations. In this case, the source-sensors distances must be greater than one wavelength (Havskov, 2016). According to this relationship, a sparse network may be used as an array for those events characterized by longer wavelength, such as LP or VLP events.

As mentioned above, seismic arrays are very useful to investigate the nature of volcanic signals and to understand magmatic phenomena. However, a quantitative assessment of the source signal processes must take into account all the other properties of wavefield, such as spectral, amplitude and polarization features. In fact, temporal changes of these parameters can provide insights on the relationship between the source mechanisms and the volcanic activity, also allowing to improve the reliability of array analysis results (e.g. Saccorotti et al., 2004). Therefore, in the next sections, we present not only the concepts and the main methods used to perform the array analysis, but all algorithms used to perform a complete analysis of seismo-volcanic signals properties.

1.3.1 BASIC ARRAY CONCEPTS

The propagation direction of elastic waves arriving at a seismic array can be described by three parameters (Fig. 1.8; Fig.1.9):

(i) Back azimuth Θ, that is the angle of wavefront measured clockwise from North to the direction pointing towards the source.

(ii) Slowness u, that is the inverse of the apparent velocity v_{app} of wavefront across the array.

(iii) Incidence angle i, that is the vertical angle of wavefront measured from the vertical ($0° < i < 90°$).

In spherical geometry (Fig. 1.9), all parameters are combined in the slowness vector u (Rost and Thomas (2002):

$$u = (u_x, u_y, u_z) = \left(\frac{\sin\theta}{v_{app}}, \frac{\cos\theta}{v_{app}}, \frac{1}{\tan i}\ v_{app}\right) =$$

$$= \frac{1}{v_0}(\sin i \ \sin\theta\,, \sin i \cos\theta\,, \cos i)$$

(1.0)

where v_0 is the medium velocity beneath the array. The magnitude of the vector u, also called ray parameter P, and the back azimuth Θ are related to the horizontal components of slowness (u_x , u_y; Chouet et al. (1997)):

$$\theta = \frac{\pi}{2} - \tan^{-1}\frac{u_x}{u_y}$$

(1.1)

$$P = \sqrt{u_x^2 + u_y^2}$$

(1.2)

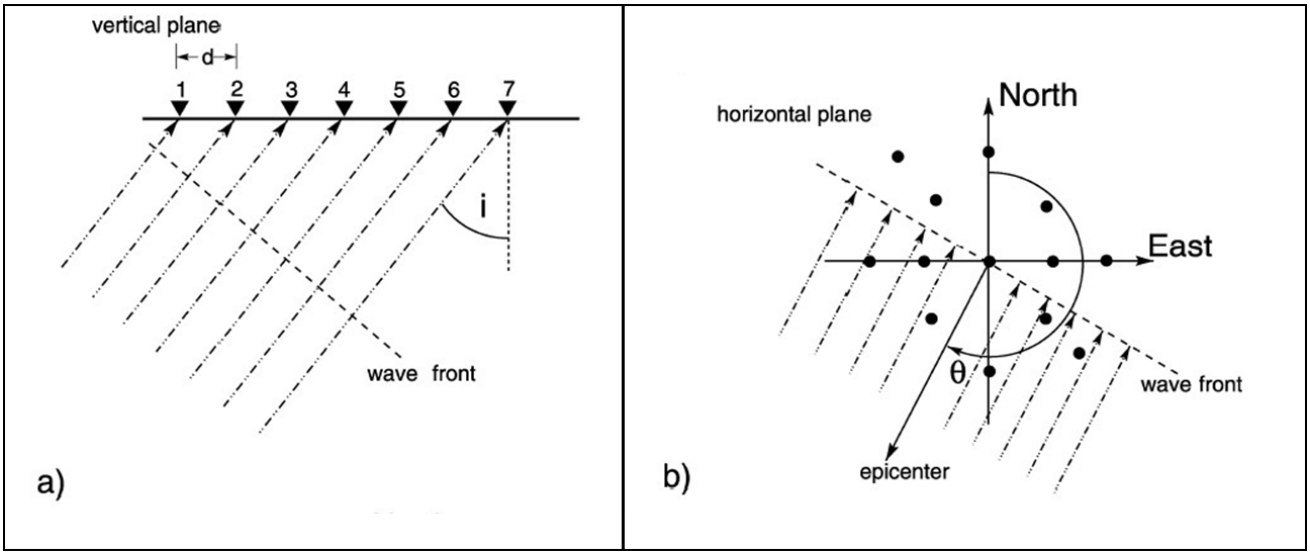

Figure 1.8. a) The vertical plane of an incident wavefront crossing an array at an angle of incidence *i*. b) Sketch of the horizontal plane of an incident plane wave arriving with a back azimuth Θ (from Rost and Thomas, 2002).

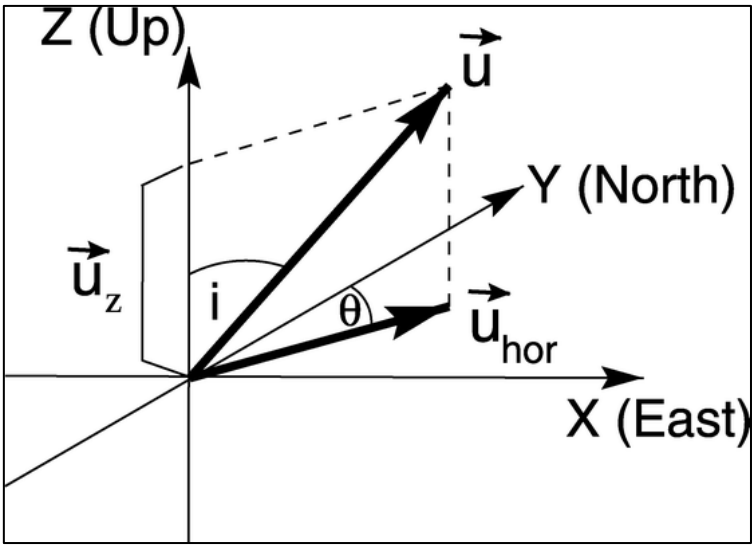

Figure 1.9. Representation of the slowness vector and its three components (from Rost and Thomas, 2002).

The propagation velocity of the waves depends on the physical and mechanical properties of the medium. However, the time necessary for the propagation of the waves from source to array sensors is related to medium velocity v_0 beneath the array and incidence angle i. Considering an incident wavefront crossing an array (Fig. 1.8a), the effective distance travelled by the wavefront is much shorter than that measured at Earth's surface. Therefore, the apparent velocity v_{app} is always greater than or equal to the effective propagation velocity v_0 (Rost and Thomas, 2002):

$$v_{app} = v_0 \,/\, sin\, i \tag{1.3}$$

Knowing the values of the ray parameter P and the medium velocity v_0 beneath the array, the incidence angle i can be estimate as (Rost and Thomas, 2002):

$$i = arsin\ (v_0\ P) \tag{1.4}$$

Arrays can be used to measure the apparent velocity or slowness and the back azimuth of the wavefront that is moving horizontally across the stations, determining the type of phases and the region of the Earth from where the seismic energy comes (Rost and Thomas, 2002). As mentioned above, an important aspect of array methods is the separation of the coherent signals and noise. Many methods have been developed for special purposes, but most of them are based on the basic concept of array beam forming (Barlett,1948). Beam forming

uses the differential travel times across the array. If each record of array sensors is appropriately time shifted for a certain back azimuth and slowness, all signals can be summed constructively. Considering the geometrical center of the array, the incident wavefield with coherent signal $f(t)$ and noise $n_i(t)$ is recorded as (Rost and Thomas, 2002):

$$x_{center}(t) = f(t) + n_i(t) \tag{1.5}$$

Given the various locations of array sensors, the incident wavefront has different travel times to each station. The travel time difference is related to the slowness of the wavefront and the station position. Therefore, the time series associated to with the *i-th* sensor with the location r_i can be expressed as (Rost and Thomas, 2002):

$$x_i(t) = f(t - r_i u_{hor}) + n_i(t) \tag{1.6}$$

where u_{hor} is the horizontal slowness vector. Removing the time shifts with appropriate slowness, the equation 1.6 can be written as (Rost and Thomas, 2002):

$$x'_i(t) = x_i(t + r_i u_{hor}) = f(t) + n_i(t + r_i u_{hor}) \tag{1.7}$$

Considering an array with M sensors, the summation of the time shifted traces provides an evaluation of the signal coherence (Rost and Thomas, 2002):

$$b(t) = \frac{1}{M}\sum_{i=1}^{M} x'_i = f(t) + \ 1/M \ \sum_{i=1}^{M} n_i(t + r_i * u_{hor}) \tag{1.8}$$

In general, seismic arrays use these techniques or similar methods to amplify phases with the appropriate slowness and to suppress incoherent noise and phases with different slowness. However, most of the array methods shows some limitations. In fact, the noise suppression is dependent on the number of stations used for the processing. At the same time, the slowness estimation is affected by multiple factors, such as array characteristics, wavelengths or frequencies analyzed, amount of coherence, noise content and topographic, propagation and site effects.

1.3.2 ARRAY RESPONSE

As mentioned before, any array method is based on a common waveform model of the signal (Aki e Richards, 1980), requiring that the wavefield is sampled both in space and in time. This means that each array sensor acquires the same waveform, except for a delay time related to the propagation across the array. The results of array analysis depend on the number of stations, the array aperture and configuration and the contribution of spatial aliasing. The array response function is as a good tool to plan the array geometry required to investigate a signal of interest. One of the best ways to compute the array response is to use a modified version of the Beam Pattern relationship (Capon, 1969):

$$B(S,w) = \frac{1}{M}\sum_{j=1}^{M} e^{iwSx_j} \tag{1.9}$$

where M is the number of stations, x their locations, w is the angular frequency, S the slowness vector and i the imaginary unit. For a given slowness and angular frequency, the function B (S, w) depends on only the station positions and it returns the array response of a monochromatic plane wave with vertical incidence. It consists of a central peak of unit amplitude and many secondary peaks at different locations in the slowness space. When the amplitude of the secondary peaks is much smaller than the central one, the spatial aliasing is negligible. An example is reported in figure 1.10 that show a small contribution of spatial aliasing in the array response. Regarding the frequency range, the broad peak observed at frequency 0.5 Hz indicates that the array resolution is poor at so low frequency (Fig. 1.10a), as expected being the signal wavelength larger than the array extension (Fig. 1.10b). The upper frequency limit is more difficult to estimate in practice because it depends on the station distances and by site effects, which reduce the coherence of the seismic wavefield among the array stations. In this example, the results of array analysis revealed to be reliable up to frequency of 4 Hz (Fig. 1.10a).

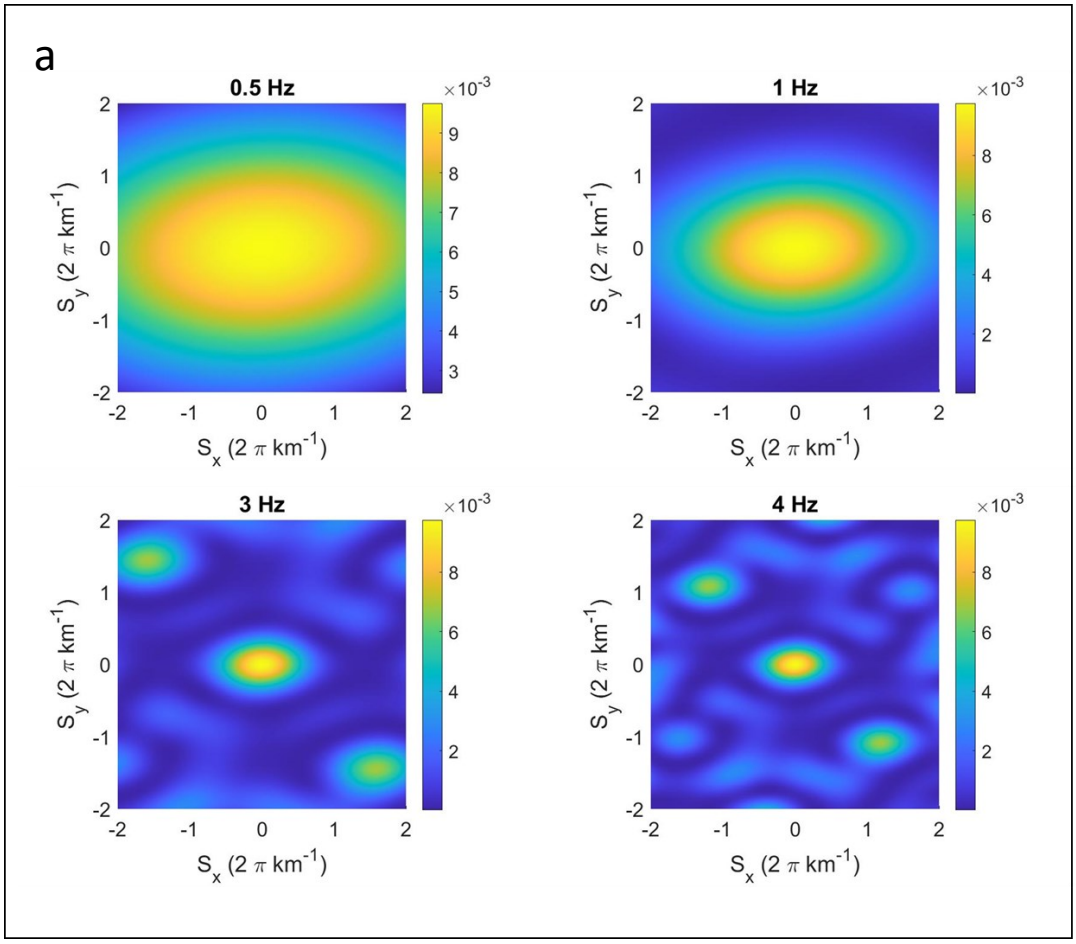

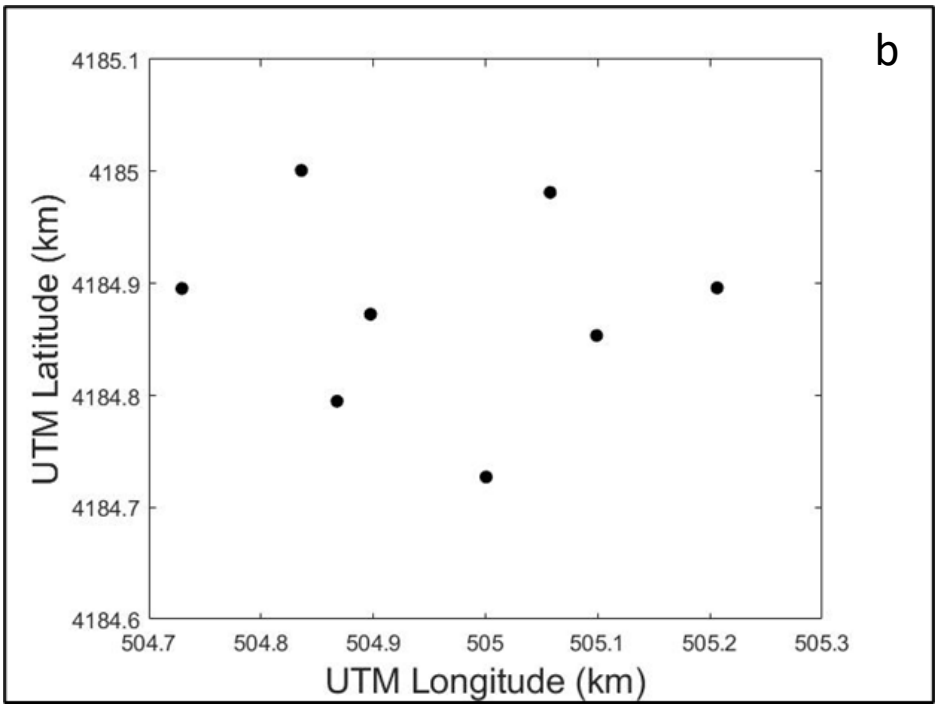

Figure 1.10. a) Array response computed for a vertically incident wave at four different frequencies. b) array configuration used in order to compute Beam pattern function.

1.3.3 SPECTRAL AND AMPLITUDE ANALYSIS

To investigate the nature of seismic signals, it is necessary to analyse their frequency content. The Fourier transform is one of the common frequency representations of signals, because it breaks a signal into different harmonics providing information on power and phase content at different frequencies. The main relationship to perform this type of analysis is (Papoulis, 1987):

$$X(w) = \int_{-\infty}^{+\infty} x(t) e^{-iwt}\, dt \tag{1.10}$$

where t is time, w is the angular frequency, i is the imaginary unit, $x(t)$ and $X(w)$ are the signal in time and frequency domains, respectively. An example of signal in time and frequency domains is reported in figure 1.11.

However, an efficient representation of temporal variations of spectral amplitude and frequency of the signals is given by spectrogram (Schlindwein et al., 1995). Its calculation requires moving a sliding window over the whole length of the time series and estimating the amplitude spectrum by performing an implementation of the Fourier transform, that is the Fast Fourier Transform (FFT, Cooley and Tukey, 1965), for overlapping positions of the window. An example of spectrogram is shown in figure 1.12.

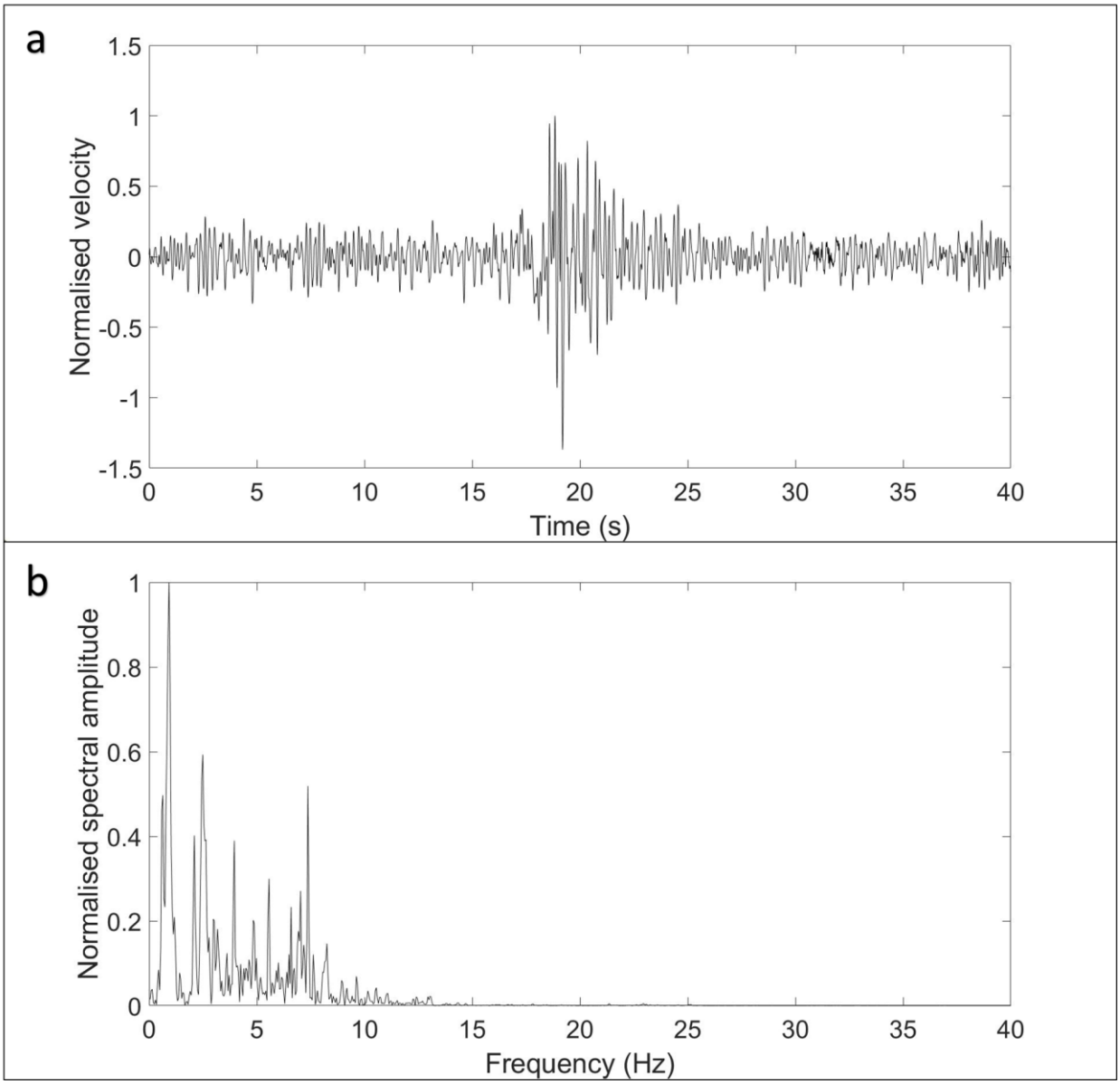

Figure 1.11. Seismic signal recorded at Mt. Etna showing a LP event (a) and its spectrum (b) obtained by applying the FFT on a 20-second-long time window centred around the maximum peak-to-peak amplitude of the event.

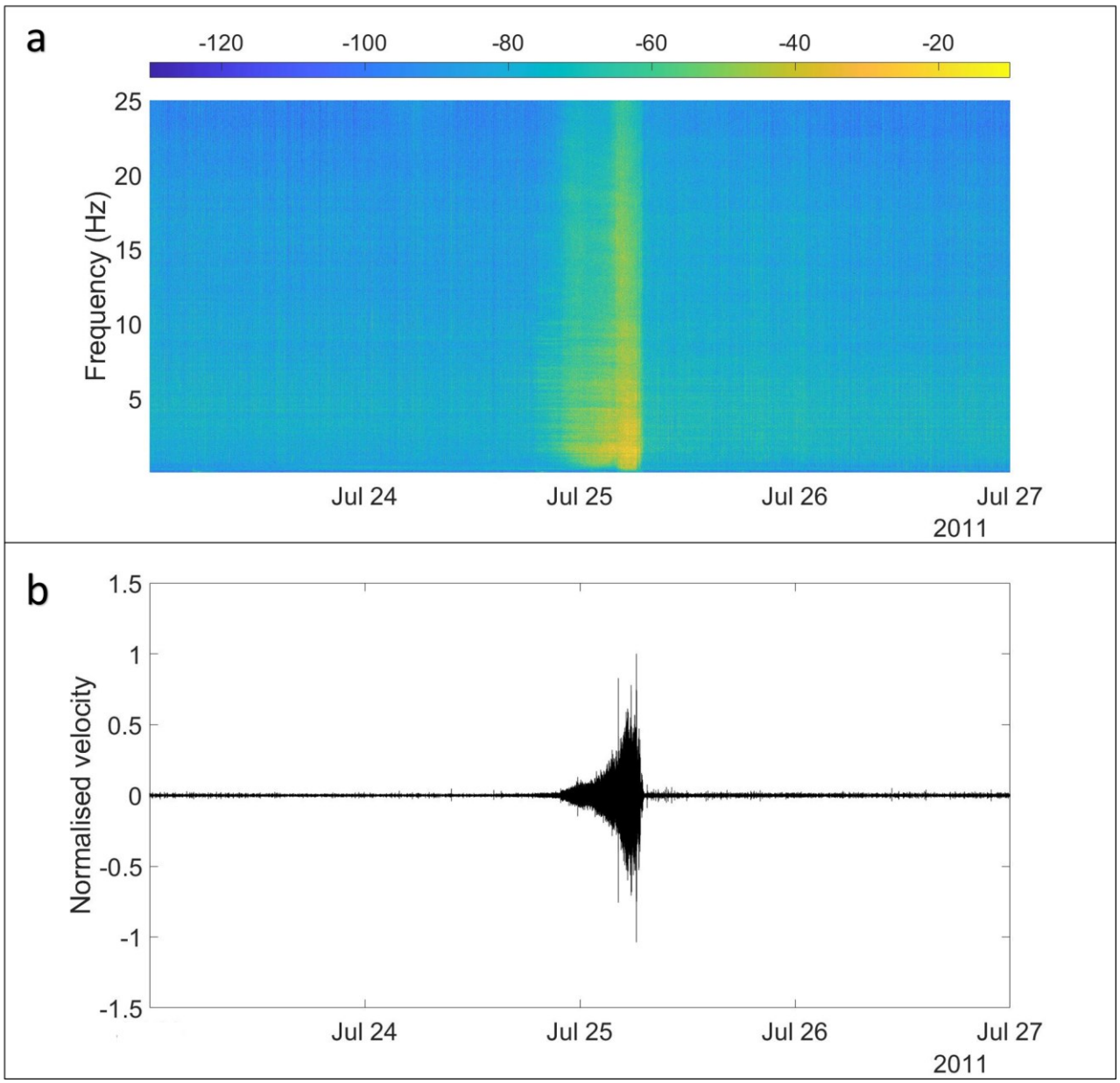

Figure 1.12. Spectrogram (a) of seismic signal recorded at Mt. Etna showing volcanic tremor (b), obtained by using 60-second-long windows. The colorbar on the top refers to spectral amplitude calculated in decibel.

Coheregram is an additional frequency representation, used mainly to evaluate the spectral interval that maximizes the coherence among stations. Its calculation is very similar to the spectrogram one, except for the basic function. In fact, it is based on the computing of the Magnitude-Squared Coherence function (MSC; Welch, 1967). Given two signals x and y, the MSC is a function of the power spectral densities, P_{xx} (f) and P_{yy} (f), and the cross power spectral density, P_{xy} (f), of x and y (Welch, 1967):

$$Cxy(f) = \frac{\left| Pxy(f) \right|^2}{Pxx(f)Pyy(f)} \tag{1.11}$$

An example of signal coherence in time and frequency domains is reported in figure 1.13.

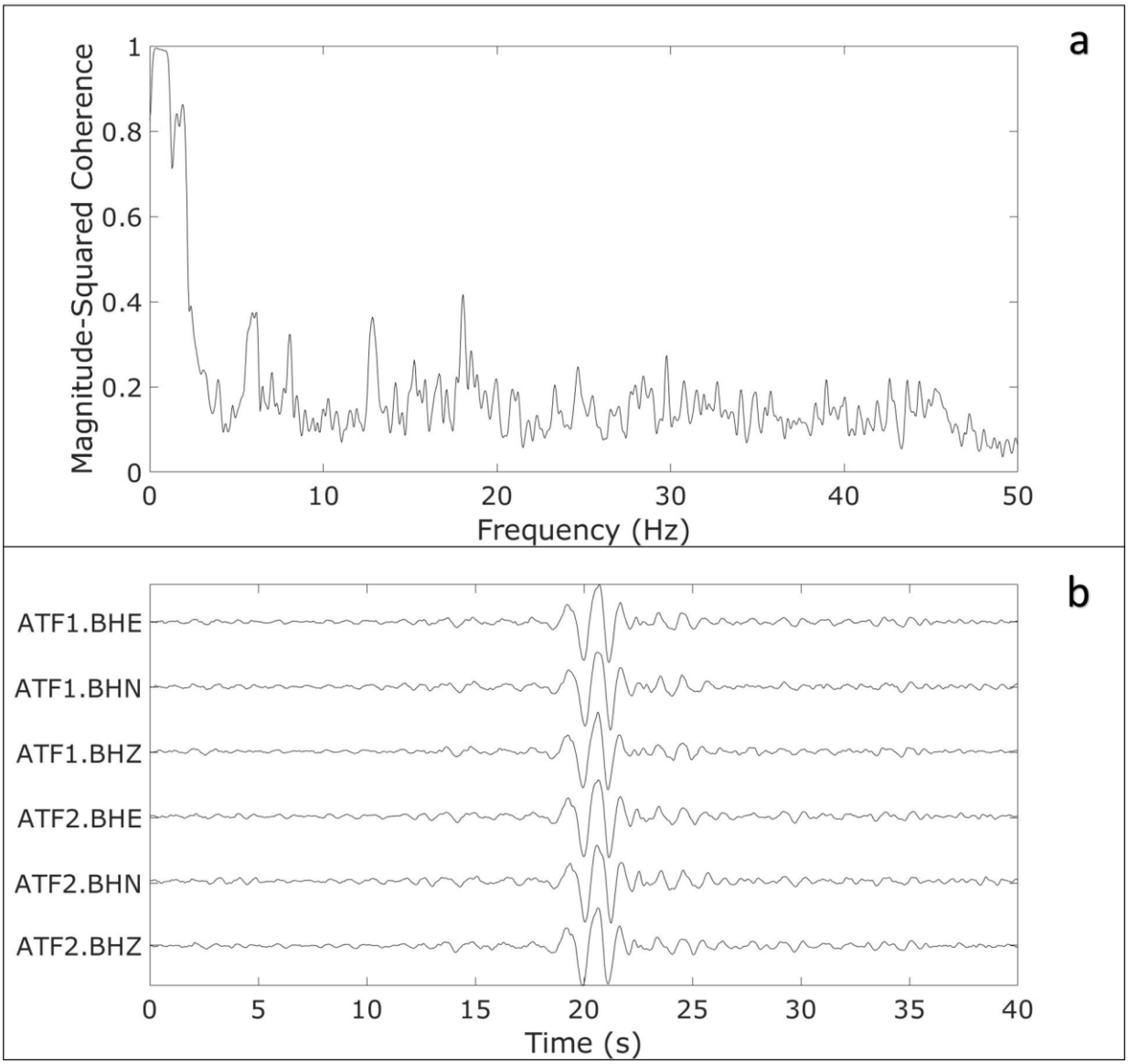

Figure 1.13. MSC function (a) of seismic signals recorded at Mt. Etna through seismic array and showing a LP event (b). The signal coherence is obtained by computing the MSC function on a 20-second-long time window centred around the maximum peak-to-peak amplitude of the event.

Considering an array or network with N elements, the equation 1.11 is applied for the $N(N-1)/2$ independent pairs of signals and the results are averaged to obtain a normalized function of coherence with values between 0 and 1. In this way, it is possible to extract only in the coherent part of the examined wavefield. An example of coheregram is shown in figure 1.14.

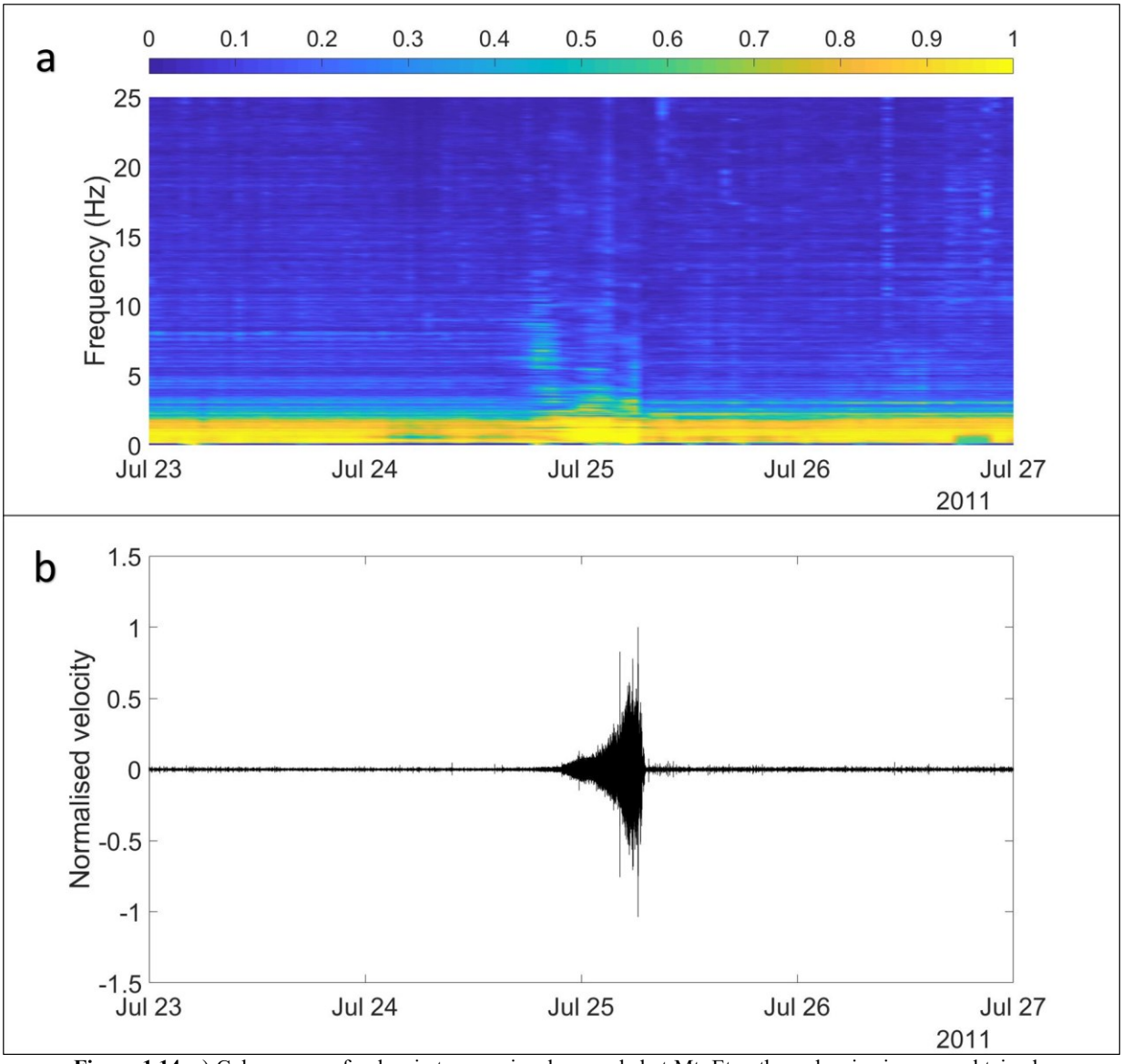

Figure 1.14. a) Coheregram of volcanic tremor signals recorded at Mt. Etna through seismic array, obtained by using 60-second-long windows. The colorbar on the top refers to MSC values. b) Seismic signal recorded at Mt. Etna showing volcanic tremor.

Another way to characterize the nature of the signals is represented by the Root Mean Square analysis (RMS) of the amplitude (Kenney and Keeping, 1962). This kind of analysis consists of the square root of the arithmetic average of the squares of the signal amplitudes. Before computing the RMS, the traces are band-pass filtered, in order to compute their amplitudes in different frequency bands. Given N points of the band-pass filtered traces x_i, the RMS is calculated as (Kenney and Keeping, 1962):

$$RMS = \sqrt{\frac{1}{N}\sum_{i=1}^{N} x_i^2(t)} \tag{1.12}$$

In addition, the RMS amplitude can be also computed in the frequency domain through Parseval's theorem. In this case, performing the discrete Fourier transform on the signal x_i, the RMS is (Battaglia and Aki, 2003):

$$RMS = \sqrt{\frac{1}{N}\sum_{k=0}^{N} [X_k]^2} \tag{1.13}$$

where X_k (k=0,1, …, N-1) represents the spectrum of the signal x_i. Considering a specific frequency band, it is possible to compute the RMS as the sum over the selected part of the spectrum. Generally, the RMS amplitude is much more stable than the peak-to-peak amplitude, which may be strongly influenced either by a single peak in the signal or by a technical glitch. An example of RMS of signal is shown in figure 1.15.

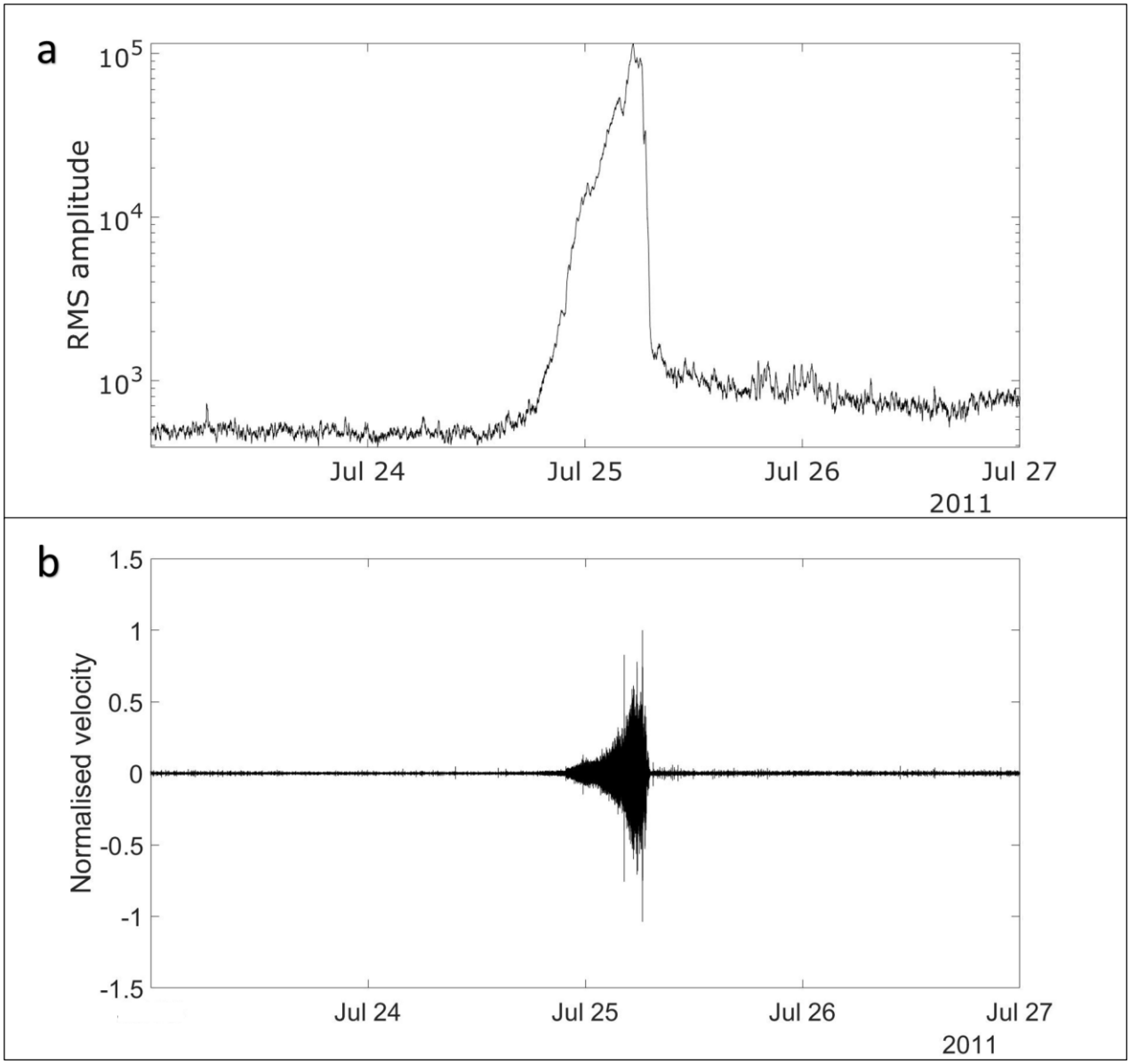

Figure 1.15. Logarithmic RMS amplitudes (a) of seismic signal recorded at Mt. Etna showing volcanic tremor (b), obtained by using 2-second-long windows. The tremor signal is filtered between 0.5 and 2.5 Hz.

1.3.4 POLARIZATION ANALYSIS

Another tool to investigate the features of seismic signals is the polarization analysis. Following Jurkevics (1988), it is possible to determine the polarization properties of the traces by using eigen-decomposition of the covariance matrix of the three components of ground motion over time windows sliding along the band-pass filtered traces. For a single three component station, the covariance matrix S is evaluated as the following relationship (Jurkevics, 1988):

$$S_{jk} = \frac{XX^T}{N} = \left[\frac{1}{N}\sum_{i=1}^{N} x_{ij}x_{ik}\right] = \begin{bmatrix} S_{zz} & S_{zn} & S_{ze} \\ S_{zn} & S_{nn} & S_{ne} \\ S_{ze} & S_{ne} & S_{ee} \end{bmatrix} \tag{1.14}$$

where X is the data matrix, x_{ij} is the *i-th* sample of the *j-th* component, N is the number of samples. It is a 3x3, real and symmetric matrix, the terms of which represent the auto- and cross-variances of the three components of motion. From the solution of the algebraic eigen problem for S, it possible to obtain the principal axis directions and lengths of the polarization ellipsoid, that is the best-fit to the data in a least-squares sense (Jurkevics, 1988):

$$(S - \lambda^2 I)u = 0 \tag{1.15}$$

where I is the 3x3 identity matrix, u and λ are the eigenvectors and eigenvalues matrices, respectively. The directions of the principal axes of the ellipsoid are provided by the eigenvector, whereas the axes lengths are given by the eigenvalues. Sorting the eigenvalues, the rectlinearity coefficient *rect* is calculated for quantifying the degree of linearity of particle motion (Jurkevics, 1988):

$$rect = 1 - \frac{\lambda_{int}}{\lambda_{max}} \tag{1.16}$$

where λi_{nt} and λ_{max} are intermediate and maximum eigenvalues of the covariance matrix, respectively. The *rect* values are defined between 0 and 1, assuming theoretically 1 for body waves and 0 for particle motion with no privileged direction. Instead, from eigenvectors values azimuth and incidence angles are estimated. The first one is the angle

measured from the horizontal orientation of the rectilinear motion, given by the largest eigenvalue of u_1 (Jurkevics, 1988):

$$azimuth = \tan^{-1} \frac{u_{21} sign(u_{11})}{u_{31} sign(u_{11})}$$

(1.17)

where u_{j1} (j=1…3) are the three direction cosines of eigenvector u_1. The second one is rather the angle measured from the respective vertical orientation as the vertical direction cosine of u_1 (Jurkevics, 1988):

$$incidence = \cos^{-1} \left| u_{11} \right|$$

(1.18)

An example of polarization parameters calculated on successive windows of seismic signal is reported in figure 1.16.

For the evaluation of the polarization attributes with a three-component array this method needs to compute the average covariance matrix of all array sensors. The three component covariance matrix $\bar{S}$ for an array with M stations is given by the following equation (Jurkevics, 1988):

$$\bar{S} = \frac{1}{M} \sum_{n=1}^{M} S_n$$

(1.19)

where S_n is the covariance matrix for the *n-th* sensor. Particle motion estimates are very sensitive to timing errors between the component of the motion. Therefore, for the covariance averaging it is necessary to remove the delay shifts between stations due to the propagation of the arriving wavefront across the array.

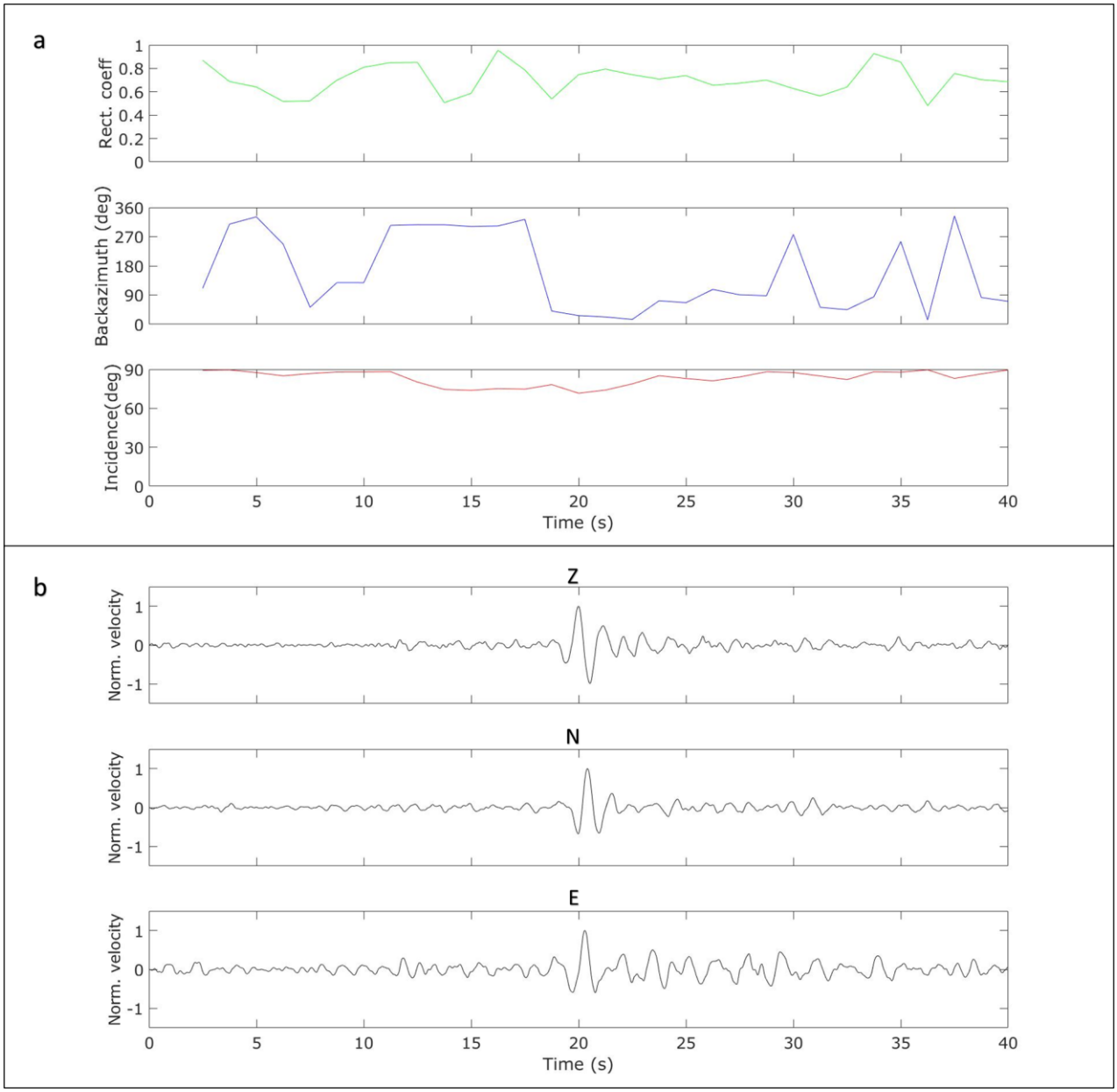

Figure 1.16. a) Polarization parameters, calculated by using 2.5-second-long window sliding every 1.25 s. b) LP event recorded at Mt. Etna by a three-component station and filtered in the frequency range 0.5-1.2 Hz.

1.3.5 DETECTION ANALYSIS

One of most important aspect of volcano seismology is the detection of different events, such as LP and VLP events and volcanic explosions. One of the common algorithms used for automatic detection is the Short Term Average/Long Term Average method (STA/LTA; Allen, 1978), isolating pieces of signal that contains a generic event. It continuously calculates the RMS values of band-pass filtered signals x_i in two consecutive moving-time windows of N_{short} and N_{long} samples (Allen,1978):

$$STA/LTA = \frac{STA}{LTA}$$

with

$$STA = \sqrt{\frac{1}{N_{short}} \sum_{i=Nshort}^{N_{long}} x_i^2(t)} \qquad LTA = \sqrt{\frac{1}{N_{long}} \sum_{i=1}^{N_{long}} x_i^2(t)}$$

(1.20)

where *STA* is the short term average window and *LTA* is the long one. *STA* is sensitive to events, while *LTA* provides information about the temporal amplitude of the noise at the site. When the ratio of both terms (*STA/LTA*) exceeds a threshold value, an event is detected and data starts being recorded (Fig. 1.17).

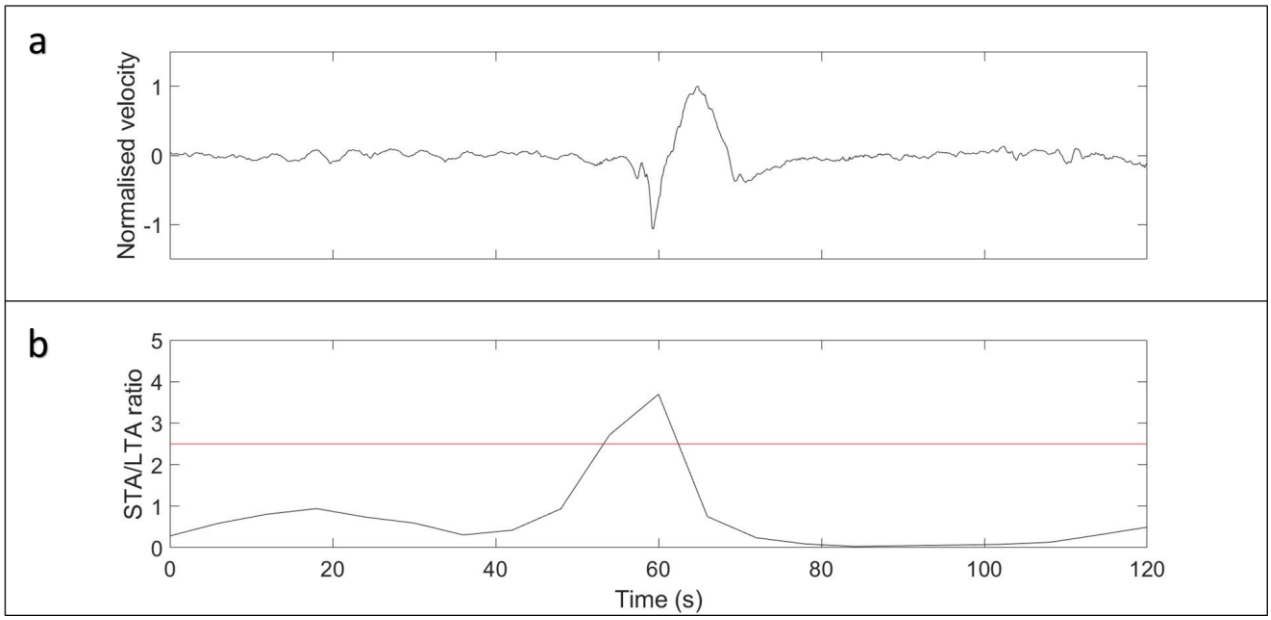

Figure 1.17. a) Seismic signal filtered between 0.01 and 0.15 Hz, recorded at Mt. Etna and showing a VLP event. b) STA/LTA series calculated on the signal reported in (a). The horizontal red line refers the threshold chosen for the detection.

Another method recently developed is the Subband-based Automatic LP Events Detection algorithm (SALPED; Garcia et al., 2017). It is exclusively designed for the detection and classification of LP events on the basis of their characteristic shape, duration, and frequency band of activity. This algorithm, in fact, differentiates LP events from the rest of events, such as volcanic tremor and VLP and VT events, that usually show different frequency contents and duration. It applies a subband processing, including envelope detection, noise reduction, undersampling and enhancement of spindle-shaped arrivals, in order to obtain a characteristic function *CF* that contains all information for the LP detection (Fig. 1.18).

The main procedure includes several steps. First of all, SALPED algorithm band-pass filters the vertical component of the seismograms, splitting the frequency content of the signals into three frequency subbands: the central band $x_C(n)$, specific for LP events; the lower band $x_L(n)$, for the lower frequency components of the signal; the upper band $x_U(n)$, for the upper frequency components of the traces. For a generic subband x_i ($i = \{L, C, U\}$ lower, central and upper subbands, respectively), the envelope of the signal is extracted as (Garcia et al., 2017):

$$e'_i(n) = \sqrt{x_i(n)^2 + x_{ih}(n)^2} \tag{1.21}$$

where $x_{ih}(n)$ is the Hilbert Transform of $x_i(n)$ and n is the envelope duration. Each of these envelopes are passed through linear low-pass filters and are downsampled, preserving the envelope duration and eliminating the remaining noise in the band. Subsequently, the background noise (BN) envelope is calculated by using the following equation (Garcia et al., 2017):

$$e'_{BN}(m) = \left(e'_L(m) + e'_C(m) + e'_U(m)\right) * h_{LP}(m) \tag{1.22}$$

where $h_{LP}(m)$ is the impulse response of a low-pass filter with a very low cutoff frequency, * is convolution operator and m is the envelope duration. This step is oriented to obtain robustness against noise, computing for the *i-th* subband a noise-robust envelope $z_i(m)$ (Garcia et al., 2017):

$$z_i(m) = \begin{cases} z_{oi}(m) & if\ z_{oi}(m) \geq z_{thri} \\ z_{thri} & if\ z_{oi}(m) < z_{thri} \end{cases} \quad \text{with } z_{oi}(m) = \frac{e'_i(m)}{e'_{BN}(m)} \tag{1.23}$$

where z_{thri} is a threshold value set as a percentile of the local normalized envelope $z_{oi}(m)$. In the next step, the *i-th* noise-robust envelope is filtered through a discriminant detector, that is a linear phase filter used to reinforce LP-like envelopes and to penalize long duration envelopes with a negative impulse response $h(m)$ (Garcia et al., 2017):

$$h(m) = \begin{cases} \psi(m) & if\ \psi(m) \geq 0 \\ \beta\psi(m) & if\ \psi(m) < 0 \end{cases}$$

with

$$\psi(m) = \frac{2}{\pi^{\frac{1}{4}}\sqrt{3}}\left(1 - \left(\frac{m}{L/2}\right)^2\right)e^{-\frac{1}{2}\left(\frac{m}{L/2}\right)^2}$$

(1.24)

where $\psi(m)$ is the discrete Mexican-Hat wavelet, L is the average duration of LP events and β is the factor used to punish durations longer than L.

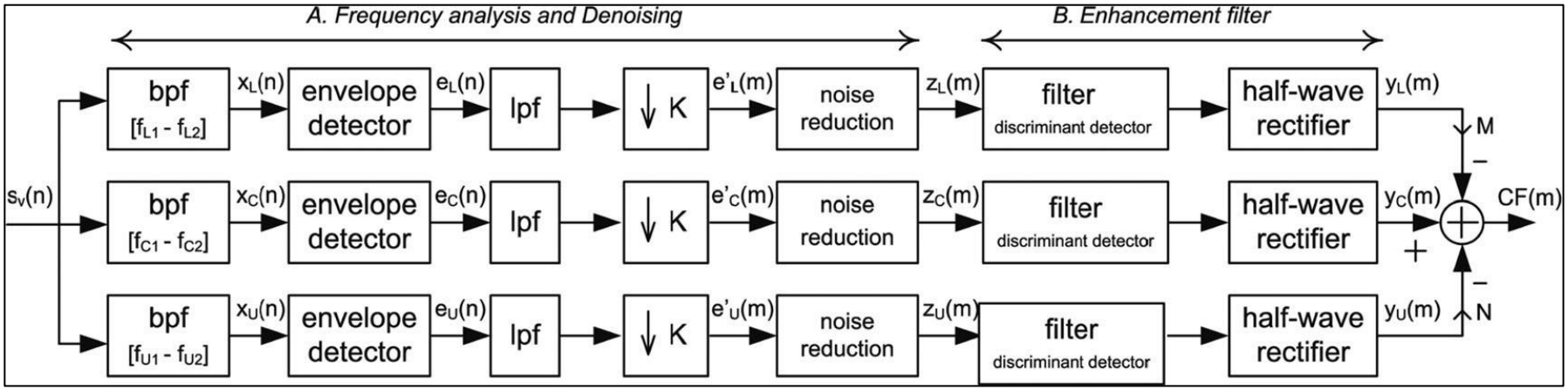

Figure 1.18. Schematic diagram of the subband-based procedure to obtain the *CF* to detect LP events. *bpf* corresponds to *band-pass filtering*, in which the filters are used to split the signal into subbands of frequency. *lpf* stands for low-pass filtering, representing the filter used to smooth the envelopes and permit decimation. *K* is the decimation factor of the decimation block, using the output of the low-pass filter as input to reduce its sampling frequency in a factor *K* (from Garcia et al., 2017).

After filtering, in order to eliminate negative amplitudes and to punish long duration envelopes with small amplitudes, a half-wave rectifier is performed to obtain the y_i (m) envelope (Fig. 1.19).

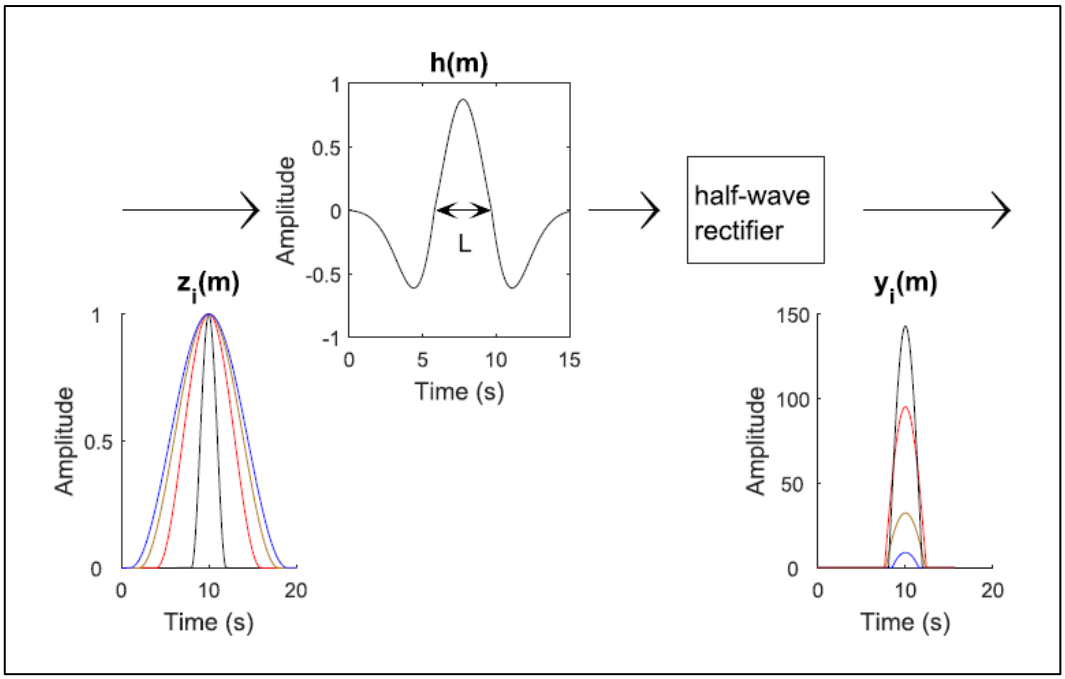

Figure 1.19. Impulse response of the discriminant detector $h(m)$. Example inputs z_i (m) with durations of 4, 12, 16, and 18 s. Filter outputs for each example input after half-wave rectification y_i (m) (from Garcia et al., 2017).

Finally, the CF (m) is calculated to emphasize short events with activity in the central subband (Garcia et al., 2017):

$$CF(m) = y_C(m) - My_L(m) - Ny_U(m) \tag{1.25}$$

where M and N are spectral penalty factors used to punish false positive detections of LP events. When the CF (m) exceeds a threshold value, an LP event is detected and stored (Fig. 1.20).

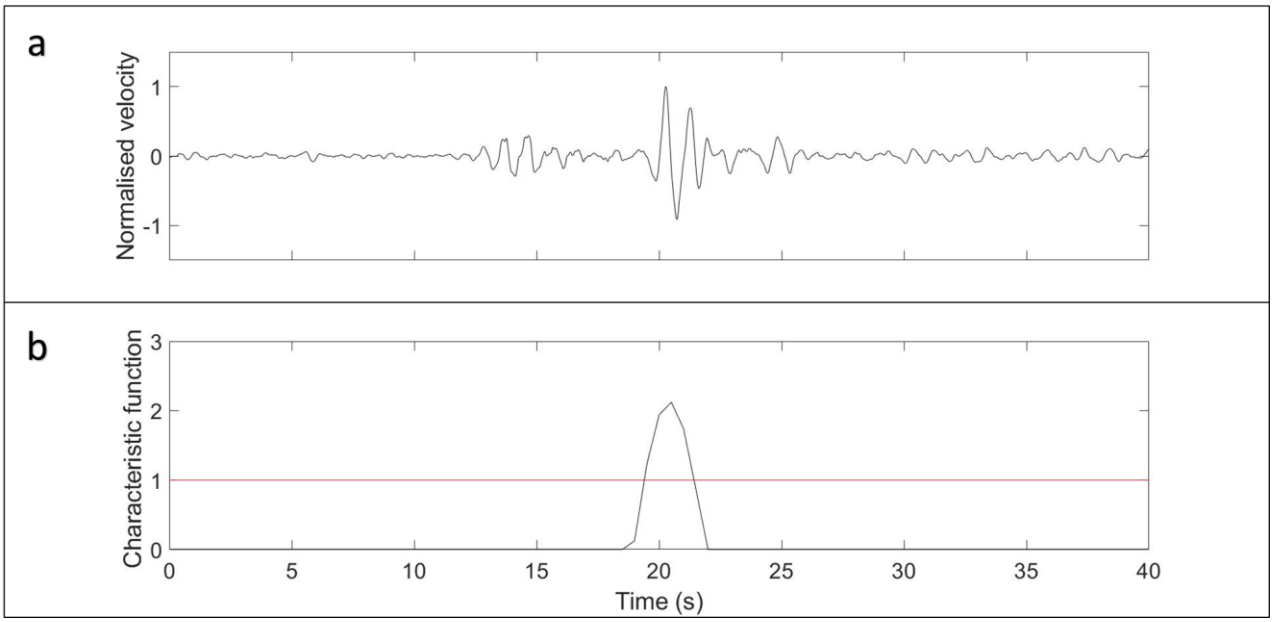

Figure 1.20. a) Seismic signal filtered between 0.5 and 1.2 Hz, recorded at Mt. Etna and showing a LP event. b) CF values calculated on the signal reported in (a). The horizontal red line refers the threshold chosen for the detection.

1.3.6 LOCALIZATION ANALYSIS

Most of the array techniques assume a plane wave approximation, that it is realistic for epicentral distances greater than four or five times the array aperture. They allow to retrieve estimates of the propagation parameters of the wavefield, such as back azimuth and slowness, providing information about the volcano processes and the geometry of the magmatic system. As aforementioned, array methods utilize mainly beamforming, improving the SNR by stacking the coherent part of the signals and suppressing noise in the data (Bormann, 2012). However, many specific techniques were implemented in recent years, improving the reliability of source localizations of signals recorded in volcanic areas. Generally, they can be divided into two main categories, that are the time-domain and the frequency-domain techniques.

The first kind of methods is based on the estimation of the delay times maximizing the coherence among the seismic traces for a certain value of back azimuth and slowness. Zero Lag Cross Correlation analysis (ZLCC; Frankel et al., 1991) fits perfectly this category. Considering a plane wave $x(t)$ propagating through an array, the normalized cross-correlation coefficient between the *i-th* and the *j-th* stations is given by (Neidell and Taner, 1971):

$$c(\tau_{ji}) = \frac{\sum_{t=1}^{T} x_j(t)x_i(t+\tau_{ji})}{\sqrt{\sum_{t=1}^{T} x_j^2(t) \quad \sum_{t=1}^{T} x_i^2(t+\tau_{ji})}}$$

(1.26)

where t is the time sample, T is the number of samples in the window analysis and τ the delay time. The ZLCC method consists of the application of the equation 1.26 between station pairs over time windows sliding along the band-pass filtered traces. For $N(N-1)/2$ independent station pairs, these coefficients return the delay times of the impinging plane waves that maximize the coherence among signals (Fig 1.21).

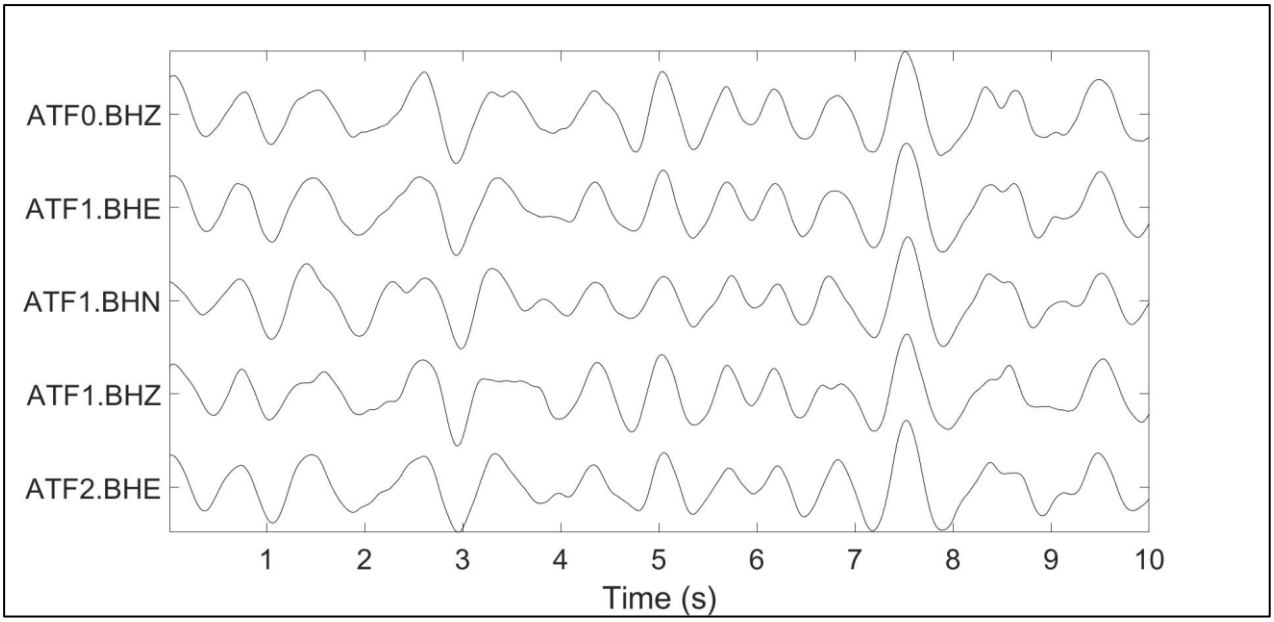

Figure 1.21. Example of seismic signals recorded at Mt. Etna through seismic array and showing volcanic tremor. The traces are time-shifted by using the delays time computed through ZLCC method.

According to the common waveform model, the time τ_{ji} taken by the wave to propagate from the *i-th* to the *j-th* station can be expressed as a function of the horizontal slowness u and the position vector X of the array sensors (Olson and Szuberla, 2005):

$$\tau_{ji} = u(X_i - X_j)$$

(1.27)

Expressing in matrix form, the equation 1.27 can be written as (Olson and Szuberla, 2005):

$$d = G\,m$$

with

$$m = \begin{vmatrix} u_x \\ u_y \end{vmatrix}, \quad d = \begin{vmatrix} \tau_{12} \\ \tau_{13} \\ \cdot \\ \cdot \\ \tau_{ji} \end{vmatrix}, \quad G = \begin{vmatrix} x_{12} & y_{12} \\ \cdot & \cdot \\ \cdot & \cdot \\ x_{ji} & y_{ji} \end{vmatrix}$$

(1.28)

where *m* is the vector of the components of horizontal slowness, *d* is the vector containing the *N*(*N-1*)*/2* estimations of delay times and *G* is the matrix of the sensor positions. The estimation of the slowness vector *m* is performed by solving the previous system of equations through the generalized inverse matrix (Olson and Szuberla, 2005):

$$m = (G^T G)^{-1} G^T d$$

(1.29)

where *T* is the transpose operator and *-1* is the inverse operator. Eventually, it is possible to compute the average of the *N*(*N-1*)*/2* cross-correlation coefficients, obtaining a coherence function of the back azimuth and slowness. An example of estimation of back azimuth and slowness is shown in figure 1.22.

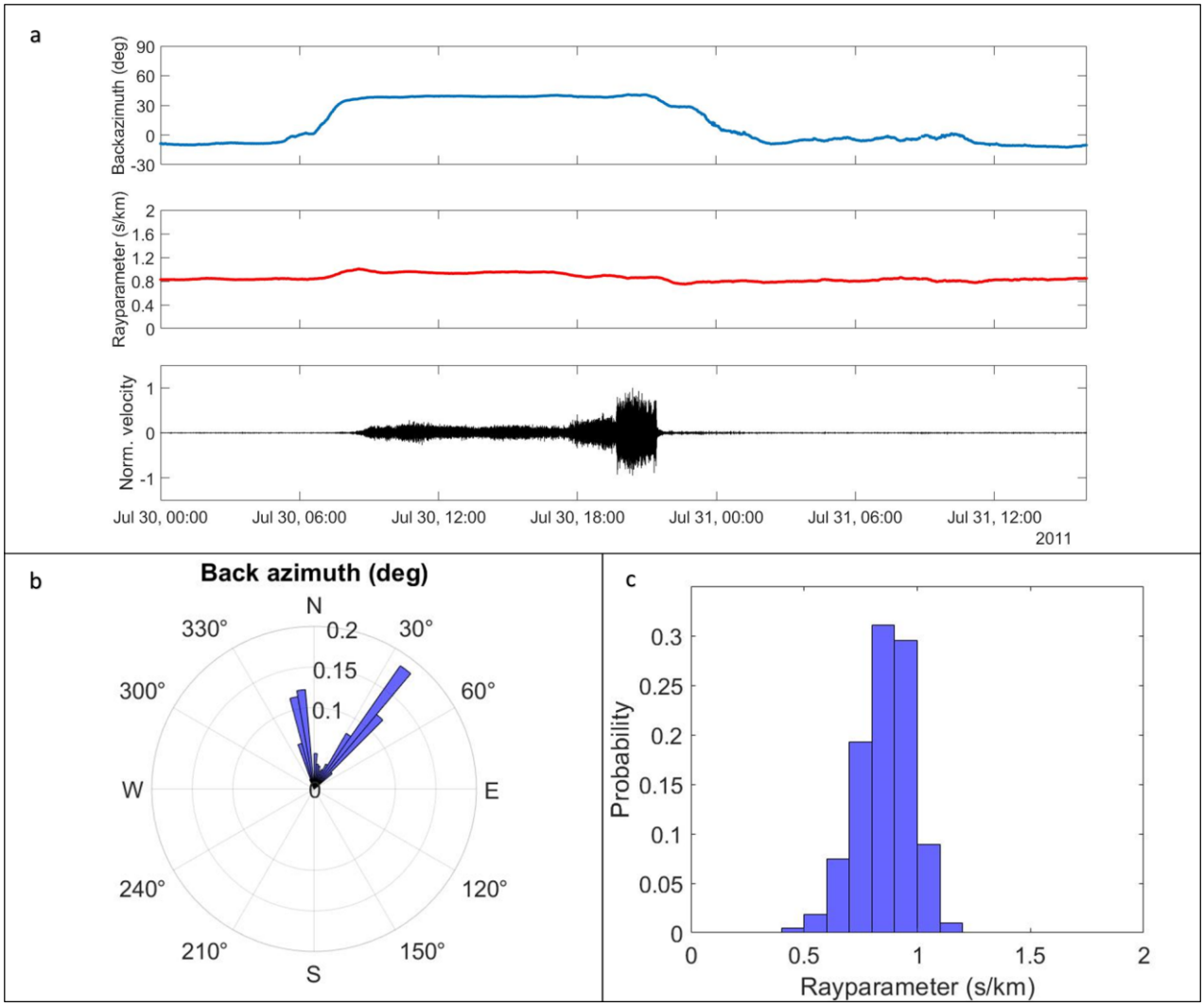

Figure 1.22. Example of back azimuth and ray parameter calculated by using 10-second long sliding window in the 0.5-1.5 Hz frequency range. a) Time series of back azimuth (upper panel) and ray parameters (central panel) related to volcanic tremor signal (lower panel) recorded at Etna volcano. b) Polar histogram of back azimuth showed in (a). c) Histogram of ray parameter displayed in (a).

The second type of methods consists of the minimization between the theoretical phase delays of planes waves passing through array with specific propagation parameters and the phase differences measured at the different array positions. One of the common algorithms used is the MUltiple SIgnal Classification (MUSIC; Schmidt, 1986). It offers the advantage to resolve multiple, closely spaced sources simultaneously impinging at the array. This method is based on some assumptions: (*i*) for an array with *N* sensors, the wavefield is considered as the summation of *M* plane waves, with *M<N;* (*ii*) the *M* components of the wavefield propagate across the array with the same amplitude and velocity; (*iii*) the medium beneath the array is considered elastic and homogenous. The MUSIC method

consists of the computation of the spatial cross-spectral matrix over windows sliding along traces by averaging the Fourier coefficients over overlapped frequency bands. For each time window and frequency band, the number of its eigenvalues provides the number of source signals M arriving at the array, estimated by using the Akaike's information criterium (AIC; Wang and Kaveh, 1985). According to Chiou and Bolt (1993), the slowness spectrum $Q(u)$ is derived as:

$$Q(u) = \frac{1}{1 - D(u)} D(u) = \frac{1}{N} \sum_{i=1}^{M} |A^H V_i|^2 \tag{1.30}$$

where u is the horizontal slowness vector, N is the number of array sensors, A^H is the Hermitian of the array response vector for the *i-th* plane wave propagating with slowness u, V_i are the cross-spectral matrix eigenvectors spanning the signal subspace of dimension M, $D(u)$ is the null spectrum estimate. Applying the equation 1.30 over a square slowness search grid, the slowness spectra are estimated. The dominant peaks of these spectra provide the horizontal component of the slowness (u_x, u_y), from which it is possible to derive the back azimuth and the ray parameter (Fig. 1.23).

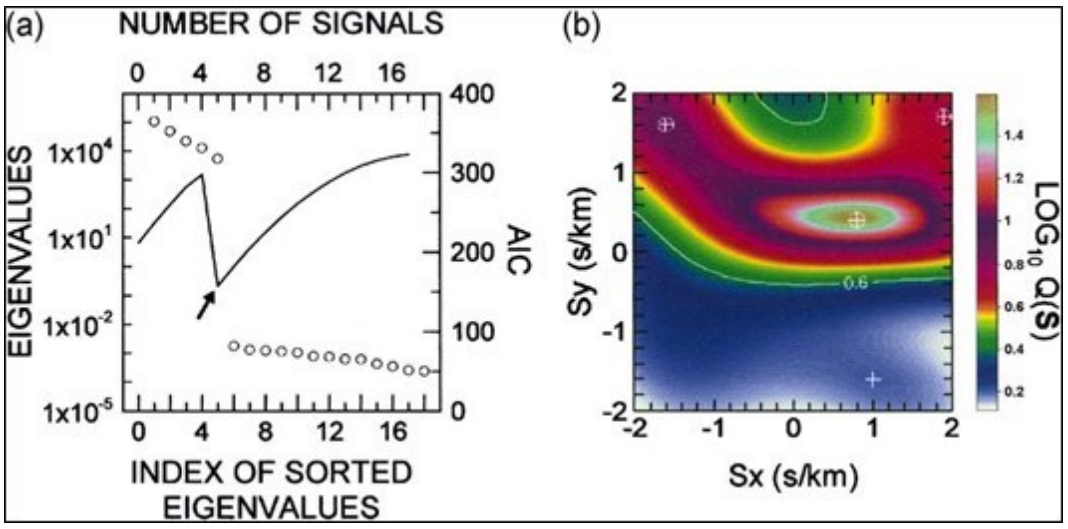

Figure 1.23. Example of results obtained with MUSIC algorithm by analysing volcanic tremor recorded at Mt. Etna through seismic array (From Saccorotti et al., 2004). a) Sample eigenvalues of the spatial cross-spectral matrix evaluated over a 2.56-s-long window of tremor at the central frequency 1.95 Hz (circles). Continuous line indicates the AIC function, whose minimum (arrow) indicates the number of signals propagating across the array. b) Slowness spectrum, expressed as the logarithm of the $Q(u)$ function. The white line bounds the region of the u plane for which the $D(u)$ function takes values above the selected threshold (0.6). Only those

peaks (indicated by circled crosses) which are located in this region are used to derive propagation back azimuth and ray parameter of the detected plane waves.

Other kinds of array methods take into account the curvature of the wavefront and use sometimes a slightly different approach compared to the previous ones. Unlike the previous ones, these methods can be applied by using both arrays and sparse networks depending on the wavelength of analyzed signals. A significant example is represented by the Semblance algorithm (Neidell and Taner,1971). This represents a measure of the similarity of multichannel data, not only in waveform but also in amplitude. Semblance is defined as (Neidell and Taner,1971):

$$S_0 = \frac{\sum_{j=1}^{M}\left(\sum_{i=1}^{N} U_i(\tau_i + j\Delta t)\right)^2}{N \sum_{j=1}^{M}\sum_{i=1}^{N} U_i(\tau_i + j\Delta t)^2}$$

(1.31)

where Δt is the sampling interval, t_i is the origin time of the window sampling the *i-th* channel, $U_i(t_i+j\Delta t)^2$ is the *j-th* time sample of the signal *U* recorded by the *i-th* channel, *M* is the number of samples in the window and *N* represents the number of channels. As mentioned previously, a sparse network may be used as an array for those events characterized by longer wavelength. Therefore, in order to underline only the similarity among waveforms regardless of the amplitude, it possible to use a new definition of Semblance in which the signals U_i are normalized by their respective RMS (Almendros and Chouet, 2003):

$$S'_0 = \frac{\sum_{j=1}^{M}(\sum_{i=1}^{N} U_i(\tau_i + j\Delta t)/\sigma_i)^2}{N \sum_{j=1}^{M}\sum_{i=1}^{N} U_i(\tau_i + j\Delta t)^2/{\sigma_i}^2}$$

with

$$\sigma_i = \sqrt{\frac{1}{M}\sum_{j=1}^{M} U_i(\tau_i + j\Delta t)^2}$$

(1.32)

where σ_i is the RMS of the signal within the selected time window sampling the *i-th* channel. Another way to enhance only the coherence among signals regardless of the

amplitude consists of modifying some assumption of the amplitude-decay-based location technique (Battaglia et al., 2005). Assuming that the amplitude of the traces decays with *i-th* distance source-sensor r_i, the amplitude U_i measured at the *i-th* station can be expressed by the following general law (Battaglia et al., 2005):

$$U_i(f,r) = U_0(f) {r_i}^{-b} e^{-\frac{\pi r_i f}{Qv}} \tag{1.33}$$

where U_0 is the amplitude at the source, f is the frequency, v is the velocity of the waves, b is the exponent, which takes values of 0.5 or 1 for the cases of surface and body waves, respectively, and Q is the ray-path-averaged quality factor. Therefore, in order to underline only the similarity among waveforms regardless of the amplitude, the equation 1.31 can be implemented by the measuring the amplitude at source (Battaglia et al., 2005):

$$U_0(f) = U_i(f,r)\, {r_i}^{b} e^{\frac{\pi r_i f}{Qv}} \tag{1.34}$$

Another modified definition of Semblance is represented by the Radial Semblance (Kawakatsu et al., 2000), designed to take into account the three-component data. This definition is very similar to the previous ones even if it uses the radial component of the ground motion to calculate the Semblance values. In fact, it introduces a penalty function in order to discriminate the weight of receivers for which highly rectilinear particle motions are measured. The definition of Radial Semblance is given by the following equation (Kawakatsu et al., 2000):

$$S_{iso} = \frac{\sum_{j=1}^{M}(\left(\sum_{i=1}^{N} U_i^p(\tau_i + j\Delta t)\right)^2 - N \sum_{i=1}^{N} U_i^v(\tau_i + j\Delta t)^2 + U_i^h(\tau_i + j\Delta t)^2)}{N \sum_{j=1}^{M} \sum_{i=1}^{N} (U_i^p(\tau_i + j\Delta t)^2 + U_i^v(\tau_i + j\Delta t)^2 + U_i^h(\tau_i + j\Delta t)^2)} \tag{1.35}$$

where the superscript p represents the component of the ground motion in the source-sensor direction, v and h are two mutually perpendicular directions contained in the plane perpendicular to the p direction. As done before, to avoid the effect of the amplitude of signals on the calculation, it is possible to normalize the traces by the RMS of three component data σ_i (Almendros and Chouet, 2003):

$$S'_{iso} = \frac{1}{MN^2}\left(\sum_{j=1}^{M}\left(\sum_{i=1}^{N}\frac{U_i^p(\tau_i+j\Delta t)}{\sigma_i}\right)^2 + N\left(\sum_{i=1}^{N}\left(\frac{U_i^p(\tau_i+j\Delta t)}{\sigma_i}\right)^2\right)\right) - 1$$

(1.36)

In order to scale S'_{iso} to the range between 0 and 1, the equation 1.36 can be written as (Almendros and Chouet, 2003):

$$S_0 = \frac{S'_{iso}+1}{2} = \frac{1}{2MN^2}\sum_{j=1}^{M}\left(\sum_{i=1}^{N}\frac{U_i^p(\tau_i+j\Delta t)}{\sigma_i}\right)^2 + N\left(\sum_{i=1}^{N}\left(\frac{U_i^p(\tau_i+j\Delta t)}{\sigma_i}\right)^2\right)$$

(1.37)

However, both Semblance and Radial Semblance methods share the same main location procedure that consists in finding a set of arrival times that yields a maximum Semblance value for the *N*-channel data. It includes several steps. First of all, a three-dimensional grid of assumed source positions is defined in order to determine the spatial extent of the region of interest. The start time t_s is fixed as the time of the first arrival at a reference station, chosen on the basis of the highest signal-to-noise ratio. For each node of the grid, the origin time t_0 and the theoretical travel times t_i are calculated, assuming a certain value of propagation velocity of the waves *v* (Almendros and Chouet, 2003):

$$t_0 = t_s - r/v$$

$$t_i = r_i/v$$

(1.38)

where *r* is the distance between the reference station and the node of the grid and r_i is the distance between the *i-th* station and the node of the grid assumed to be the source location. Then, the traces at the different receivers are delayed to estimate the Semblance values for every node position, by using the computed travel times and the time origin. Finally, the source location is determined at the node where the delayed signals show the largest Semblance value. Examples of Semblance and Radial Semblance applications are shown in figure 1.24 and 1.25, respectively.

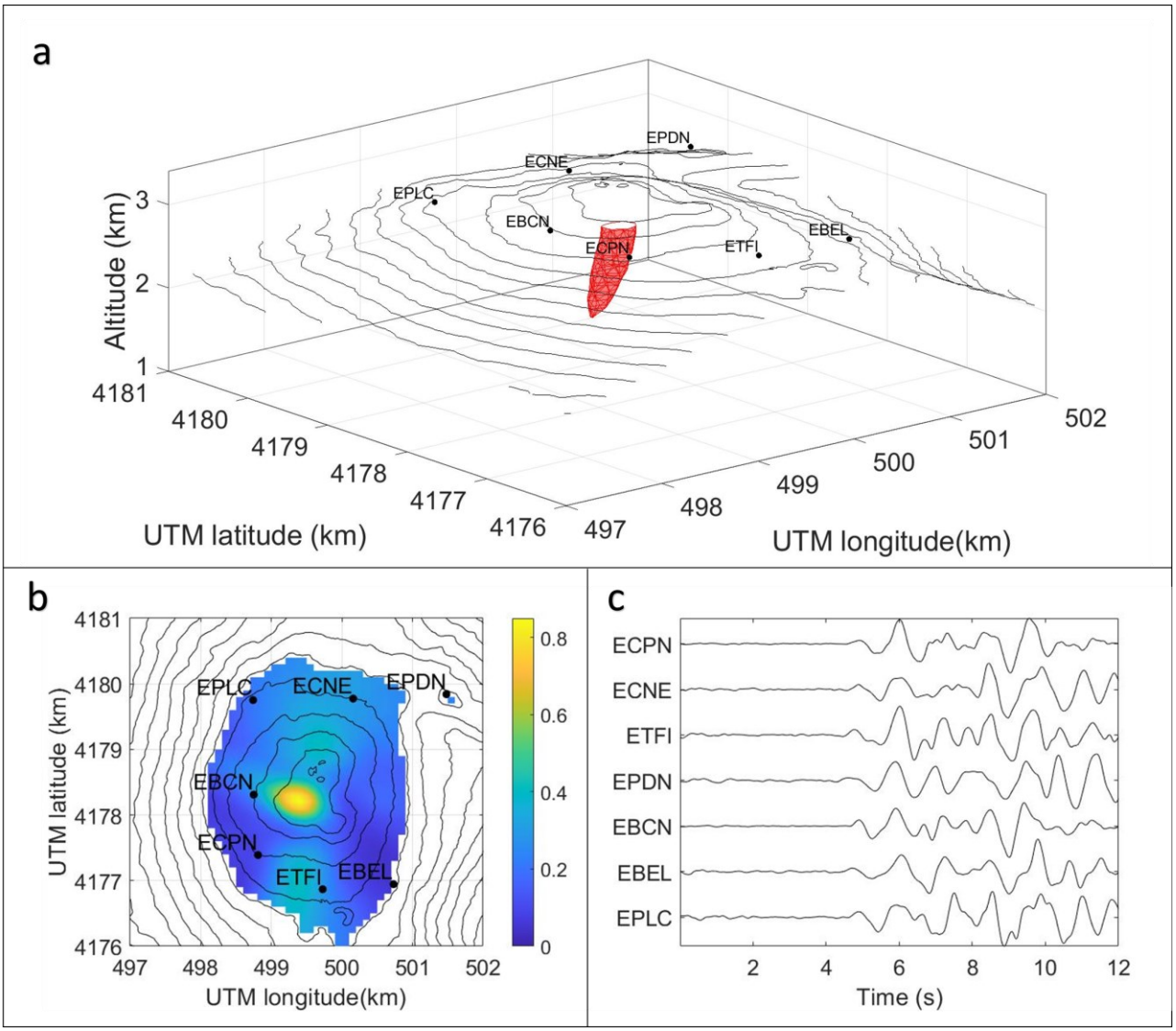

Figure 1.24. a) Example of volume comprising the grid nodes with semblance higher than a certain value, obtained by locating a LP event at Mt. Etna. b) Example of space distribution of semblance values calculated by locating a LP event at Mt. Etna. (c) Seismic signals at the different stations shifted by the time delay that allows obtaining the maximum semblance.

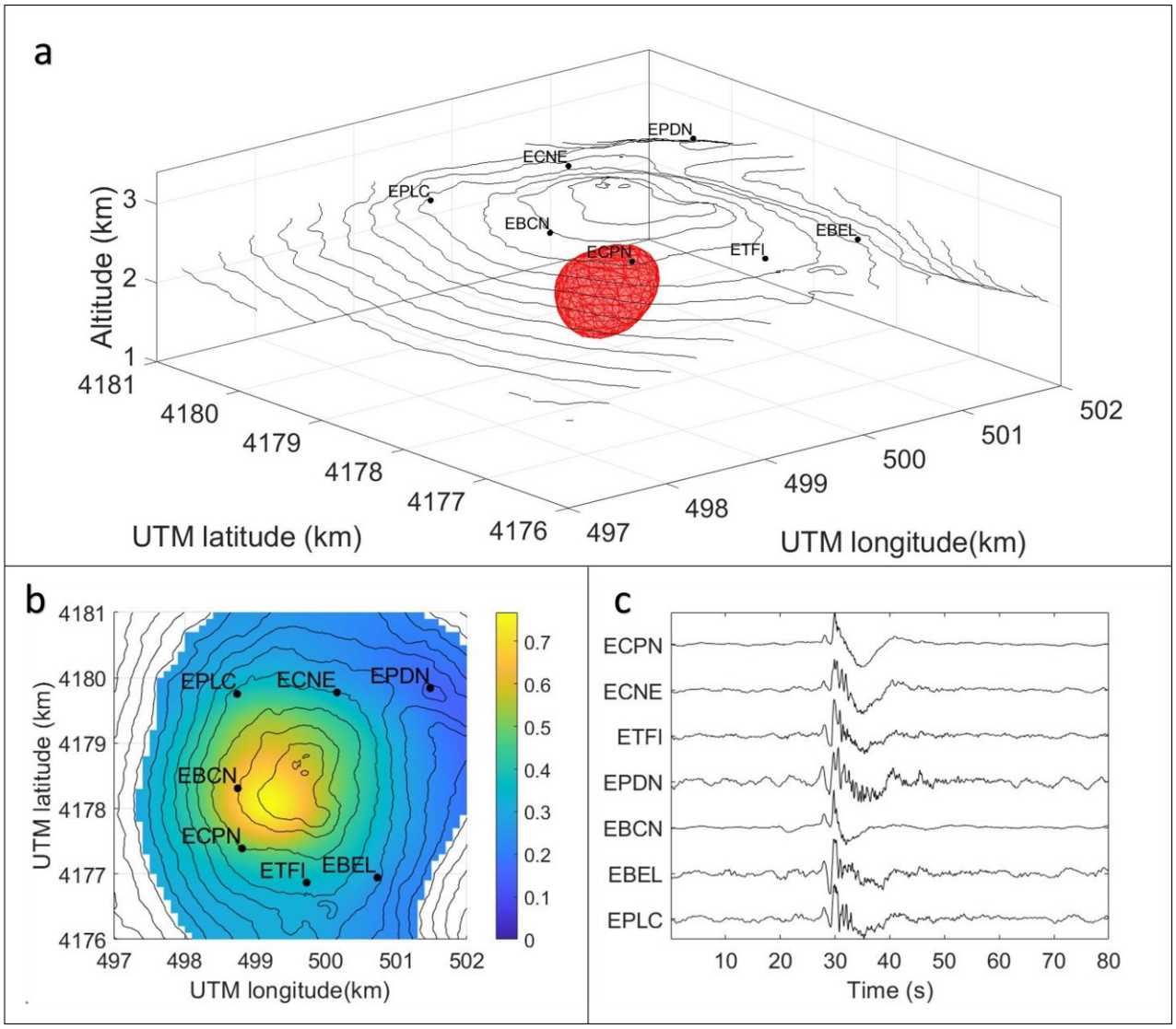

Figure 1.25. a) Example of volume comprising the grid nodes with semblance higher than a certain value, obtained by locating a VLP event at Mt. Etna. b) Example of space distribution of semblance values calculated by locating a VLP event at Mt. Etna. (c) Seismic signals at the different stations shifted by the time delay that allows obtaining the maximum semblance.

All these array approaches, however, share the common problem of the evaluation of the uncertainties in the estimate of the source position or medium velocity. One way to assess the stability of the localization solutions is provided by JackKnife method (Efron, 1982). This technique is very helpful when the statistical distribution of the calculated parameters is unknown. It is also called as “leave one out”, because it is a sequential bootstrap method. In this procedure, estimates of an unknown parameter P (for example latitude, longitude, and depth of volcanic source or back azimuth and slowness) are computed for each source

location by omitting the *i-th* station at a time. These estimates are used to compute the so-called pseudovalues (Cannata et al., 2013):

$$J_i = n\,\acute{\mathrm{P}} - (n-1)\,P_i \tag{1.38}$$

where $\acute{\mathrm{P}}$ is the parameter computed by considering all the stations, P_i is the parameter calculated by leaving out the *i-th* station and n is the number of stations. The standard error of these values returns the bias affecting the observed parameter (Cannata et al., 2013):

$$\boldsymbol{\delta}_{\mathrm{J}(\acute{\mathrm{P}})} = \sqrt{\frac{1}{n(n-1)}\sum_{i=1}^{n}(J_i - \mathrm{J}(\acute{\mathrm{P}}))^2} \tag{1.39}$$

where $\mathrm{J}(\acute{\mathrm{P}})$ is the JackKnife estimator given by the arithmetic mean of the *i-th* pseudovalues.

Although these methods offer several advantages, they also suffer from some limitations. Generally, in most part of the previous methods, the goodness of localizations depends on different technical constraints (Chiou and Bolt, 1993; Almendros et al., 1999; Almendros and Chouet, 2003; Cannata et al., 2009a; Inza et al., 2011; Almendros et al., 2014), such as the length of analysis window, the frequency range, the size of slowness or spatial grid and the propagation parameters (for example, velocity of the waves, quality factor, attenuation coefficient, ecc…). At the same time, source estimation is affected by multiple factors, such as array/network characteristics, amount of coherence, noise content and topographic, propagation and site effects (e.g. Neuberg and Pointer, 2000; Almendros and Chouet, 2003; Saccorotti et al., 2004; Kumagai et al., 2011; Cauchie and Saccorotti, 2013; Zuccarello et al., 2016). JackKnife estimation is very useful to improve the quality of the results because it allows to assess a general contribution given from each factor. However, it represents a time consuming method and, it can only provide a measure of stability of the solutions (e.g. Di Grazia et al., 2009; Cannata et al., 2013). Techniques such as ZLCC, Semblance and Radial Semblance are not reliable to resolve multiple simultaneous sources and are characterized by longer computing time (Neidell and Taner, 1971; Frankel et al., 1991; Del Pezzo et al., 1997), in contrast to MUSIC one (Schmidt, 1986; Chiou and Bolt, 1993). However, methods as MUSIC could fail with non-stationary, quasi-monochromatic signals

or with restricted array configurations (Schmidt, 1986; Chiou and Bolt, 1993). In addition, ZLCC and MUSIC methods are confined to only records from array and they show lower resolution in the depth, especially by using only one seismic array (e.g. Almendros et al., 1999; Almendros et al., 2014). Instead, techniques as Semblance and Radial Semblance can be used for data from both arrays and sparse networks (e.g. Di Lieto et al., 2007; Zuccarello et al., 2013), but they are more affected by the relationship between inter-station distances and the wavelength signals or by the use of particle motion as in the case of the Radial Semblance (Kawakatsu et al., 2000; Almendros and Chouet, 2003).

CHAPTER 2 – FEATURES OF SEISMIC SIGNALS AT MT. ETNA

2.1 INTRODUCTION

The quantification of the wavefield properties of seismo-volcanic signals represents one of the most powerful tools for the study of the different phases of volcano activity. In fact, an interesting feature of signals such as volcanic tremor, LP and VLP events is their close relationship to changes in volcanic activity, highlighted by variations in amplitude, spectral content, polarization attributes, waveforms, occurrence rate and source locations (e.g. Gresta et al., 1991; Alparone et al., 2007; Patane` et al., 2008; Di Grazia et al., 2009; Cannata et al., 2010a; Zuccarello et al., 2013). One of the toughest challenges is the determination of source position of signals recorded in volcanic areas, due to their sustained or emergent nature. Thanks to the availability of different data and the ever-increasing computing power, many different approaches were developed for a reliable interpretation of the eruptive phenomena that characterize a volcano such as Mt. Etna (e.g. Battaglia et al., 2003; Kumagai et al., 2002; De Barros et al., 2009; O'Brien et al., 2011; Marioka et al., 2017). One of these strategies is represented by the array techniques.

As explained in the previous Chapter, array methods are based on the common waveform model (Aki e Richards, 1980), allowing to improve the signal-to-noise ratio of the traces. The reliability of array processing depends on different factors, such as the relationship between array/network configuration and the signal wavelengths analyzed, the geological homogeneity of area of interest and the influence of path and site effects and local noise on wavefield (Tokimatsu, 1997; Almendros et al., 2012; Havskov et al., 2016). The evaluation of the degree of wavefield coherence and the separation of path/site and source effects are very important to ensure the best performance of array methods (e.g. Inza et al., 2014; Zuccarello et al., 2016). Therefore, the determination of wavefield properties, such as coherence, frequency features, particle motions and energy levels, can help obtain more constraints about the source location of the signals and the magma dynamics in the plumbing system (e.g. Saccorotti et al., 2004,2007; Zuccarello et al., 2013; Almendros et al., 2014; Eibl et al., 2017).

Another important aspect of data processing is the detection of different volcanic signals. In the past, experts carried out the manual individuation of seismo-volcanic events, such as LP and VLP events. This is very tedious, especially with a great amount of data and the presence of background and nonstationary noises (Ibànez et al., 2003). The ever-increasing

amount of seismic data required the implementation of automatic processing tools (e.g. Allen, 1982; Evans and Pitt, 1995; Kao et al., 2007; Rouland et al., 2009; Ciaramella et al., 2011; Cortés et al., 2017; Bueno et al., 2020).

In the following paragraphs of this chapter, a study of volcanic signals recorded at Mt. Etna during the 2010-2011 period will be illustrated. Considering the data recorded during some seismic experiments by small-aperture arrays, as well as INGV permanent network, we analysed the wavefield properties associated with volcanic tremor and LP and VLP events, in order to assess their temporal evolution concurrently to the different states of volcano. In addition, we applied methods to evaluate the coherence response of arrays and signal wavefield, trying to define a frequency range in which the array processing could be reliable. The chapter will be organized as follows: firstly, we will describe the experimental set-up and the data collection procedures; then, we will present the array response function of the seismic antennas; we will proceed by showing the spectral, amplitudes and polarization properties of volcanic tremor signals in time; we then will illustrate temporal variations of occurrence rate, energy and particle motions of the LP and VLP activity, taking into account the waveform classification of the events; successively, basing on these results, we will provide preliminary information about dynamics of magma extrusion in the plumbing system of Etna volcano and frequency ranges retrieved for the best performance of array processing, taking into account the technical limits of each method; finally, we will discuss on the possible future works needed for improving the knowledge about the wavefield properties of volcanic signals.

2.2 SEISMIC FRAMEWORK AND DATA

In order to investigate the volcano activity that characterized Mt. Etna between 2010 and 2011, we analysed data recorded during a seismic experiment conducted by “Istituto Nazionale di Geofisica e Vulcanologia” (INGV) during 2010 and 2011 summertime. The experiment consisted in the deployment of one dense, small-aperture (150-200 m) seismic array at 1 km SW from SEC (Fig. 2.1a), nearby the single station called “Torre del Filosofo” (ETFI). This array consisted of 6 vertical component receivers deployed in an irregular pattern with an inter-spacing of 100 m (Fig. 2.1b). The array was equipped with Lennartz® (LE-3D/20s) broad-band (0.05-40.0 Hz; sampling rate of 100 Hz) sensors connected via cable to two 3-channel Nanometrics® “Taurus” data loggers (Tab. 3). In 2010, this array acquired efficiently seismic data during two main periods, spanning the 1

July-20 October time interval. During this period, the array operated continuously, suffering a major technical failure lasting from 24 July to 2 August (Fig. 2.2a). During 2011 summertime, this array was deployed in same area of the previous year, showing the same geometry, location and instrumental features and acquiring data from 1 July to 24 August (Fig. 2.3a). However, during this time interval, the seismic array was characterized by some technical problems, leading poorly functioning of one of the two data loggers and some sensors (Tab. 4). Unfortunately, the size of array is reduced to only 5 sensors (Fig. 2.1c).

In addition, we used data from seismic monitoring network managed by INGV. At Mt. Etna, in 2010-2011 the seismic permanent network comprised 33 broadband and 12 short-period stations. The analyses of seismo-volcanic signals are performed on the recordings of 7 of these stations (Fig. 2.1a), each equipped with a broadband (40 s cutoff period), three-component Trillium seismometer (Nanometrics®) and acquired in real time at sampling rate of 100 Hz (Tab. 5). In this case, the seismic network operated efficiently in the 2010-2011 period, allowing to complete/improve the array dataset (Fig. 2.2a and Fig. 2.2b). In particular, for the volcanic tremor investigation, we used data recorded during the functioning periods of the two seismic arrays, including those from permanent network. Instead, for the study of LP and VLP activity, we performed most of the analyses on the data acquired by the sparse network shown in figure 2.1, integrating the results obtained from arrays. Therefore, in this case, we completed the dataset with the sparse network data recorded between June and October 2010 and along the whole year 2011.

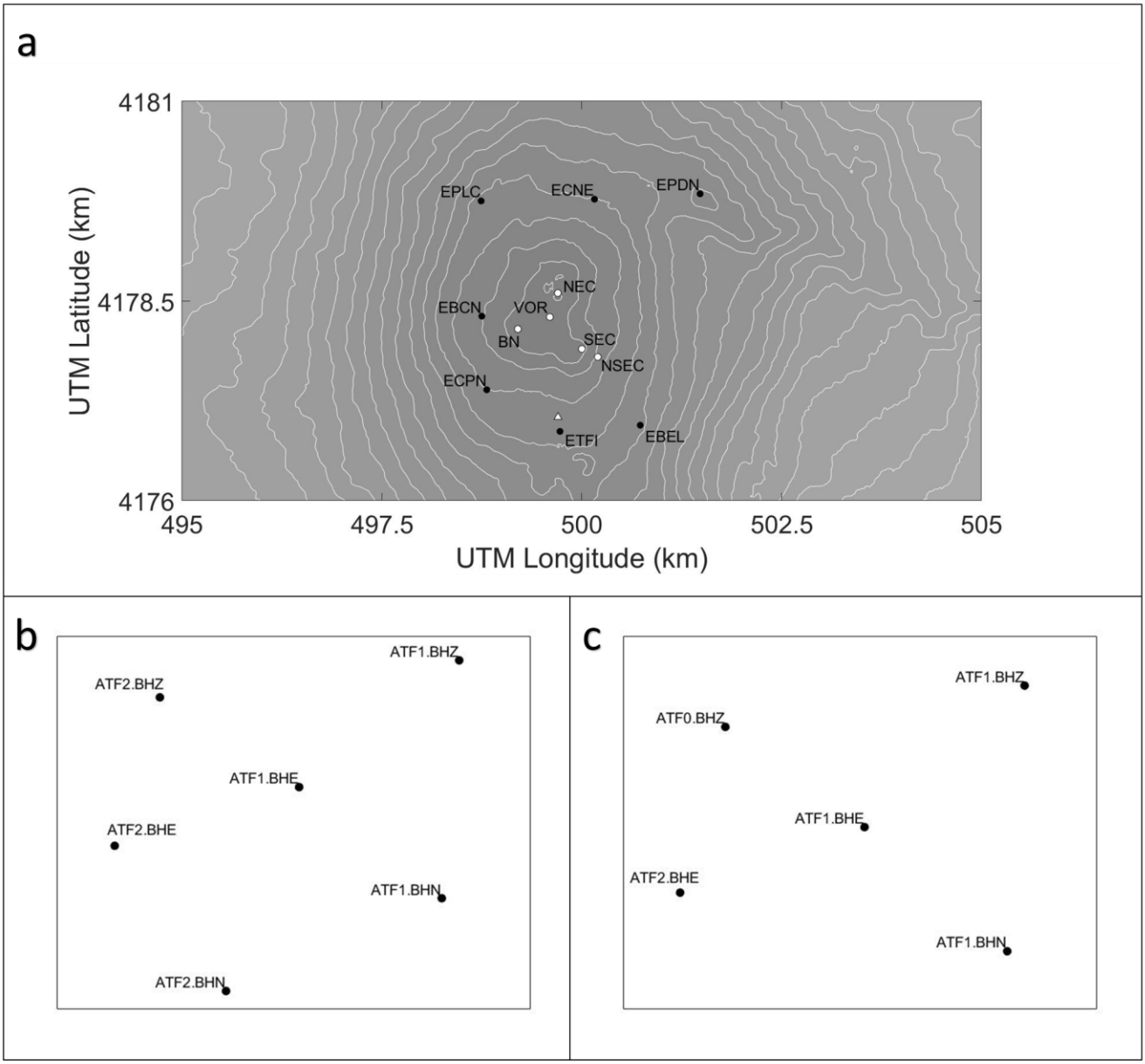

Figure 2.1. a) Digital Elevation Model (DEM) of the summit area of Mt. Etna with the main craters (white circles; Bocca Nuova: BN; Voragine: VOR; North-East Crater: NEC; South-East Crater: SEC; New South East Crater: NSEC), the INGV seismic permanent stations (black circles) and the array location (white triangle) during 2010-2011 time interval. b) Array geometry in 2010. c) Array geometry in 2011.

Name	Station	Sensor	UTM Longitude (km)	UTM Latitude (km)	Elevation (km)
ATF1.BHE	Taurus S/N 966	LE-3D/20s S/N G133	499,7019	4177,0476	2,9730
ATF1.BHN	Taurus S/N 966	LE-3D/20s S/N G132	499,7621	4176,9811	2,9640
ATF1.BHZ	Taurus S/N 966	LE-3D/20s S/N G139	499,7695	4177,1234	2,9850
ATF2.BHE	Taurus S/N 631	LE-3D/20s S/N G129	499,6241	4177,0125	2,8480
ATF2.BHN	Taurus S/N 631	LE-3D/20s S/N G128	499,6711	4176,9256	2,8400
ATF2.BHZ	Taurus S/N 631	LE-3D/20s S/N G130	499,6432	4177,1013	2,9730

Table 3. Array configuration and location of the sensors expressed in UTM geographic coordinate system during 2010.

Name	Station	Sensor	UTM Longitude (km)	UTM Latitude (km)	Elevation (km)
ATF1.BHE	Taurus S/N 966	LE-3D/20s S/N G133	499,7019	4177,0476	2,9730
ATF1.BHN	Taurus S/N 966	LE-3D/20s S/N G132	499,7621	4176,9811	2,9640
ATF1.BHZ	Taurus S/N 966	LE-3D/20s S/N G139	499,7695	4177,1234	2,9850
ATF2.BHE***	Taurus S/N 631	LE-3D/20s S/N G130	499,6241	4177,0125	2,8480
ATF2.BHN**	Taurus S/N 631	LE-3D/20s S/N G128	499,6711	4176,9256	2,8400
ATF0.BHZ *	Taurus S/N 626	LE-3D/20s S/N G203	499,6432	4177,1013	2,9730

Table 4. Array configuration and location of the sensors expressed in UTM geographic coordinate system during 2011. * Poorly functioning of the data logger and sensor ATF2.BHZ. They were replaced and the receiver was renamed. ** Bad acquisition of the seismic traces. This sensor was neglected during data analysis. *** Poorly functioning of the data logger and sensor ATF2.BHE. The sensor was replaced, while the data logger was recovered. As consequence of some technical problems, the sensor was replaced with a three components one, renamed as ATF2.BHZ3D.

Name	Station	Sensor	UTM Longitude (km)	UTM Latitude (km)	Elevation (km)
EBCN	Trident	Trillium/40s	498,7491	4178,3107	3,0900
EBEL	Trident	Trillium/40s	500,7313	4176,9460	2,8990
ECNE	Trident	Trillium/40s	500,1585	4179,7751	2,9570
ECPN	Trident	Trillium/40s	498,8106	4177,3898	3,0500
EPDN	Trident	Trillium/40s	501,4797	4179,8418	2,8700
EPLC	Trident	Trillium/40s	498,7405	4179,7530	2,9680
ETFI	Trident	Trillium/40s	499,7269	4176,8683	2,9960

Table 5. INGV seismic permanent network configuration and location of the sensors expressed in UTM geographic coordinate system during 2010.

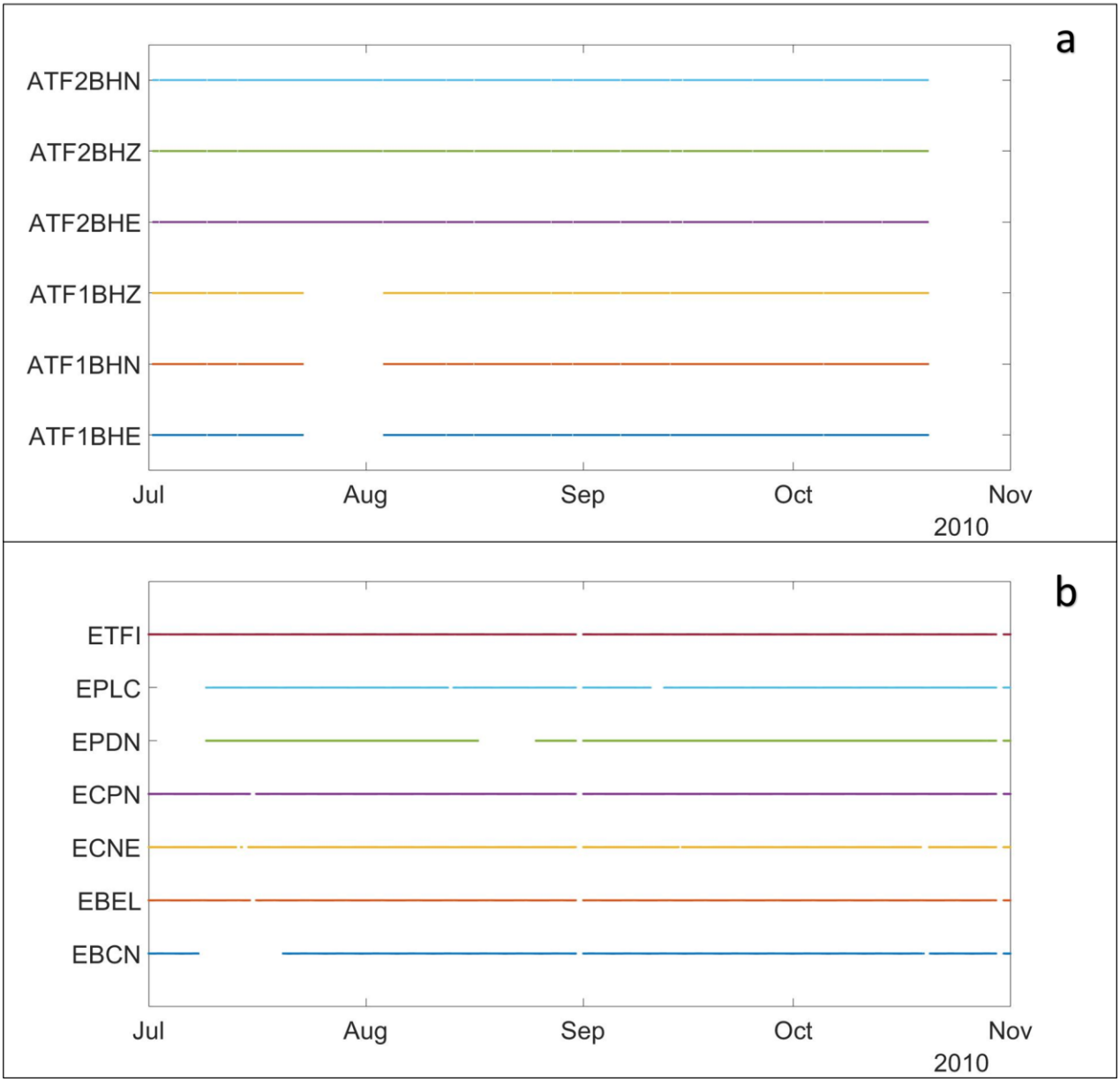

Figure 2.2. Temporal coverage of array (a) and permanent network (b) during 2010. The array acquired data in continuous in the following periods: 01 July 12:00-23 July 03:00 and 03 August 11:00-20 October 08:00.

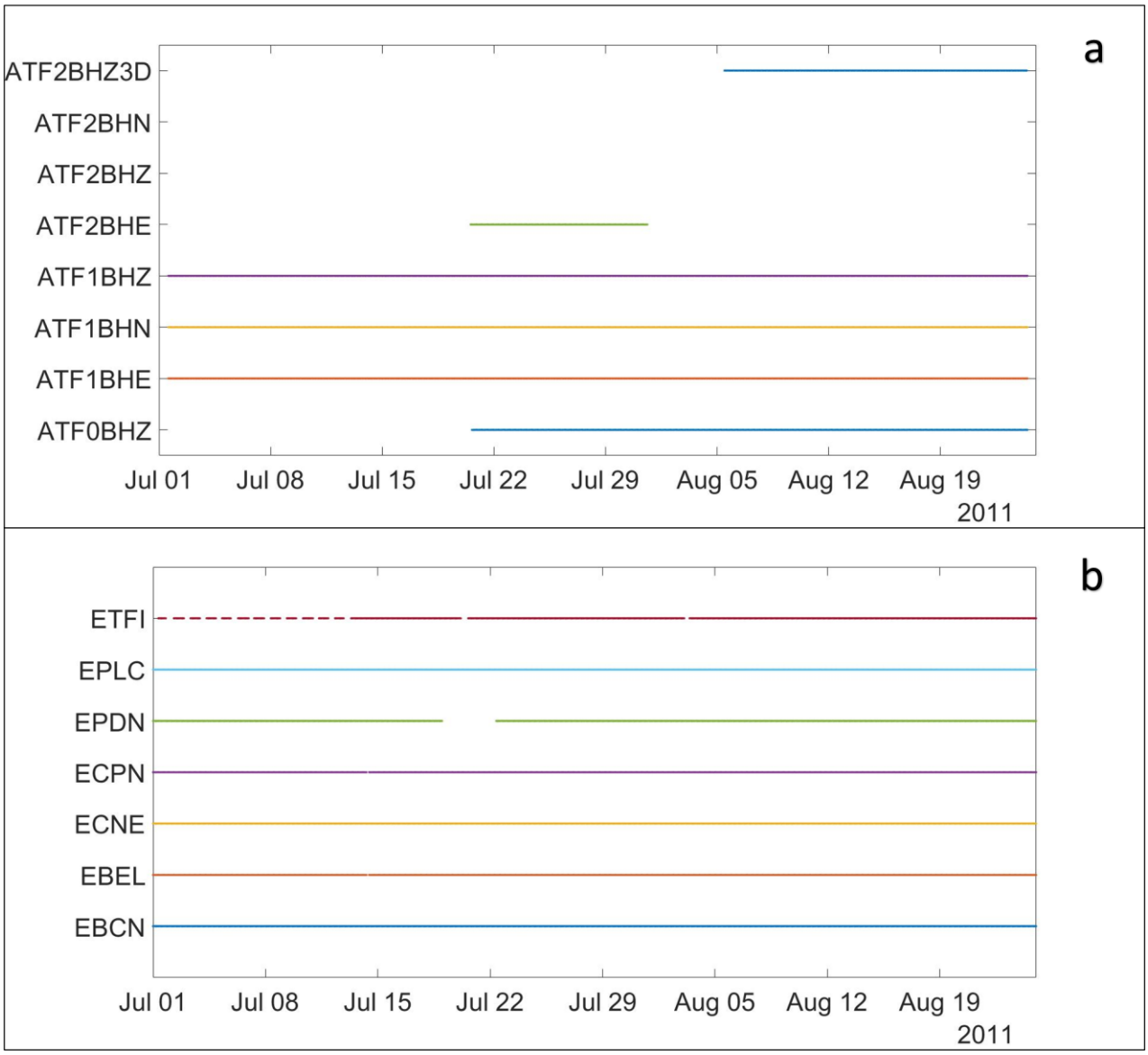

Figure 2.3. Temporal coverage of array (a) and permanent network (b) during 2011. The array acquired data in continuous in the following periods: 20 July 13:00-31 July 15:00 and 05 August 11:00-24 August 13:00.

2.3 DATA ANAYSIS

As mentioned before, the analysis of the seismo-volcanic signal plays a key role in the performance of the array analysis or the localization techniques, because it provides important information about wavefield composition and the dynamics involving eruptive phenomena such as paroxysm or minor explosive events. In fact, taking into account the assumptions seen in section 1.3.6 (Chapter 1), it is necessary to define the frequency range in which the coherence among traces is maximized, making the localization analysis more reliable. In addition, the characterization of the wavefield, in terms of spectral, amplitude and polarization features, could represent an efficient tool to understand better the seismic source mechanisms during volcanic activity. In the next sections, we will show the results obtained through the analysis of the volcanic tremor and LP and VLP events recorded at Etna during 2010-2011.

2.3.1 BEAM PATTERN

The results of array analysis are affected by different factors. Among them, the choice of the number of stations, the aperture and the location of the seismic antennas may be crucial in order to optimize their acquisition capabilities, especially in terms of coherence among different waveforms. In fact, it necessary to distinguish between primary or secondary or fictitious sources during the data processing. The array geometry, in turn, depends on the geology of the situ and the azimuthal coverage of the area of interest, while the inter-spacing of the array is related to the wavelength of the signal of interest. During the experiment in 2010 and 2011, two arrays were deployed taking into consideration these constraints. In particular, the arrays were located in a homogenous area from the geological point of view, reducing the influence of the site effects on the coherence among signals. Their geometry and location were studied in order to ensure as much as possible a good azimuthal coverage of the summit area of Mt. Etna. Taking into account that the velocity of seismic waves is about 1-3 km/s and the aperture of the arrays are about 150-200 m, the dominant wavelengths of the signals are nearly 1 km, providing a good resolution of the wavefield. In addition, as mentioned in the previous chapter (section1.3), source-array sensors distances must be greater than one wavelength so that the wavefront arriving at each array can be assumed as planar (Havskov, 2016). In this case, considering the velocity and the frequency content of the seismic waves observed at Mt. Etna (e.g. Patanè et al., 2013), the arrays were deployed at 1.5-2 km from summit area of the volcano, ensuring reliable conditions for the use of array methods.

One way to quantify the coherence capabilities of the arrays is given by the Beam Pattern analysis (see the section 1.3.2, Chapter 1). The array response corresponding to the configuration used at two arrays deployed in 2010 and in 2011 is shown in figure 2.4. This function was computed for many different frequencies ranging 0.5 to 5.0 Hz with a step of 0.5 Hz. For the lowest frequencies, results indicated a small contribution of spatial aliasing in the array response of the two configurations. In both cases, from the broad peak observed at 0.5 Hz, it was possible to deduct that the arrays showed a poor resolution at low frequency because of the signal wavelength larger than the array aperture. The upper frequency limit depended on the array inter-spacing and site effects, reducing the coherence among the seismic receivers. In both arrays, the results of Beam Pattern analysis revealed that the arrays had a coherent response up to frequency of 3.5 Hz, while the influence of the spatial aliasing was more prevalent for increased frequencies.

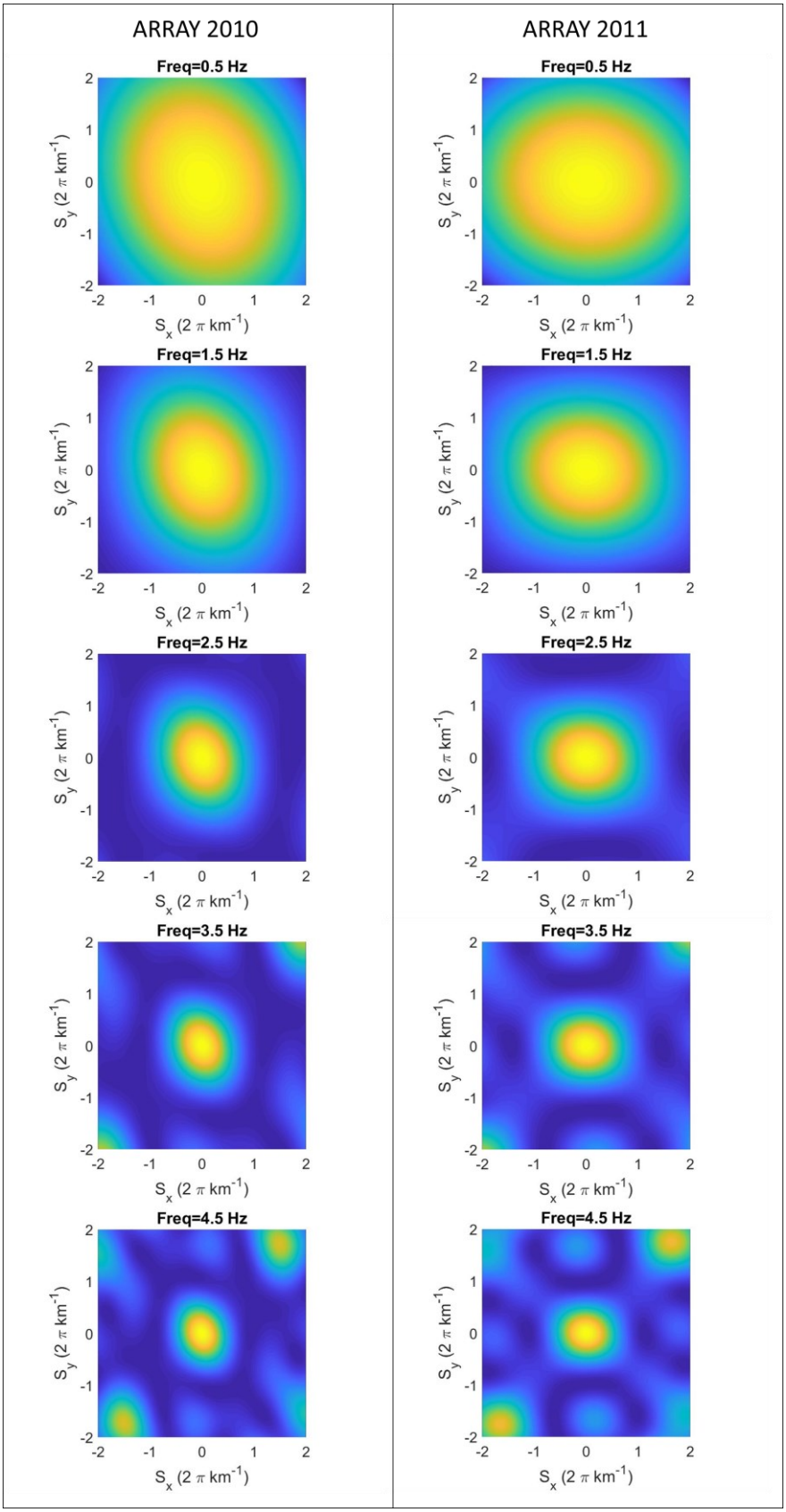

Figure 2.4. Array response computed for a vertically incident wave at different frequencies and for the arrays deployed in 2010 (left-hand of the diagram) and 2011 (right-hand of the diagram).

2.3.2 VOLCANIC TREMOR

As explained before, the efficiency of the array analysis could be improved by analysing the main properties of the wavefield, such as the frequency content, the amplitude and polarization features. In fact, evaluating the frequency range in which most part of the signal energy is radiated, is a better way to understand the nature and the origin of volcanic tremor. At the same time, the determination of the polarization attributes contributes to this purpose, because it is very helpful to investigate the kind of phases that composed the wavefield.

Temporal variations of the spectral properties of the volcanic tremor can be observed by the spectrogram calculation (see section 1.3.3, Chapter 1). During the periods of interest, this representation was retrieved by computing FFT algorithm over 1-minute-long time sliding window along recordings of the central station of the arrays. The window length was chosen so that the spectra obtained showed good frequency-time resolution. The spectra were successively averaged every 30 minutes and normalized, obtaining the spectrograms shown in figures 2.5a and 2.6a. During 2010, the seismic radiation was bounded in the 0.5-6.0 Hz frequency band, showing a complex distribution of primary and secondary peaks. In particular, tremor spectra were mainly peaked at frequencies of about 5 and 6 Hz especially during the months of July and August. Instead, starting from the last days of August, most of seismic energy was confined in the 1.0-2.0 Hz band in accordance with the increase of the explosion activity at BN (Fig. 2.5b), remaining unchanged throughout the remainder of period. In 2011 summertime, the frequency features of the volcanic tremor were quite similar to the previous year, showing rather a different temporal evolution. Here too, different spectral peaks were recognized in the 0.5-6.0 Hz frequency band, especially during the quiescent periods of the Etna volcano. This complexity probably was related to a combination of source and path/site effects. However, most of the seismic radiation was bounded in the 1.0-2.0 Hz frequency range during the lava fountaining at NSEC (Fig. 2.6b).

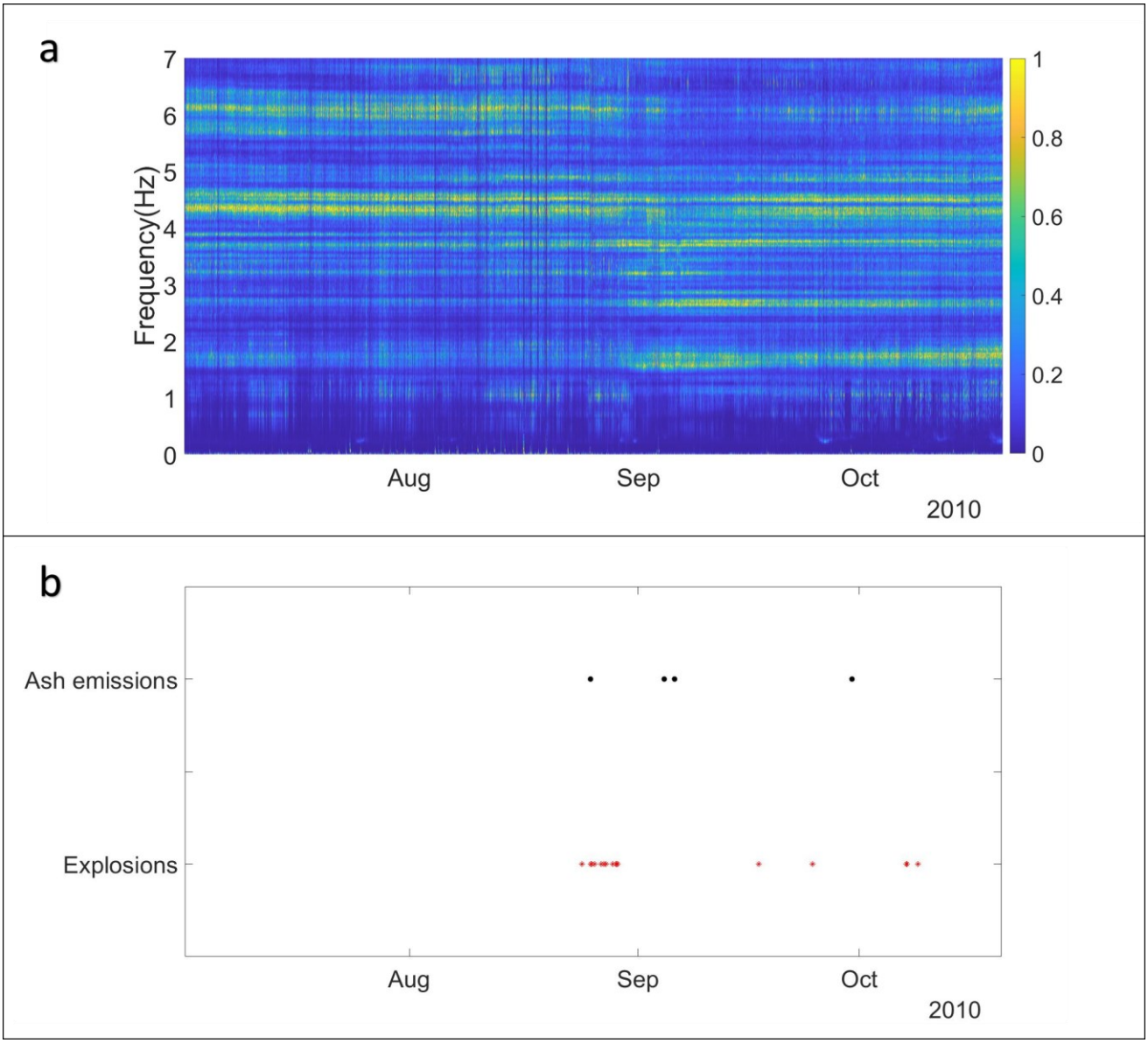

Figure 2.5. Spectral properties of volcanic tremor during 2010. a) Spectrogram of traces of the central station of the array (ATF1.BHE). The colorbar on the right-hand refers to the normalized values of the spectral amplitudes. b) Volcanic activity observed at BN crater (data from Andronico at al., 2013).

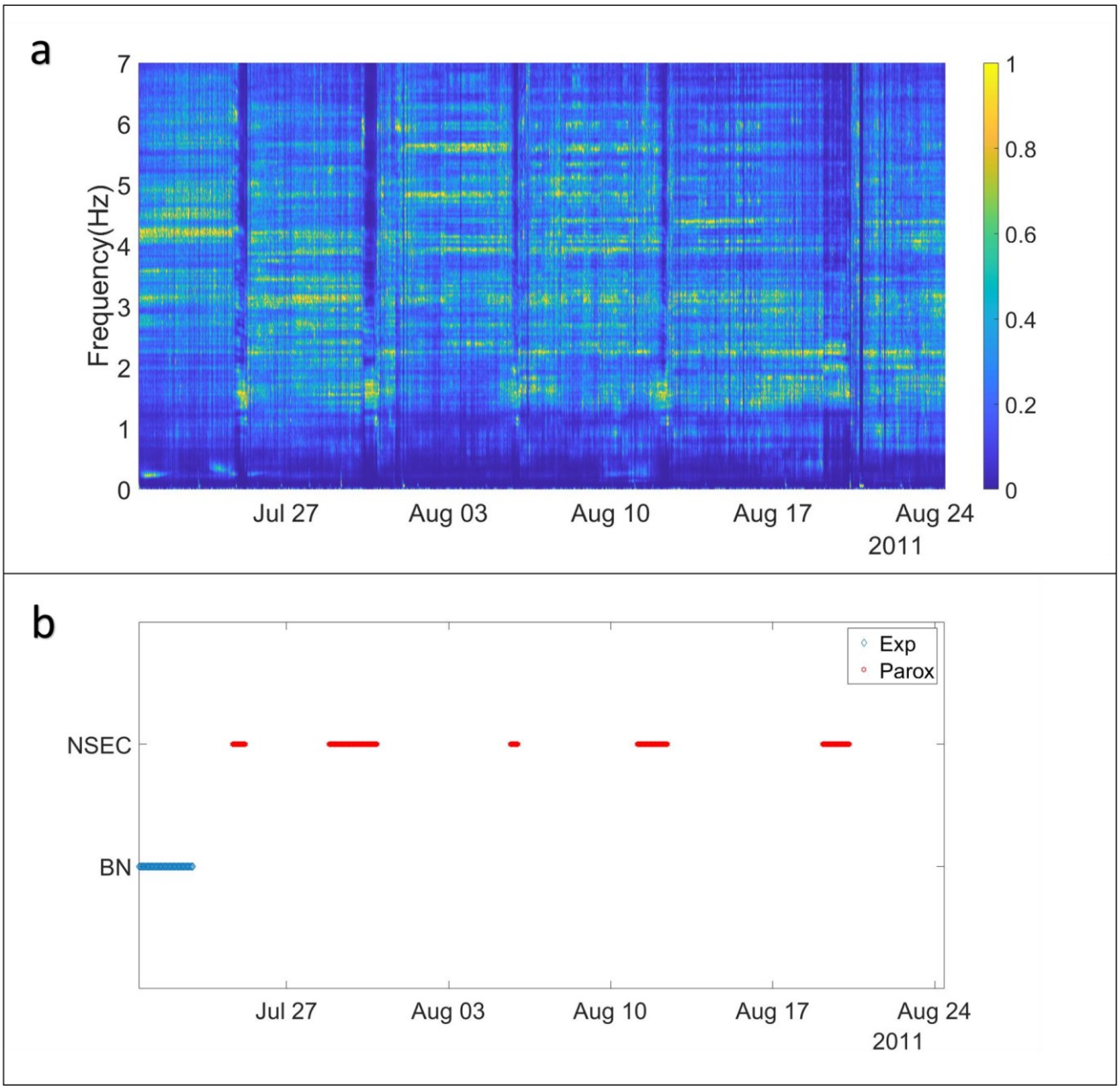

Figure 2.6. Spectral properties of volcanic tremor during 2011. a) Spectrogram of traces of the station of the array ATF2.BHZ. The colorbar on the right-hand refers to the normalized values of the spectral amplitudes. b) Volcanic activity observed at NSEC and BN crater. The legend on the upper right-hand of the diagram shows the type of volcanic event: Exp= single explosions or series of minor explosions, minor and/or intense ash emissions; Parox= Strombolian, lava effusion and lava fountaining activity (data from Behncke et al., 2014).

As explained before, seismic waves propagating from the source to receivers are certainly influenced by the medium, reducing the coherence of wave field recorded by the array. However, the signal coherence can be also degraded by the array configuration, especially with increased inter-station distance. The inter-sensor coherence of a seismic wavefield is frequency dependent, limiting the optimal bandwidth for array processing. One way to evaluate a frequency range reliable is represented by the calculation of the coheregram (see section 1.3.3 Chapter 1). This representation allowed us to observe the temporal changes of the spectral coherence of the volcanic tremor recorded during 2010-2011. It was obtained by the same procedure seen previously for the spectrogram, but sliding 60-minute-long time window along the seismic traces of the array. In this case, the results were only normalized. During the experiment of 2010, the tremor wavefield recorded by the array was mainly coherent in the 0.1-2.0 Hz frequency range, keeping these features for the whole period (Fig 2.7a). Generally, the maximum values of the spectra were bounded in the 0.1-1.2 and 1.4-2.0 Hz frequency bands, although sometimes they were recognized for higher values of frequency. One exception was represented by the minor peaks distributed from September onwards, concurrently with the intensification of the volcanic activity at BN crater (Fig 2.7b). In this case, it was possible to observe high values of coherence between 2.5 and 3.0 Hz. In 2011, the array recorded volcanic tremor that showed similar features to the previous case (Fig. 2.8a). In particular, the spectral coherence was focused on the 0.1-2.0 Hz frequency band, showing higher values during lava fountaining activity (Fig. 2.8b). The main peaks were rather bounded at the frequency of about 1 Hz.

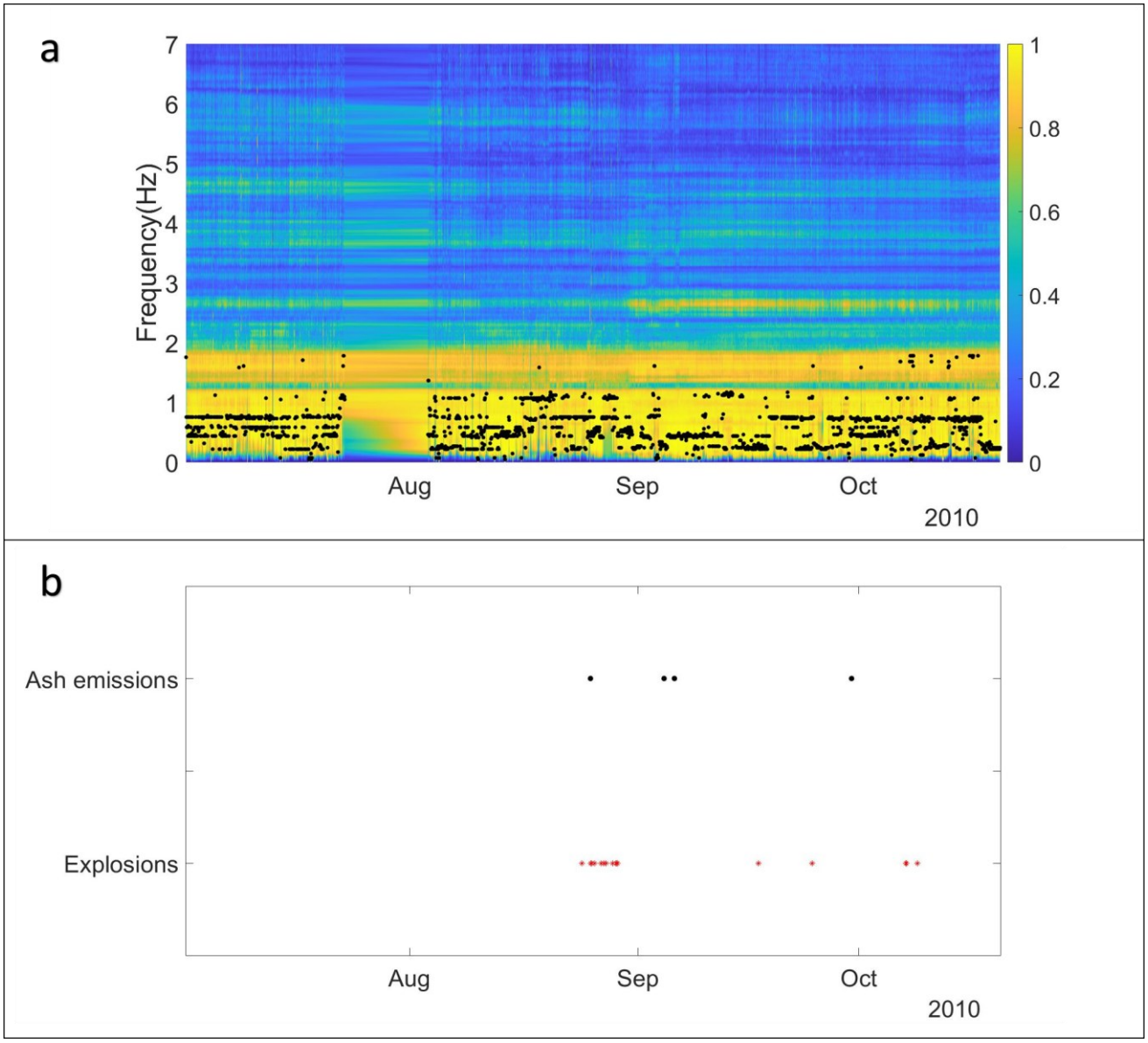

Figure 2.7. Spectral coherence of volcanic tremor during 2010. a) Coheregram of traces recorded at array. The colorbar on the right-hand refers to the normalized values of MSC function. The black marks indicate the maximum values of the MSC function. b) Volcanic activity observed at BN crater (data from Andronico at al., 2013).

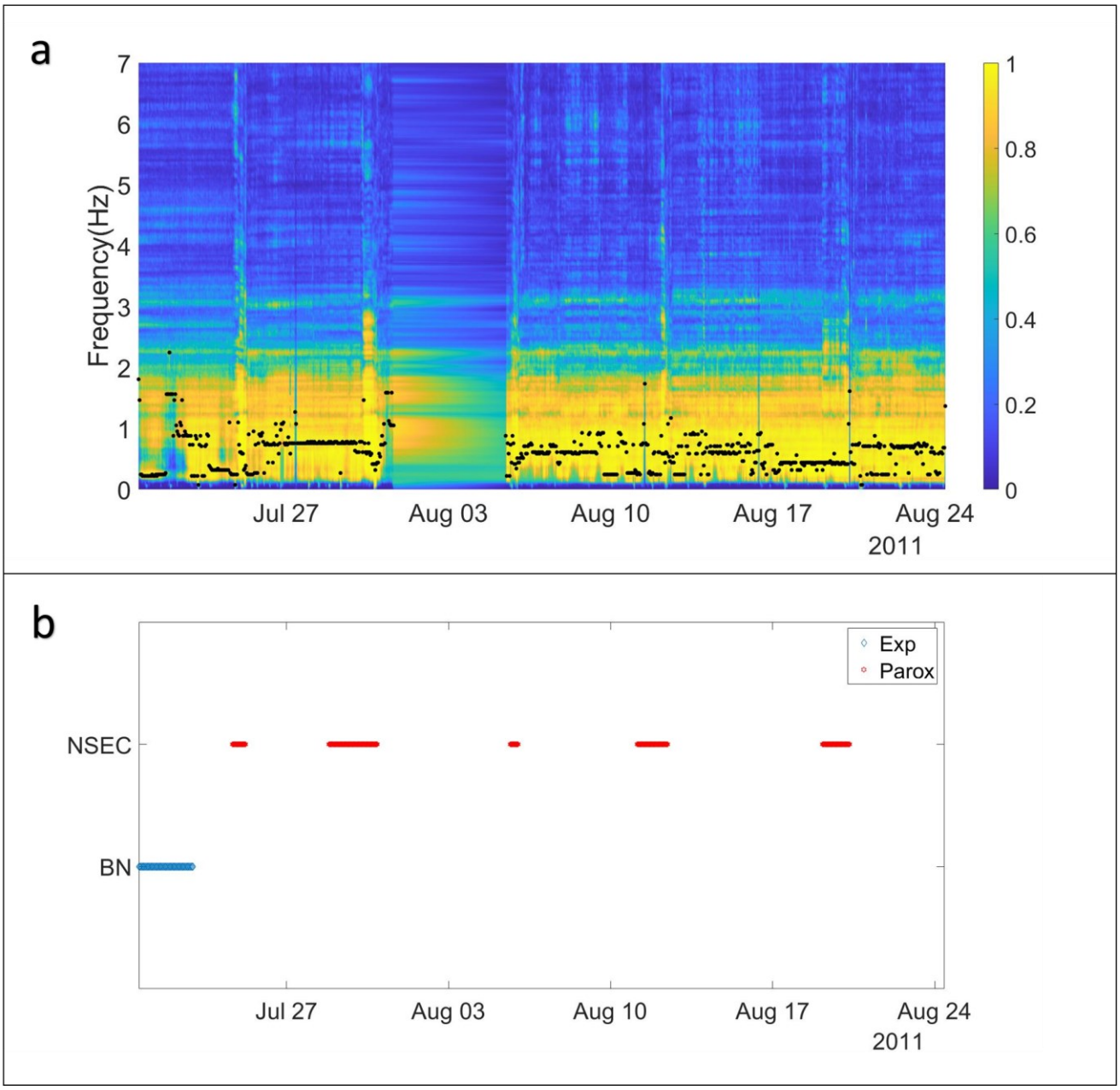

Figure 2.8. Spectral coherence of volcanic tremor during 2011. a) Coheregram of traces recorded at array. The colorbar on the right-hand refers to the normalized values of MSC function. The black marks indicate the maximum values of the MSC function. b) Volcanic activity observed at NSEC and BN crater. The legend on the upper right-hand of the diagram shows the type of volcanic event: Exp= single explosions or series of minor explosions, minor and/or intense ash emissions; Parox= Strombolian, lava effusion and lava fountaining activity (data from Behncke et al., 2014).

Another way to characterize the nature of the volcanic tremor is represented by the calculation of the RMS of the seismic amplitude (see section 1.3.3, Chapter 1). The time variation of the amplitudes was computed on 10-second-long time sliding windows along the traces of central station of the two arrays. This analysis was performed in the 0.1-3.5 Hz frequency range, filtering the recordings in different frequency bands with a band-pass cosine filter. The RMS amplitudes were also averaged in time by 3-hour moving average. The results for 2010 and 2011 experiments are shown in the figures 2.9 and 2.10, respectively. In the first case, we observed significant variations of the tremor amplitudes, especially during the last two months of recording. At the same time as the occurrence of the increase of the explosions at BN crater, the RMS amplitudes gradually increased up to medium-low levels compared to those exhibited during quiescent periods, keeping these features in the remainder of the period. The higher values of the seismic radiation were observed in the 1.5-3.5 Hz frequency interval, while slightly lower values of the tremor amplitudes were recorded in the remaining part of the considered frequency band. The RMS patterns were very coherent in this frequency range, although they showed differences between the 0.1-1.5 Hz and the 1.5-3.5 Hz bands. In the second case, the volcanic tremor amplitudes presented similar features as shown previously in the 2010 experiment, especially during quiescent periods of volcanic activity. However, a gradual increase in the tremor amplitude was observed in occurrence of the paroxysms, precisely at the beginning of the Strombolian activity. At the same time as the intensification of the explosive activity, the amplitudes increased abruptly, achieving high levels with the development of the lava fountaining. When the phenomena disappeared, the RMS amplitudes dropped abruptly, returning to the background levels exhibited before the onset of the paroxysmal activity. Some exceptions were represented by the paroxysms of the 30 July and 20 August, when the tremor amplitudes gradually decreased just before the onset of lava fountaining activity. The RMS time series presented high values of coherence in the entire frequency range of analysis, especially during the paroxysms. Some differences were recognized in the energy distributions. In fact, during the quiescent periods of the volcano, the higher RMS amplitudes were focused on the 1.5-3.5 Hz frequency interval; instead, in occurrence of lava fountaining, the seismic radiation was more bounded in the 0.1-1.5 Hz band. One exception was the episode of the 20 August. In this case, the higher amplitudes and the lack of coherence were related to technical problems that occurred during the maximum intensity of the lava fountaining. This was confirmed by the results obtained by coherence analysis (Fig. 2.8a).

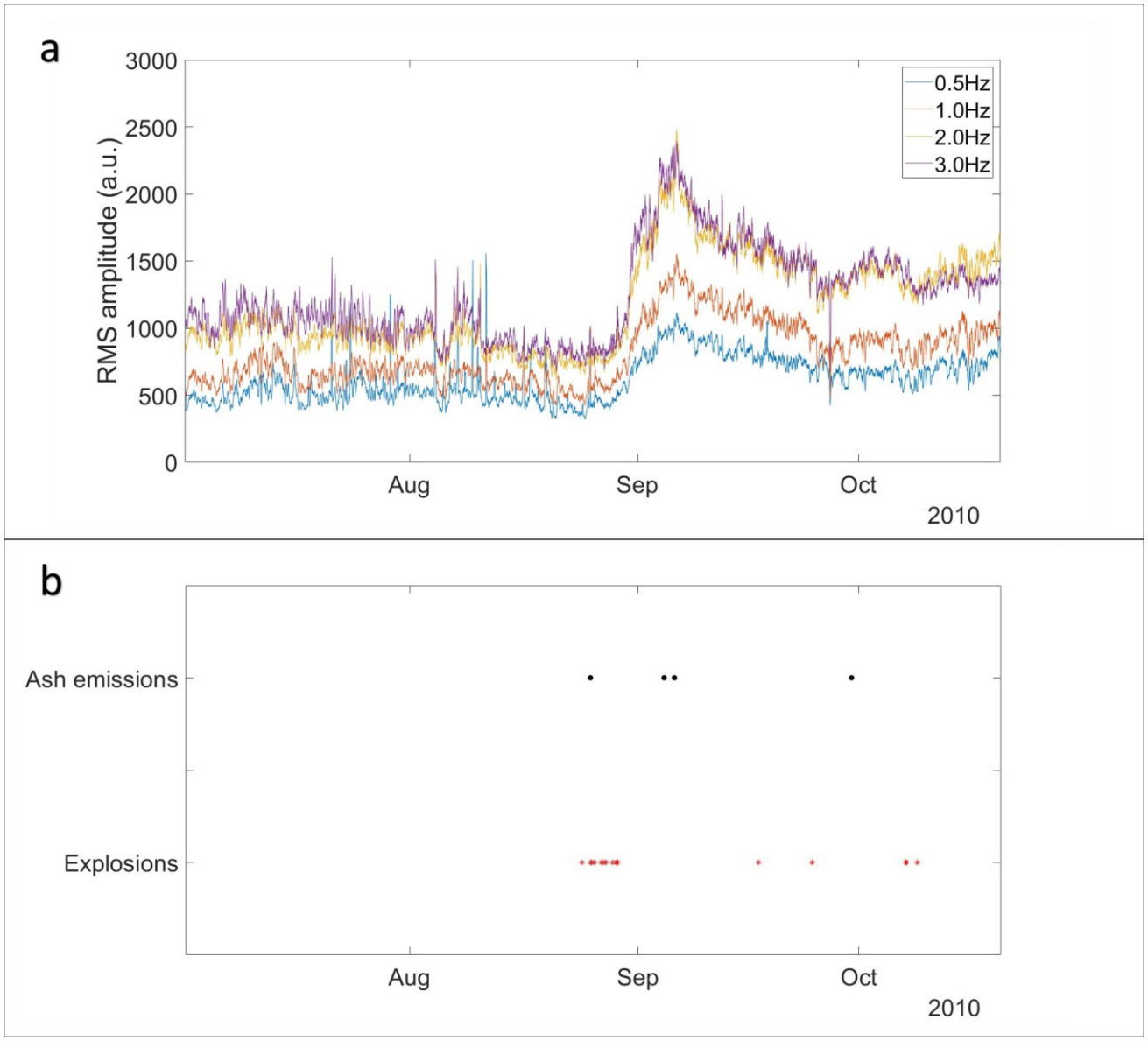

Figure 2.9. Amplitude properties of volcanic tremor during 2010. a) Moving average of the RMS amplitude of the tremor recorded at central sensor of array. The legend at the top right refers to the central frequency of analysis bands, that are wide 1 Hz. The axes of plots are set in semi-logarithmic scale. b) Volcanic activity observed at BN crater (data from Andronico at al., 2013).

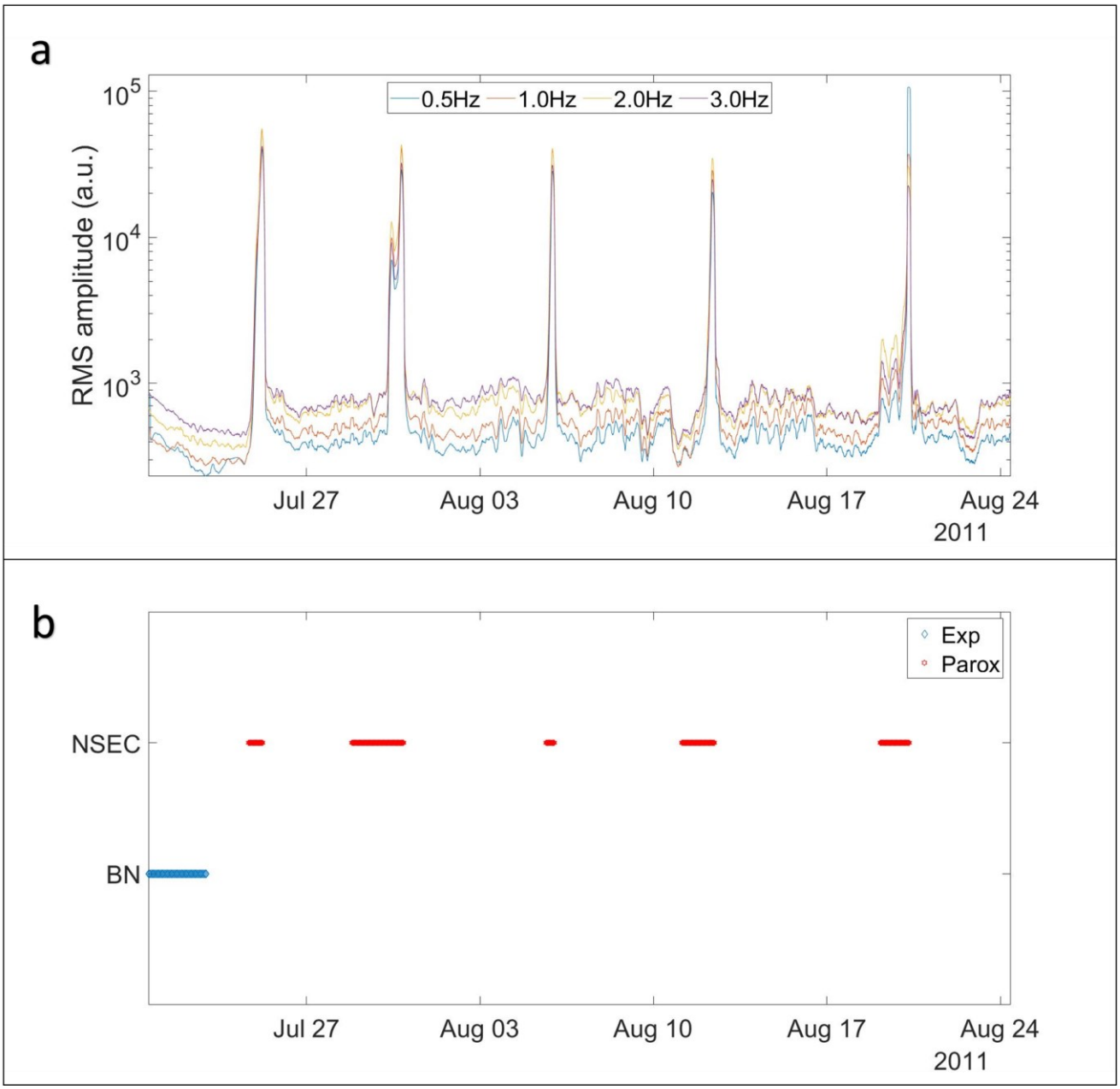

Figure 2.10. Amplitude properties of volcanic tremor during 2011. a) Moving average of the RMS amplitude of the tremor recorded at ATF2.BHZ sensor of array. The legend at the top refers to the central frequency of analysis bands, that are wide 1 Hz. The axes of plots are set in semi-logarithmic scale. b) Volcanic activity observed at NSEC and BN crater. The legend on the upper right-hand of the diagram shows the type of volcanic event: Exp= single explosions or series of minor explosions, minor and/or intense ash emissions; Parox= Strombolian, lava effusion and lava fountaining activity (data from Behncke et al., 2014).

As aforementioned, an additional tool that supports the signal processing is represented by the polarization analysis. We determined the polarization properties of the wavefield by using the eigen-decomposition of the covariance matrix of the three components of ground motion (see section 1.3.4, Chapter 1). Considering the configuration limits of the two arrays deployed in 2010-2011, the analysis was performed by using the traces recorded at the permanent seismic station "Cratere del Piano" (ECPN). The polarization attributes were evaluated over 10-second-long time windows along tremor signal, filtering the recordings in different frequency bands (0.5-2.0 Hz, with a step of 0.5 Hz). In addition, the analysis was supported by the inspection of particle motions computed over the same time windows and frequency intervals at ECPN, ETFI ("Torre del Filosofo") and EBCN ("Bocca Nuova") stations. The main results obtained for the 2010 and 2011 time intervals are shown in the figures 2.11, 2.12, 2.13 and 2.14, 2.15, 2.16, respectively. During the first period, the distribution of back azimuth, incidence angle and coefficient of rectilinearity revealed that the polarization properties were quasi-stationary in time and changeable in frequency. At ECPN station, for high values of rectilinearity (>=0.8), the back azimuths were mainly clustered in the N70°E-N100°E interval, pointing toward the direction corresponding to SEC, while incidence angles were representative of a quasi-horizontal particle motion (Fig. 2.17). Instead, considering lower values of rectilinearity, the wavefield resulted to be more complex to analyze, especially at increased frequency ranges of analysis (Fig. 2.13). In fact, the results were generally more stable in the 0.5-1.5 Hz frequency interval. Some exceptions were recognized during the intensification of the explosion activity at BN crater, when the back azimuth was also focused on the N100°E-N130°E interval (Fig. 2.17), pointing toward the directions from BN crater. Further insights into the polarization properties were gained from particle motion analysis. These were compatible with the polarization directions observed previously, especially for the higher values of rectilinearity. However, for those analysis windows in which the coefficient of rectilinearity was lower, it was possible to observe elliptical orbits of the particle motions (Fig. 2.19). During the 2011 experiment, the results were slightly different from what shown previously (Figs. 2.14, 2.15 and 2.16). Generally, during the quiescent periods of the volcanic activity, the polarization back azimuths were clustered in the N30°E-N60°E interval with shallow angles and high rectilinearity values, pointing toward the direction corresponding to BN crater. At the same time as the beginning of the Strombolian activity of the paroxysms, the back azimuths migrated focusing on the N45°E-N75°E interval, up to the N70°E-N100°E with the development of the lava fountaining (Fig. 2.18) and pointing toward NSEC. At the end of the episode, the polarization attributes returned to the values

observed before the paroxysm. During these paroxysmal phases, the rectilinearity values were higher and stable, while the incidence angles were slightly shallower than quiescent periods (Fig. 2.18). For the lower values of rectilinearity, the polarization properties were very similar compared to those of 2010, showing elliptical orbits of the particle motions in the whole period of interest (Fig. 2.20). However, here too, the results were more stable in the 0.5-1.5 Hz, exhibiting a major complexity of the tremor wavefield with increased frequencies of analysis.

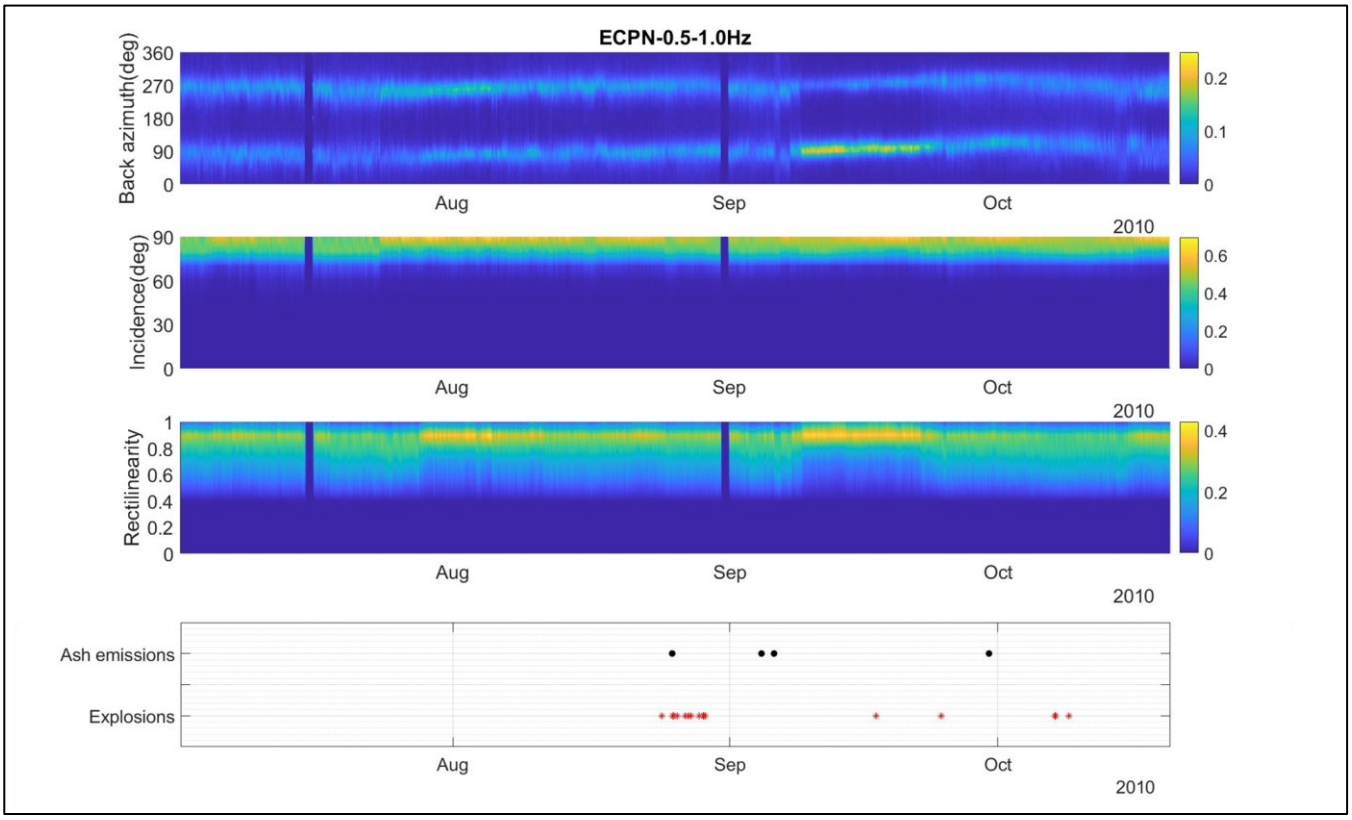

Figure 2.11. Temporal histogram of polarization attributes of three components of motion recorded by ECPN station during 2010 (upper, central and lower panels). For each diagram, the colorbar on the right-hand refers to normalized histogram probability. The analysis was performed in 0.5-1.0 Hz frequencies range. The lowest panel of each diagram refers to volcanic activity observed at BN crater (data from Andronico at al., 2013).

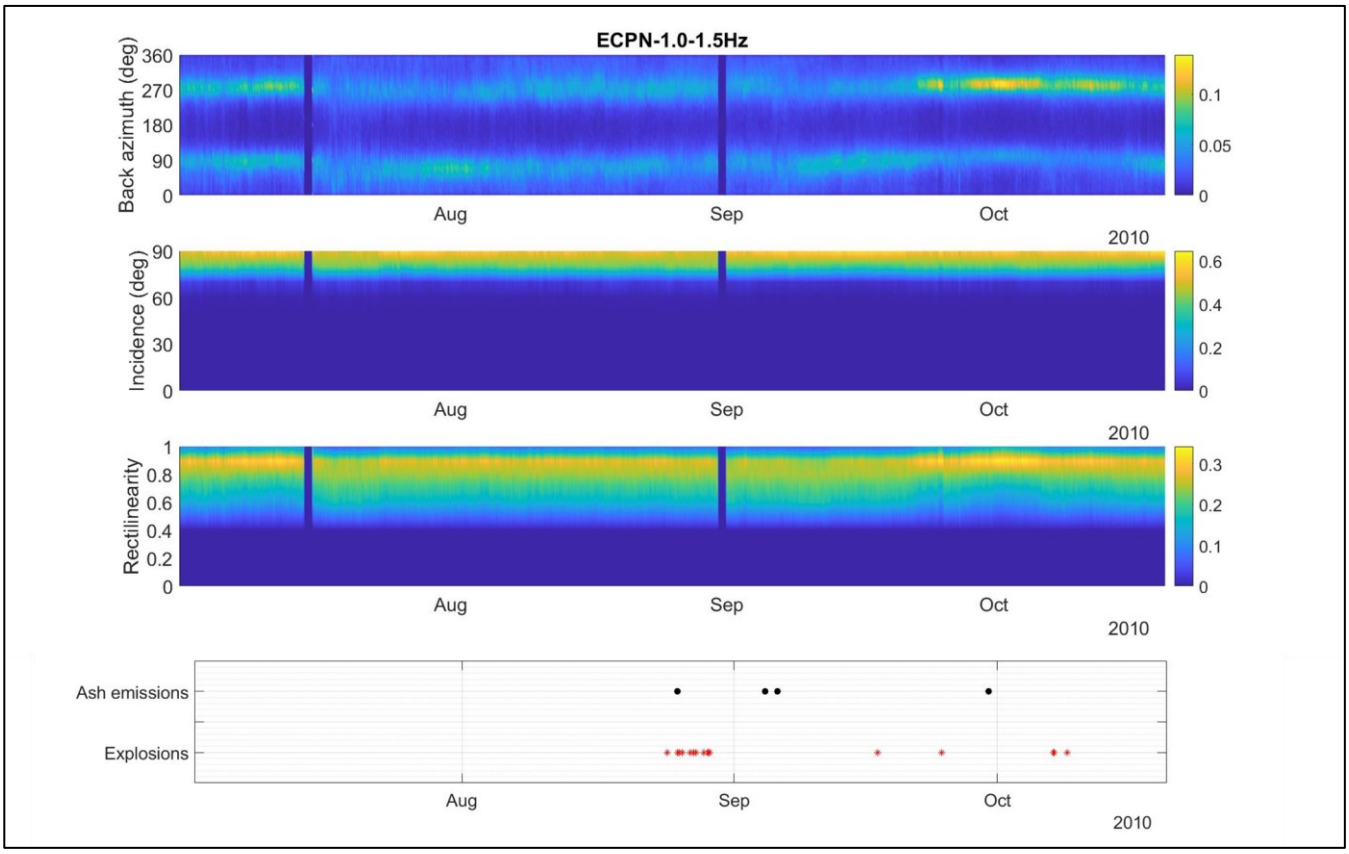

Figure 2.12. Temporal histogram of polarization attributes of three components of motion recorded by ECPN station during 2010 (upper, central and lower panels). For each diagram, the colorbar on the right-hand refers to normalized histogram probability. The analysis was performed in 1.0-1.5 Hz frequencies range. The lowest panel of each diagram refers to volcanic activity observed at BN crater (data from Andronico at al., 2013).

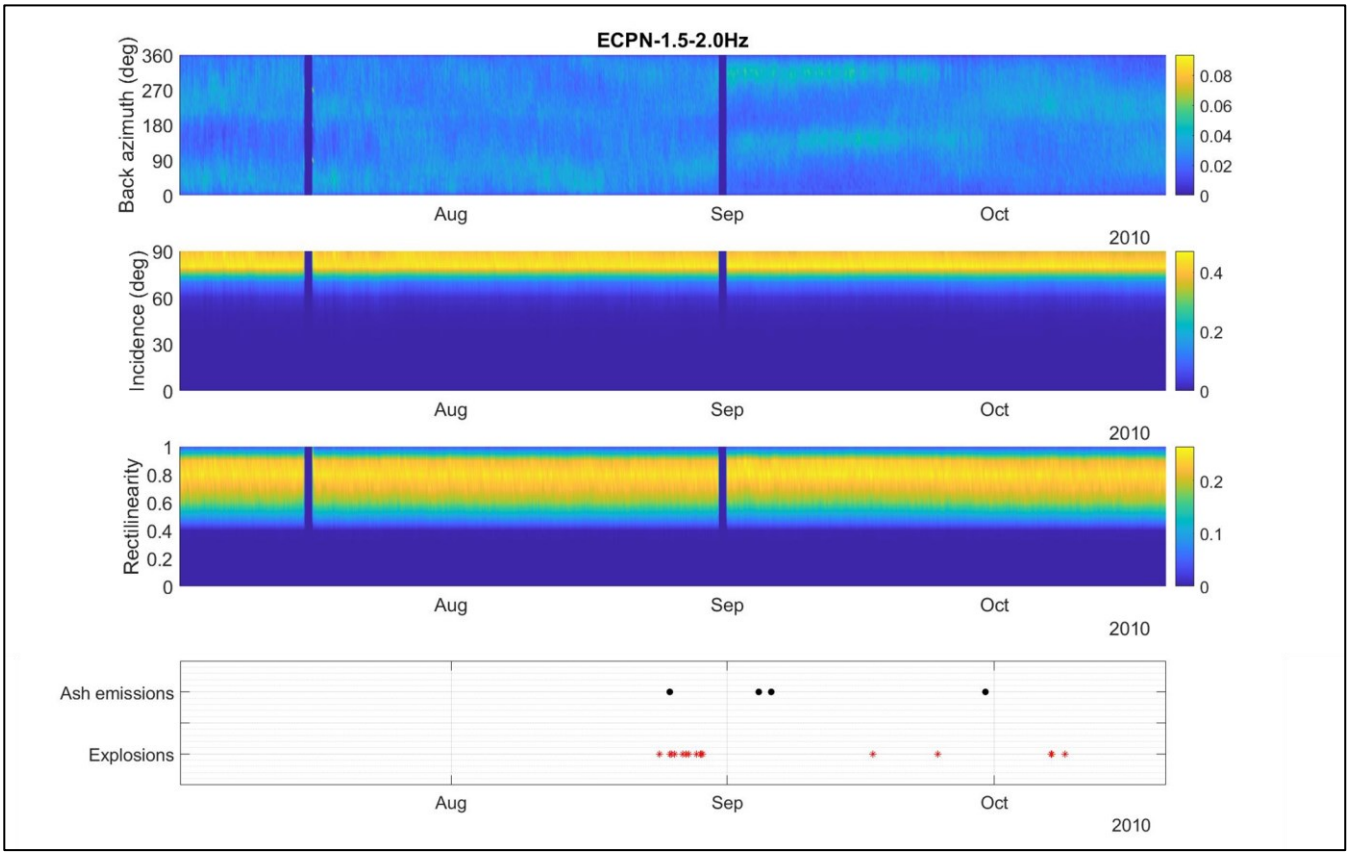

Figure 2.13. Temporal histogram of polarization attributes of three components of motion recorded by ECPN station during 2010 (upper, central and lower panels). For each diagram, the colorbar on the right-hand refers to normalized histogram probability. The analysis was performed in 1.5-2.0 Hz frequencies range. The lowest panel of each diagram refers to volcanic activity observed at BN crater (data from Andronico at al., 2013).

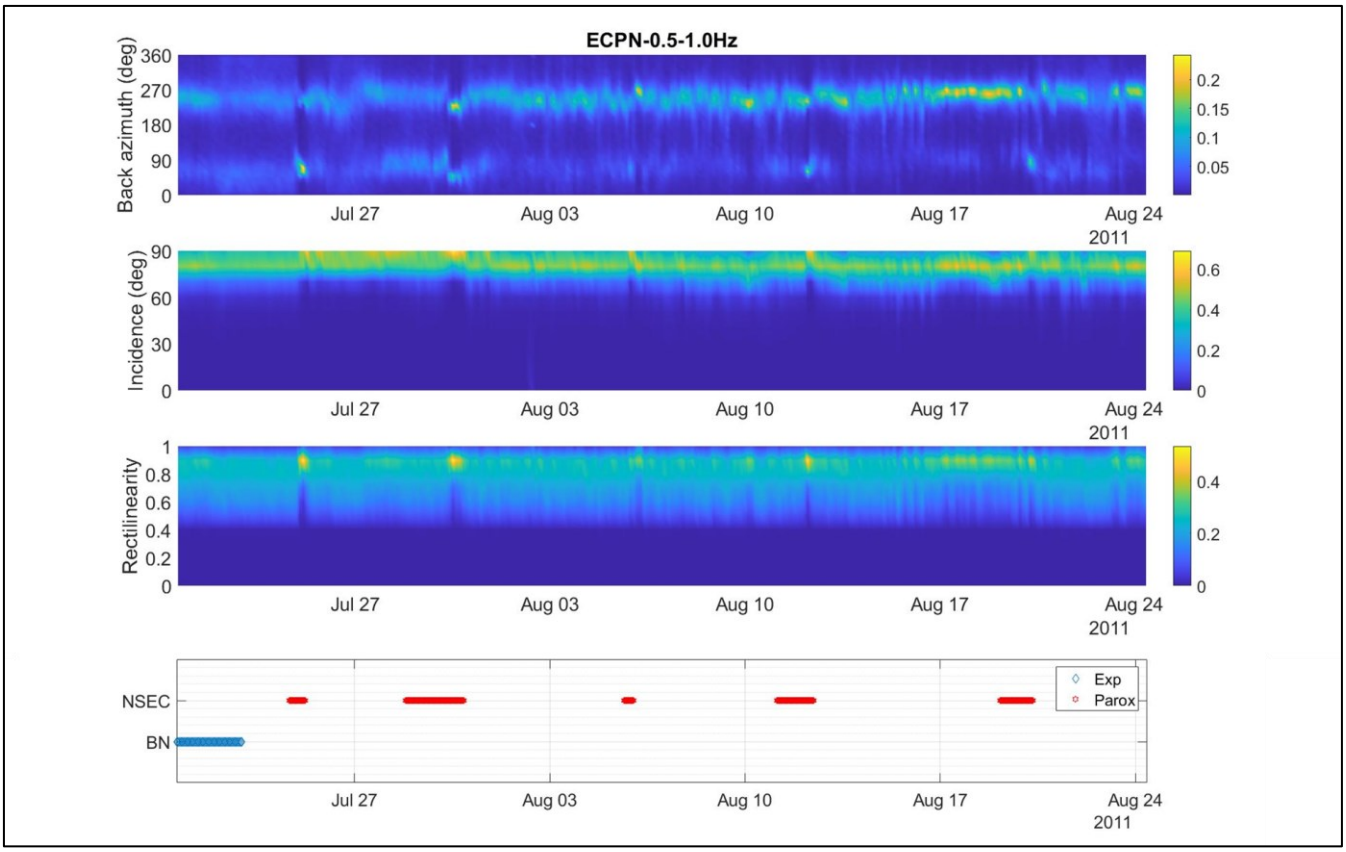

Figure 2.14. Temporal histogram of polarization attributes of three components of motion recorded by ECPN station during 2011 (upper, central and lower panels). For each diagram, the colorbar on the right-hand refers to normalized histogram probability. The analysis was performed in 0.5-1.0 Hz frequencies range. The lowest panel of each diagram refers to volcanic activity observed at NSEC and BN crater. The legend on the upper right-hand of these panels shows the type of volcanic event: Exp= single explosions or series of minor explosions, minor and/or intense ash emissions; Parox= Strombolian, lava effusion and lava fountaining activity (data from Behncke et al., 2014).

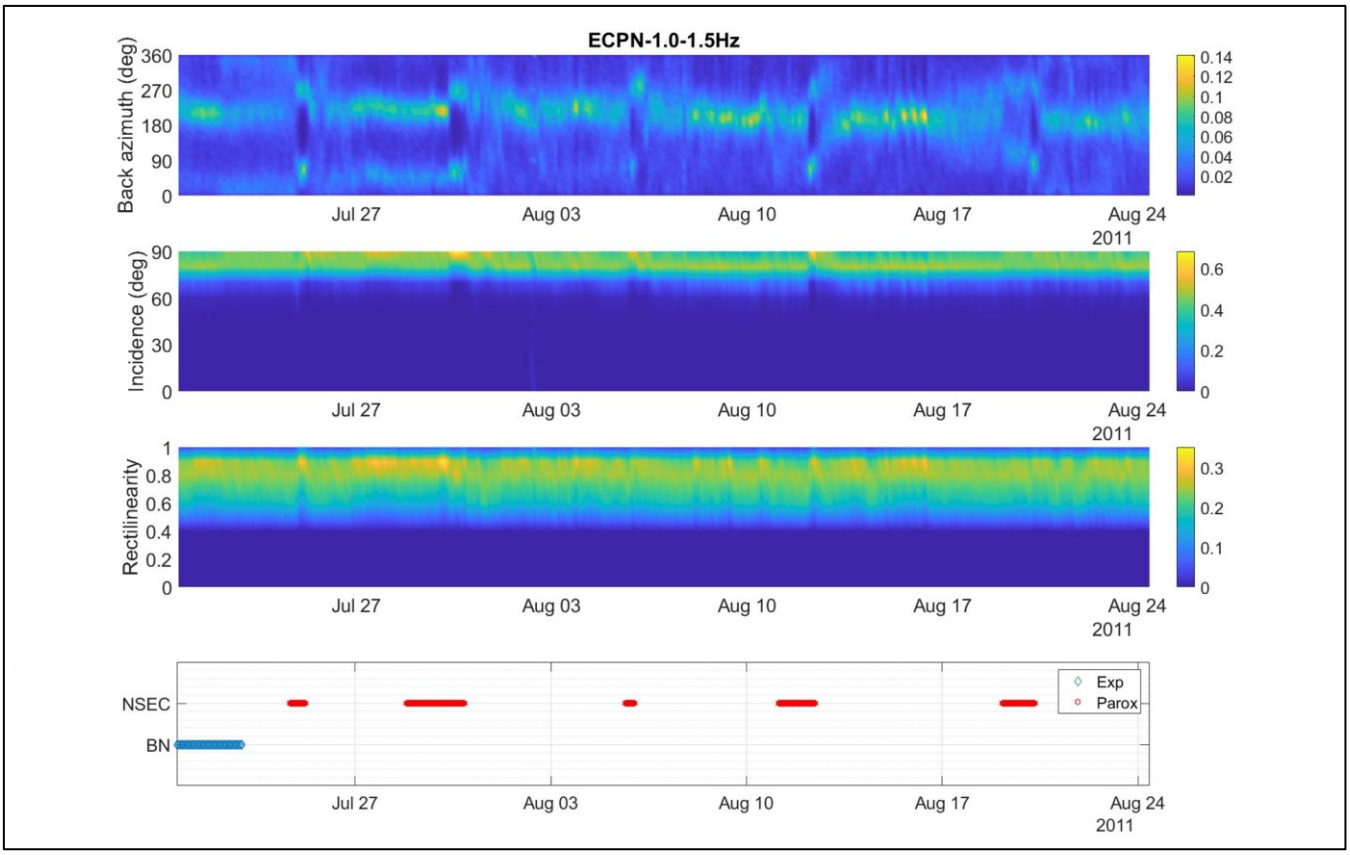

Figure 2.15. Temporal histogram of polarization attributes of three components of motion recorded by ECPN station during 2011 (upper, central and lower panels). For each diagram, the colorbar on the right-hand refers to normalized histogram probability. The analysis was performed in 1.0-1.5 Hz frequencies range. The lowest panel of each diagram refers to volcanic activity observed at NSEC and BN crater. The legend on the upper right-hand of these panels shows the type of volcanic event: Exp= single explosions or series of minor explosions, minor and/or intense ash emissions; Parox= Strombolian, lava effusion and lava fountaining activity (data from Behncke et al., 2014).

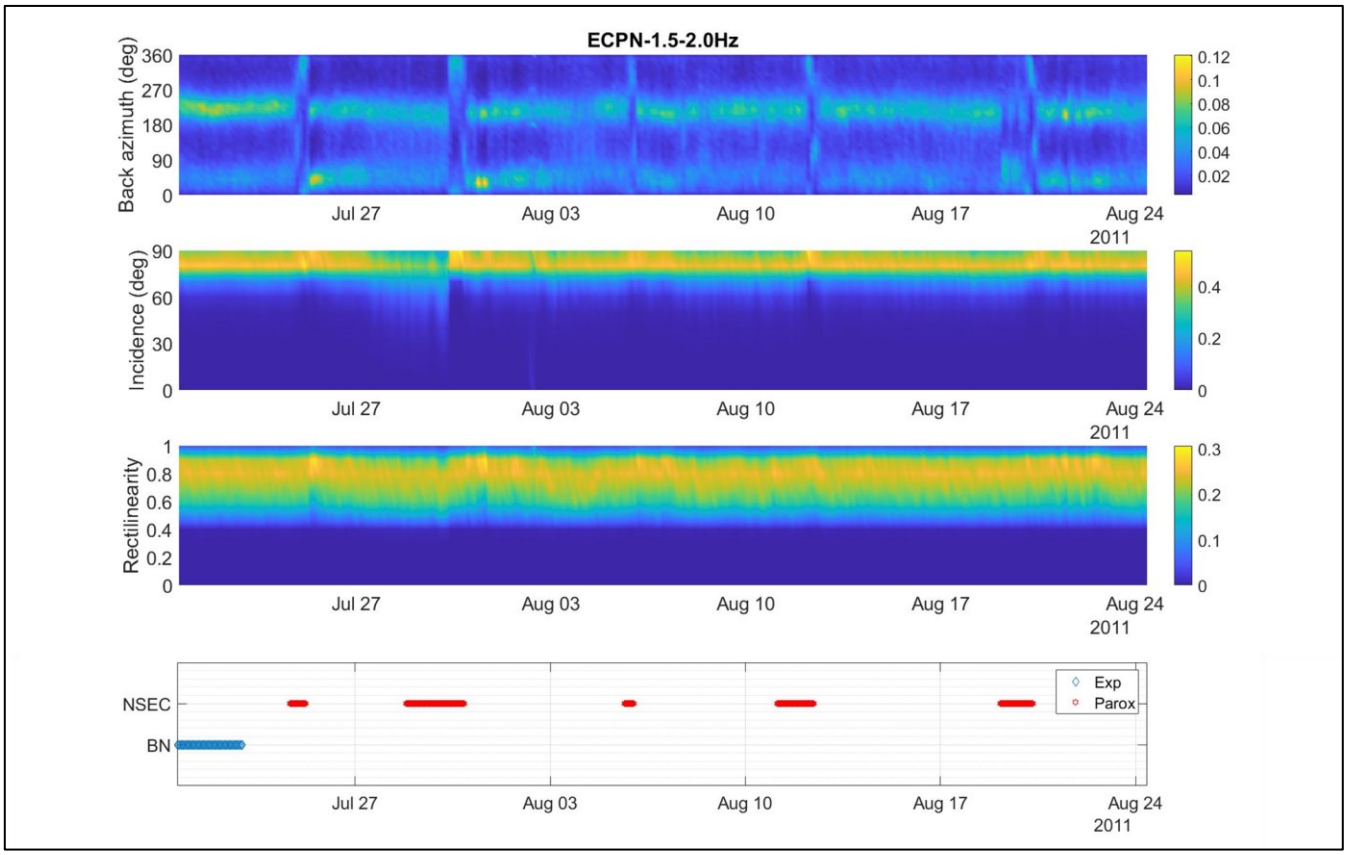

Figure 2.16. Temporal histogram of polarization attributes of three components of motion recorded by ECPN station during 2011 (upper, central and lower panels). For each diagram, the colorbar on the right-hand refers to normalized histogram probability. The analysis was performed in 1.5-2.0 Hz frequencies range. The lowest panel of each diagram refers to volcanic activity observed at NSEC and BN crater. The legend on the upper right-hand of these panels shows the type of volcanic event: Exp= single explosions or series of minor explosions, minor and/or intense ash emissions; Parox= Strombolian, lava effusion and lava fountaining activity (data from Behncke et al., 2014).

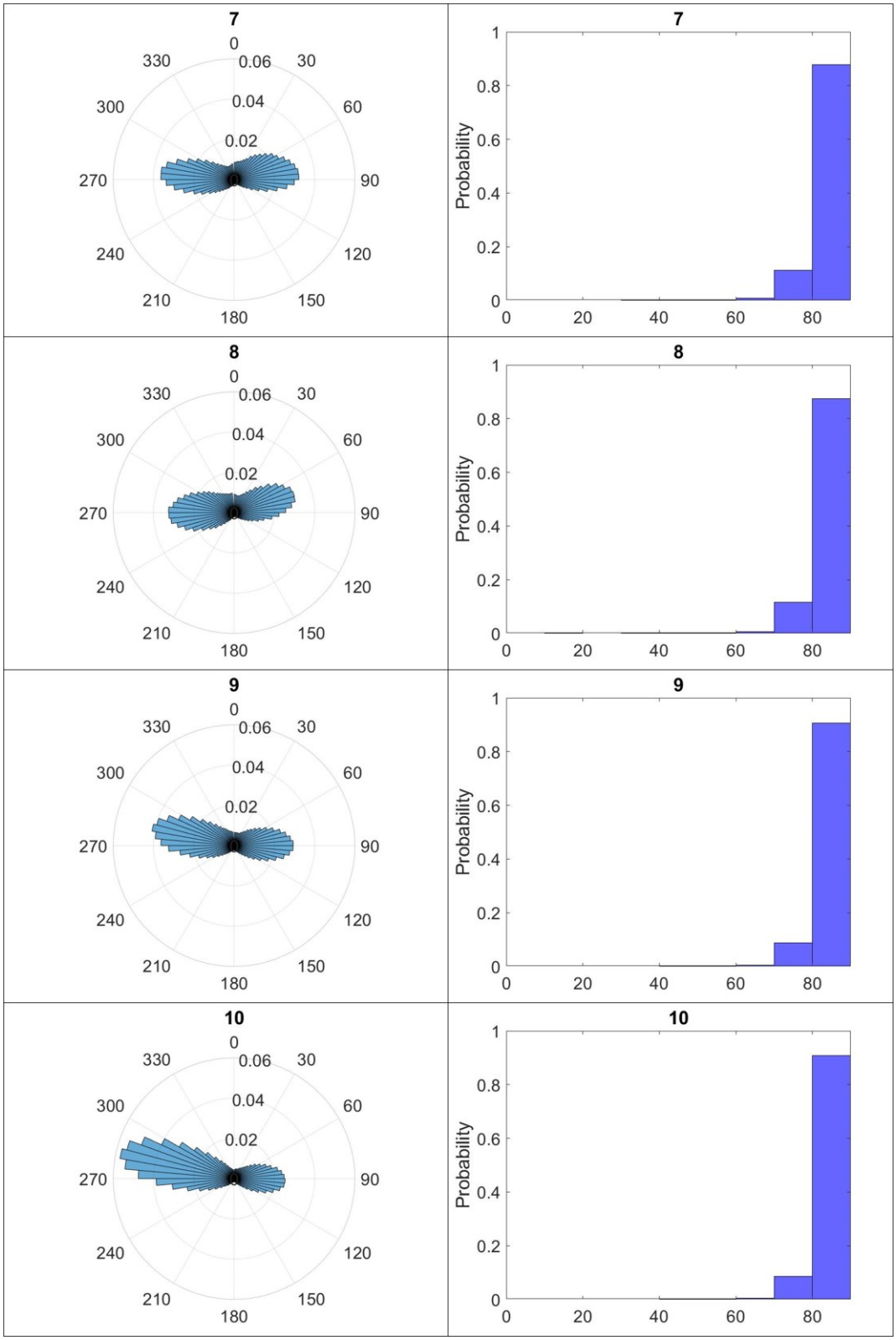

Figure 2.17. Histograms of back azimuth (on the right-hand) and incidence angles (on the left-hand) during 2010. The data were representative for the 0.5-2.0 Hz frequency range of analysis, selecting those attributes for which the coefficient of rectilinearity was larger than 0.8. For each diagram, the title refers to the month of investigated period: 7=July; 8=August; 9=September; 10=October.

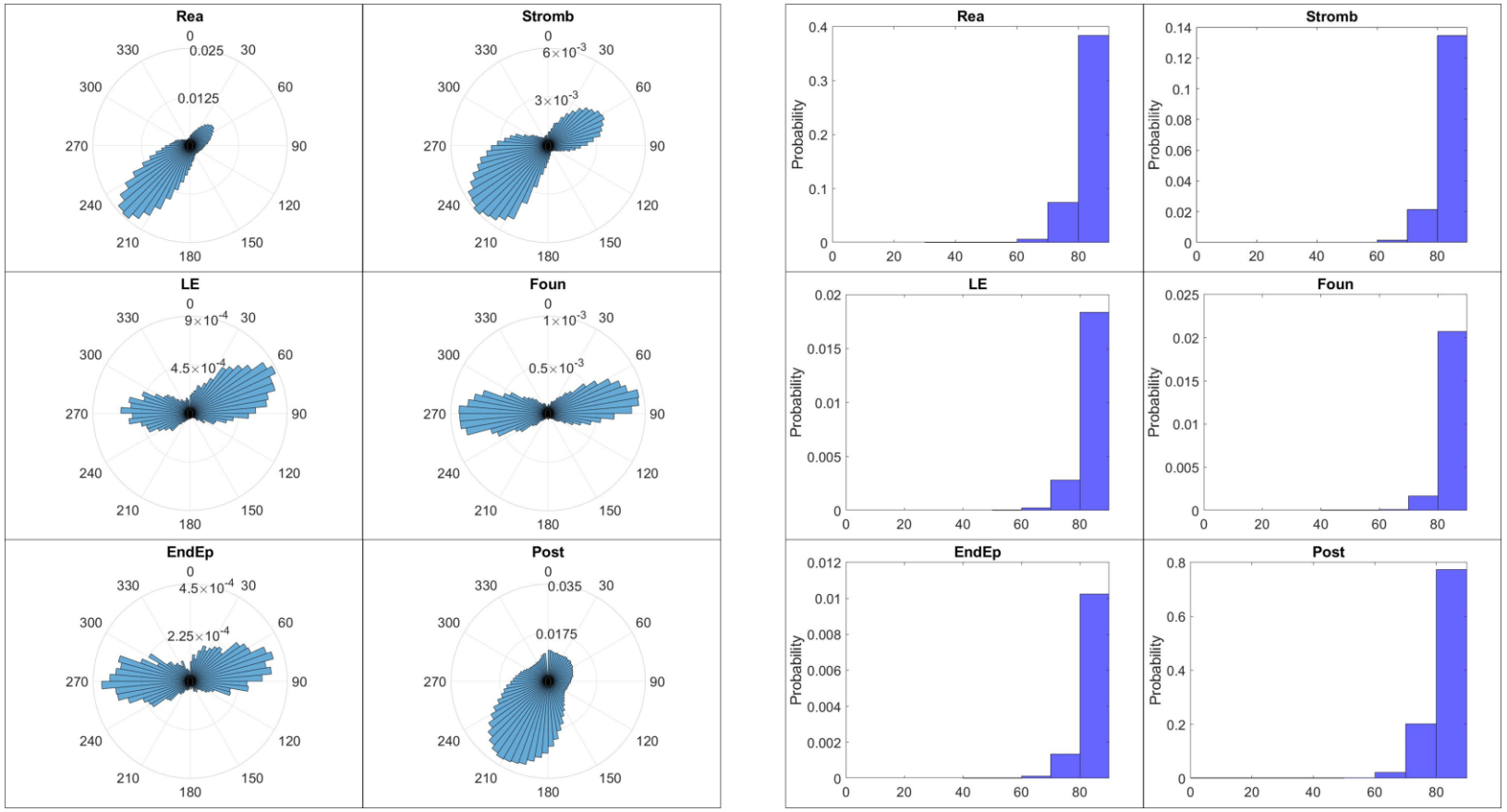

Figure 2.18. Histograms of back azimuth (on the left-hand) and incidence angles (on the right-hand) during the main phases of paroxysms of 2011. The data were representative for the 0.5-2.0 Hz frequency range of analysis, selecting those attributes for which the coefficient of rectilinearity was larger than 0.8. For each diagram, the title refers to the period comprised from the onset of a paroxysmal phase and the successive one (time interval from Behncke et al., 2014): Rea=Reactivation; Stromb=Strombolian activity; LE=Lava effusion; Foun=Lava fountaining; EndEp=End of episode; Post=Post quiescent period.

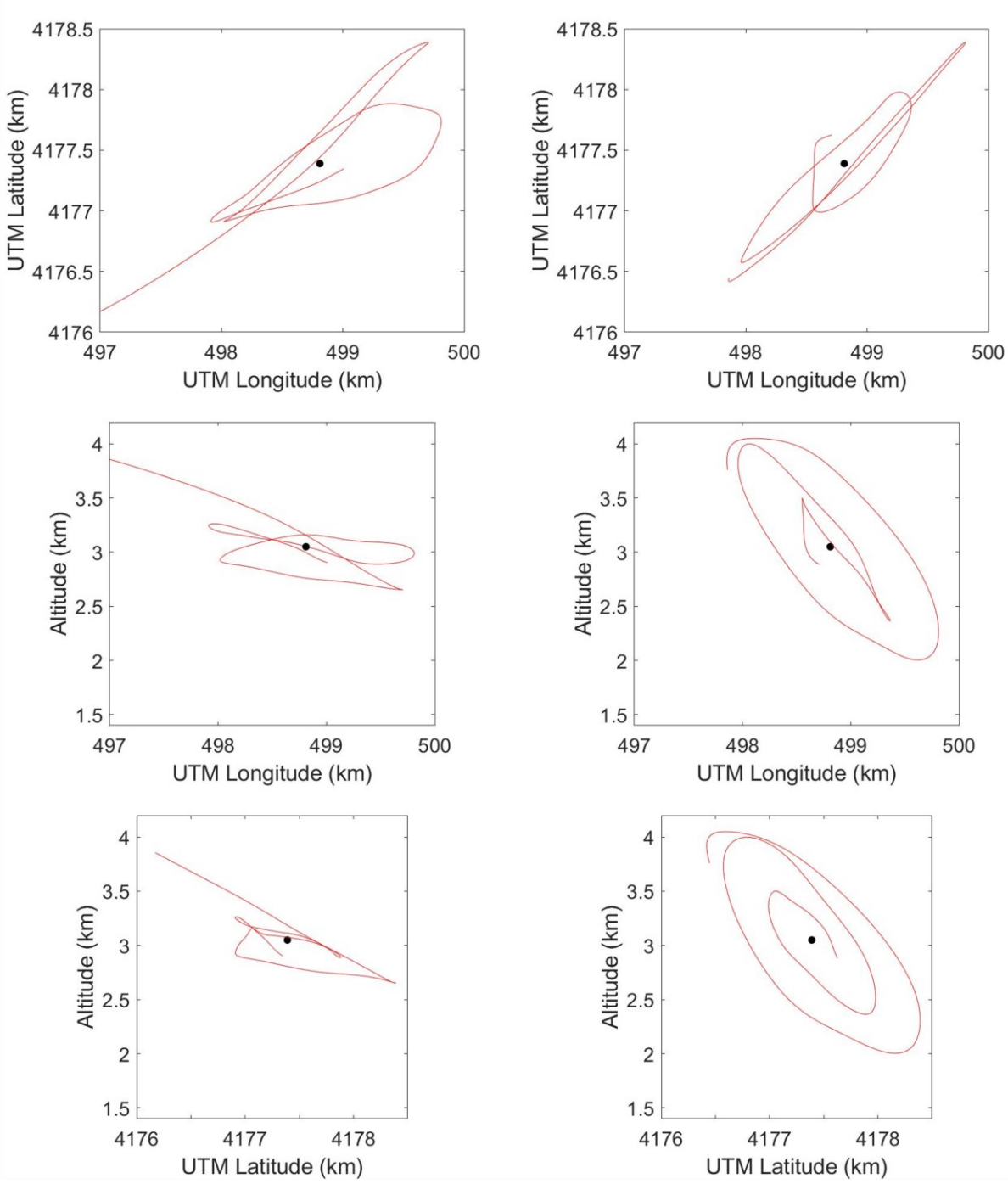

Figure 2.19. Example of particle motions in 2-s window on volcanic tremor signal recorded at ECPN station on 12 August 2010 12:00. The analysis was performed in 0.5-2.0 Hz frequency range.

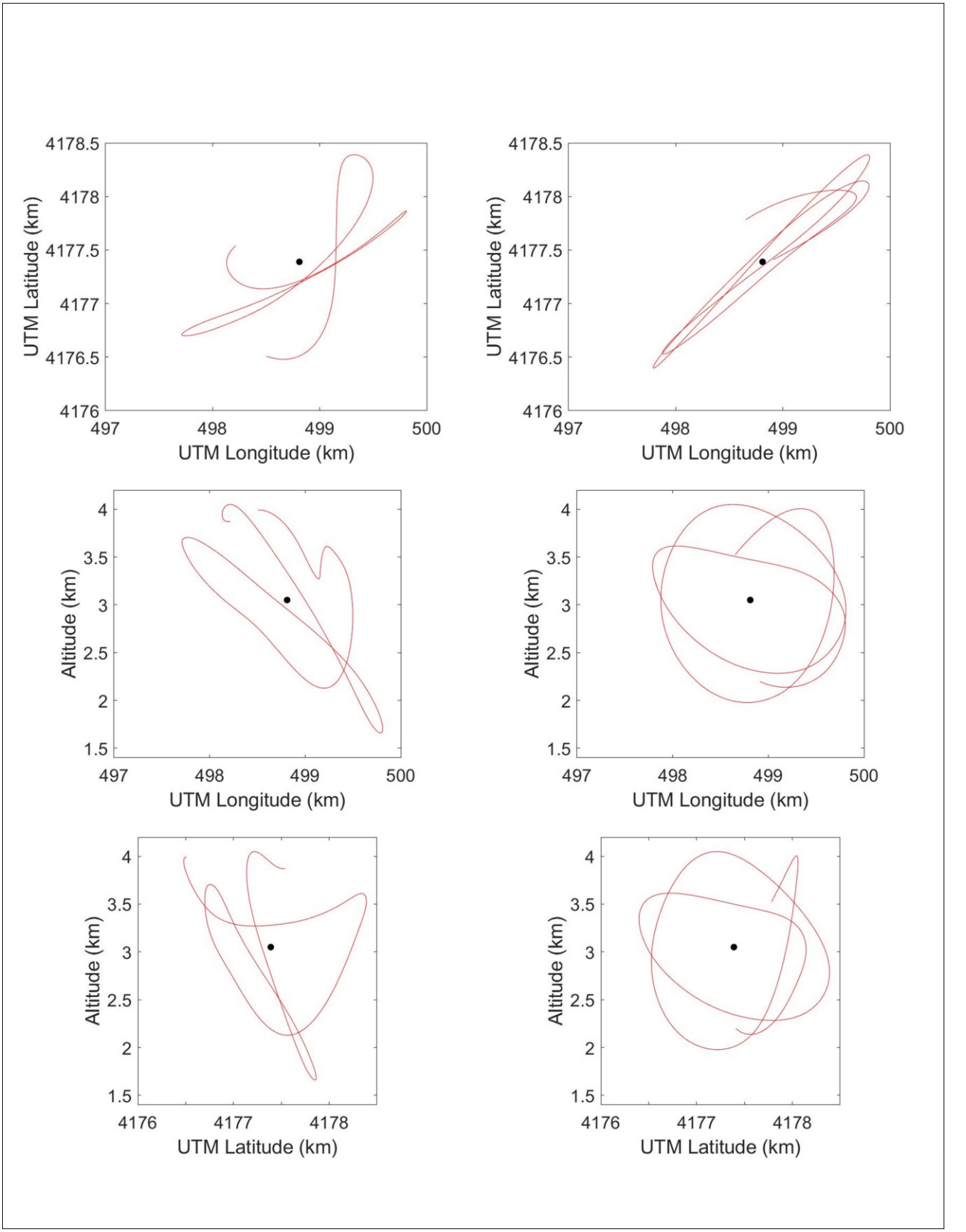

Figure 2.20. Example of particle motions in 2-s window on volcanic tremor signal recorded at ECPN station on 30 July 2011 20:00. The analysis was performed in 0.5-2.0 Hz frequency range.

2.3.3 LP AND VLP EVENTS

As in the case of the volcanic tremor, the analysis of LP and VLP activity provides very valuable information to model its source dynamics during volcanic phenomena and to improve the successive localization analysis. Due to its importance, the automatic detection of these events also represents a crucial element for the rapid and efficient processing of the data. In order to overcome the limited temporal coverage of the two arrays, we performed the successive analyses by using the seismic traces recorded by the INGV seismic permanent network (see section 2.2, Chapter 2), in the period between June and October 2010 and for the full year 2011. For the detection of the LP events during these periods, we used the SALPED algorithm (see section 1.3.5, Chapter 1). In particular, LP events were individuated by using the seismic traces recorded by the ECPN permanent station, chosen on the basis of the best signal-to-noise ratio. Following the procedure explained in the Chapter 1, we set the lower, central and upper subbands in the 0.1-0.4 Hz, 0.5-1.2 Hz and 3.0-10.0 Hz frequency ranges, respectively. The characteristic function was calculated by using spectral penalty factors equal to 2 and 4. The determination of the LP trigger times was completed by selecting all events with a characteristic function larger than one. The events were also catalogued in a digital archive of 20 s long waveform recordings, starting 10 s before the maximum peak-to-peak amplitude. For the detection of the VLP events we performed the STA/LTA method by using the same seismic traces recorded by ECPN permanent station. Following the procedure described in the section 1.3.5 (Chapter 1), we set the STA and LTA windows at 6 s and 60 s, respectively, filtering the traces in the 0.01-0.15 Hz frequency band with band-pass cosine filter. From some preliminary tests, we chose the value of 2.5 as detection threshold, extracting the VLP events through 100-seconds-long seismic recordings around their maximum peak-to-peak amplitudes. In this manner, we were able to detect more than 43,000 LPs and almost 10,000 VLPs between 2010 and 2011.

In order to gain further insights into low frequency activity, the waveform classification of the LP and LP events was manually performed through the visual inspection of the waveform events. In both periods, we recognized three main families and one unique family of LP and VLP events, respectively. The stacked signals associated with the different families are shown in figure 2.21. The LP waveform belonging to the first family showed in displacement records a positive onset (up), followed by a greater downward displacement (down). The second family of events was identical to the first one, except for the onset that, in this case, was characterized by double up and down shapes. These two

families also showed the same M-shaped coda. Instead, the LP waveform belonging to the third family was characterized by opposite pulses. In fact, in this case, the onset was composed by a negative displacement followed by an upward pulse, so that the family could be considered as the specular image of the first one. The VLP waveform showed in displacement records a positive onset (up), followed by a greater downward displacement (down).

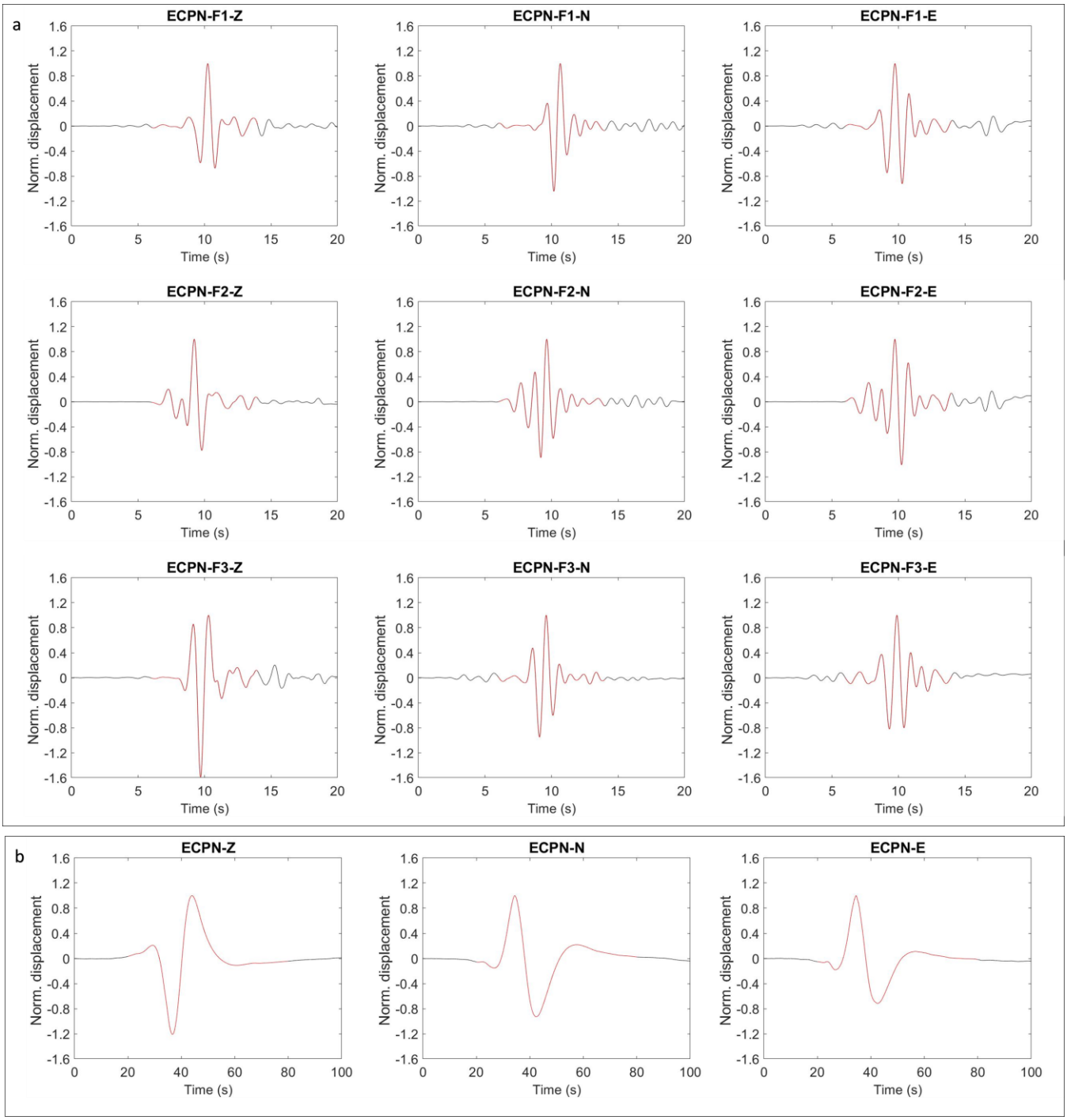

Figure 2.21. LP and VLP waveforms obtained from visual classification. These characteristic waveforms are derived by delaying and summing the events belonging to each family. The events are displayed in displacement. a) LP family waveforms filtered in the 0.5-1.2 frequency band. The red line underlines the LP event in the 20-seconds-long time window used for the extraction. For each diagram, the title indicates the seismic station used for the detection (ECPN), the type of family of events (F1, F2 or F3) and the component of ground motion (Z=vertical, N=North or E=East). b) VLP family waveform filtered in the 0.01-0.0.15 Hz frequency range. The red line shows the VLP event in a 100-seconds-long time window. For each diagram, the title indicates the seismic station used for the detection (ECPN) and the component of ground motion (Z=vertical, N=North or E=East).

Considering the previous selected families, we refined the LP and VLP catalogues by analysing the particle motions of the events through the covariance matrix method (see section 1.3.4, Chapter 1). In this case, we filtered the LP and VLP waveforms in the 0.5-1.2 Hz and 0.01-0.15 Hz frequency ranges, respectively. Considering the times series obtained by the polarization analysis, a further event discrimination was performed by selecting those LPs or VLPs for which the coefficient of rectilinearity is larger than 0.8. Successively, we determined the main wavefield properties of the LP events (amplitude estimates, polarization attributes) by using the same techniques applied during the processing of volcanic tremor data (see the previous section). For the 2010 experiment, the results are shown in the figures 2.22 and 2.23. Generally, for both type of events, the polarization back azimuths were clustered in N10°E-N40°E range, pointing toward direction corresponding to BN crater with shallow incidence angles (Fig. 2.22) and low RMS amplitudes (Fig. 2.23). However, in the case of the LPs, it was possible to observe some significant changes of wavefield properties with the intensification of the explosive activity at BN crater. In fact, between August and October 2010, the signal amplitudes gradually increased up to medium-low levels and the incidence angles became shallower than those values exhibited during the previous month, especially with the development of volcanic activity at Mt. Etna. The features of VLP events were generally quasi-stationary in time and were uncorrelated with variations in the volcanic activity. The only exception was represented by RMS values that gradually increased with the occurrence of the explosion activity. In addition, the VLPs were characterized by lower incidence angles and energy values than LP ones. Taking into account the frequency of occurrence of the LP and VLP events (Fig. 2.23), we observed some interesting relationships with the volcanic activity. While the VLPs were randomly distributed in time, the number of LP events gradually decreased between June and August, reaching the minimum values at the starting of the volcanic activity at BN crater, due to the increase of the background noise. With the intensification of explosion events, the frequency of occurrence of LPs grew again up to assume similar values to those observed in the previous period.

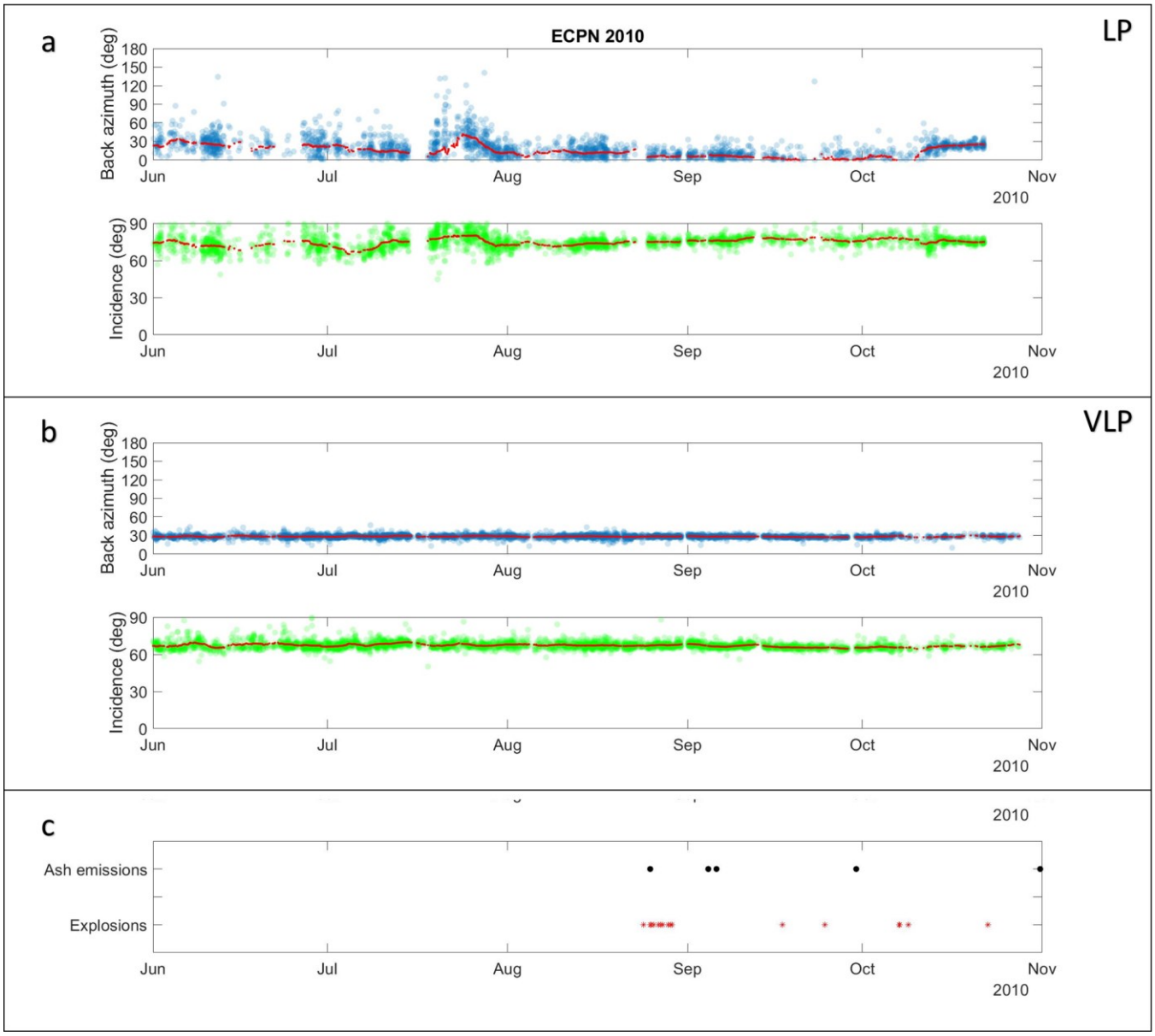

Figure 2.22. Polarization attributes of LP and VLP activity obtained by analysing the events recorded at ECPN station during 2010. All results are filtered selecting those values for which the coefficient of rectilinearity is larger than 0.8. The diagrams (a) and (b) represent the temporal evolution of the polarization back azimuths (upper panel) and incidence angles (lower panel) obtained by analysing LP and VLP events, respectively. The red lines indicate 3-days moving averages. The diagram (c) shows volcanic activity observed at BN crater (data from Andronico at al., 2013).

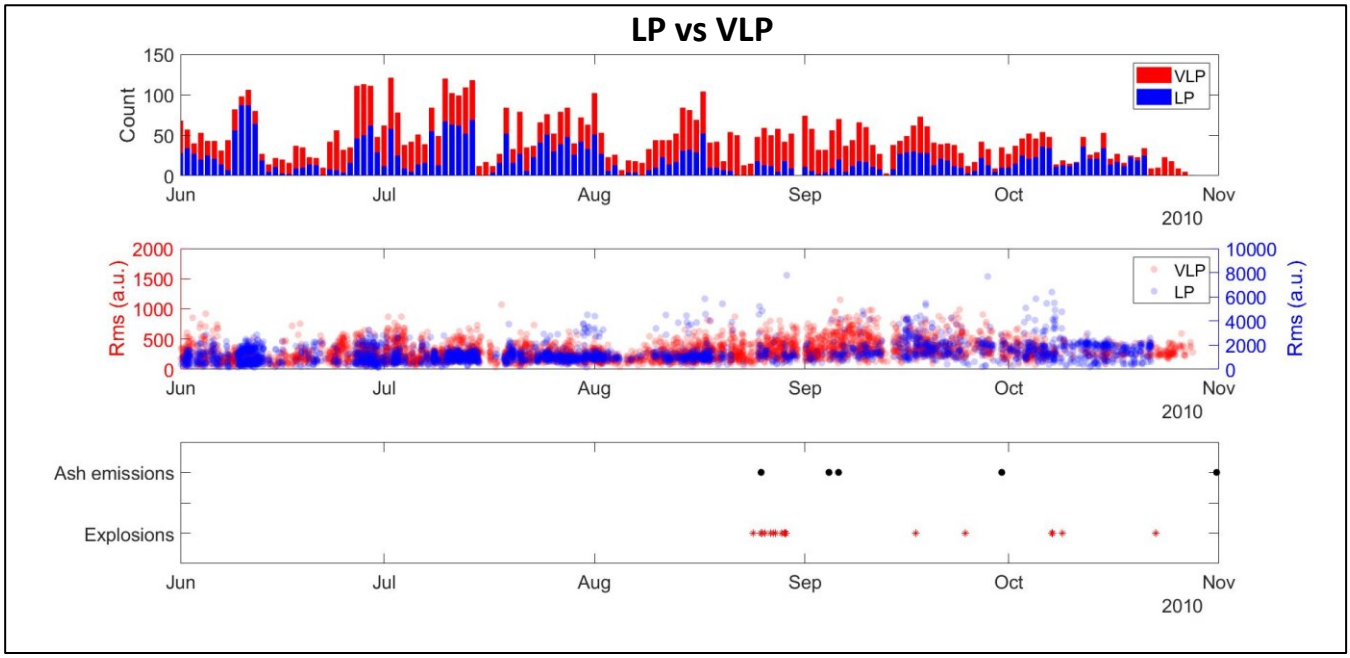

Figure 2.23. Comparison between LP (blue) and VLP (red) events in terms of daily frequency of occurrence (upper panel), expressed as stacked histograms, and RMS values (central panel) during 2010. These properties are related to volcanic activity observed at BN crater (lower panel; data from Andronico at al., 2013).

Further insight into them can be obtained from the time distributions of the LP families (Figs. 2.24 and 2.25). In particular, the first family occurred along the whole period, with the highest occurrence during the first two months of recordings. One exception was from the last days of July to the beginning of September, when the events were detected with lower frequency of occurrence. The second family gradually increased at the beginning of June and reached the maximum frequency of occurrence between mid-July and the last weeks of September, disappearing in the month of October. However, these two groups of events were characterized by similar properties that follow the temporal trends described in the previous paragraph (Figs. 2.22 and 2.23). Instead, the third family was detected with lower occurrence frequency than the previous ones, especially during the first three months of recording. From the end of August, this family gradually reappeared, reaching higher frequency during the month of October. In this case, we observed lower incidence angles and higher amplitude values than the other families. However, in occurrence of the explosive activity at BN crater, this family was dominated by the shallowest incidence angles. In general, the wavefield properties of the LP and VLP can be summarized in the figures 2.25 and 2.26, respectively.

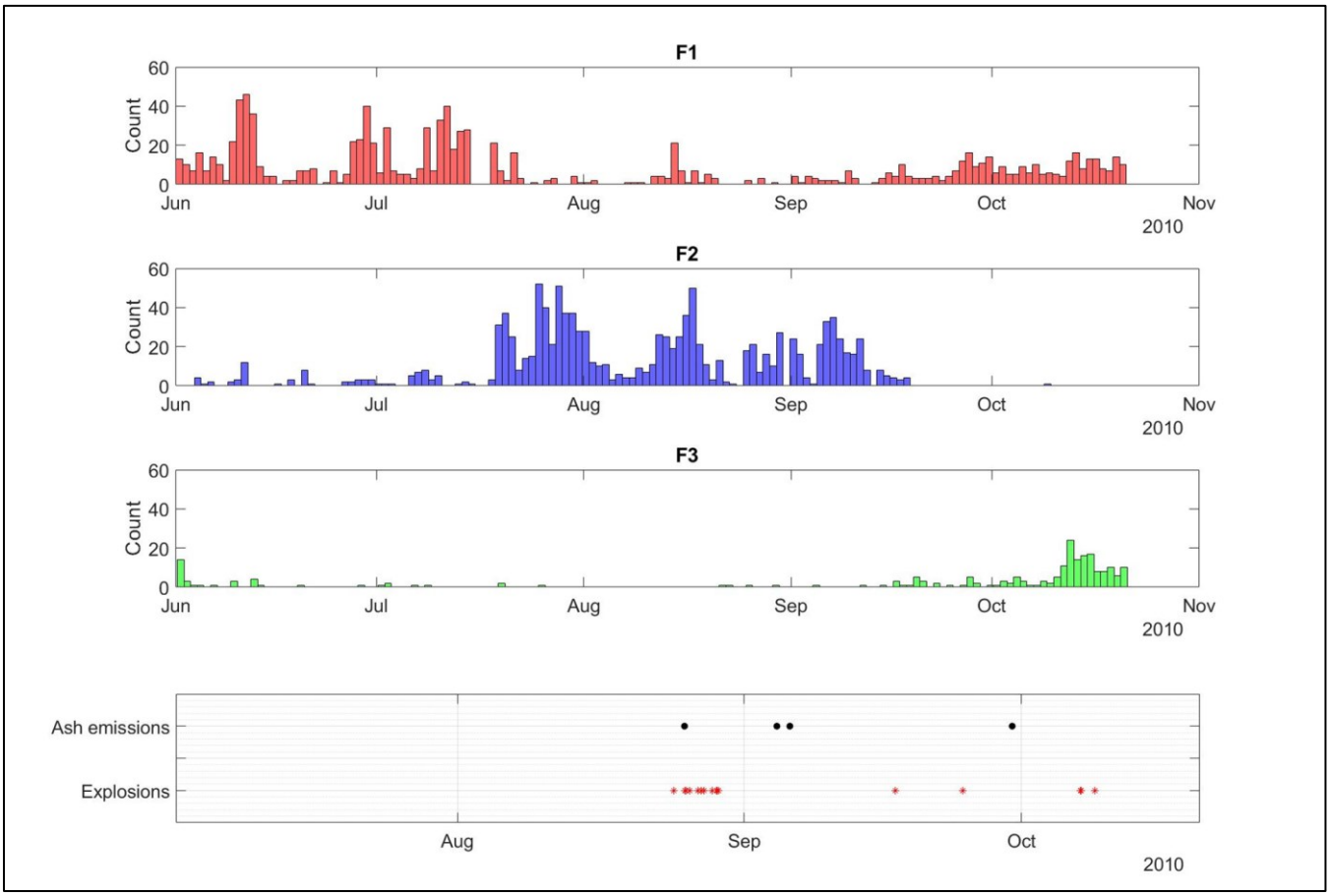

Figure 2.24. Temporal distribution of LP Families F1 (red), F2 (blue) and F3 (green) relating to the volcanic activity at BN in 2010 (data from Andronico at al., 2013). The event counts are calculated on daily scale.

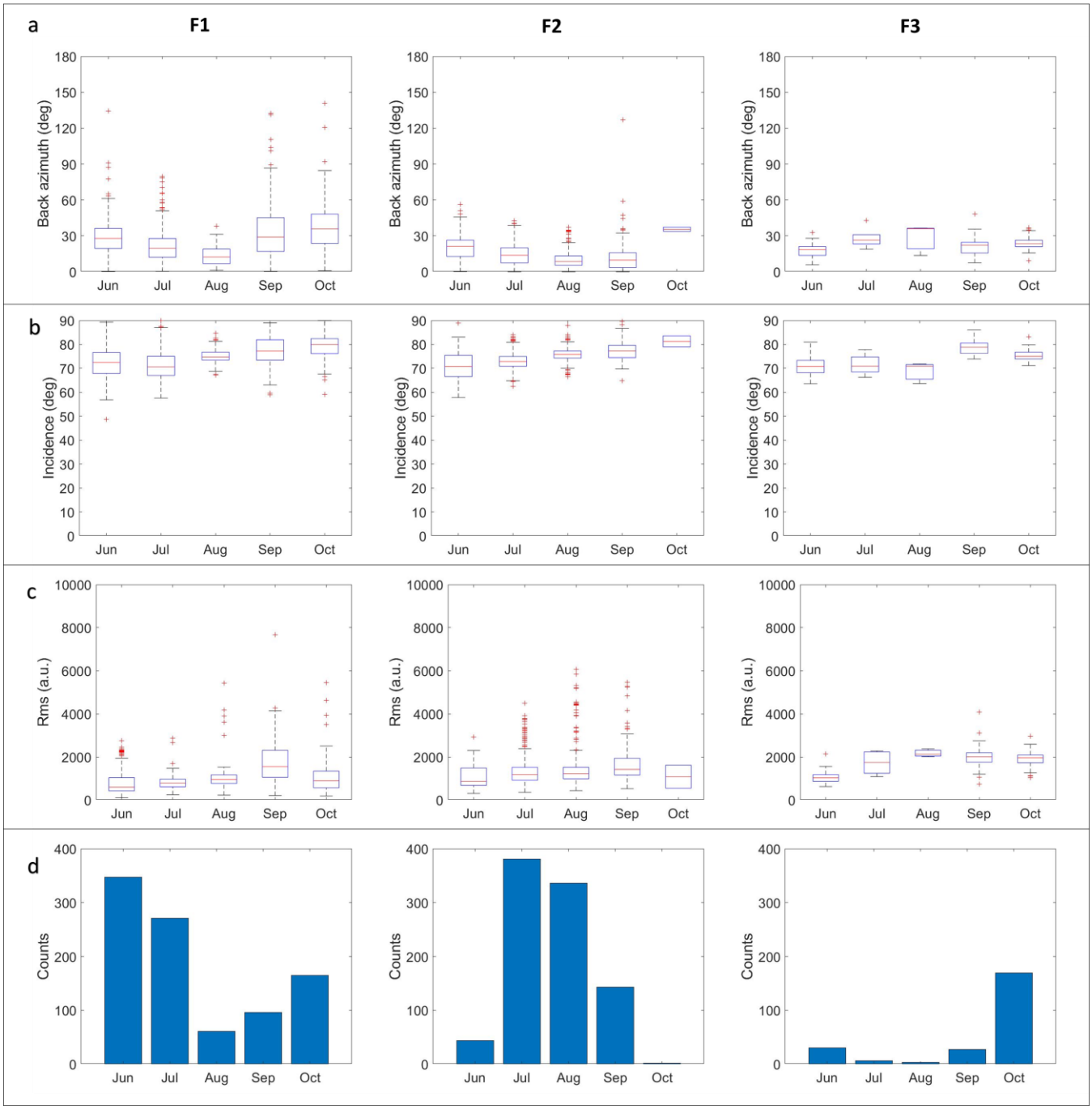

Figure 2.25. Statistical overview of the wavefield properties about LP Families recorded during 2010. a) Boxplot of polarization back azimuths. b) Boxplot of incidence angles. c) Boxplot of RMS amplitudes. d) Bars diagram of the number of LPs. For each diagram, the horizontal axis refers to the first 3 letters of the name of month.

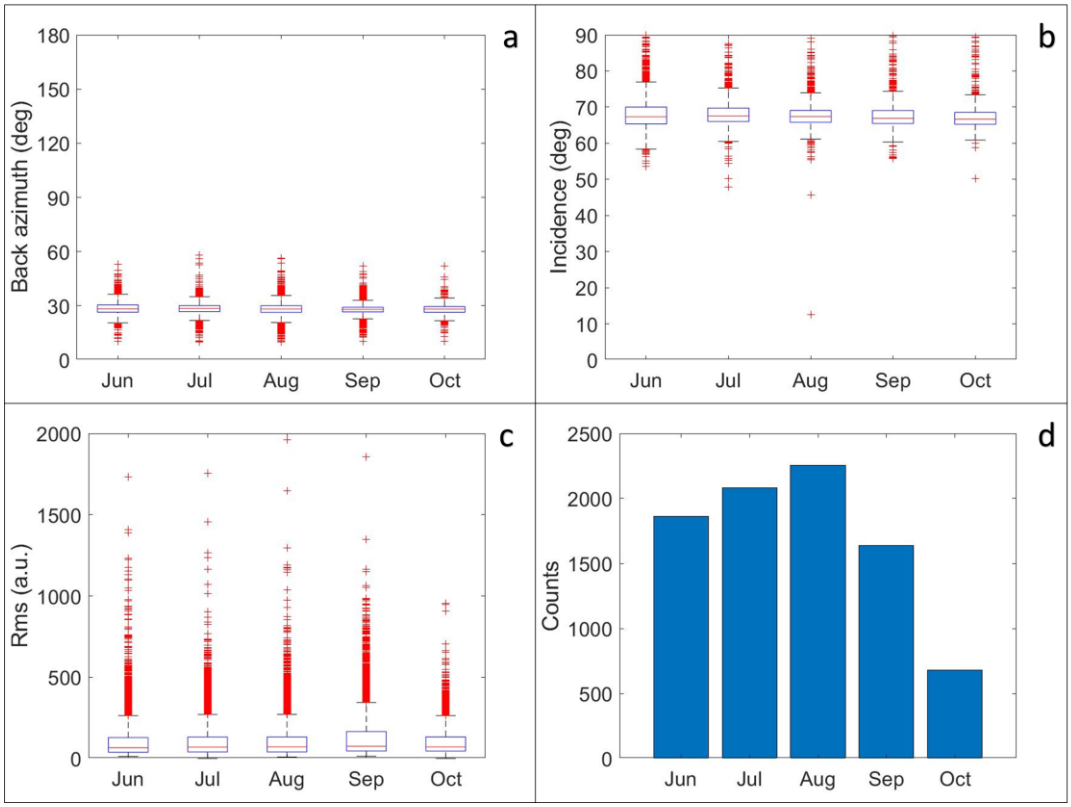

Figure 2.26. Statistical overview of the wavefield properties about VLPs recorded during 2010. a) Boxplot of polarization back azimuths. b) Boxplot of incidence angles. c) Boxplot of RMS amplitudes. d) Bars diagram of the number of VLPs. For each diagram, the horizontal axis refers to the first 3 letters of the name of month.

During the 2011 (Figs. 2.27 and 2.28), we observed significant variations of some LP wavefield properties, especially during paroxysmal activity. Instead, almost all VLP properties were stationary in time, except for the frequency of occurrence. During the quiescent periods of the Etna volcano or during the explosive activity at BN crater, the polarization back azimuths were focused on the N10°E-N60°E and on N10°E-N40°E intervals for the LP and VLP activity, respectively, pointing toward from BN crater. The LP events were characterized by quasi-horizontal particle motions and low levels of RMS amplitude, while the VLPs showed deeper incidence angles and smaller amplitudes than LP events. In both cases, the frequency of occurrence was very high, reaching its maximum between a paroxysm and another one. However, in some cases, LP or VLP activity resulted almost absent during some quiescent periods of the volcano. With the development of paroxysms, the LP/VLP wavefield was more complex to observe, showing also unstable results due to the increase of the intensity of tremor linked to eruption. In fact, the occurrence frequency of the events decreased as quickly as the intensification of explosive

activity, so that few or no events were detected during lava fountaining due to the decrease of the signal-to-noise ratio. In particular, for the LP events, RMS amplitudes gradually increased in occurrence of paroxysms, reaching sometimes the same levels of the volcanic tremor; the VLP amplitude values rather were no affected by the changes in the volcanic activity. In both types of events, the polarization incidence angles became deeper with the development of lava fountaining, although some polarization values were difficult to interpret because of the reduced number of detected events. While the back azimuths were almost stationary for VLPs, the LP events showed back azimuths focused on N60°E-N110°E interval during the intensification of explosive activity at NSEC, pointing toward NSEC. In general, brief resumes of the analysis results for LP and VLP events can be observed in the figures 2.29 and 2.30, respectively.

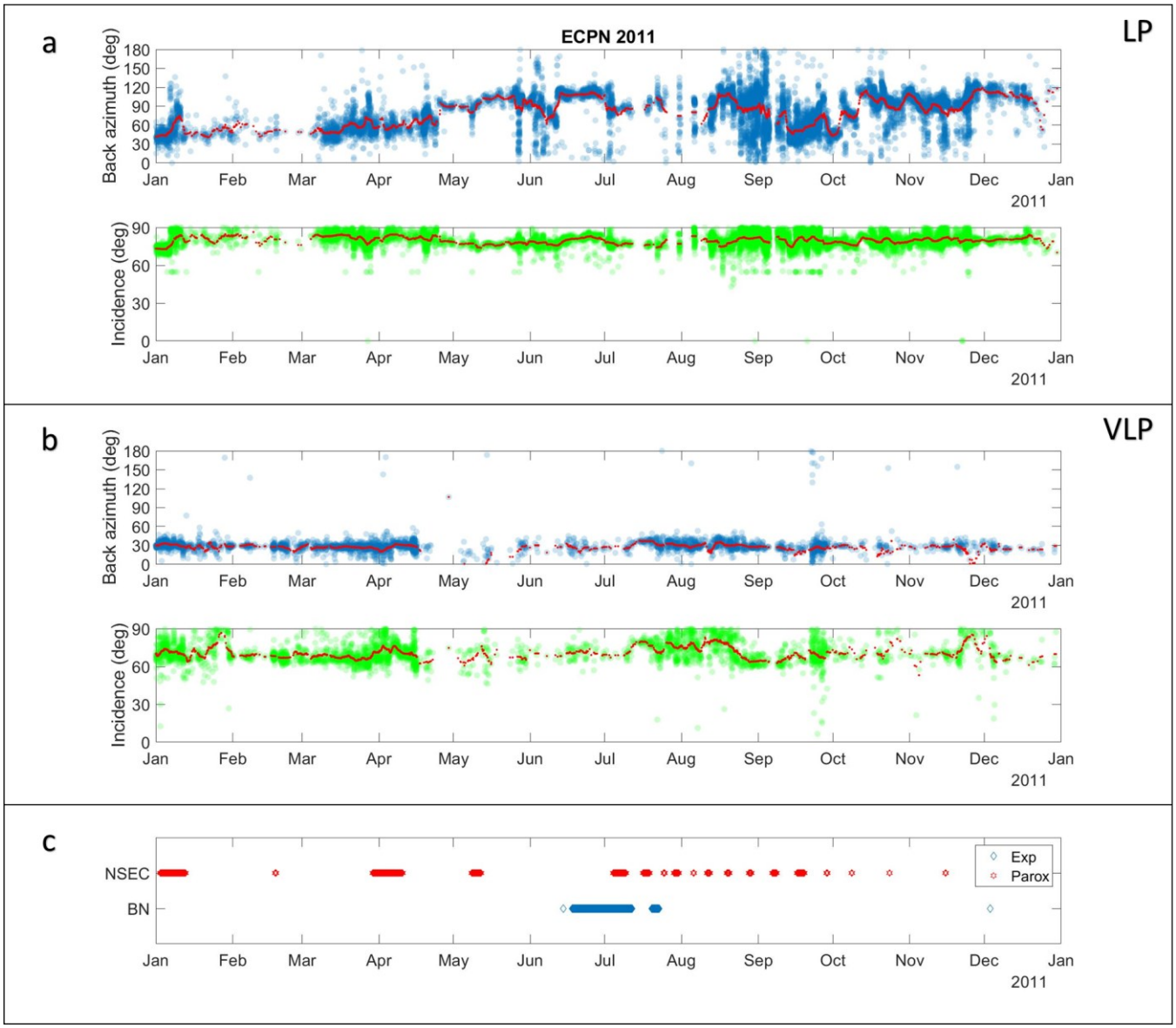

Figure 2.27. Polarization attributes of LP and VLP activity obtained by analysing the events recorded at ECPN station during 2011. All results are filtered selecting those values for which the coefficient of rectilinearity is larger than 0.8. The diagrams (a) and (b) represent the temporal evolution of the polarization back azimuths (upper panel) and incidence angles (lower panel) obtained by analysing LP and VLP events, respectively. The red lines indicate 3-days moving averages. The diagram (c) shows volcanic activity observed at NSEC and BN crater (data from Behncke et al., 2014). The legend on the upper right-hand of this panel shows the type of volcanic event: Exp= single explosions or series of minor explosions, minor and/or intense ash emissions; Parox= Strombolian, lava effusion and lava fountaining activity.

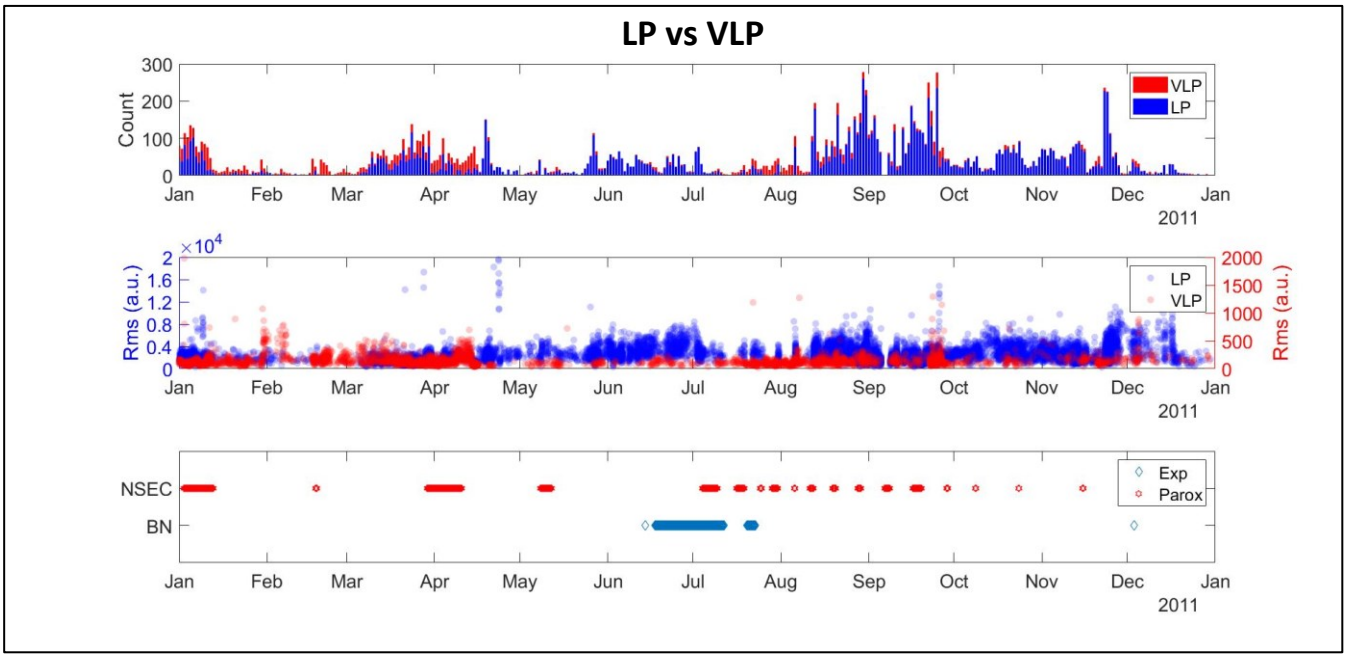

Figure 2.28. Comparison between LP (blue) and VLP (red) events in terms of daily frequency of occurrence (upper panel), expressed as stacked histograms, and RMS values (central panel) during 2011. These properties are related to volcanic activity observed at NSEC and BN crater (lower panel; data from Behncke et al., 2014). The legend on the upper right-hand of this panel shows the type of volcanic event: Exp= single explosions or series of minor explosions, minor and/or intense ash emissions; Parox= Strombolian, lava effusion and lava fountaining activity.

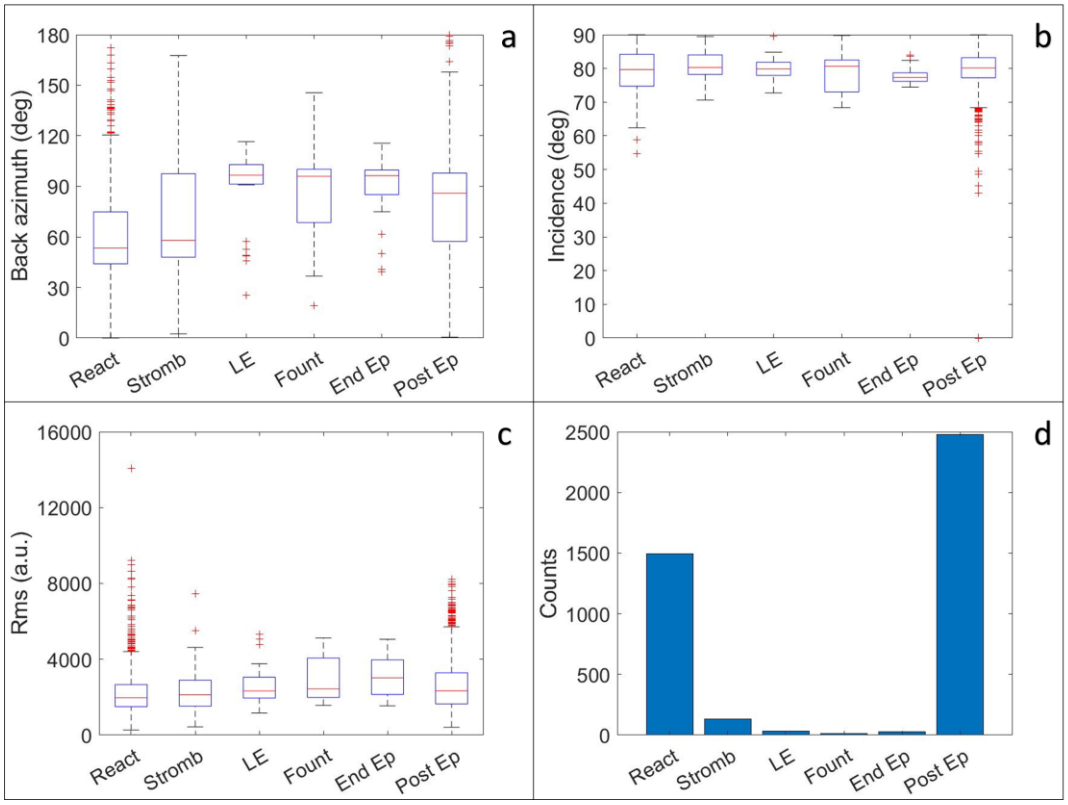

Figure 2.29. Statistical overview of the wavefield properties about all families of LP recorded during the different phases of paroxysmal activity in 2011. a) Boxplot of polarization back azimuths. b) Boxplot of incidence angles. c) Boxplot of RMS amplitudes. d) Bars diagram of the number of LPs. For each diagram, the horizontal axis refers to the period comprised from the onset of a paroxysmal phase and the successive one (time interval from Behncke et al., 2014): Rea=Reactivation; Stromb=Strombolian activity; LE=Lava effusion; Foun=Lava fountaining; EndEp=End of episode; Post=Post quiescent period.

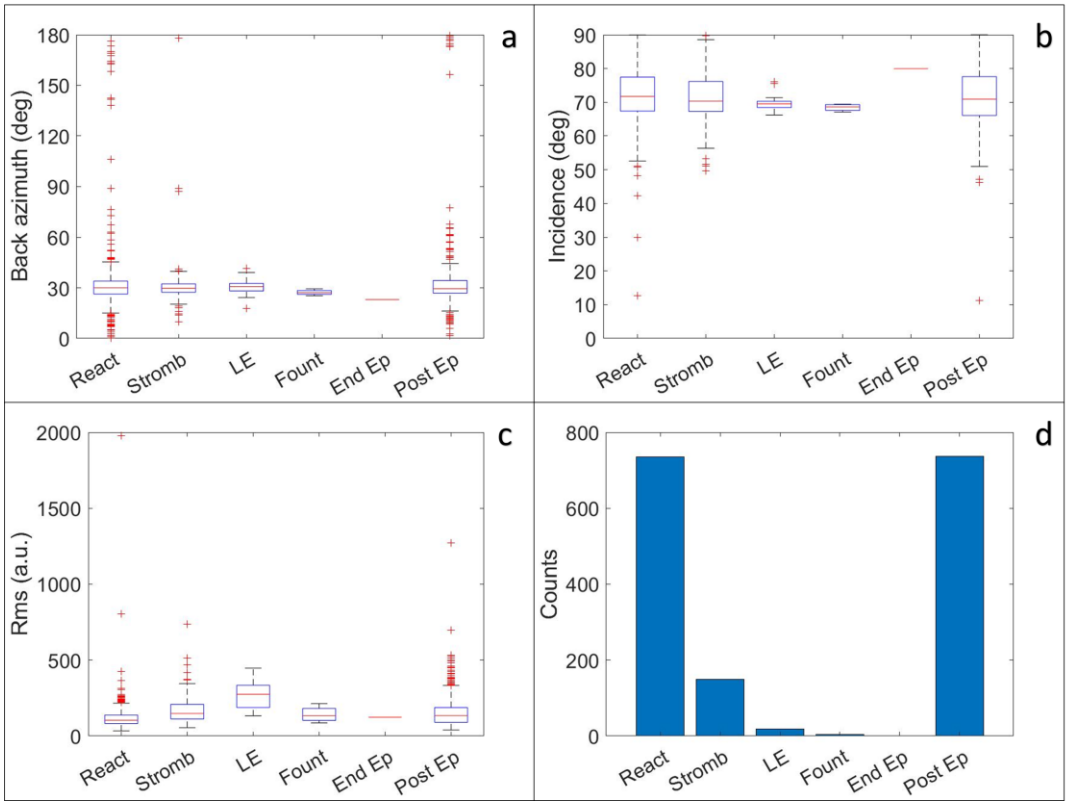

Figure 2.30. Statistical overview of the wavefield properties about VLPs recorded during the different phases of paroxysmal activity in 2011. a) Boxplot of polarization back azimuths. b) Boxplot of incidence angles. c) Boxplot of RMS amplitudes. d) Bars diagram of the number of VLPs. . For each diagram, the horizontal axis refers to the period comprised from the onset of a paroxysmal phase and the successive one (time interval from Behncke et al., 2014): Rea=Reactivation; Stromb=Strombolian activity; LE=Lava effusion; Foun=Lava fountaining; EndEp=End of episode; Post=Post quiescent period.

Generally, there were not significant differences among families of LP events in terms of polarization attributes and amplitudes features. One exception was represented by the distribution of the events in time (Fig. 2.31). The first and second families were detected along the entire period, reaching their maximum frequencies of occurrence almost in the same time intervals. In these cases, most of this LP activity was focused on the August-December and March-June intervals, with some sporadic peaks during the remaining periods. However, the second family was recorded with a lower frequency than the first one. The third family was slightly different in terms of temporal distribution of the events compared to what was seen previously. The frequencies of occurrence of this family shared similar values and time trend to the first one, except for the peak activity. In fact, the first and the second families reached maximum frequencies of occurrence during the months of August and September, while the third one was characterized by a maximum peak of

activity between November and December. However, each family of LP events showed the same properties relating them to paroxysmal activity, as explained before for the general trend.

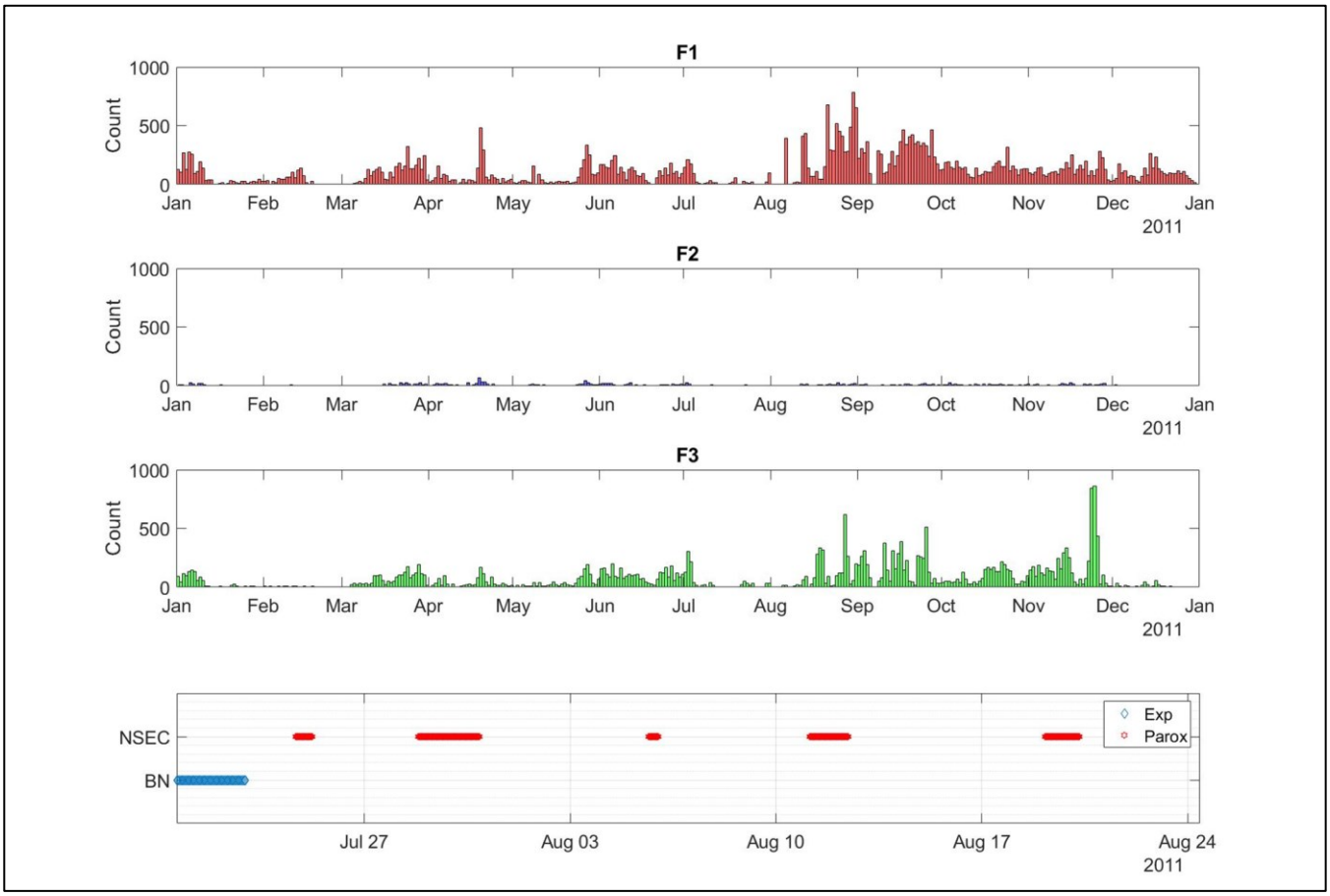

Figure 2.31. Temporal distribution of LP Families F1 (red), F2 (blue) and F3 (green) relating to the volcanic activity at NSEC and BN crater in 2011. The event counts are calculated on daily scale The legend on the upper right-hand of this panel shows the type of volcanic event: Exp= single explosions or series of minor explosions, minor and/or intense ash emissions; Parox= Strombolian, lava effusion and lava fountaining activity (data from Behncke et al., 2014).

2.4 DISCUSSION AND CONCLUSIONS

What is illustrated in this chapter consists of a study of the main properties of the seismic wavefield time-related to changes in the volcanic activity, focusing the attention to volcanic tremor and LP and VLP events. This is very important not only for the determination of the frequency range in which the successive localization analyses may be more reliable, but for the interpretation of those dynamics of magma extrusion that lead to volcanic phenomena such as paroxysms or sequences of explosions. In particular, this study was focused on the activity of Mt. Etna that occurred between June and October 2010 and throughout the 2011, when the volcano had been affected by a series of minor explosive events at BN crater (Tab. 1, section 1.2.5) and by 18 episodes of lava fountaining at NSEC (Tab. 2, section 1.2.5), respectively. In these cases, we referred to data recorded during seismic experiments in the 2010 and 2011 summertime, when two seismic arrays were deployed in summit area of the volcano, nearby ETFI permanent station (Fig. 2.1). In addition, we integrated these data with those acquired by the seismic permanent network managed by INGV (Fig. 2.1).

For the investigation of the nature and the properties of the seismo-volcanic signals, we used different methods and/or algorithms, such as spectral, amplitude and polarization analyses, as well as routines for the detection of seismic events such as LP and VLP events. At the same time, we included those techniques used to assess the wavefield coherence of the signals and to verify the capabilities of the arrays of recording coherent traces.

In order to perform the analysis of the volcanic tremor recorded during 2010-2011, six different methods were used:

(i) Beam pattern analysis (Capon, 1969), for the evaluation of the array response function, at different frequencies, of the two arrays deployed during the experiments.

(ii) Spectrogram calculation (Schlindwein et al., 1995), for the determination of the frequency range in which most of the seismic tremor radiation was generated and for the study of its temporal evolution.

(iii) Coheregram calculation (Welch, 1967), enhancing the frequency range in which the tremor wavefield is as coherent as possible.

(iv) RMS amplitude (Kenney and Keeping, 1962), to track significant energy changes of the tremor source in time and to verify the similarity of the amplitude patterns among different frequency ranges of analysis.

(v) Covariance matrix method (Jurkevics, 1988), to track variations in the directional properties of tremor source during the volcanic activity.

(vi) Particle motion calculation, to obtain qualitative information about the type of waves composing the tremor wavefield and further information about the directional properties determined through the previous method.

Considering the results illustrated in the section 2.3, most of coherent wavefield was recorded in the 0.5-1.5 Hz frequencies range (Figs. 2.7a and Fig. 2.8a). On the basis of the two arrays deployed during 2010 and 2011, the theoretical response was reliable up to 3.5 Hz (Fig. 2.4); for increased frequencies, the arrays did not provide a unique solution due to the spatial aliasing (e.g. Schweitzer et al., 2012; Zuccarello et al., 2016). Calculations of the tremor coherence between the different elements of the seismic arrays allowed to identify the optimal bandwidth for array processing. However, taking in account the results obtained through coheregram calculation (Figs. 2.7a and 2.8a), the coherency decreased at progressively higher frequencies, due to inter-sensors spacing and the scattering phenomena generated by steep topography and strong structural heterogeneity of volcano (e.g. Neuberg and Pointer, 2000; Kumagai et al., 2010, 2011; Qin et al., 2019). Therefore, the maximum peaks of coherence were recorded at lower frequencies in both periods, although significant values can be observed at slightly higher frequencies, due to the increase of signal-to-noise ratio, during eruptive phenomena such as explosions or lava fountaining (Figs. 2.7b and 2.8b). This can be also observed by comparing the time series of RMS amplitude values (Figs. 2.9a and 2.10a) with those obtained from coheregram (Figs. 2.7a and 2.8a): for lower energy values of seismic tremor radiation, the best waveform coherence was confined in lower frequency portion of the spectrum; with the increase of tremor energy, accordingly to the intensification of volcanic activity, high waveform coherence of the seismic traces was also recorded for frequencies greater than 1.5 Hz. In general, by comparing the results obtained through these methods, we were able to discriminate a reliable frequency band of analysis for the successive array processing. However, it was not possible to obtain a complete solution of the coherence wavefield, because of the limitations of array configurations and relationship between analysis parameters and resolution/stability of the results.

Regarding the tremor wavefield properties, we observed interesting relationships with the temporal evolution of the volcanic activity during the periods of interest. In both periods, these properties could be compatible with shallow seismic sources that mainly radiated a complex wavefield composed by both body and surface waves.

From the results obtained through spectral (Figs. 2.5a and 2.6a) and RMS analyses (Figs. 2.7a and 2.10a), the most part of seismic radiation was focused around 1 Hz, especially during the increase of the frequency rate of explosion events at BN crater (Figs. 2.5b and 2.9b) or during the paroxysmal episodes at NSEC (Fig. 2.6b and 2.10b) during 2010 and 2011, respectively. Averaging and normalizing the spectra in time (e.g. Saccorotti et al., 2004; Inza et al., 2014), we were able to better highlight the frequency content associated with tremor source, neglecting the influence of medium effects. It can be clearly observed in occurrence of the increase of RMS values (Figs. 2.9a and 2.10a), due to better signal-to-noise ratio related to the increase of the seismic energy of volcanic tremor. Taking into account the length of time window chosen for the analyses, we obtained a good resolution of spectral and amplitudes properties. The RMS amplitude analysis was very sensitive to signal peaks or technical glitches, affecting the amplitudes of RMS values (Kenney and Keeping, 1962; Battaglia et al., 2003). A good time and frequency resolution of the spectrogram required a narrow window in time and a narrow filter in the frequency domain (and then a large window in time), respectively. Unfortunately, Heisenberg's uncertainty principle prohibits the existence of a window with arbitrarily small duration and small bandwidth (Harris, 1978; Leseage, 2002). Therefore, we set the analysis parameters in order to obtain a good trade-off between resolution and reliability of results. For eruptive phenomena at Mt. Etna such as lava fountains or minor explosive events, some studies on volcanic tremor have evidenced similar properties to those shown previously (e.g. Alparone et al, 2003; Cannata et al., 2008; Patané et al, 2008; Coltelli et al., 2012; Patanè et al., 2013; Cannata et al., 2013, 2015; Cannavò et al., 2017; Moschella et al., 2018), noting that variation over time of the seismic RMS amplitude and frequency content was strongly related to changes in volcanic activity and source location. Other studies showed how these properties were not necessarily influenced by state of volcano (e.g. McNutt, 1992; Privitera et al, 2003; Di Grazia et al., 2006; Andronico et al., 2013). However, most of these authors concorded to attribute variations of the spectral and amplitude content of the volcanic tremor recordings to tremor source changes; in fact, the tremor spectral and amplitude content depended on the size of the resonant structure (Chouet, 1996a) and on the physical-chemical features of the fluid in the structure (Morrissey and Chouet, 2001). However, worldwide observations of volcanic tremor showed a large variability in time durations,

signal amplitudes, and frequencies content. This wide variety could indicate that volcanic tremor is probably the result of different processes (Chouet and Matoza, 2013).

Considering the polarization attributes, no significant variations were recognized along 2010 period (Figs. 2.11, 2.12 and 2.13), but they were almost stationary in time. Instead, during 2011 period, particle motion estimates were more unstable and changed according to variations in paroxysmal activity (Figs. 2.14, 2.15 and 2.16). In addition, the qualitative analysis of the particle motion revealed that tremor wavefield was very complex to interpret, because it was composed by both body and surface waves (Figs. 2.17 and 2.20). Significant information could be retrieved by exploring the limits of the methods. The quality of particle-motion information obtained for a given arrival depended on the positioning of the analysis window and choice of frequency interval (Kanasewich, 1981; Jurkevics, 1988). Hence, both window length and bandwidth were chosen on the basis of the usual trade-offs between resolution and estimation variance. The covariance matrix method was also less sensitive to largest-amplitude arrivals characterized by elliptical orbits of particle motion (Jurkevics, 1988; Saccorotti et al., 2004). The energy associated to these arrivals on radial plane was weak once compared to that observed on the transverse one. Therefore, for this reason, the contribute of surface waves was detected during visual inspection of particle motions rather than the covariance analysis. Covariance matrix method was also very sensitive to the number of sensors used for the analysis (Jurkevics, 1988). Unlike polarization analysis of array (Jurkevics, 1988), the use of single station-method could increase the variance and the instability of polarization attributes, making them difficult to interpret especially for low values of rectilinearity. For this reason, to decrease as much as possible this effect, we selected only properties computed during intervals characterized by high rectilinearity. In addition, local earth heterogeneities could introduce random time shifts and waveform distortions, affecting the accuracy and the quality of the polarization parameters (e.g. Jurkevics, 1988; Neuberg and Pointer, 2000; Saccorotti et al., 2004; Alparone et al., 2007). Therefore, the combination of these effects could explain the complexity of the results.

Taking into account the previous analysis and the volcanological observations, similar changes of polarization attributes, concurrently to those of the eruptive activity, have been largely observed at Mt. Etna (e.g. Ripepe et al., 2001; Di Grazia et al., 2006; Carbone et al; 2006; Cannata et al., 2008). These properties could be interpreted as the result of a complex wavefield, generated by the combination of source and path effects. In terms of source

effects, a resonating fluid-driven crack has been demonstrated to contribute large P, SV and SH components to the radiated wavefield (e.g. Chouet, 1988; Hagerty et al., 2000). However, for instance, SH-Rayleigh components, observed in the records of tremor in the past studies (e.g. Saccorotti et al., 2004; Alparone et al., 2007; Cannata et al., 2010) could be due entirely to a path effect. In this case, a possible mechanism concerns a wave conversion of P and SV energy impinging at the topographic and structural complexities affecting the summit volcanic edifice (Ohminato and Chouet, 1997; Ripperger et al., 2003). However, the results obtained in the previous analysis were not sufficient to discriminate between source and/or path effects, but they need to be compared to those related to tremor source positions. Therefore, further interpretations about these properties can be found in the Chapter 3.

Regarding the study of LP and VLP events recorded during 2010-2011, five different analysis steps were performed:

(i) Detection analysis (Allen, 1982; Garcia et al., 2017), for the automatic identification of the events during the periods of interest.

(ii) Waveform classification, to distinguish different families of events on the basis of their waveform.

(iii) Polarization analysis (Jurkevics et al., 1988), to track variations in the directional properties related to only LP and VLP source during the volcanic activity.

(iv) RMS amplitude analysis (Kenney and Keeping, 1962), to track significant energy changes of the LP/VLP source in time.

(v) Family characterization, for comparing the wavefield properties of the different families of events accordingly volcanological observations.

As mentioned in the previous section, we applied the SALPED (Garcia et al., 2017) and STA/LTA (Allen, 1982) algorithms to automatically detect the LP and VLP events, respectively. The analysis parameters were set on the basis of the features of signals observed at Mt. Etna in the recent years (e.g. Patanè et al., 2008; Di Grazia et al., 2009; Cannata et al., 2013; Zuccarello et al., 2013), such as frequency content, signal duration and waveforms. The detection thresholds were chosen taking into account the trade-off between the amount of transients in the signal that must be included or excluded in our calculations and the best signal-to-noise ratio. However, while the SALPED algorithm was

very performant for LP individuation (Garcia et al., 2017), the STA/LTA method was more sensitive to those energy transients which showed similar duration or frequency of VLPs (such as earthquakes or transient noises). Therefore, the visual inspection of the waveforms was also performed, not only for the waveform classification, but also to obtain a reliable dataset of events. In addition, similar to volcanic tremor, LPs and VLPs were affected by the effect of both free surface and complex stratigraphy (Neuberg and Pointer, 2000; Almendros and Chouet, 2003). Concerning the former, the problem was more serious due to the fact that volcanoes have generally pronounced topography, causing severe timing and waveform perturbations. Unlike volcanic tremor, these effects were less pronounced in the low frequency signals, especially for VLPs which can be considered relatively insensitive to km-scale structures due to their long wavelength. For this reason, we selected only those events characterized by highly rectilinear particle motions, trying to isolate as much as possible only the source contributes. In addition, the parameters of polarization and amplitude analyses were set to characterize the first two wave cycles of the events, taking into account also the technical limitations explained before for the volcanic tremor processing.

During 2010-2011 interval, the wavefield properties of LP and VLP events were closely related to eruption activity (Figs. 2.22, 2.23, 2.27 and 2.28). In general, these features could be associated with shallow seismic sources that generated body waves, accordingly to the high rectilinear quasi-horizontal particle motions. Probably, considering the polarization attributes, the VLP source was slightly deeper than LP one, although this was difficult to prove without any localization information. Taking into account the volcanic activity in the periods of interest, we observed significant variations about seismic amplitude, back azimuth and incidence angle of particle motions and frequency of occurrence of the LP events; on the contrary, the properties of VLPs were almost stationary in time and not always correlated to volcanic activity (Figs. 2.22, 2.23, 2.27 and 2.28), showing similar behaviour to LPs only during the paroxysmal activity in 2011. During the quiescent periods of Etna volcano, LP events were recorded with the highest occurrence frequencies and the lowest amplitude and incidence values; the back azimuth angle indicated waves propagating radially from summit area of volcano. Instead, the number of detected signals gradually decreased with the intensification of explosion events at BN crater during 2010 (Figs. 2.22 and 2.23) or the development of paroxysmal activity at NSEC during 2011 (Figs. 2.27 and 2.28), showing progressively higher energies values and more horizontal and/or tangential particle motions. Similar LP and VLP features were observed at Mt. Etna in the last decades (e.g. Saccorotti et al., 2007; Lokmer et al., 2007;2008; Cannata et al.,

2008, 2009a, 2013; Patané et al., 2008; Zuccarello et al., 2013). LP wavefield changes observed during 2010 and 2011, as the same time as the eruptive activity, could be related to a resonator system such as a fluid-filled crack, as suggested by other recent studies (e.g. Chouet, 1996a; Nakano et al., 2003; Kumagai et al., 2006; Lokmer et al., 2007; De Barros et al., 2009; Cauchìe et al., 2015). However, the quasi-stationary behaviour in time and the different amplitude and incidence values of VLPs suggested that these signals could be triggered by mass transfer (e.g. Chouet et al., 2003; Saccorotti et al., 2007; Cannata et al., 2009a, 2013).

As regards the properties retrieved for each family of events, we did not individuate significant difference among families, except for LPs during 2010 (Figs. 2.24 and 2.25). In fact, the frequency rates of the two first families were higher during the quiescent period of volcano (Fig. 2.24); the third family mainly occurred with the highest rates during the explosive sequence that occurred at BN crater (Fig. 2.24). In addition, in the first cases, the amplitudes and the particle motion incidence angles gradually increased up to the end of the explosion activity (Fig. 2.25); while those associated to the third family were clustered around the highest values among the families only in the first part of the explosive sequence (Fig. 2.25). The difference in wavefield properties and waveform shape could be caused by a different source position and/or source mechanism, especially in the initial part of the source time function (e.g. Cannata et al, 2009a; De Barros et al., 2009,2011; Zuccarello et al., 2013).

In general, the time variation of LP and VLP properties could be interpreted as due to pressurization/depressurization phenomena involving the shallowest magma storage zone of volcano (e.g. Saccorotti et al., 2007; Aiuppa, 2010; Cannata et al., 2013; Zuccarello et al., 2013). In addition, the repetitiveness of the features of these signals could be a clear indication of the repeated action of non-destructive sources (Cannata et al., 2009a; Di Grazia et al., 2009; Saccorotti et al., 2007; Patanè et al, 2008, 2013; Zuccarello et al., 2013). However, all these hypotheses will be further explored in the next chapter when source location of events will be investigated.

2.5 SUGGESTED FUTURE WORK

In order to improve the knowledge about dynamics of injection and transport of magma affecting the shallow plumbing system of Mt. Etna, future works could be aimed at:

(i) Installation of more than one three component array close to the summit area of volcano, featuring a greater number of sensors with different spacing (Saccorotti et al., 2004; Di Lieto et al., 2007; Almendros et al., 2014; Inza et al., 2014). The deployment of many sensors could allow to use different sub-geometries and, therefore, to extend the seismic wavefield investigation to a larger wavelength range. The simultaneous use of more arrays could improve the resolution of wavefield properties and better constrain the volcanological phenomena.

(ii) Quantification of the propagation/site effects on the seismic signals by using analysis techniques implemented for the evaluation of the variations of waves velocity in the Etna volcano, the noise content of wave field and the seismic response of the site (O'Brein and Bean, 2004; Chàvez-Garcìa et al., 2005, Cauchie and Saccorotti, 2013; Zuccarello et al., 2016). This could improve the stability and quality of results, diversifying as much as possible the source contributes from the others.

(iii) Application of three component arrays methods for the assessment of seismic wave field properties, especially for the polarization attributes (Jurkevics, 1988). The use of beamforming methods could improve the resolution and the variance estimates on the features of signals by increasing the signal-to-noise ratio of the traces.

(iv) Implementation of detection algorithms for the automatic individuation and classification of different volcanic signals on the basis of their main characteristics (Álvarez et al., 2013; Garcia et al., 2017; Bueno et al., 2019). This could reduce time processing of the data and could better constrain the features of signals such as volcanic tremor, LPs, VLPs, VTs, etc…

(v) Application of these approaches to longer periods of volcanic activity of Mt. Etna when similar eruptive phenomena, such as paroxysms and/or minor explosions, have been observed. This could allow to create a large dataset containing as much information as possible about the characteristic properties of the volcanic signals and their short and long-term variations during volcanic eruptions at Mt. Etna.

A successful application of these analyses would not only improve the knowledge about magma dynamics in the plumbing system of Etna volcano but could allow the development of strategies able to provide a significant improvement in hazard assessment.

CHAPTER 3 – SOURCE LOCATION OF SEISMIC SIGNALS AT MT. ETNA

3.1 INTRODUCTION

Features of seismo-volcanic signals and their temporal changes are often related to eruptive activity, providing insight on the physical processes controlling explosive eruptions (Sparks et al., 2012; Chouet and Matoza, 2013; McNutt et al., 2015). At Mt. Etna, the behaviour of seismic signals, such as volcanic tremor, LP and VLP events, strongly reflects the evolution of explosive activity, also involving source location which generally becomes shallower and closer to the eruptive vent during the explosive eruptions (e.g. Patanè et al., 2013; Viccaro et al., 2014; Cannavò et al., 2017). Concerning the source location of these signals, it is not always possible to use techniques based on the inversion of the arrival time of the seismic phases. Except for the techniques based on spatial distribution of amplitudes (e.g. Battaglia and Aki, 2003; Di Grazia et al., 2006; Kumagai et al., 2010; Jones et al., 2011), most of the methods used to locate volcanic tremor and/or LP and VLP events are based on array analysis (e.g. Neidell and Taner, 1971; Schmidt, 1986; Kawakatsu et al., 2000; Rost and Thomas, 2002).

In recent years, the use of array techniques has progressively become more popular for the analysis and interpretation of signals recorded at different volcanoes in the world, such as Izu-Ochima vocano (Japan; Furumoto et al., 1990), Kilauea (Hawaii, USA; Almendros et al., 2001a,b), Stromboli (Italy; La Rocca et al., 2004), Ubinas volcano (Perù; Inza et al., 2014) and Bárdarbunga volcano (Iceland; Eibl et al., 2017a,b). At Mt. Etna, array methods have been demonstrated to be a power tool to track the source of complex signals such as volcanic tremor (e.g Saccorotti et al., 2004; Di Lieto et al., 2007), LP (e.g. Cannata et al., 2013) and VLP events (e.g. Zuccarello et al., 2013), obtaining further insight on magma dynamics in the shallower portion of plumbing system.

As explained in the Chapter 1 (section 1.3), seismic arrays usually differ from sparse networks of stations mainly by the techniques used for data analysis: in a network, the arrival times are determined on each station, while, in an array, all sensors are processed together on the basis of the common waveform model (Aki e Richards, 1980). However, considering that array methods are wavelength-dependent (Havskov, 2016), a sparse network may be used as an array, especially for events characterized by long wavelength, such as LPs and VLPs.

In the following paragraphs of this chapter, for the source localization of seismic signals recorded at Mt. Etna between 2010 and 2011, we will illustrate the results obtained through array methods. Using data recorded by seismic arrays and the permanent monitoring network (for more details, see section 2.2, Chapter 2), we analysed the kinematic properties of the tremor wavefield by applying ZLCC method. With kinematic properties, we refer to parameters describing the propagation direction of elastic waves arriving at a seismic array, that are back azimuth, ray parameter and incidence angle (for more details, see section 1.3.1, Chapter 1). For LP and VLP source localizations, we applied the Semblance and Radial Semblance algorithms, respectively, integrating these results with their kinematic properties of LPs and VLPs obtained through ZLCC analysis. Each of these techniques was complemented by the application of the JackKnife method, to assess the stability of the results. The choice of these localization methods was related to: (*i*) array and/or permanent network features (geometry, number of available stations, inter-sensor spacing, etc…); (*ii*) frequency/wavelength content of the seismic wavefield; (*iii*) theoretical assumptions of each method. Concerning these methods, we also set some input parameters on the basis of average physical and mechanical properties of Mt. Etna edifice. In particular, for the calculation of incidence angles in ZLCC analysis or the delay times in Semblance/Radial Semblance methods (see section 1.3.6, Chapter 1), we assumed a velocity value of 1.6 km/s of seismic waves, such as a trade-off of the velocity models obtained in the last years for the shallowest portion of the volcano (e.g. Saccorotti eta l., 2004; Cauchy and Saccorotti, 2013; Zuccarello et al., 2016); for the application of the equation 1.34 in the Semblance method (see section 1.3.6, Chapter 1), we set the input parameters on the basis of some past studies (e.g. De Gori et al., 2005; Di Grazia et al., 2006, 2009). However, these assumptions, concerning the homogeneity of the propagation medium, increased the uncertainty on source location of the seismic signals, due to the lack of a detailed velocity model that allows to reconstruct a reliable tracing of the seismic rays across the volcano edifice.

This chapter will be organized as follows: firstly, we will show the kinematic properties of volcanic tremor signals, and compared them with the evolution in time of the eruptive activity during 2010-2011; then, we will illustrate the locations and the temporal variations of the seismic sources associated to the LP and VLP activity and will evaluate the performance of the methods through some synthetic tests; successively, on the basis of these results and those illustrated in the previous chapter, we will provide a conceptual model about dynamics of pressurization and depressurization of the plumbing system of Etna volcano during 2010-2011, trying to identify a source mechanism able to explain the

observed wavefield properties and source locations; finally, we will discuss on the possible future works needed for improving the knowledge about source position and mechanisms of the seismo-volcanic signals recorded at Mt. Etna.

3.2 DATA ANALYSIS

3.2.1 VOLCANIC TREMOR

In order to evaluate the kinematic properties of the volcanic tremor, we performed the ZLCC analysis (see section 1.3.6, Chapter 1) by using the seismic traces acquired from arrays during 2010 and 2011 time intervals (see section 2.2, Chapter 2). In both the periods, the analysis was performed by 10-seconds-long sliding window along the traces of the arrays, which were filtered between 0.5 and 1.5 Hz through band-pass cosine filter. The results mainly consist of time series of back azimuth and ray parameter, while the incidence angles were retrieved by using a value of waves velocity of 1.6 km/s. To assess the stability of these solutions, we also used the JackKnife method, computing the analysis errors associated with kinematic parameters. In addition, we filtered the results by selecting those values for which the average cross correlation coefficient is greater than 0.75.

The kinematic properties of the volcanic tremor obtained for the 2010 period are illustrated in the figures 3.1 and 3.2. During this period, no significant changes were recognized in the kinematic wavefield properties of the tremor, but all parameters were stationary and stable in time (Fig. 3.1), nonetheless we observed important variations in the tremor amplitude. In particular, the back azimuth was mostly focused in the 20°N-E40° range (Fig. 3.2a), associated to directions of arrival encompassing the east slope of the SEC. Ray parameters of these waves were clustered in the 0.5-1 s/km range (Fig. 3.2b), corresponding to apparent velocities between 1.0 and 2.0 km/s. Most of the incidence angles were comprised between 60° and 70° (Fig. 3.2c). These solutions were also very stable and reliable in time, because most of analysis error values did not exceed the values of about 7°, 0.15 s/km and 10° for the back azimuth (Fig. 3.2d), ray parameter (Fig. 3.2e) and incidence angles (Fig. 3.2f), respectively.

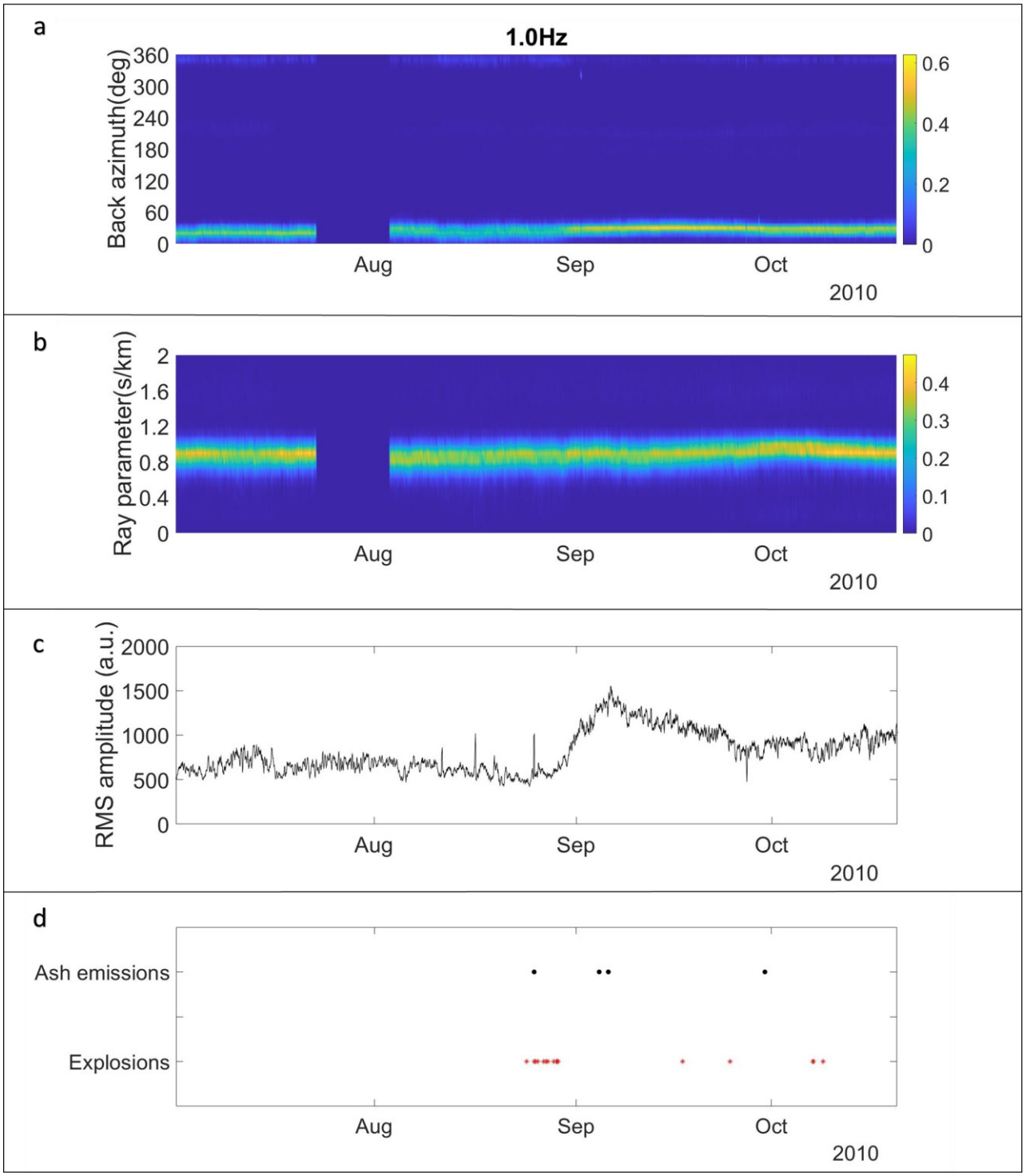

Figure 3.1. Kinematic properties of volcanic tremor during 2010 for the 0.5-1.5 Hz frequency band. a) Temporal histogram of back azimuth calculated on time and angular intervals of 3 hours and 10°, respectively. The colorbar on the right-hand refers to the values of histogram probability. b) Temporal histogram of ray parameter calculated on time and angular intervals of 3 hours and 0.1 s/km respectively. The colorbar on the right-hand refers to the values of histogram probability. c) 3 hours moving average of the RMS amplitudes of the tremor. The RMS amplitudes are calculated over 10-seconds-long sliding window along the traces of the central sensor of array. The axes of plots are set in linear scale. d) Volcanic activity observed at BN crater (data from Andronico at al., 2013).

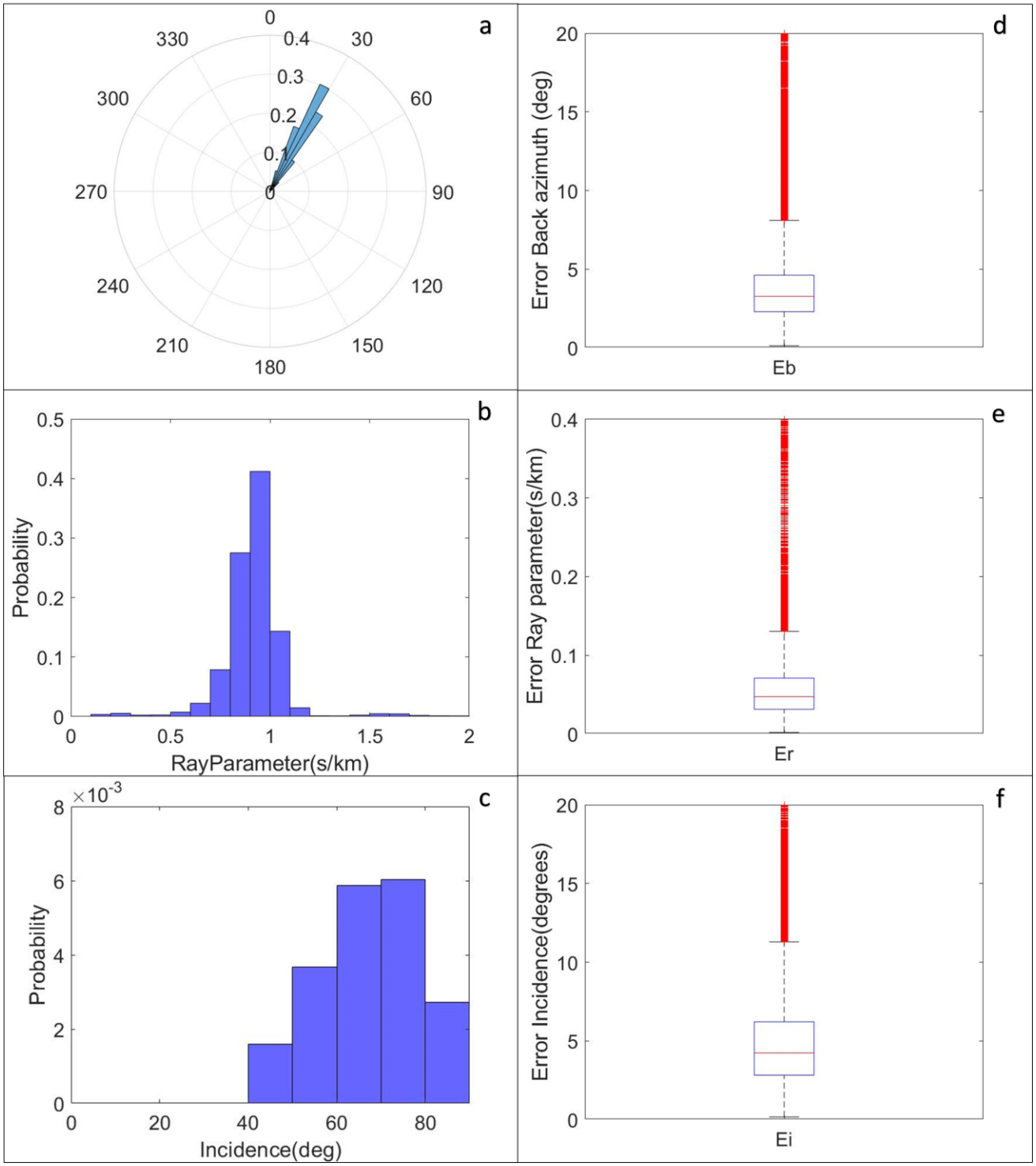

Figure 3.2. Statistical overview of the kinematic properties of volcanic tremor during 2010 for the 0.5-1.5 frequency band. a) Polar histogram of back azimuth (bin=5°). b) Histogram of ray parameter (bin=0.1 s/km). c) Histogram of incidence angles (bin=10°) calculated with velocity=1.6 km/s. d) Boxplot of errors of back azimuth. e) Boxplot of errors of ray parameter. f) Boxplot of errors of incidence angles.

During the 2011 summertime, the kinematic properties of the volcanic tremor were different form those obtained in the previous year (Fig. 3.3). In fact, in this case, they were well correlated to the variations of the volcanic activity observed at NSEC and BN crater and to the changes in the tremor amplitudes, especially during the time intervals around paroxysms. In the quiescent period of the Etna volcano, the wavefield features were stationary in time. The back azimuths were clustered in the N330°E-N10°E range (Fig. 3.4a), pointing toward BN crater, while the ray parameter was focused in 0.5-1.0 s/km interval (Fig. 3.4b). Considering a wave velocity of 1.6 km/s, the incidence angles ranged between 55 ° and 75° (Fig. 3.4c). At the onset of the reactivation of the paroxysmal activity, the back azimuths gradually migrated to N20°E-N40°E (Fig. 3.4a), corresponding to arrival directions from NSEC and stabilising in this interval for the entire duration of the paroxysms. The ray parameter values gradually increased up to range 0.7-1.2 s/km with the development of the lava fountaining (Fig. 3.4b), while the incidence angles progressively became shallower (65°-75°, Fig. 3.4c). Simultaneously with end of the paroxysmal episode, the kinematic parameters gradually returned to the ranges exhibited before the onset of the volcanic activity, although the back azimuth variation was more abrupt than the other parameters (Fig. 3.4). In general, these results were very reliable in terms of error of analysis, although they were more unstable than those observed in the 2010 experiment. In fact, they did not exceed the values of about 12°, 0.15 s/km and 18° for the back azimuth (Fig. 3.4d), ray parameter (Fig. 3.4e) and incidence angles (Fig. 3.34), respectively. In addition, it was possible to observe how these parameters became more stable every time the explosion activity or the tremor amplitude increased, showing a minor number of outliers (Fig. 3.4).

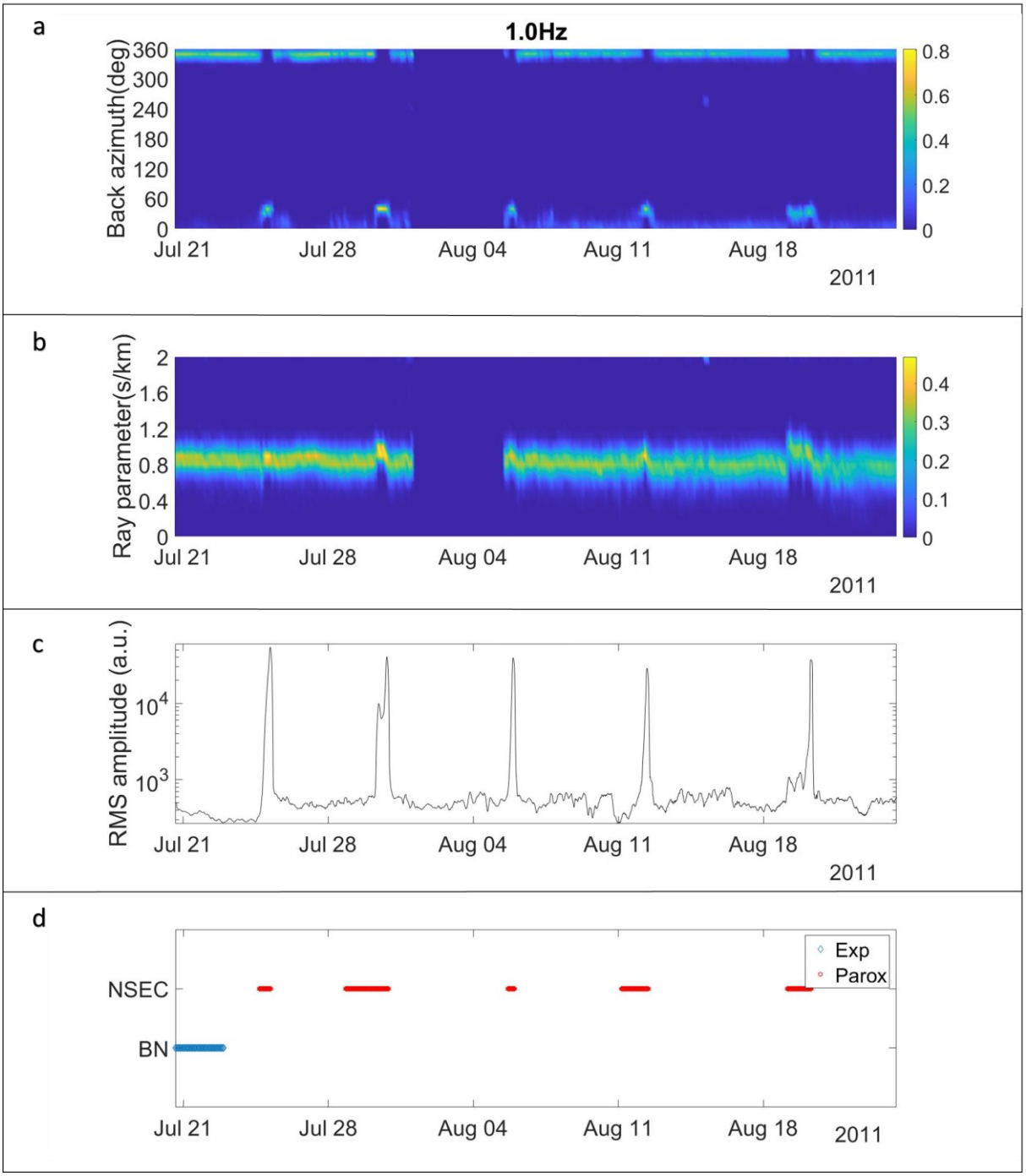

Figure 3.3. Kinematic properties of volcanic tremor during 2011 for the 0.5-1.5 Hz frequency band. a) Temporal histogram of back azimuth calculated on time and angular intervals of 3 hours and 10°, respectively. The colorbar on the right-hand refers to the values of histogram probability. b) Temporal histogram of ray parameter calculated on time and angular intervals of 3 hours and 0.1 s/km respectively. The colorbar on the right-hand refers to the values of histogram probability. c) 3 hours moving average of the RMS amplitude of the tremor. The RMS amplitude values are calculated over 10-seconds-long sliding window along the traces of the central sensor of array. The axes of plots are set in linear scale. d) Volcanic activity observed at NSEC and BN crater. The legend on the upper right-hand of the diagram shows the type of volcanic event: Exp= single explosions or series of minor explosions, minor and/or intense ash emissions; Parox= Strombolian, lava effusion and lava fountaining activity (data from Behncke et al., 2014).

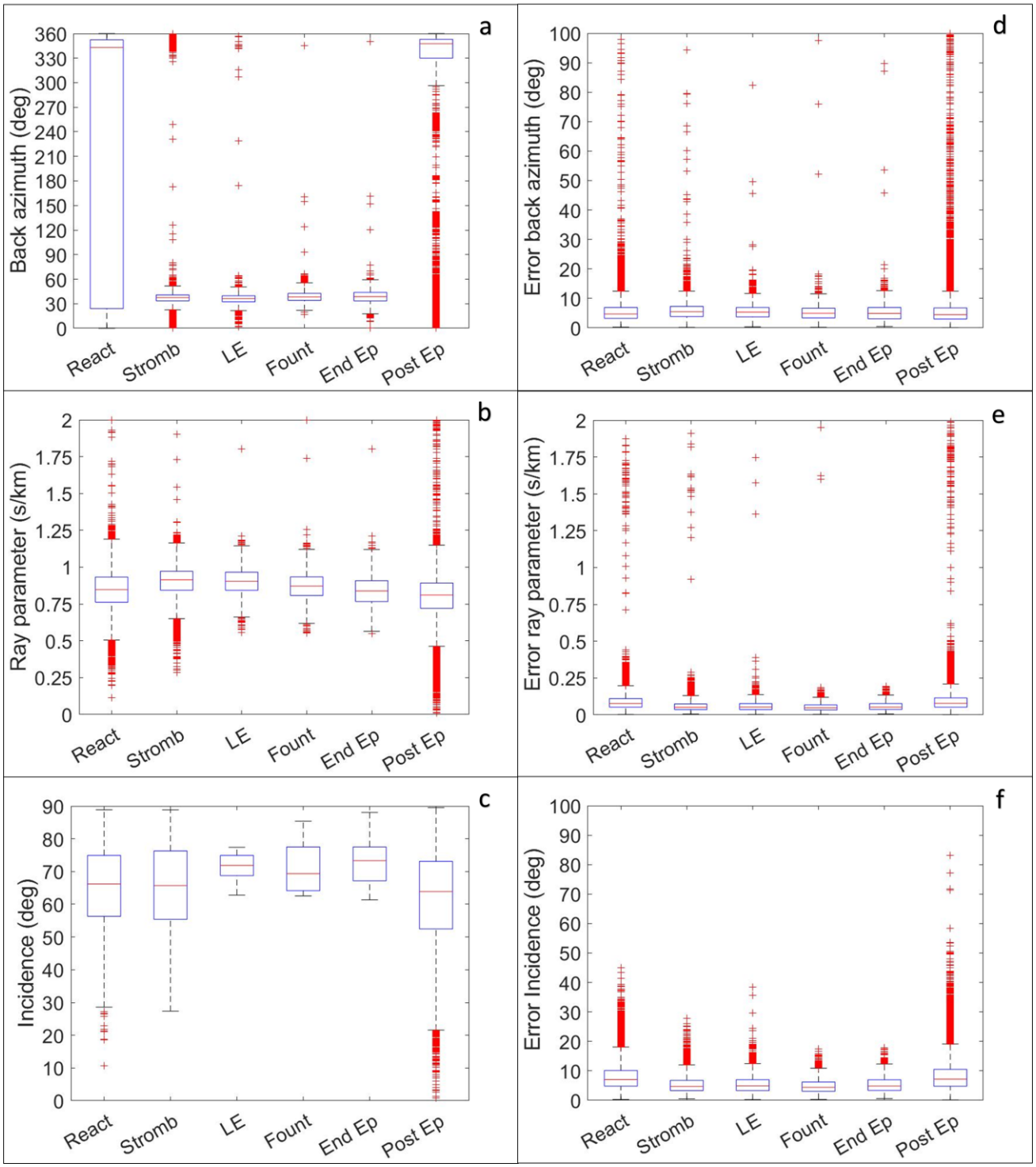

Figure 3.4. Statistical overview of the kinematic properties of volcanic tremor during 2011 for the 0.5-1.5 Hz frequency band. a) Boxplot of back azimuth. b) Box plot of ray parameter. c) Boxplot of incidence angles calculated with velocity=1.6 km/s. d) Boxplot of errors of back azimuth. e) Boxplot of errors of ray parameter. f) Boxplot of errors of incidence angles. For each diagram, the horizontal axis refers to the period comprised from the onset of a paroxysmal phase and the successive one (time interval from Behncke et al., 2014): Rea=Reactivation; Stromb=Strombolian activity; LE=Lava effusion; Foun=Lava fountaining; EndEp=End of episode; Post=Post quiescent period.

3.2.2 LP AND VLP EVENTS

As done in the previous chapter, the localization of low frequency events was performed by using the seismic traces recorded by the INGV seismic permanent network (see section 2.2, Chapter 2), in a period comprised between June and October 2010 and for the full year of 2011. In this case, we used the Semblance and Radial Semblance methods for the individuation of the seismic sources associated with LP and VLP events, respectively. In addition, we used the data acquired from the seismic array during their functioning periods (see section 2.2, Chapter 2). Therefore, we determined the kinematic properties of LP and VLP wavefields by performing the ZLCC analysis. All of these algorithms were also implemented through JackKnife method (see section 1.3.6, Chapter 1), to evaluate the largest number of solutions potentially reliable and then their uncertainties.

Following the procedure explained in the section 1.3.6 (Chapter 1), LP events were located by using a 3D grid-search of 5x5x2 km^3 (E-W, N-S and vertical directions) centred on the volcanic edifice and with a vertical extent from 1 km a.s.l. to the top of the volcano. The horizontal and the vertical grid spacing was 100 m. The events, previously archived in 20 s long waveform recordings, were filtered in the 0.5-1.2 Hz frequency band, that was the same one used for their detection. For each waveform, the first emergent arrival of the LPs was fixed on 2.5 s long time window by performing the manual picking of the recordings at ECPN station, chosen on the basis of the highest signal-to-noise ratio. In addition, assuming that amplitude of the trace decays with the distances between the grid points and the stations, we fixed the quality factor, the central frequency and the waves velocity at 40, 1.0 Hz and 1.6 km/s (e.g. Di Grazia et al., 2006; Cannata et al., 2013), respectively, considering that the wave field was mainly dominated by body waves.

For the VLP events, we performed the localization through the same 3D grid-search used for the LPs one, with a different algorithm (see section 1.3.6, Chapter 1). In this case, the 100 s long VLP recordings were filtered in the same frequency range used for their identification (0.01-0.15 Hz). The picking of their first arrivals was performed at the same station used previously for LPs, ECPN, fixing the phases of interest on 10 s long time window. In order to avoid the effect of the signal amplitudes on the calculation, we normalized the traces by the RMS amplitude of three component data.

In order to define the maximum probability region where the events were spatially located, firstly we selected only those LPs and VLPs for which the Semblance/Radial Semblance results were very stable (semblance values >=0.6, latitude and longitude errors <=0.4 km and altitude errors <=0.6 km). Finally, semblance distributions obtained for all these events

were averaged, determining the node coordinates with the largest beam value and the volume whose semblance values were higher than 90 % of the absolute maximum. For the events detected during 2010 and 2011, the results thus obtained are shown in figures 3.5, 3.6 and 3.7. In terms of spatial probability distribution, we did not identify significant differences among families of events. In general, LP and VLP epicentres were permanently located in the south-western sector of the summit area (Figs. 3.5 and 3.6; Tab. 6), approximately on the BN crater. In both type of events, the errors of source location had a magnitude on the order of hundreds of meters, although the VLP semblance distribution was slightly larger than LP one (Tab. 6). The extension in altitude was much wider, ranging between 2.0 and 3.0 km a.s.l. (Fig. 3.5 and Fig 3.7). On average, the centroids of LP and VLP clusters were located at about 2.9 and 2.8 km a.s.l., respectively.

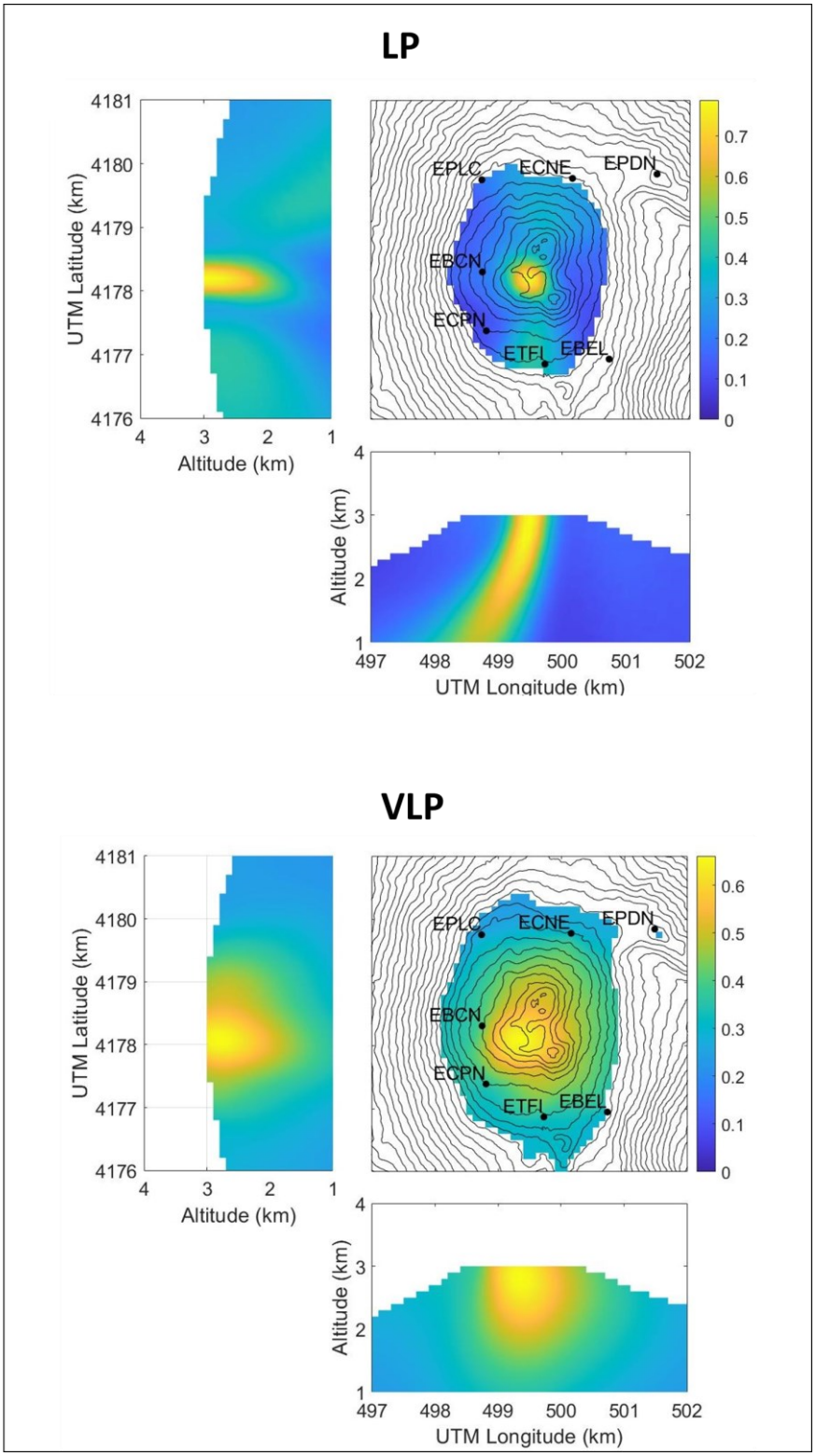

Figure 3.5. Three sections of Semblance and Radial Semblance grids passing through the largest value node. The results represent the average distributions calculated on 1868 LPs and 400 VLPs recorded between 2010 and 2011 and chosen on the basis of the best errors of analysis. The grids are interpolated to the DEM of Mt. Etna. The colorbars on the right-side refer to the normalized values of the Semblance/ Radial Semblance. The black marks represent the station locations.

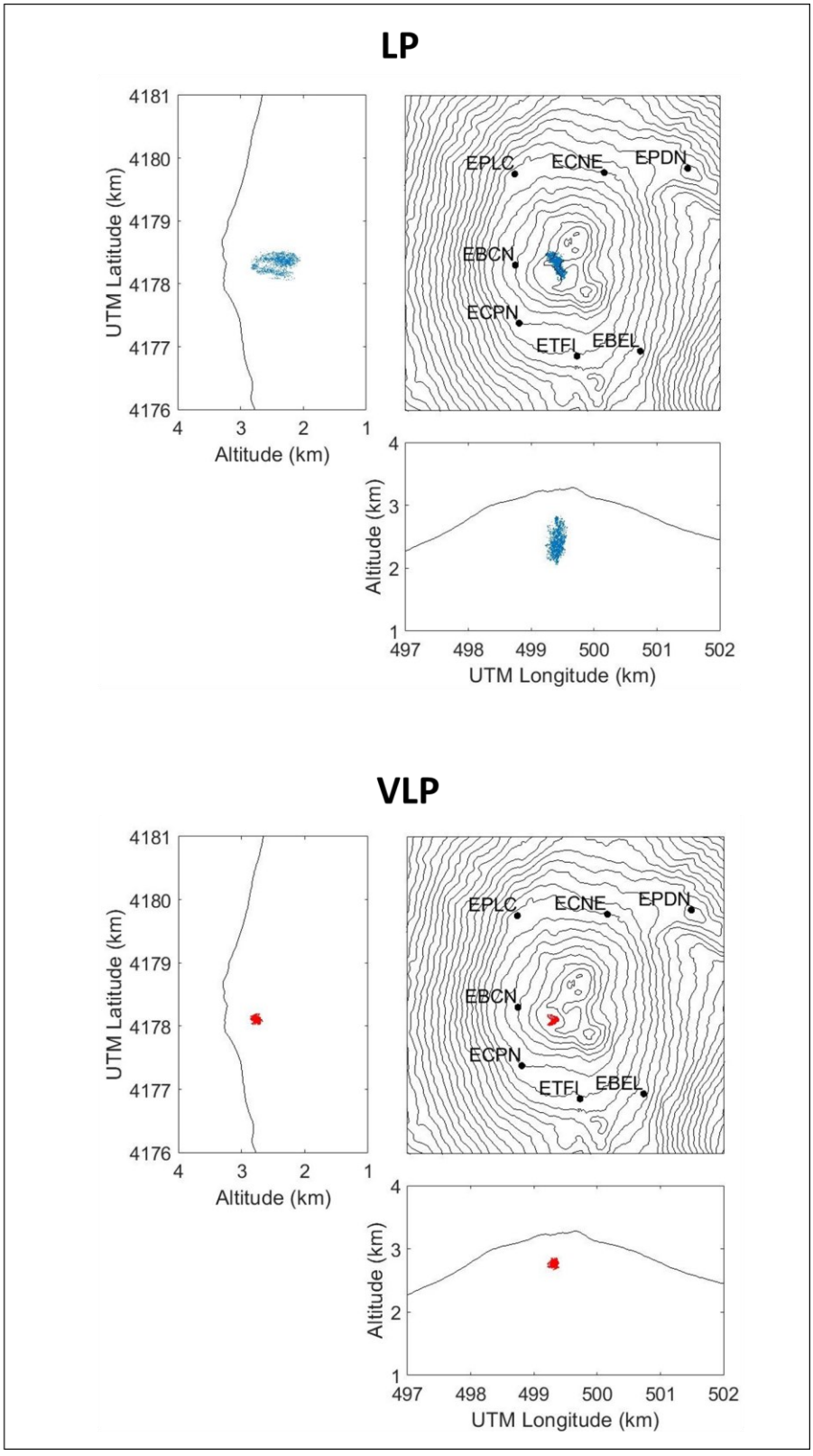

Figure 3.6. LP (blue marks) and VLP (red marks) epicentres on the three sections of the DEM of Mt. Etna. The results represent the average distributions calculated on 1868 LPs and 400 VLPs recorded between 2010 and 2011 and chosen on the basis of the best errors of analysis. The black marks represent the station locations.

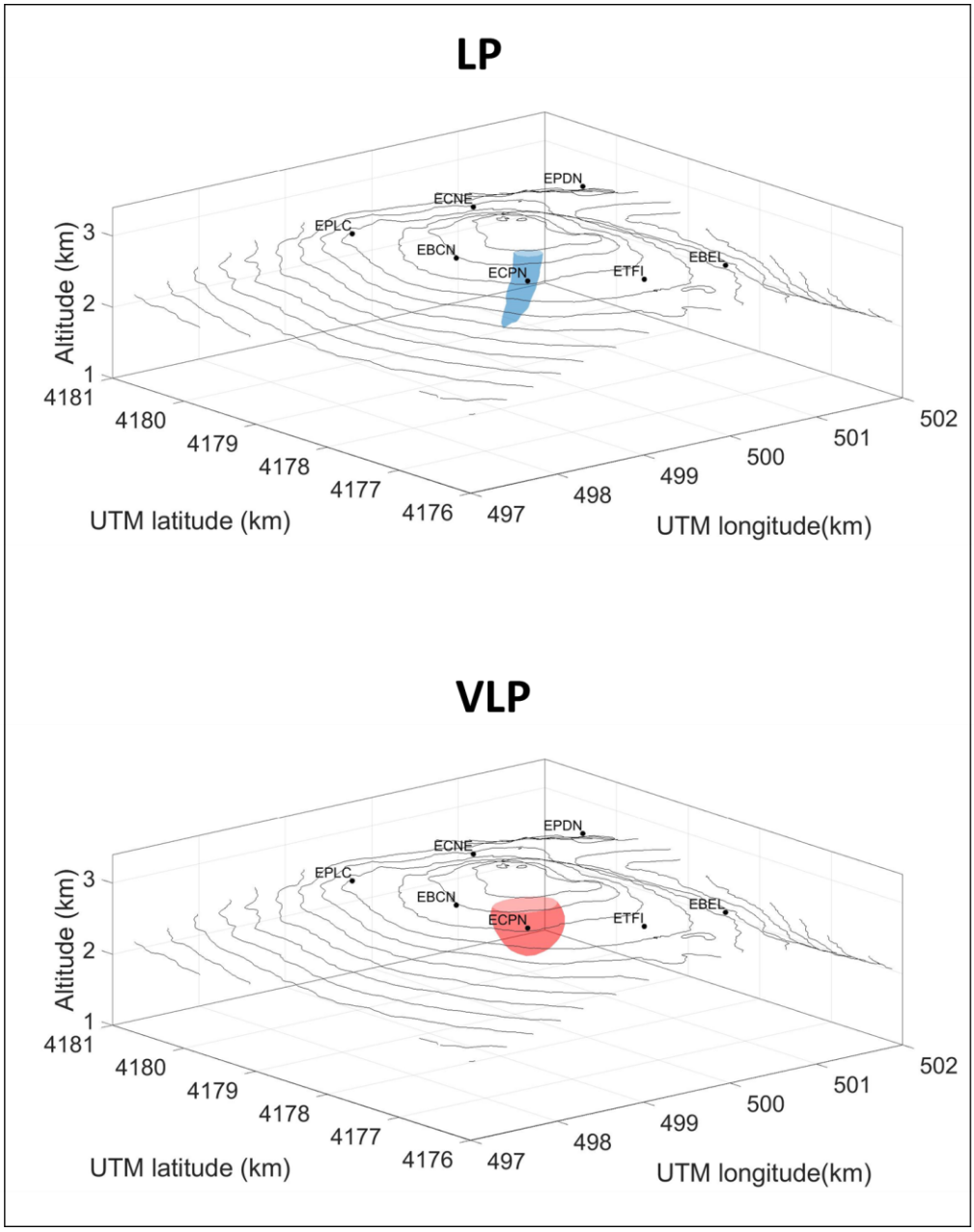

Figure 3.7. Probability source regions (blue and red volumes for LPs and VLPs, respectively) calculated on the basis of the results shown in figure 3.5. The results consist of the 10% Semblance/Radial Semblance distributions around the largest solutions. The black marks indicate the station positions.

	LP	VLP
Maximum semblance value	0.79	0.66
UTM Longitude (km)	499.50	499.40
UTM Latitude (km)	4178.20	4178.10
Altitude (km a.s.l.)	2.90	2.80
Error longitude (km)	0.11	0.11
Error latitude (km)	0.10	0.12
Error altitude (km)	0.32	0.11

Table 6. Weighted average of localization parameters of LP and VLP during 2010 and 2011.

Once the major probability region of source locations has been defined, we tried to identify important temporal relationships between LP/VLP seismicity and the volcanic activity. Also in this case, we selected only those events characterized by stable source parameters, filtering for semblance values greater than 0.6, latitude and longitude errors smaller than 0.4 km and altitude errors smaller than 0.6 km. As seen before, during the 2010, the epicentres of both type of events were well located in close proximity of the BN crater, without evidencing significant variations in time or among different families of events (Fig. 3.8). Important temporal changes in the source parameters were recognized rather in the hypocentres of LPs and VLPs, especially in terms of altitude. In particular, the altitude variations of the LP/VLP source locations were shown in figure 3.9. Generally, the altitude of the events gradually increased along the whole period, reaching the highest values in occurrence of explosion activity at BN crater (Fig. 3.9b). The LP altitudes averagely were focused between 2.4 and 3.0 km a.s.l., showing a major variability and large localization errors overcoming the hundreds of meters. Instead, those of VLPs were almost stationary and stable in time, clustering mainly around 2.8 km a.s.l. and showing errors much lower than the previous ones. The altitude of LP locations showed also important differences in time among the different families (Fig. 3.9a). Altitudes of the first and second families were distributed with the major variability (2.4-2.9 km a.s.l.), following approximately the general trend displayed in the figure 3.9b. For the third family of LPs, the altitude values ranged between 2.7 and 3.0 km a.s.l., clustering close to 3.0 km a.s.l. during the final part of the explosive sequence at BN crater.

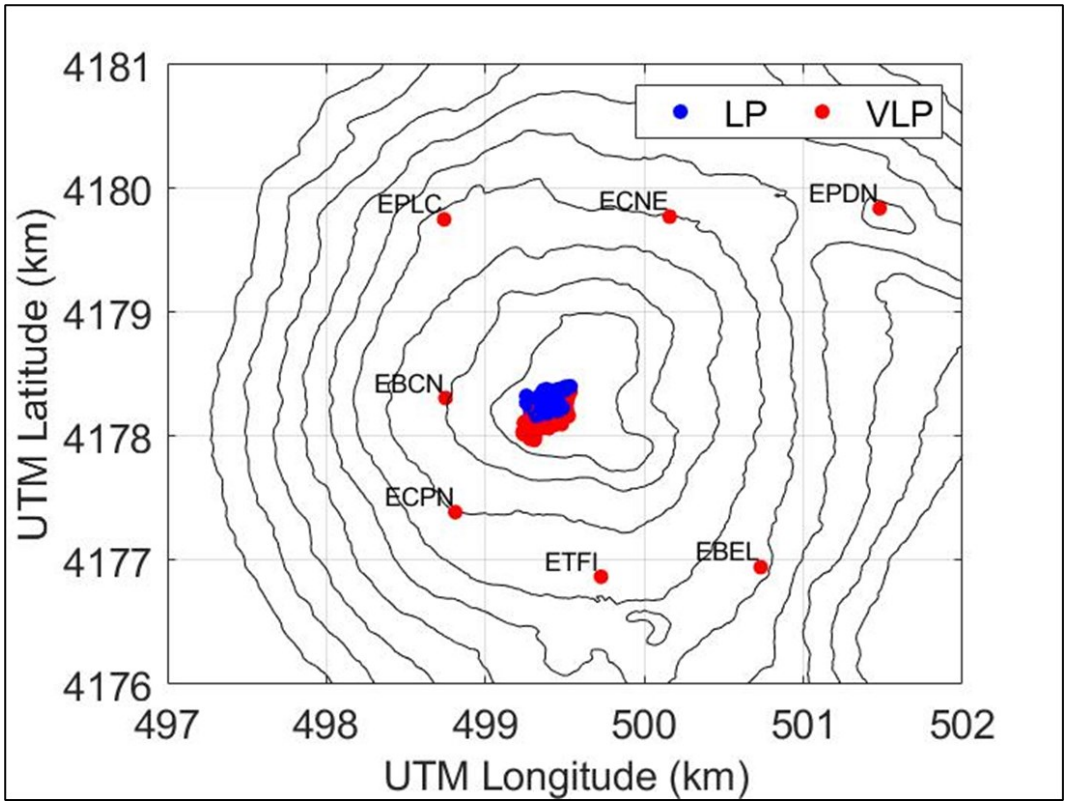

Figure 3.8. LP and VLP average epicentres on the DEM of Mt. Etna during 2010-2011. The clusters of events are determined by 3-day moving averaging the source parameters (latitude and longitude) during all periods of interest. The red diamonds indicate the station positions used for the localization. In the upper right-hand of the diagram, the legend refers to the type of event represented: blue for LP events; red for VLP events.

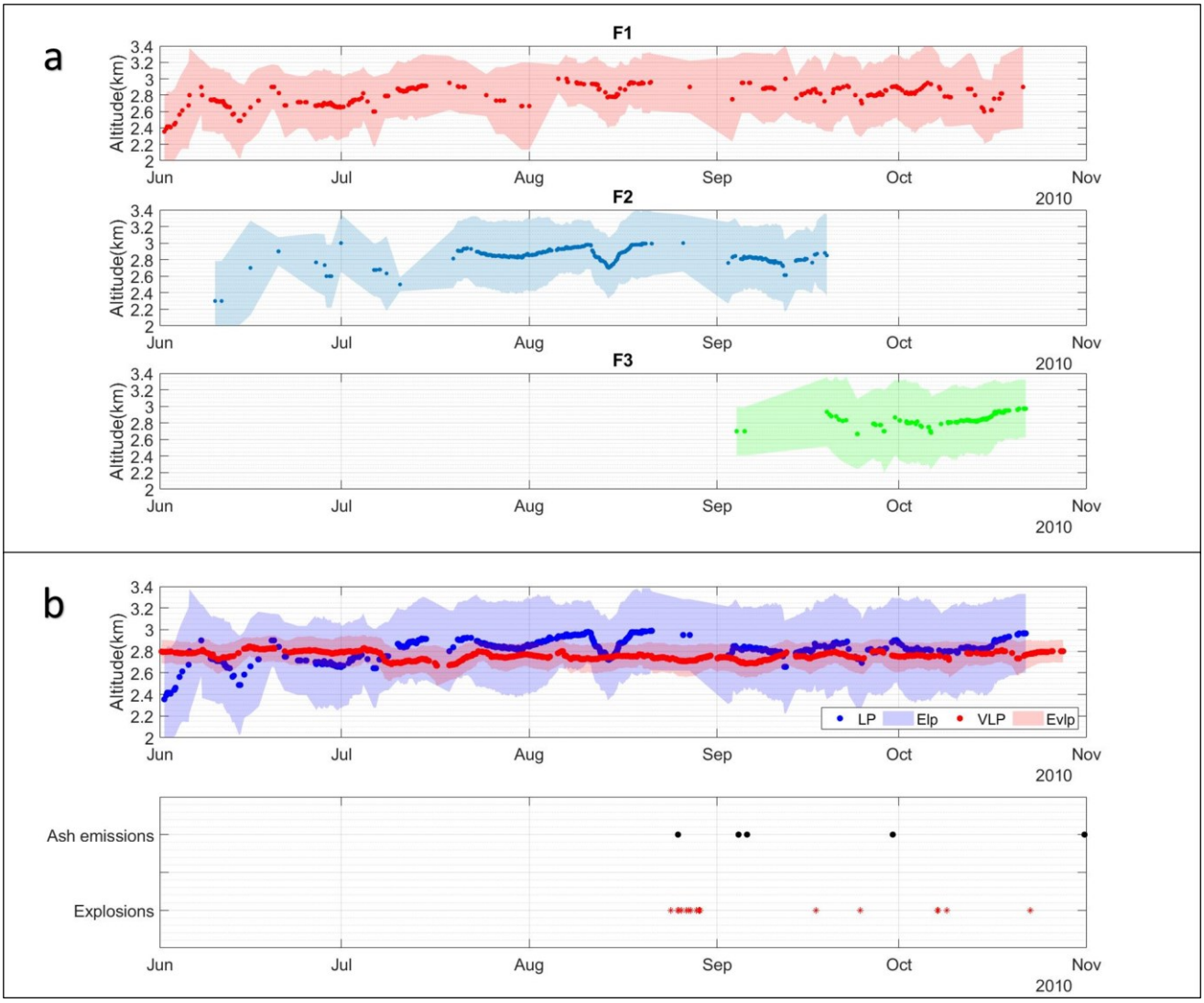

Figure 3.9. Temporal variation of LP and VLP localization related to the volcanic activity in 2010. a) 3-days moving average of source locations altitude (km a.s.l.) and corresponding errors of different LP families. The title refers to the type of family (F1, F2 and F3). For each diagram, the coloured bands indicate the average errors of localization. b) 3-days moving average of source locations altitude (km a.s.l.) and corresponding errors of LP (blue) and VLP (red) events (upper panel) and time distribution of the main volcanic events observed at BN crater (lower panel; data from Andronico at al., 2013). In the right-hand of the upper diagram, the legend refers to the type of events displayed, while the coloured bands indicate the average errors of localization.

As mentioned before, in order to obtain further information about the source locations during 2010, we determined the kinematic properties of the LP/VLP wavefield trying to identify important relationships between the seismic and the volcanic activity. In this case, we performed the ZLCC method on the same analysis windows and frequencies used for the previous localizations, selecting only those kinematic properties for which the cross correlation coefficient is greater than 0.75. The results of array analysis for these events are

illustrated in figures 3.10 and 3.11. In terms of back azimuth and ray parameter, we did not observe any significant difference between LPs and VLPs or among the LP families. In fact, the back azimuths were stably focused on the N340°E-N350°E (Fig. 3.10a), corresponding to arrival directions from BN crater. The ray parameter ranged mainly in the 0.6-0.8 s/km interval (Fig.3.10b), corresponding with 1.25 and 1.66 km/s in terms of apparent velocity. The major temporal differences were observed in the incidence angles, calculated considering a wave velocity of 1.6 km/s (Fig. 3.11). In general, for both types of events, the incidence angles were very shallow, clustering between 70° and 80°, although those of VLP sometimes showed values slightly smaller (3.10b). In this case, for both LPs and VLPs, the incidence values gradually increased reaching the highest values with the development of explosion activity at BN crater. However, unlike before, they became deeper in the last part of the explosive sequence. This can be mainly observed in the temporal distributions associated with the LP families (Fig. 3.11a). In fact, while the first and the second families described temporal trends of incidence very similar to those shown previously, the third one was characterized by the deepest incidence angles among the families.

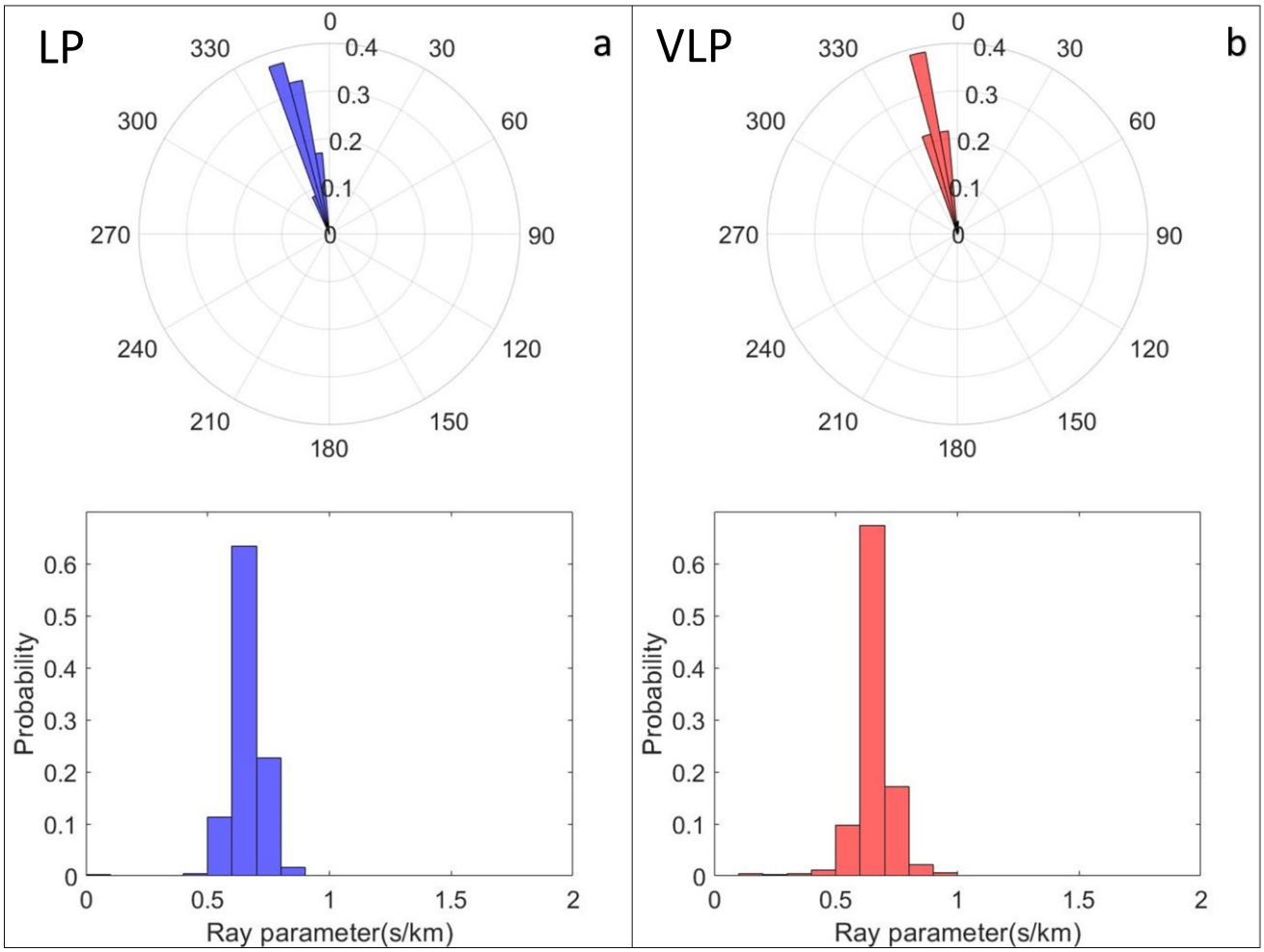

Figure 3.10. Statistic overview of LP (a) and VLP (b) kinematic properties during 2010. The upper diagrams are polar the histograms of back azimuth (bin=5°), while the lower ones are the histograms of ray parameter (bin=0.1 s/km).

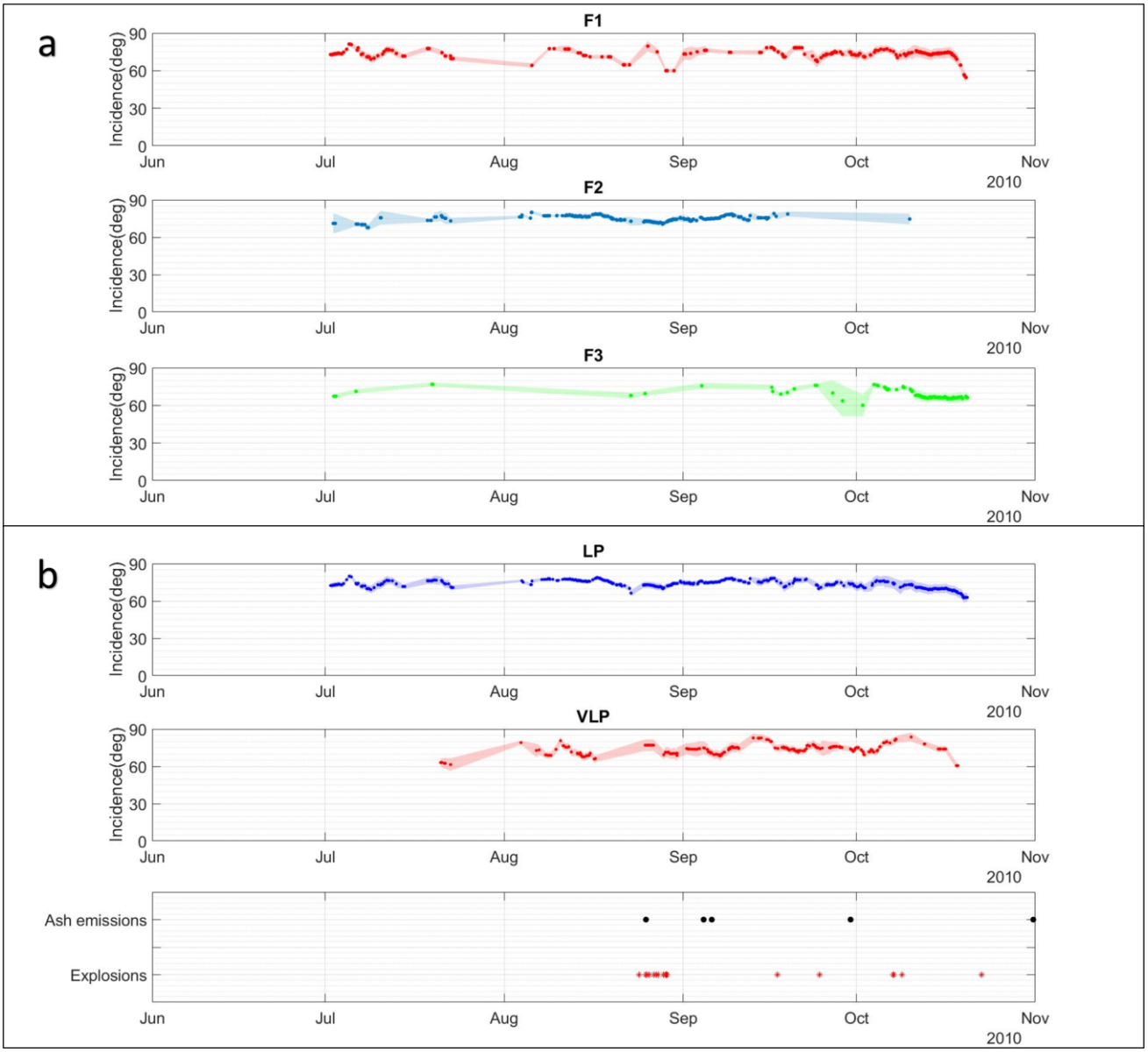

Figure 3.11. Temporal variation of LP and VLP kinematic properties related to the volcanic activity in 2010. a) 3-days moving average of incidence angles and errors of different LP families. The title refers to the type of family (F1, F2 and F3). For each diagram, the coloured bands indicate the average errors of analysis. b) 3-days moving average of incidence angles and errors of LP (upper panel) and VLP (central panel) events and time distribution of the main volcanic events observed at BN crater (lower panel; data from Andronico at al., 2013). For the upper and central diagrams, the coloured bands indicate the average errors of analysis.

Considering the results obtained for 2011 interval through Semblance and Radial Semblance methods, the source parameters of LPs and VLPs were more unstable than those of 2010. It was not possible to retrieve a sufficient number of reliable source parameters for the definition of their temporal evolution. In this case, we used the seismic array data for evaluating variations of LP/VLP wave field in occurrence of the changes of the volcanic

activity. The ZLCC method was performed by using the same input parameters set in the 2010 experiment, selecting only results that shown coherent wavefield (cross correlation coefficient greater than 0.75). The results thus obtained are showed in figures 3.12 and 3.13. During the 2011 summertime, we did not observe any significant difference among the kinematic properties of LP families and VLP events. In general, back azimuth values were stationary in time, ranging in the N330°E-N340°E and N345°E-N355°E intervals for LPs and VLPs, respectively (Fig 3.12a). However, all angles corresponded to those directions pointing approximately toward the area of BN crater. As for the previous experiment, most of ray parameters values were clustered between 0.6 and 0.8 s/km, although, in this case, the contribution of slower apparent velocities was more evident (Fig. 3.11b). The incidence angles rather were more affected by the changes in the volcanic activity (Fig. 3.13). Generally, for both types of events, incidence angles ranged between 50° and 80°, although VLPs were more focused on deeper values than LP ones. Considering that the number of events reduced as quickly as the intensification of paroxysmal activity, we did not observe coherent kinematic properties during the lava fountaining episodes. However, in the case of LPs (Fig. 3.13a), it was possible to note how the incidence angles gradually increased at the onset of reactivation of the paroxysmal phase of each episode, clustering around 80 °. When the volcanic phenomena disappeared, the number of stable parameters increased, showing incidence angles progressively returning to those values exhibited during quiescent periods of volcano (around 60°). For the VLPs (Fig. 3.13b), the evolution of incidence angles were more difficult to evaluate, because of the minor number of coherent and stable results. However, the incidence values were apparently stationary during the period of interest.

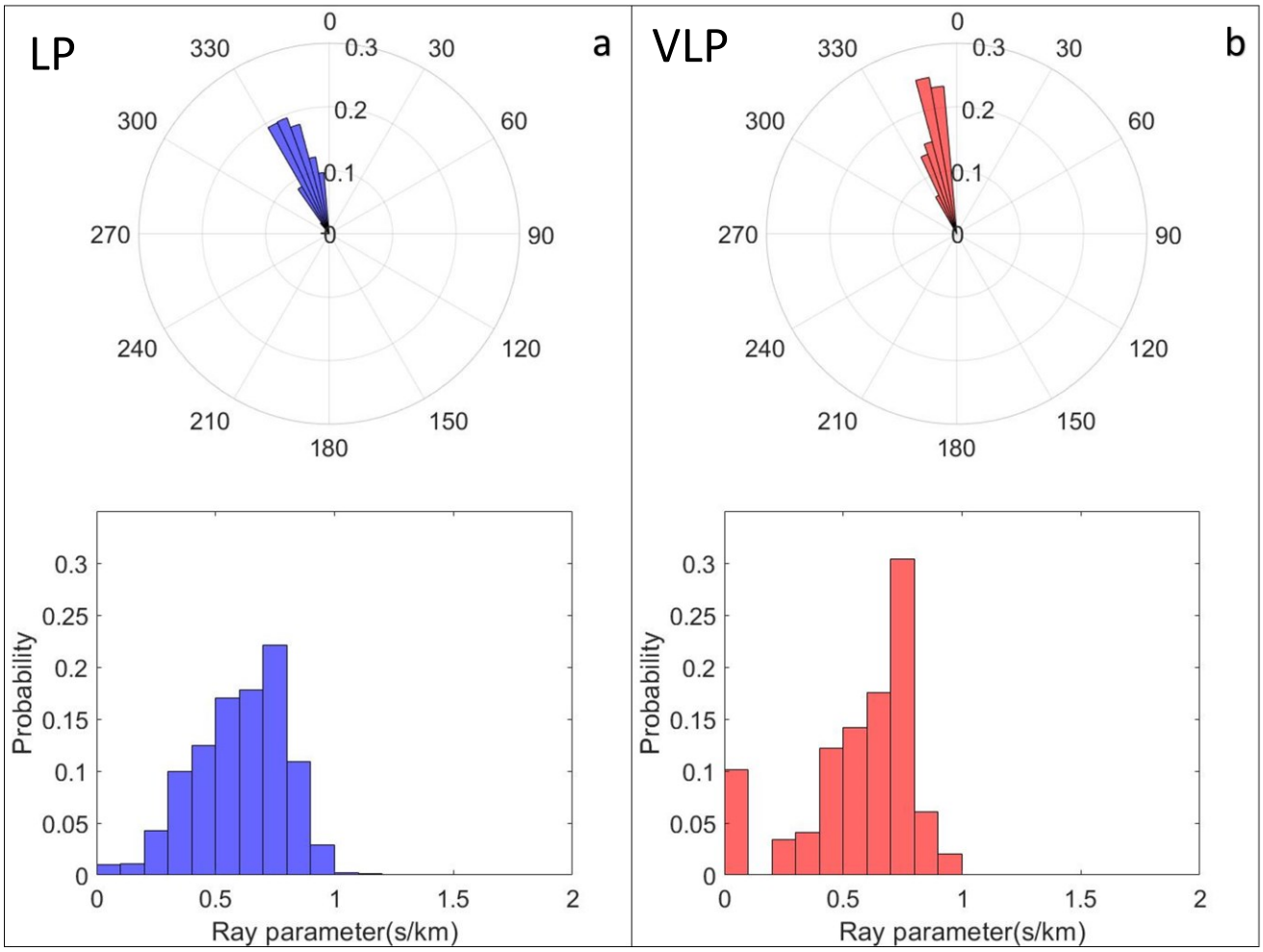

Figure 3.12. Statistic overview of LP (a) and VLP (b) kinematic properties during 2011. The upper diagrams are polar the histograms of back azimuth (bin=5°), while the lower ones are the histograms of ray parameter (bin=0.1 s/km).

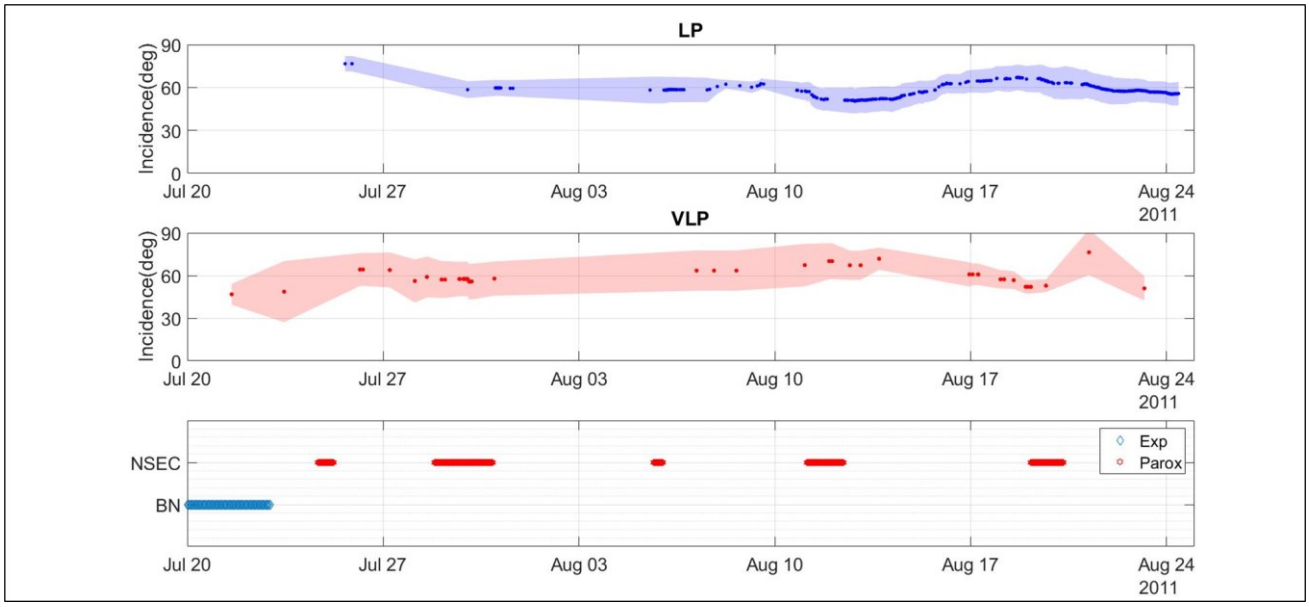

Figure 3.13. Temporal variation of LP and VLP kinematic properties related to the volcanic activity in 2011. 3-days moving average of incidence angles and errors of LP (upper panel) and VLP (central panel) events and time distribution of the main volcanic events observed at NSEC and BN crater (lower panel). For the upper and central diagrams, the coloured bands indicate the average errors of analysis. The legend on the upper right-hand of these panels shows the type of volcanic event: Exp= single explosions or series of minor explosions, minor and/or intense ash emissions; Parox= Strombolian, lava effusion and lava fountaining activity (data from Behncke et al., 2014).

In order to analyze the performance of the Semblance and Radial Semblance method, we generated synthetic LP and VLP seismograms for the same sparse network used in the previous analyses. Assuming that the network was embedded in an infinite homogeneous medium with constant velocity (1.6 km/s), we considered an isotropic source with source time function given by (Almendros and Chouet, 2003):

$$u(t) = A\left(\frac{t}{t_0}\right)^n \exp\left(-\frac{t}{t_0}\right)\sin(2\pi f t) \tag{3.0}$$

with A=2.2 and 0.22 μm/sec, n=3 and 4, t_0=0.3 and 6 s and f=1 and 0.05 Hz for LP and VLP, respectively. The source signals had spindle-shaped envelopes and they consisted of a few monochromatic oscillations, mimicking the LP and VLP events observed previously at Etna volcano (see section 2.3.3, Chapter 2). LP amplitude at the considered stations was calculated on the basis of the distance source-receiver (r), by using the following equation (Battaglia et al., 2005):

$$U_i(f,r) = U_0(f) r_i^{-b} e^{-\frac{\pi r_i f}{Qv}}$$

(3.1)

where U_i is the amplitude measured at the *i-th* station, U_0 is the amplitude at the source, f is the frequency, v is the velocity of the waves, b is the exponent, which takes values of 0.5 or 1 for the cases of surface and body waves, respectively, and Q is the ray-path-averaged quality factor. We assumed the propagation of only P waves, generating the LP seismograms by fixing the values of b, Q and f at 1, 40 and 1 Hz, respectively. Instead, assuming radial propagation away from an isolated isotropic source, we expressed the three-component VLP seismograms as (Almendros and Chouet, 2003):

$$U_i^k(t) = u(t - t_i) \frac{r^k - r_i^k}{|\vec{r} - \vec{r_i}|} \frac{D^2}{|\vec{r} - \vec{r_i}|^2}$$

(3.1)

where k=1, 2, 3 is an index representing the east, north and vertical directions, respectively, $\vec{r}$ and $\vec{r_i}$ are the positions of the source and *i*-th receiver in the network, D is the distance between the source and the closest receiver.

To better understand the capabilities and the limitations of the Semblance, Radial Semblance and JackKnife methods, firstly, we generated 300 LP and 300 VLP synthetic seismograms from isotropic sources uniformly distributed in a volume 5x5x0.5 km (E-W, N-S and vertical directions) centred on the BN crater with a vertical extent from 2.5 km a.s.l. to the top of the Etna volcano. Considering the same procedures performed in the previously analyses, we relocated these events trying to define the region in which the source events were clustered. The results of the synthetic tests are shown in the figures 3.14 and 3.15. In both cases, the methods allowed to locate the events with good resolution and errors of analysis. The average centroids of LP and VLP clusters matched the theoretical source position of the synthetic signals, showing errors of analysis with magnitude on the order of hundreds of meters. The Semblance method was more affected by the altitude of source locations, losing resolution and showing the highest analysis errors (about 300 m) along the vertical direction of the semblance distribution. The Radial Semblance method rather was more sensitive to latitude and longitude source coordinates, obtaining a semblance distribution much widespread on horizontal directions. The errors of localization coordinates were very similar among them, focusing around 100 m. Considering also the volume whose semblance values were higher than 90 % of the

absolute maximum, the two methods were characterized by different spatial resolutions. In the case of LP localizations, the probability source region consisted of 0.2x0.2x2.5 km volume (E-W, N-S and vertical directions) centred on the average source position of the events. Instead for VLP ones, it was confined in a 1x1x1.5 km (E-W, N-S and vertical directions) 3D distribution. However, in both cases, the results were compatible with the theoretical volume of sources generated during the tests.

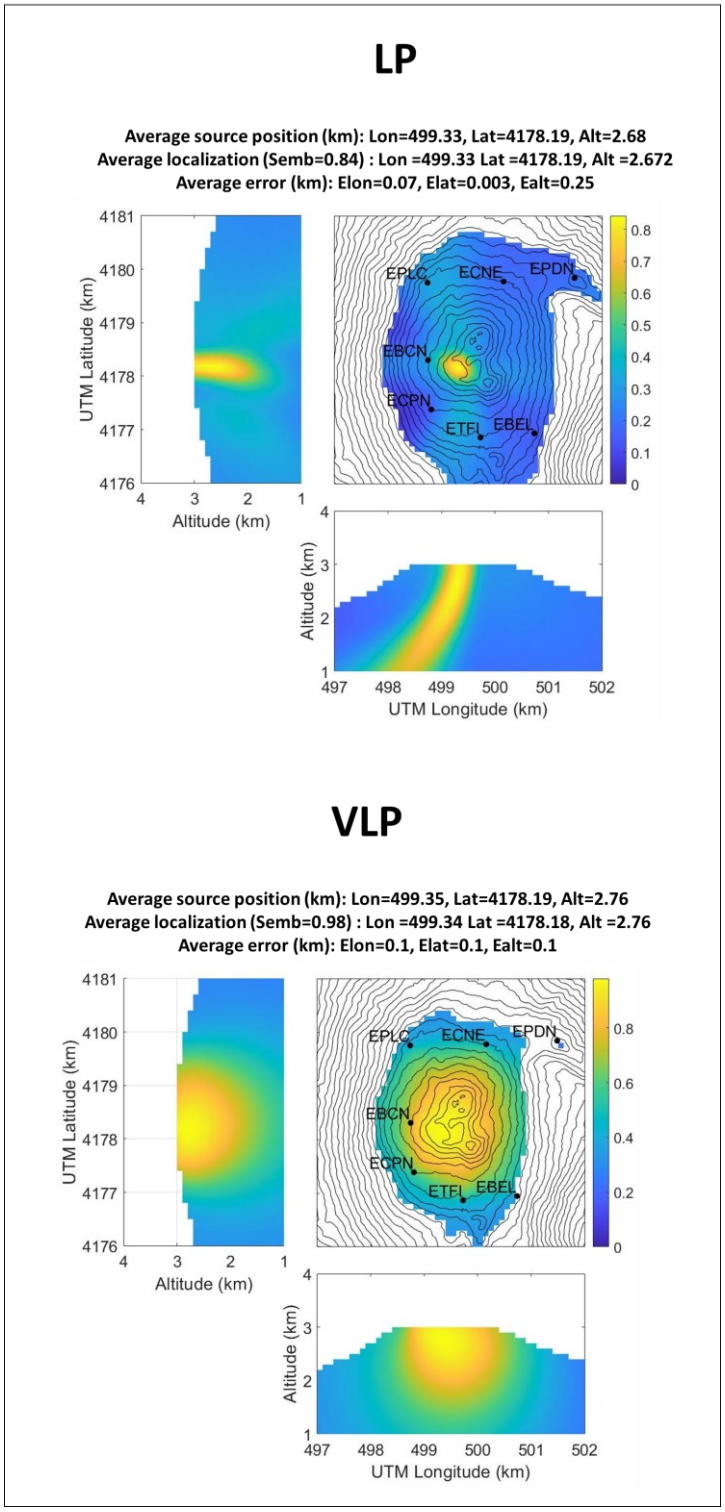

Figure 3.14. Localizations of synthetic signals generated by uniform distributions of artificial isotropic sources of 300 LPs and 300 VLPs. Three sections of Semblance and Radial Semblance grids passing through the node with the highest value. The titles on the top indicate the average position of the synthetic events and that calculated by using Semblance or Radial Semblance and the analysis errors expressed in kilometres. The colorbars on the right-side refer to the normalized values of the Semblance/ Radial Semblance. The black marks represent the station locations.

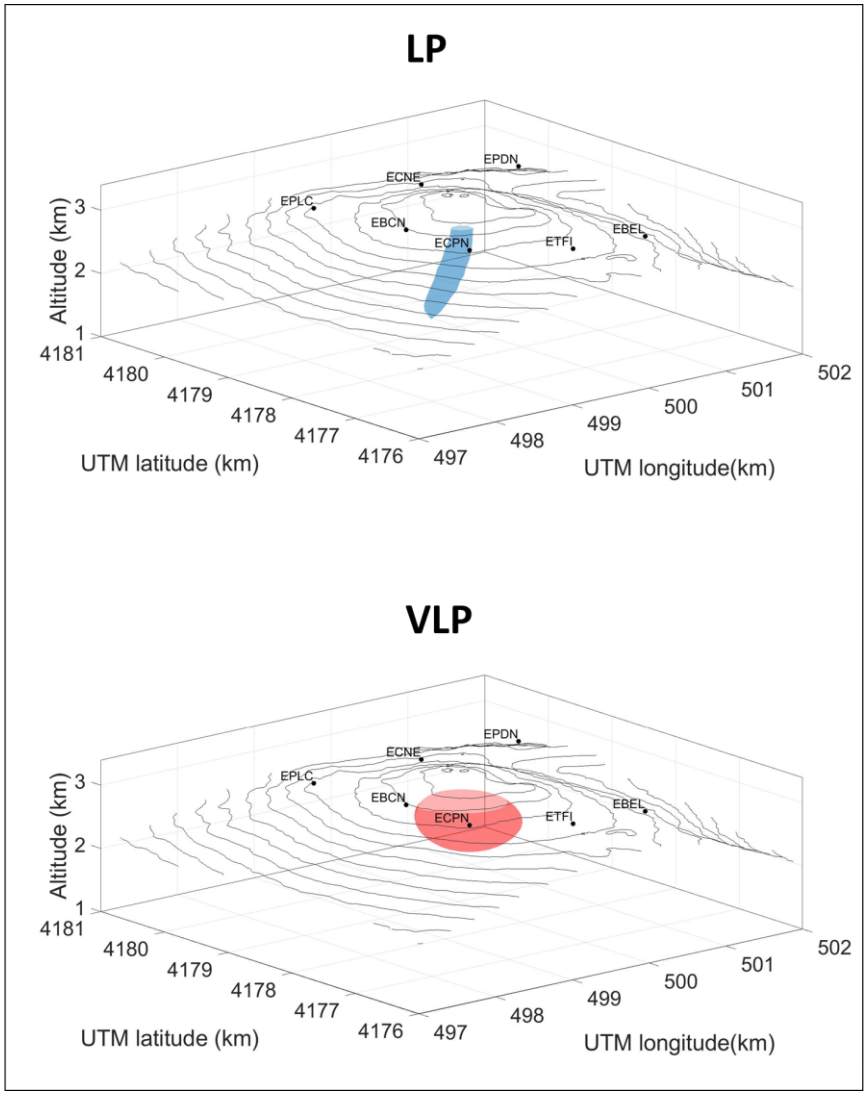

Figure 3.15. Probability source regions (red volumes) calculated on the basis of the results shown in figure 3.14. The results consist of the 10% Semblance/Radial Semblance distributions around the largest solutions. The black marks indicate the station positions.

Successively, we fixed the source location of the synthetic LP and VLP events in the summit area at different depths (1.0, 1.5, 2.0, 2.5 and 3.0 km a.s.l.) by using the same parameters set in the previous test for the event generation. Therefore, we located the source of the synthetic LP and VLP events by using Semblance and Radial Semblance methods, respectively, using different velocity values (Figs. 3.16 and 3.17). By plotting the highest semblance/radial semblance value versus the velocity value, we observed similar trends, that consisted of bell shapes reaching the maximum value in correspondence of the fixed P velocity. The results obtained by the Radial Semblance (Fig. 3.17) method were very reliable and steady. In fact, the Radial Semblance method was less affected by the wave

velocity and the location errors. Instead, the Semblance method (Fig. 3.16) was more affected by the P waves velocity in terms of both semblance value and errors of analysis. However, in both methods, the minimum value of errors, and then the best location of the source, was obtained when we used the velocity value characterised by the maximum semblance/radial semblance value.

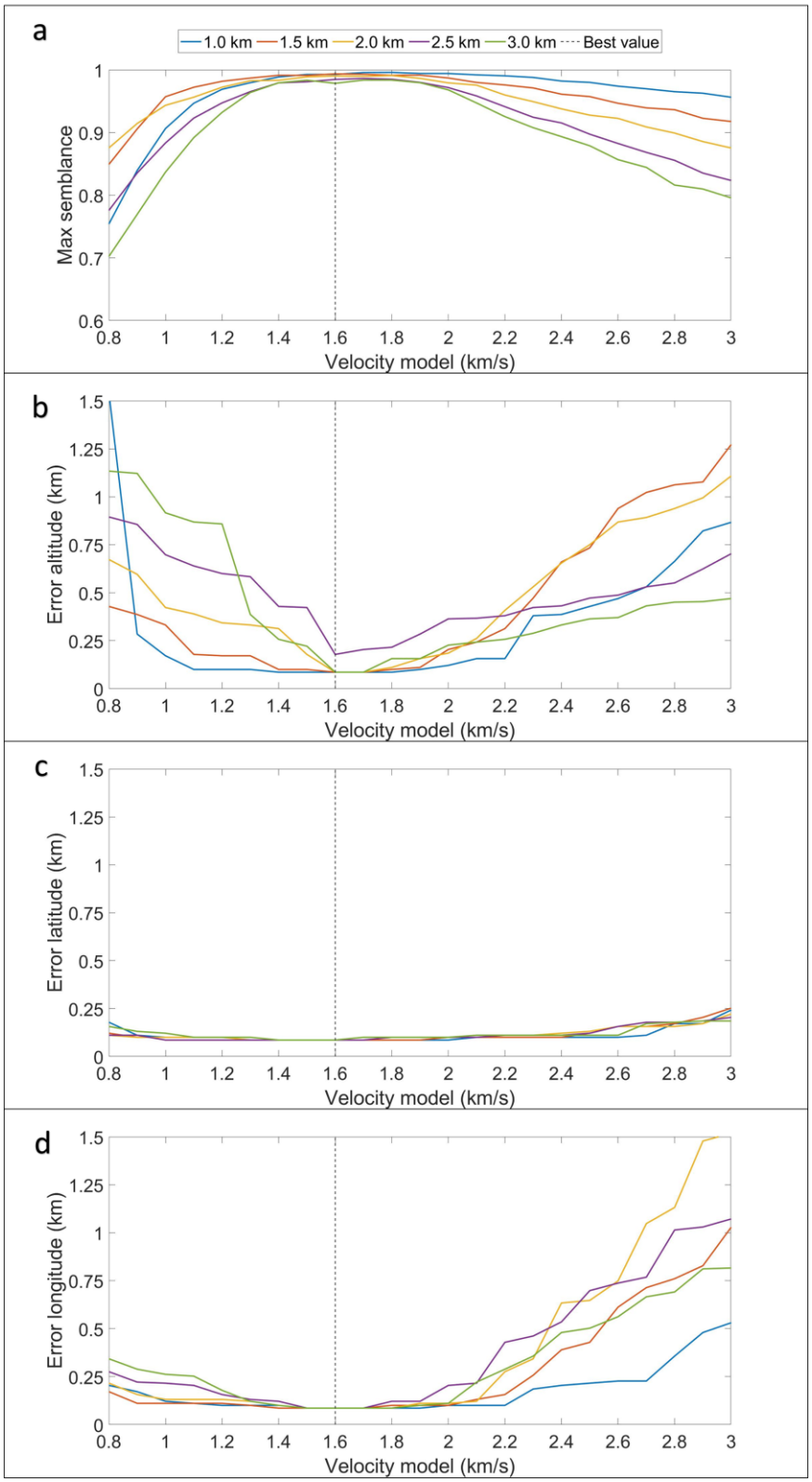

Figure 3.16. Maximum semblance value (a) and (b, c, d) errors of analysis versus the velocity model used to locate the source. The legend on the top of the diagram (a) indicates the best velocity value for source location (dashed black line) and the results obtained by fixing five different source depths (1.0, 1.5, 2.0, 2.5 and 3.0 km a.s.l).

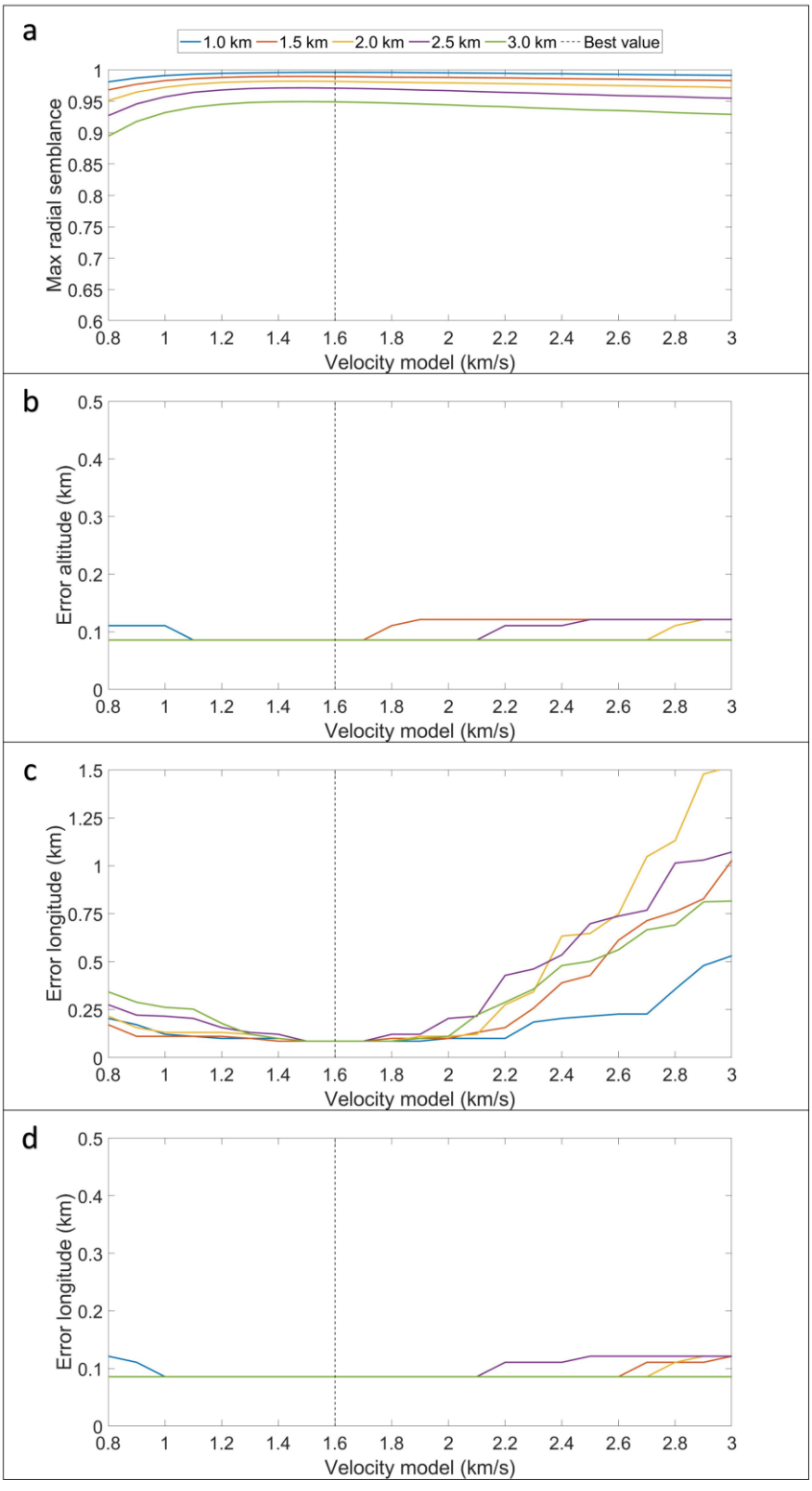

Figure 3.17. Maximum radial semblance value (a) and (b, c, d) errors of analysis versus the velocity model used to locate the source. The legend on the top of the diagram (a) indicates the best velocity value for source location (dashed black line) and the results obtained by fixing five different source depths (1.0, 1.5, 2.0, 2.5 and 3.0 km a.s.l).

3.3 DISCUSSION AND CONCLUSIONS

As shown in the previous chapter, the study of volcanic tremor and LP and VLP events, occurring at Mt. Etna between 2010 and 2011, has evidenced periods characterised by steadiness of the features of signals, alternating with important time variations. The investigation of the time variability of the source position of these seismo-volcanic signals allowed to obtain further information about the magma transport leading to volcanic phenomena such as paroxysms or sequences of explosions. For this type of study, we used data recorded by the two seismic arrays deployed nearby the summit area of the volcano, integrated with data acquired by the INGV seismic permanent network (see Chapter 2, section 2.2). For the localization analysis, we used different array methods on the basis of data availability and the features of signals described in the Chapter 2.

In order to retrieve information about the tremor source position during 2010-2011, two different methods were performed:

(i) ZLCC (Frankel et al., 1991), to track variations in the kinematics properties (back azimuth, ray parameter and incidence angle) of the tremor wavefield at the same time as the changes in the eruptive activity.

(ii) JackKnife method (Efron, 1982), to quantify the uncertainty of the results.

Considering the results illustrated in the section 3.2, the kinematic properties of volcanic tremor were compatible with shallow seismic sources that mainly radiated a complex wavefield composed by volume and surface waves.

During 2010, these properties were stationary in time, without showing any significant changes concurrently the increase of RMS amplitude (Fig. 3.1c) or the intensification of explosive activity at BN crater (Fig. 3.1d). Most of back azimuths pointed toward the east slope of SEC (Figs. 3.1a and 3.2a), with shallow incidence angles (Fig. 3.2c). The ray parameters values (Figs. 3.1b and 3.2b) corresponded to apparent velocities compatible with the propagation of body waves. In addition, comparing the polarization attributes, shown in the previous chapter, with those retrieved from array processing, the tremor wavefield was mainly composed by P waves. In fact, the polarization back azimuth and incidence angle values (Figs. 2.11, 2.12, 2.13 and 2.17, section 2.3.2) were quasi-consistent with the time series of the slowness analysis, showing high grade of rectilinearity. The qualitative analysis of the particle motions (Fig. 2.19, section 2.3.2) revealed also the irradiation of Rayleigh waves related to the lowest values of rectilinearity and the highest values of ray parameters. Moreover, considering the equation 1.3 (Chapter 1, section 1.3.1),

it was possible to estimate approximately the waves velocity beneath the array by using the polarization incidence angles calculated at seismic permanent station ETFI and the ray parameter values obtained from ZLCC analysis in the same analysis windows. In this case, a value of velocity of about 1.6 km/s could be considered reliable to compute the incidence angles associated to tremor source.

Unlike 2010, the kinematic properties of tremor wavefield changed during the 2011 summertime at the same time as the variation in the eruptive activity (Figs. 3.3 and 3.4). During the quiescent periods of volcano, the back azimuth corresponded to directions pointing toward the BN crater (Figs. 3.3a and 3.4a), with deep incidence angles (Fig. 3.4c) and ray parameters values consistent with the propagation velocity of body waves (Figs 3.3b and 3.4b). With the intensification of eruptive activity (Fig. 3.3d), 4-5 hours before the onset of Strombolian activity, the back azimuths "migrated" pointing toward the NSEC for the whole duration of the paroxysmal episode; the incidence angles became progressively shallower and the ray parameters highlighted seismic wave velocities typical of both volume and surface waves. At the end of the episode, these parameters gradually returned to those values exhibited before the onset of eruptive activity (Figs. 3.3 and 3.4). Taking into account the results described in the Chapter 2, these parameters were well correlated with the spectral (Fig. 2.6a, section 2.3.2), amplitude (Fig. 2.10a, section 2.3.2) and polarization (Figs. 2.14, 2.15, 2.16 and 2.18, section 2.3.2) changes of tremor wavefield. In addition, comparing these kinematic parameters with those retrieved from polarization and particle motion analysis (Figs. 2.18 and 2.20, section 2.3.2), the tremor wavefield was mainly dominated by both P and Rayleigh waves, especially during the lava fountaining activity. Also in this case, following the same procedure explained in the previous paragraph, a value of 1.6 km/s could be considered reliable to evaluate the variations of incidence angles.

As also illustrated in the previous chapter, the important variations of volcanic tremor in 2010-2011 consisted in spectral and wavefield changes, most of which occurred at the same time as changes of source location and eruptive activity. Even if we have not always identified significant changes of the source location or polarization attributes (for example during 2010), spectral and wavefield variations could be attributed to changes in source features, and in particular to the resonant phenomena of a fluid-filled crack (e.g. Chouet et al., 1996a; Morrissey and Chouet, 2001; De Barros et al., 2011; Davi et al., 2012), due to the relationship among spectral features of volcanic tremor, size of the resonant structure and the physical properties of the magmatic fluid. This type of resonating structure could

also explain the irradiation of P waves (e.g. Chouet, 1988; Hagerty et al., 2000), while the observation of elliptical particle motion could be related to path effects. In fact, the body waves could interact with the topographic and structural complexities affecting the Mt. Etna edifice, generating surface waves such as Rayleigh waves (e.g. Ohminato and Chouet, 1997; Ripperger et al., 2003). Taking into account that the tremor source was tracked in the shallower portion of the volcano, our data support this hypothesis.

These data were compatible with those retrieved in some studies in which localization methods different from array techniques were used, such as the spatial amplitude distribution-based one (Battaglia et al., 2005). In fact, assuming epicentral distances of 1.5-2.5 km from array location to summit area of volcano, for incidence angles of 60-90° (Figs 3.2c, 3.4c) the tremor source was placed at 1.0-3.0 km a.s.l. According to studies of some authors (e.g. Andronico et al., 2013; Patanè et al., 2013), from June to November 2010, volcanic tremor sources were mainly located East of the summit area at altitude 1.5–2.0 km a.s.l., roughly below the fissure of the 2008–2009 eruption. Concerning the paroxysmal activity observed during 2011, important and short-lived changes, time related to the lava fountaining episodes, were identified (e.g. Patané et al., 2013; Cannata et al., 2013; Viccaro et al., 2014; Moschella et al., 2018). As shown by these authors, the volcanic tremor source was fairly stable at 1.0–2.0 km a.s.l. below NEC, while, during such paroxysmal episodes, the tremor sources migrated toward NSEC at shallow depths (roughly 3 km a.s.l.). Similar changes in the source location were also observed during other periods of eruptive activity of Mt. Etna (e.g. Privitera et al., 2003; Patané et al., 2008; Cannata et al., 2015; Spampinato et al., 2015).

About the source position of volcanic tremor during 2010-2011, further insights could be obtained by highlighting the limits of the methods used for the slowness analysis. As mentioned in the previous paragraphs, we were able to track a tremor source, fairly stable during 2010 but affected by a phenomenon of migration during 2011. However, techniques such as ZLCC are not reliable to resolve multiple simultaneous sources sharing the same frequency content (e.g. Frankel et al., 1991; Saccorotti and Del Pezzo, 2000; Saccorotti et al., 2004). Therefore, we could make two hypotheses: (*i*) the observed wavefield was generated by the combination of multiple seismic sources, sharing similar frequency content but different source locations and energy values (e.g. Almendros et al., 2014); (*ii*) the tremor wavefield was the results of vertical and lateral migration of one seismic source (e.g. Eibl et al., 2017a,b). Considering also the source investigation of the infrasonic signals at Mt. Etna (e.g. Ripepe et al., 2001; Sciotto et al., 2013; Diaz-Moreno et al., 2019), the

first hypothesis could be more plausible. However, our data do not allow us to exclude any of these hypotheses. Another important aspect consisted of the resolution and accuracy of the results. As shown in the previous chapter, both window and frequency band of the analysis were chosen to obtain a tremor wavefield as coherent as possible. In addition, we filtered the results selecting only those back azimuth and ray parameter values showing average cross correlation coefficient greater than 0.75. In this way, we were able to obtain reliable values of these properties, as also confirmed by the error of analysis (Figs. 3.2d,e,f and 3.4d,e,f). However, it was not possible to obtain further information about the source position for two reasons. The first one was related to the deployment of only one single array, preventing of maximizing the azimuthal and incidence coverage of the summit area of Mt. Etna (e.g. Saccorotti et al., 2004; Di Lieto et al., 2007; Inza et al., 2014). The second one depended on the absence of a detailed velocity model of the shallower portion of volcano (e.g. Patané et al., 2013; Cauchy and Saccorotti, 2013; Zuccarello et al., 2016). In fact, as explained previously, the incidence angles were computed by assuming that tremor wavefield propagated in a homogenous medium with constant velocity. Therefore, these estimates did not provide the real angle of incidence of the waves impinging at array, but only a qualitative evaluation of the source position. In addition, the propagation of elastic waves through the complex volcanic terrain is severely conditioned by complications associated to the medium heterogeneity and the rough topography, as already observed in some recent studies (e.g. Almendros et al., 2001a,b; 2002; Saccorotti et al., 2001a,b; Ripperger et al., 2003). Even if the JackKnife method allowed to improve the stability of the results compared to other localization methods (e.g. Di Grazia et al., 2009; Cannata et al., 2013; Moschella et al., 2018), it did not separate the source and path effects, but it allowed to reduce the bias when extreme scores are present in the dataset and/or the statistical distribution of the underlying population is unknown (Efron, 1982).

Concerning the source location of LP and VLP events during 2010-2011, four different methods were applied:

(i) Semblance (Neidell and Taner,1971), to define the LP source region and to track variations in source location time-related to the changes in the eruptive activity.

(ii) Radial Semblance (Almendros and Chouet, 2003), to evaluate the source location of VLPs and their temporal and spatial evolution concurrently the variations in the volcanic activity.

(iii) ZLCC (Frankel et al., 1991), to determine the kinematic properties of the LP and VLP events, compared with the source location retrieved through the methods (*i*) and (*ii*), respectively.

(iv) JackKnife method (Efron, 1982), to quantify the uncertainty of the results obtained through the previous methods.

Taking into account the results obtained in the previous section, LP and VLP events shared the same source region (Figs. 3.5, 3.6 and 3.7) both in 2010 and 2011, fairly stable at 2.0–3.0 km a.s.l. below BN crater. Averagely, the VLPs were slightly deeper than LPs (Tab. 6), although the LP cluster was broader and affected by greater errors. Focusing on the temporal changes of the altitude of seismic sources, LP events shallowed as the same time as the intensification of eruptive activity, moving averagely from 2.4 km a.s.l. to 3.0 km a.s.l. (Figs. 3.9). This was also observed through the migration of incidence angles during 2010 (Fig. 3.11) and 2011 (Fig. 3.13). Instead, during 2010, the VLPs were very stationary in time and were clustered around 2.8 km a.s.l. (Fig. 3.9), although the slowness analysis has highlighted changes in the time series of incidence angle concurrently with the increase of the frequency of the explosive events at BN crater (Fig. 3.11); during 2011, the behaviour of these events was very similar to LPs, although the reduced number of detected VLPs did not provide a clear temporal pattern (Fig. 3.13). Considering the polarization attributes obtained in the previous chapter (Figs. 2.22 and 2.27), the polarization incidence angles were more compatible with those retrieved through slowness analysis (Figs. 3.11 and 3.13); the back azimuth and rectilinearity values suggested the propagation of both P and SH waves for LPs, especially during the lava fountaining activity (Figs. 2.25 and 2.29), and the irradiation of only P waves for VLPs (Figs. 2.26 and 2.30). Concerning the families of LP events, we did not observe any significant difference in the source location, except during 2010 (Figs. 3.9 and 3.11). In this case, the third family of events, that "appeared" concurrently with the eruptive activity at BN crater, was slightly shallower than the first one, especially during the first part of explosive sequence. In addition, following the same procedure used for the volcanic tremor, a velocity value of 1.6 km/s could be reliable to perform the Semblance/Radial Semblance methods and/or the calculation of incidence angles.

Taking in account the features of LP and VLP events (section 2.3.2, Chapter 2), variations of wavefield properties suggested a change in the source position, as well as illustrated in this chapter. On the basis of these results, LP could be attributed to a resonant fluid-filled crack (Aki et al., 1977; Chouet, 1996a, 2003; Neuberg and Pointer, 2000; Nakano et al.,

2003; Jousset et al., 2003). At Mt. Etna, similar observations are shown in different studies, some of which based on the waveform inversion (e.g. Lokmer et al., 2007; De Barros et al., 2009, 2011). In addition, our results were compatible with other investigations about the seismo-volcanic activity observed during 2010-2011 (e.g. Andronico et al., 2013; Patanè et al., 2013; Cannata et al., 2013), in terms both source location and error of analysis. This type of source mechanism could also explain the irradiation of P and SH waves (e.g. Chouet, 1988; Hagerty et al., 2000), although the propagation of SH waves could be reacted to path effects (e.g. Aki and Richards, 1980; Ohminato and Chouet, 1997; Ripperger et al., 2003). However, our data did not allow to exclude other possible types of mechanisms (e.g. Bean et al., 2014; Cauchy et al., 2015). Concerning the VLP events, the source mechanisms could be related to those of LPs. For example, Saccorotti et al. (2007) recognized a correlation between LP and VLP signals. They argued that the source trigger of the deeper VLP events was relied to mass transfer. The subsequent mass injection in overlying cavities could have driven the pressurization of a reservoir filled of hydrothermal fluids, thus triggering the LP resonance. A similar interpretation was given by Cannata et al. (2009a) who found slightly different locations for the shallow LP and the deeper VLP events. They suggested that two different interconnected sources could explain this difference. In their model, slow movements of fluids between connected cracks could have driven pressure transients in a shallower dyke. They supported their hypothesis by the fact that the onset of the VLP events preceded slightly the LP record. Considering our results, one of these hypotheses could be plausible. Concerning the differences between the first and the third family of LPs during 2010, we were not able to identify a mechanism explaining their different waveform, due to similar source location and temporal pattern. At Mt. Etna, similar LP features were observed in the last decades (e.g. Falsaperla et al., 2002; Patanè et al., 2008; De Barros et al.., 2009, 2011, O'Brein et al., 2011). In particular, De Barros et al. (2011) performed Moment Tensor inversion (MT) identifying two different interconnected source mechanisms. In their model they hypothesized that two orthogonal cracks located below the summit could be excited by the injection of gas coming from the main conduit. They supposed that the summit degassing and the flank lava flow drained the cone, producing a decrease of pressure and a consequent destabilization of those fractures. However, these authors were not able to determine if MT inversion results were real or due to artifacts in the moment tensor inversion. Therefore, we did not exclude that this hypothesis could be wrong.

Other information about LP and VLP source location could be retrieved by limitations of localization methods. Concerning the slowness analysis, the limits of ZLCC analysis and

JackKnife method were the same as those discussed before for the volcanic tremor. The results of Semblance or Radial Semblance depended on different factors (Neidell and Taner,1971; Almendros and Chouet, 2003): (*i*) window length, (*ii*) noise contributions, (*iii*) configuration of network, (*iv)* velocity of the medium, (*v*) grid spacing. In our analyses, we set the parameters trying to minimize as much as possible these effects, trying to obtain the best trade-off between maximum semblance and stability. From our synthetic test (Figs. 3.14, 3.15, 3.16 and 3.17), Semblance approach was more sensitive to velocity of medium and relationship between configuration network and source position compared to Radial Semblance one. However, as demonstrated by some studies (Kawakatsu et al., 2000; Almendros and Chouet, 2003), Radial Semblance results are affected by the use of the radial components of the ground motion. In fact, particle motions, even if produced by an isotropic source and recorded by a seismometer located at the surface, may not necessarily point to the source because of the effect of both free surface and complex stratigraphy (Neuberg and Pointer, 2000; Almendros and Chouet, 2003). In order to reduce all these effects on localization, we used only stations at close epicentral distances (Neuberg and Pointer, 2000) and selected only those events characterized by low error of analysis. However, it is worth noting that a major knowledge about the path effects on the signals is needed (e.g. Bean et al., 2008; Kumagai et al., 2010; Trovato et al., 2016; Montesinos et al., 2021).

Finally, comparing the results of volcanic tremor with those of LP and VLP events, we could conclude that:

(i) During 2010, significant variations in the seismo-volcanic signals occurred, with an increasing trend of several parameters such as the RMS amplitude of the volcanic tremor, the amplitudes and frequency of occurrence of LP events. More sustained seismo-volcanic activity has commonly been interpreted as due to pressurization of volcanic plumbing systems, at Etna (e.g. Patanè et al., 2008; Di Grazia et al., 2009; Cannata et al., 2015) and at other volcanoes around the world (e.g. Chouet et al., 1994; Moran et al., 2008; Varley et al., 2010). The explosive sequence of August-September 2010 at the BN crater could be considered as the response to slow but continuous pressurization of the shallower portion of the plumbing system (Andronico et al., 2013; Patané et al., 2013). This hypothesis was particularly corroborated by seismic data of LP and VLP events. In addition, including also volcanic tremor features and source location, these results could be interpreted as precursory to the onset

of a new eruptive phase characterizing Mount Etna's summit craters in 2011 (Andronico et al., 2013; Patané et al., 2013).

(ii) During 2011, seismic data of volcanic tremor and LP and VLP events were used to image the shallower portions of the plumbing system at Mount Etna. As already observed in other studies (e.g. Patanè et al., 2008, 2013; Aiuppa et al. 2010; Cannata et al., 2009a,b, 2013, 2015), volcanic tremor source is associated with the presence of a shallow magma storage zone located below the summit area at 1–2 km a.s.l., cyclically feeding the lava fountain activities at NSEC; LP and VLP sources, placed above this shallow magma storage zone, could be triggered by gas bubbles, feeding surface gas emission; the release of gas bubbles from this magma batch could have triggered the 2011 eruptive events. In addition, these sources were located between the eastern border of a low-velocity zone and the western border of a high-velocity body (Patané et al., 2013) that some authors supposed to represent a path for rising and accumulating magma (e.g. Aloisi et al., 2002; Patanè et al., 2003, 2006, 2013).

3.4 SUGGESTED FUTURE WORK

In order to improve the knowledge about source position and mechanisms of the seismo-volcanic signals recorded at Mt. Etna, future works could be focused on:

(i) Installation of more than one three-component array close to the summit area of volcano, featuring a greater number of sensors. The deployment of many sensors could allow to use methods able to resolve multiple simultaneous sources sharing the same frequency content (e.g. Inza et al., 2014). The simultaneous use of more arrays could improve the azimuthal and incidence coverage of the edifice of the volcano and the constraints about the source position (e.g. Métaxian et al., 2002).

(ii) Evaluation of the influence of the path effects on the seismic signals and localization methods (e.g. Bean et al., 2008; Montesinos et al., 2021). This could improve the accuracy and quality of results, separating as much as possible the source contributes from the others.

(iii) Application of techniques based on waveform inversion (e.g. Lokmer et al., 2007; De Barros et al., 2009, 2011), to obtain more information about source mechanisms of seismo-volcanic signals.

(iv) Investigation of the acoustic signals (e.g. Ripepe et al., 2001; Sciotto et al., 2013; Diaz-Moreno et al., 2019), to obtain further constraints on volcanic processes.

(v) Application of these techniques to a larger dataset containing eruptive episodes such as those observed in this thesis. This could provide more consistent information about short and long-term variations of source locations and mechanisms.

A successful performance of these methods could lead to a better understanding of the source mechanisms of the seismo-volcanic signals. In addition, it could provide a significant improvement in hazard assessment and volcano surveillance.

CHAPTER 4 – CONCLUSIONS

4.1 GENERAL SUMMARY

During 2010-2011, an intense activity at the summit craters of Mt. Etna, characterized by more than 30 minor explosions and 18 episodes of lava fountaining at the NSEC (Andronico et al., 2013; Behncke et al., 2014), was observed. Understanding the dynamics of volcanic activity at Mt. Etna by array analysis of volcanic tremor, LP and VLP events during the considered period was the main goal of the conducted research.

For this purpose, two types of analysis were carried out. A first investigation was based on the analysis of the features of volcanic tremor and LP and VLP events recorded between 2010 and 2011, while a second study was focused on their source location through array methods. The first study was applied to highlight the wavefield properties of volcanic tremor and LP and VLP events (for example, frequency content, amplitude properties and polarization attributes, waveform features), which allow us to describe the dynamics of transport and injection of magma in the plumbing system of Mt. Etna, and to obtain a frequency range of analysis reliable for the array processing. The second study, instead, was applied to determine the source location and the kinematic properties of these seismo-volcanic signals and to obtain more information about the source mechanisms and the dynamics involving interplay between magmatic-hydrothermal fluids and their host rock during eruptive activity. For these studies, we referred to the data acquired during some seismic array experiments performed in the 2010-2011 period, integrated with those recorded by INGV seismic permanent network.

From the results obtained from these studies, we can draw some conclusions. Changes of the wavefield properties and source locations of volcanic tremor, LP and VLP events, at the same time as the evolution of eruptive activity, suggested variations in the physical and chemical condition of magmatic fluids filling the resonant structures inside volcanoes (e.g Chouet et al., 1996a; Saccorotti et al., 2007; Cannata et al., 2009a; Davi et al., 2012; Chouet and Matoza, 2013). During paroxysmal activity, pre-eruptive evidence about the variations of the depressurization and pressurization dynamics of the volcano was given by: (*i*) focusing of the frequency content of volcanic tremor around 1 Hz (e.g. Moschella et al., 2018); (*ii*) gradual and/or abrupt increase of the RMS amplitude of volcanic tremor, LP and VLP event and progressive reduction of the detected number of LP/VLP events due to the decrease of signal-to-noise ratio (e.g. Andronico et al., 2013; Patané et al., 2013); (*iii*) vertical or/and lateral migration of signal sources, moving toward shallowest portion of

plumbing system of the volcano (e.g. Cannata et al., 2013 and references therein); (i*v*) irradiation of P and SH-Rayleigh waves (e.g. Hagerty et al., 2000; Ripperger et al., 2003).

Concerning the volcanic activity of Mt. Etna during 2010-2011, we can draw other considerations. During 2010, the reactivation of the eruptive activity at BN crater, following the long-lasting 2008–2009 flank eruption, could be considered as precursory to the onset of a new eruptive phase characterizing Mount Etna's summit craters in 2011 (Andronico et al., 2013; Patané et al., 2013), and, in particular, as the response to slow but continuous pressurization of the shallower portion of the plumbing system. This could be corroborated by the source location of volcanic tremor and low frequency events, as well as their wavefield properties. During 2011, the lava fountain activity at NSEC was cyclically fed by a shallower magma storage zone located below the summit area at 1–2 km a.s.l.; the release of gas bubbles from this magma batch could have triggered the 2011 eruptive events as illustrated by volcanic tremor and LP and VLP locations (e.g. Patanè et al., 2013; Cannata et al., 2013; Moschella et al., 2018).

Further, another goal of the conducted research consisted of providing a useful and user-friendly tool for the analytical routines at volcanological observatories. In this regard, we developed MISARA (Matlab Interface for the Seismo-acoustic ARary Analysis, see Appendix A), an open source Matlab GUI that supports the visualization, characterization, detection, and localization of different volcano signals. Successfully tested on the seismic data recorded during 2010-2011 period, the software has demonstrated the power of seismic arrays as additional tool for the volcano monitoring and a better understanding of unrest at active volcanoes.

Considering the studies performed in the framework of this PhD thesis, future works could be aimed at reducing the uncertainties and the limits, that characterized the used methods and procedures, as well as at extending the dataset. In particular, the use of more one than one well-arranged three-component arrays, as well as the use of three component array methods, could extend the seismic wavefield investigation, in terms of wavelength, and improve the resolution of wavefield properties and signal source position (e.g. Métaxian et al., 2002; Inza et al., 2014). The quantification of the propagation/site effects on signals could improve the stability and quality of results of analysis (e.g. O'Brein and Bean, 2004; Bean et al., 2008; Cauchie and Saccorotti, 2013; Zuccarello et al., 2016; Montesinos et al., 2021). The application of techniques based on waveform inversion (e.g. Lokmer et al., 2007; De Barros et al., 2009, 2011) could provide more information about source mechanisms. The further implementation of MISARA, for example in terms of real-time

signal processing (e.g. Smith and Bean, 2020) and/or automated algorithms (e.g. Álvarez et al., 2013; Bueno et al., 2019), could reduce time processing of the data and provide a powerful tool for different purposes such as research, volcano monitoring and field surveys. A successful combination of these approaches could lead to a better understanding of the source mechanisms involving seismo-volcanic signals. In addition, it could provide a significant improvement in hazard assessment and volcano surveillance.

In conclusion, the array analysis of volcanic tremor and LP and VLP events allowed to obtain information about the magma dynamics in the plumbing system of Mt. Etna during the 2010-2011 activity. Temporal changes of the features of signals and source location some hours before the onset of the eruptive activity, evidenced through array methods and more, could allow to identify information on the state of Etna volcano in the short term, especially for eruptive episodes such as lava fountaining. The implementation of MISARA could represent an efficient tool for volcano monitoring and research purposes. Therefore, these results could allow the development of strategies able to provide a significant improvement in hazard assessment and/or early warning systems.

APPENDIX A – MISARA

As explained in the section 1.1, volcano seismology and infrasound deal with a large variety of seismo-acoustic signals (see e.g. Mc Nutt et al., 2015). Monitoring these events plays a key role in the surveillance of the volcanic environments and provides important information about magma and hydrothermal dynamics in the plumbing system of a volcano (e.g. Sparks et al., 2012; Chouet and Matoza, 2013; McNutt et al., 2015). One of the major challenges is the investigation of their wavefield properties, especially the determination of the source type and its location. As seen in the previous chapters, it is difficult (sometimes impossible) to apply the classical travel-time inversion methods to data from sparse networks, especially in case of emergent or sustained signals such as LP or VLP events and volcanic tremor. Due to the nature of these signals, other localization methods have been also used in recent years such as amplitude-based techniques (Di Grazia et al., 2006; Cannata et al., 2013; Morioka et al., 2017) or array methods. As attested before, array techniques are frequently used to estimate vertical and lateral migration of volcanic sources for research purposes (Saccorotti et al., 2004; Cannata et al., 2013, Inza et al., 2014; Eibl et al., 2017b), but they are not often used as an operational tool for volcano monitoring, except in some cases (i.e., Coombs et al., 2018).

Over the past 30 years, the volume of seismo-acoustic data has increased exponentially, as a result of increased coverage and improved detection capability from both array and sparse networks (Messina et al., 2011; Chunquan Yu eta al., 2017). Analyzing great amounts of data is a very difficult task without an efficient processing tool, allowing to automatically obtain the information extraction. In the past decades, many packages or tools for the signal processing have been developed in different programming environments, such as Python and MATLAB platforms. Most of these packages are either command-line-style utility toolboxes or designed for particular purposes, such as ObsPy (Beyreuther et al., 2010), SEIZMO (http://epsc.wustl.edu/~ggeuler/codes/m/seizmo/) and GISMO (Thompson et al., 2018). In order to analyze different seismo-acoustic signals, there are also several tools that provide an interactive Graphic User Interface (GUI). Some of them were designed to ensure partially the signal processing, supporting spectral or amplitude analysis and detection or basic algorithms (Lesage, 2009; Messina et al., 2011; Bueno et al., 2020). Other tools, instead, were developed to perform specific array analyses or routines on a few types of signals (Pignatelli et al., 2008; Smith and Bean, 2020).

Inspired to the design of GSpecDisp tool (Sadeghisorkhani, et al., 2017), we developed MISARA (Matlab Interface for the Seismo-acoustic ARary Analysis), a MATLAB GUI

that supports the visualization, characterization, detection and localization of different volcano signals. In the next sections, we first introduce the main features of MISARA and its functionalities. Finally, we resume the advantages and limitations of the software, suggesting the future works that could improve the software and the signal processing.

A.1 OVERVIEW OF MISARA

MISARA is an open-source Matlab Interface, that has been originally implemented in order to support the users with the application of array techniques on different volcanic signals. It is characterized by an intuitive and modular structure. Based on their major functionalities, this interface could be grouped into five different classes of modules (Fig A.1):

- The Home window.
- The Data preparation window.
- The Instrumental analysis modules.
- The Signal features analysis modules.
- The Array analysis modules.

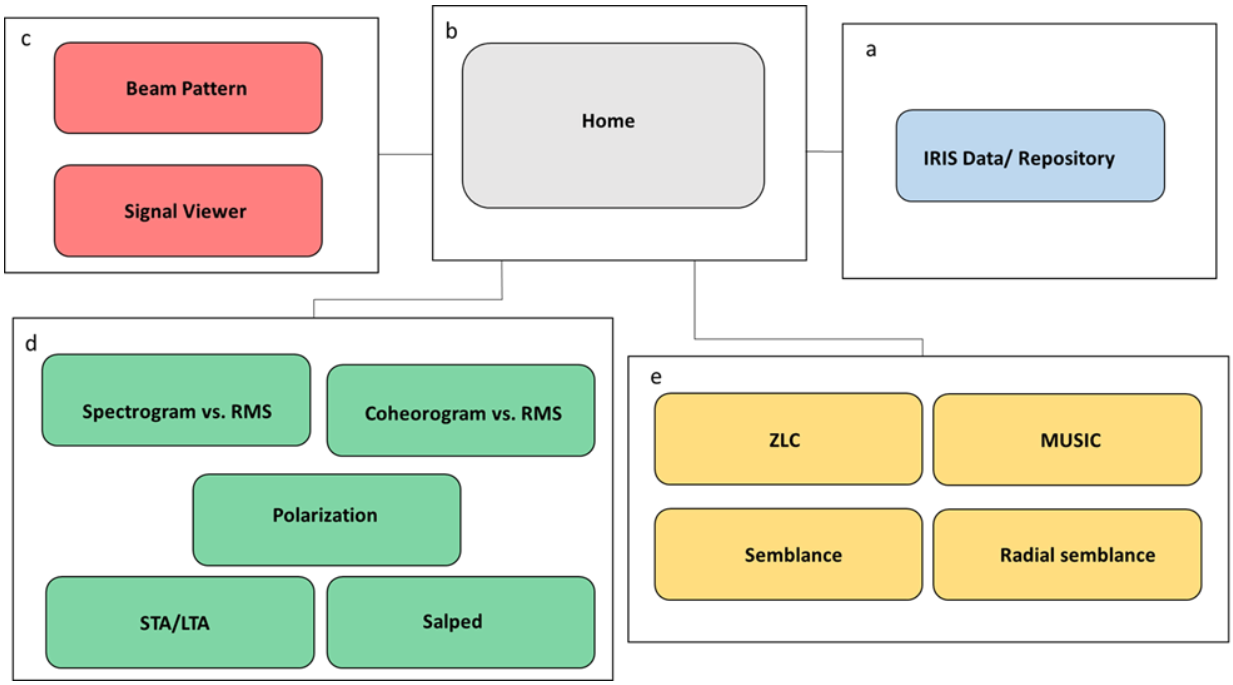

Figure A.1. Schematic overview of MISARA. a) Data preparation window, for formatting the Input data. b) Home window, the main panel for the management of all the utilities of MISARA. c) Instrumental analysis

modules, for the data quality control. d) Signal features modules, for those analytic routines that support the array techniques, such as spectral, amplitude, polarization and detection analysis. e) Array analysis modules, for the source localization methods based on the multichannel techniques.

The Home window (Fig. A.2) represents the control panel of the software, because it allows to manage every aspect of the data processing, such as configuration/formatting the data source and setting Input/Output options and parameters for different type of analysis or routines. This panel has 4 dynamic menus, able to manage independently saving and importing settings of the latest or default analysis parameters, that are contained in the appropriate repository. In addition, it allows to access to the main modules of MISARA, each of which is dedicated to the application of specific routines or algorithms.

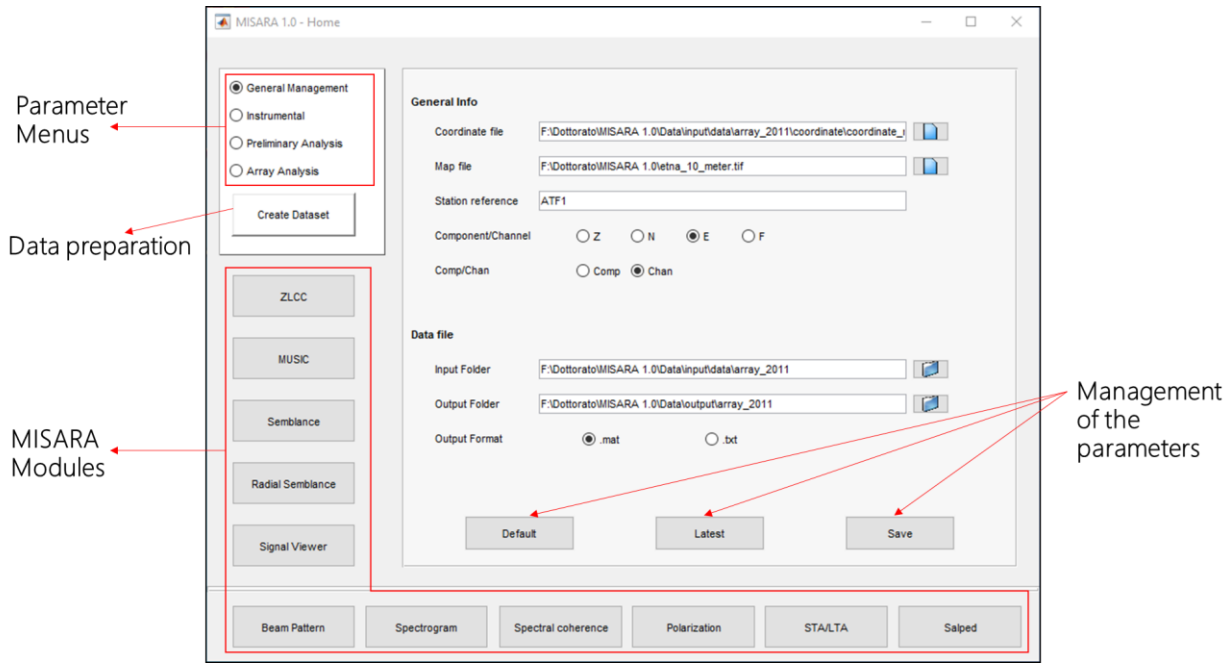

Figure A.2. Example screenshot of the Home window**,** showing some of the configurable input parameters, the buttons for the management of them and the buttons to access to modules used for data formatting or analysis.

In order to ensure the correct functioning of the software, MISARA has an entire module dedicated for the automatic creation of appropriate data structures, that is Create Dataset module. In fact, MISARA works with seismo-acoustic traces expressed in a specific Matlab format (structure arrays) and with specific file and folder names. These files contain all the information about the trace (e.g. station name, station coordinates, amplitude of the signal

etc…). In addition, MISARA modules work through some Matlab files/structures linked to the station coordinates and the parameters for the instrument response correction. To address these issues, the software can operate in two modes, depending on whether the data source is archive or web data. In the first mode, the user can read and automatically convert different file formats from a customizable user directory, such as Seismic Analysis Code (SAC), the Standard for the Exchange of Earthquake Data (SEED) and DSS-Cube/Data-Cube3 file format. In the second mode, the user can access to data stored within the IRIS-DMC via FDSN services (https://www.iris.edu/hq/), retrieving waveforms with channel metadata. While in the first case it is necessary to set manually the station coordinates and the parameters for the instrument response correction, in the second case all formatting processes are automated.

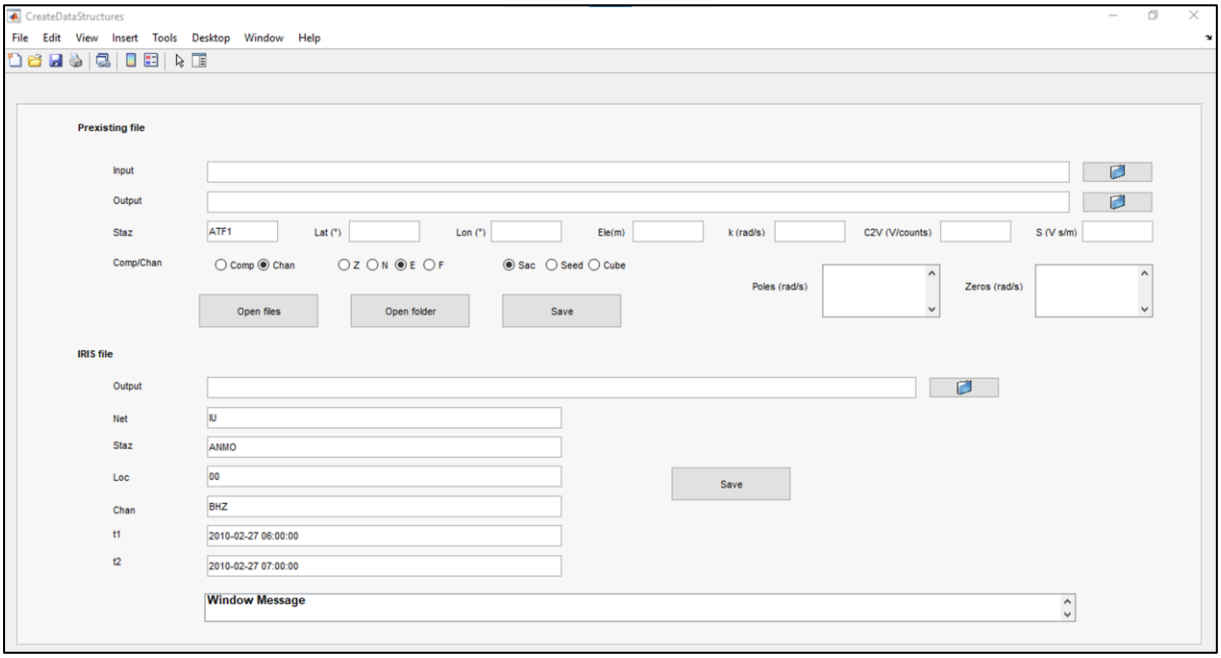

Figure A.3. Example screenshot of Create Dataset module**,** showing the configurable parameters for the conversion of the Input files, the creation of the main data structures of the software and to retrieve waveforms and channel metadata.

The other modules share similar design and workflow processes. Generally, both of them allow rapid and easy selection of the Input traces. Analysis parameters or optionally subroutines can be dynamically managed during data processing, including calculation, visualization and saving of the results (Fig. A.4). However, all of them present different functionalities for specific types of analysis. The Instrumental analysis modules permit to

check data quality, to correct traces based on instrument response parameters and to evaluate the array geometry and response function by performing the Beam Pattern algorithm. The Signal features analysis modules are based on the most popular routines used for the volcano signal processing, such as the calculation of spectrogram and coheregram, the RMS, polarization analysis, the STA/LTA method and the SALPED algorithm. The Array analysis modules support the most commonly used algorithms developed for the source localization of seismo-acoustic signals by performing array methods. In this tool, we have included Zero Lag Cross correlation analysis, MUSIC algorithm, Semblance and Radial Semblance methods. For the evaluation of the uncertainties in the estimate of the source position, most of them have implemented JackKnife method. All of these techniques of analysis have been illustrated in the section 1.3.6. For more details about MISARA utilities, we suggest you to refer its user manual from a Zenodo repository at https://doi.org/10.5281/zenodo.4642026.

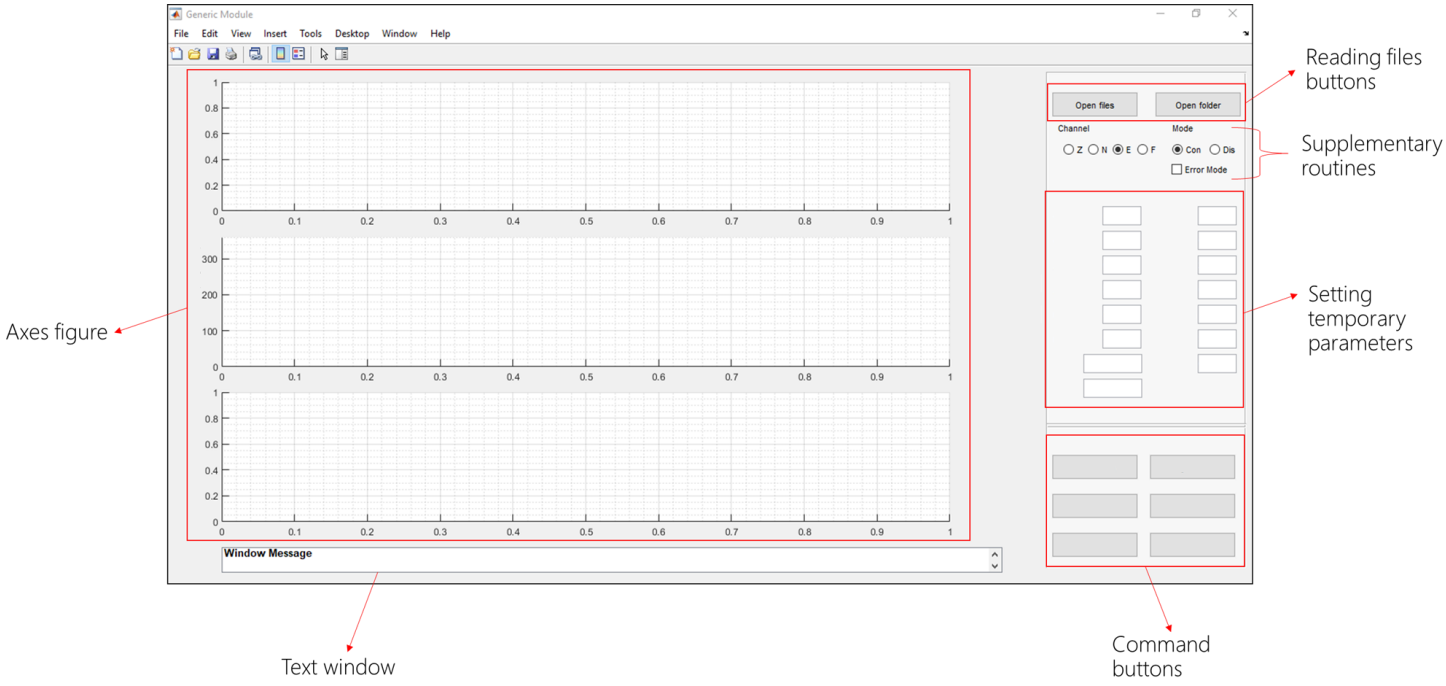

Figure A.4. Example of generic structure of MISARA modules. a) Axes figure, showing the main results. b) Reading files buttons, for the reading of the seismo-acoustic traces. c) Supplementary routines, for the management of additional analysis (for example, the calculation of the analysis error, the selection of the output results, the type of picking, etc…). d) Setting temporary parameters, for the management of those parameters that affects the analysis and the graphic elements. e) Command buttons, to control any process in the module, such as the calculation and visualization of the results, the saving of the Output data and figures and the calculation and visualization of secondary results. f) Text window, showing any information about the data processing through error, warning or command messages.

A.2 ADVANTAGES, LIMITATIONS AND SUGGESTINGS FOR FUTURE WORKS

The current version of MISARA is intended specifically to perform analysis of different seismo-acoustic signals. The most popular algorithms implemented for the volcano signal processing have been unified into one single GUI interface, giving greater attention to array techniques. They could represent efficient tools supporting sparse networks during the routine analysis at volcanological observatories. Therefore, the software could be suitable for several applications, such as academic/research uses, temporary surveys and operational purposes.

Although MISARA has been developed for these specific aims, it can be easily used or modified for any research purposes, because it is open-source and free to public. Thanks to its modular structure, it was possible to integrate many other functionalities supporting array methods, such as spectral, amplitude, polarization and detection techniques. Every module of MISARA is independent. The modules were designed to easily manage every step of the data processing and to quickly inspect the results. The main advantage, in fact, consists of the possibility to reset some parameters directly from the module itself, allowing to repeat many times the analysis. Other fundamental aspects of this modular structure are the rapid and easy selection of different formats of Input traces, the systematic saving of the results and the optionally activation of many subroutines.

The processing and calculation time for any type of analysis is crucially important, especially when there is the necessity to rapidly analyse a great amount of data. At the same time, the efficiency of automated data processing is crucial for the parameter extraction. MISARA is also developed to meet these requirements. Most of the processes is automated, reducing user's errors and efforts and speeding up the assessment of the parameters of interested. Abilities of MISARA has been successfully tested by performing the same analyses shown in the Chapters 2 and 3. In these cases, considering the array/network configuration and routines used for the elaborations, the processing time is of the order of a few seconds/minutes on a laptop with intermediate specifications (4x Intel Core i5-6198DU, 8 GB RAM).

Although MISARA has several advantages, it does not provide comprehensive solutions for all signals analysis. The quality and volume of the input data affect the goodness of the results and the duration of the processing time, respectively, as well as the setting of Input parameters (analysis windows, frequency ranges, threshold of selection, size of slowness or spatial grid, etc…) and the limitations of each technique. At the same time, the error

estimation is affected by multiple factors, such as array/network characteristics, amount of coherence, noise content and topographic, propagation and site effects. JackKnife estimation is very useful to improve the quality of the results, but it represents a time consuming method, compromising the ability of the software to rapidly process data, especially with a significant number of sensors. In addition, although all MISARA processes are automated, some routines include also manual or semi-automatic phases. These features improve the data quality control and the goodness of the results compared to exclusively automatic ones, but sometimes this can be an obstacle to fast analysis of the data, such as the manual classification or picking of LP and VLP waveforms.

As mentioned before, MISARA is designed for the investigation of different seismo-acoustic signals, especially for the array analysis of signals recorded in volcanic areas. The software shows many advantages and can be easily modified for different research or operational purposes. In addition, it allows to process quickly seismic or acoustic data, reducing user's efforts. However, taking into account the previous limitations, this software could be considered as an efficient tool supporting partially the analysis and the study of volcanic phenomena, rather than a complete package. Therefore, in order to improve the capabilities of MISARA and to provide a solution more comprehensive of volcano signals, future works could be aimed at:

- Simplifying the design and the structure of the software, providing a GUI even more user-friendly. The GUI could be structured in a unique panel from which controlling any aspect of the tool, such as the management of the I/O parameters, the creation of data structures, the processing of the signals and the visualization of the results.

- Implementing the existing algorithms or routines in order to improve the time processing and the reliability of the results obtained. The software could be improved by deepening the technical limits of each method and by automating every phase of the data processing as much as possible.

- Adding further methods for more complete investigation of volcanic or seismological phenomena. This tool could be modified by adding routines for the site characterization of the stations location and the investigation of levels of back ground noise in the wavefield. In addition, it could be implemented through statistical or algebraic methods for a better representation of the results of the analyses.

- Adapting the GUI for real- time data processing and the using from Web platforms. This may facilitate the access to a larger number of users and it may be a great resource for the continuous monitoring in volcanic areas.
- Testing the software with a larger dataset that includes different types of signals and cases of study. In this way, the validation of the methods of analysis and the capabilities of MISARA could be efficiently verified.

ACKNOWLEDGEMENTS

The PhD course at University of Catania gave me a great opportunity and I am very grateful to many people who have contributed to my research activity during the last three years.

First of all, I am grateful to my previous supervisor Professor Stefano Gresta. I am honored to have had the opportunity to be introduced into the field of volcano seismology from him. His supervision and his advice in the PhD training course were fundamental.

I am deeply grateful to my supervisor Professor Andrea Cannata, with his professionalism, his attitude in research and his infinite patience supported me constantly during the last phases of doctoral research and writing of this thesis.

I would like to thank my tutors, Dr. Luciano Zuccarello and Dr. Giuseppe Di Grazia, their contributions were essential in the development of my PhD studies. They supported me with great scientific enthusiasm and their wide scientific knowledge.

I am very grateful to Catania and Pisa Sections of INGV that gave me the chance to work on seismic data. I am indebted to all technicians and researchers who have worked on the seismic data used for the studies of this thesis.

I would like to thank Andalusian Institute of Geophysics that gave me the possibility to spend a period of study in Granada, Spain. I especially thank Professor Javier Almendros, with his availability and his patience allowed me to improve the knowledge about volcano seismology.

I am grateful to Professor Silvio De Angelis of the University of Liverpool and Professor Jesus M. Ibanez of the University of Granada for the reviews. Their comments were important to improve the originality of this thesis and gave me the opportunity for further investigations and discussion.

I would like to thank my PhD coordinator Prof. Agata Di Stefano, for the constant support to the training and all the aspects associated at PhD training program.

An invaluable thanks goes to my family, who gave me motivation and support to overcome all the difficulties in these last years.

Finally, an invaluable thanks also goes to my friends for their love, their support, their patience, for helping me to improve every day from every point of view, to believe in me and in my abilities.

LIST OF FIGURES

LIST OF TABLES

REFERENCES

- **Aiuppa**, A., et al. (**2010**). *Patterns in the recent 2007–2008 activity of Mount Etna volcano investigated by integrated geophysical and geochemical observations*. Geochem. Geophys. Geosyst., 11, Q09008, doi:10.1029/2010GC003168.
- **Aiuppa**, A., Lo Coco, E., Liuzzo, M., Giudice, G., Giuffrida, G., Moretti, R. (**2016**). *Terminal Strombolian activity at Etna's central craters during summer 2012: The most CO2-rich volcanic gas ever recorded at Mount Etna*. Geochemical Journal. 50. 123-138, doi: 10.2343/geochemj.2.0395.
- **Aki** K., **Richards**, P. G. (**1980**). *Quantitative seismology*. WH Freeman, San Francisco, doi: https://doi.org/10.1002/gj.3350160110.
- **Aki**, K., Fehler, M., Das, S. (**1977**). *Source mechanism of volcanic tremors: fluid driven crack models and their application to the 1963 Kilauea eruption*. J. Volcanol. Geotherm. Res. 2, 259–287, doi: https://doi.org/10.1016/0377-0273(77)90003-8.
- **Alidibirov**, M., **Dingwell**, D.B. (**1996**). *Magma fragmentation by rapid decompression*. Nature 380, 146–148, doi: https://doi.org/10.1038/380146a0.
- **Allard**, P., B. Behncke, S. D'Amico, M. Neri, S. Gambino (**2006**). *Mount Etna 1993–2005: Anatomy of an evolving eruptive cycle*. Earth Sci. Rev., 78, 85–114, doi: https://doi.org/10.1016/j.earscirev.2006.04.002.
- **Allen**, R.V. (**1978**). *Automatic earthquake recognition and timing from single traces Bull*. seism. Soc. Am. 68 1521 1532, doi: https://doi.org/10.1785/BSSA0680051521.
- **Allstadt**, K. E., Matoza, R. S., Lockhart, A. B., Moran, S. C., Caplan-Auerbach, J., Haney, M. M. (**2018**). *Seismic and acoustic signatures of surficial mass movements at volcanoes*. J. Volcanol. Geotherm. Res. 364, 76–106. doi:10.1016/j.jvolgeores.2018.09.007
- **Almendros**, J., Ibáñez, J.M., Alguacil, G., Del Pezzo, E., Ortiz, R. (**1997**). *Array tracking of the volcanic tremor sourceat Deception Island, Antarctica*. Geophy. Res. Lett. 24, 3069-3072, doi:10.1029/97GL03096.
- **Almendros**, J., Chouet, B., Dawson, P. (**2001a**). *Spatial extent of a hydrothermal system at Kilauea volcano hawaii, determined from array analysis of shallow long-period sismicity. part i: method*. Journal of Geophysical Research, 106:13,565–13,580, doi: 10.1029/2001JB000310.
- **Almendros**, J., Chouet, B., Dawson, P. (**2001b**). *Spatial extent of a hydrothermal system at Kilauea volcano hawaii, determined from array analysis of shallow long-period sismicity. part ii: results*. Journal of Geophysical Research, 106:13,581–13,597, doi: 10.1029/2001JB000309.
- **Almendros**, J., Chouet, B., Dawson, P., Bond, T. (**2002**). *Identifying elements of the plumbing system beneath Kilauea Volcano, Hawaii, from the source locations of very-long period signals*. Geophys. J. Int. 148, 303–312, doi: https://doi.org/10.1046/j.1365-246X.2002.01629.x.
- **Almendros**, J., **Chouet**, B. (**2003**). *Performance of the radial semblance method for the location of very long period volcanic signals*. Bull. Seismol. Soc. Am. 93, 1890–1903, doi: https://doi.org/10.1785/0120020143.
- **Almendros**, J., Carmona, E., Ibáñez, J. (**2004**). *Precise determination of the relative wave propagation parameter of similar events using a small-aperture*

seismic array. Journal of Geophysical Research, 109:B11308, 15pp, doi: 10.1029/2003JB002930.

- **Almendros,** J., Abella, R., Mora, M., Lesage, P. (**2012**). *Time-dependent spatial amplitude patterns of harmonic tremor at Arenal Volcano, Costa Rica: seismic-wave interferences?*. Bull Seismol Soc Am 102:2378–2391, doi: http://hal.univ-smb.fr/hal-00763631.
- **Almendros**, J., Abella, R., Mora, M. M., and Lesage, P. (**2014**). *Array analysis of the seismic wavefield of long-period events and volcanic tremor at Arenal volcano, Costa Rica*, J. Geophys. Res. Solid Earth, 119, doi:10.1002/2013JB010628.
- **Aloisi**, M., Cocina, O., Neri, G., Orecchio, B., Privitera, E. (**2002**). *Seismic tomography of the crust underneath the Etna volcano, Sicily*. Phys. Earth Planet. Inter., 134, 139–155, doi: https://doi.org/10.1016/S0031-9201(02)00153-X.
- **Alparone**, S., Andronico, D., Lodato, L., Sgroi, T. (**2003**). *Relationship between tremor and volcanic activity during the Southeast Crater eruption on Mount Etna in early 2000.* Journal of Geophysical Research: Solid Earth, 108(B5), doi: https://doi.org/10.1029/2002JB001866.
- **Alparone**, S., Cannata, A., Gresta, S. (**2007**). *Time variation of spectral and wavefield features of volcanic tremor at Mt. Etna (January–June 1999)*. J. Volcanol. Geotherm. Res. doi:10.1016/j.jvolgeores.2006.12.012.
- **Alparone**, S., Cocina, O., Gambino, S., Mostaccio, A., Spampinato, S., Tuvè, T., Ursino, A. (**2013**). *Seismological features of the Pernicana-Provenzana fault system and implications for the dynamics of northeastern flank of the volcano*. J. Volcanol. Geotherm. Res., 251, 16-26; doi:10.1016/j.jvolgeores.2012.03.010.
- **Álvarez**, I., García, L., Mota, S., Cortes, G., Benítez, C., De la Torre, A. (**2013**). *An automatic P-phase picking algorithm based on adaptive multiband processing*. IEEE, Geosci. Remote Sens. Lett. 10 (6), 1488–1492, doi:10.1109/LGRS.2013.2260720
- **Andronico**, D., Branca, S., Calvari, S., Burton, M., Caltabiano, T., Corsaro, R.A., Del Carlo, P., Garfì, G., Lodato, L., Miraglia, L., Murè, F., Neri, M., Pecora, E., Pompilio, M., Salerno, G., Spampinato, L. (**2005**). *A multi-disciplinary study of the 2002–2003 Etna eruption: insights into a complex plumbing system*. Bull. Volcanol., 67, 314–330, doi:10.1007/s00445-004-0372-8.
- **Andronico**, D., Cristaldi, A., Scollo, S. (**2008**). *The 4–5 September 2007 lava fountain at South–East Crater of Mt Etna, Italy*. J. Volcanol. Geotherm. Res. 173, 325–328, doi: http://dx.doi.org/10.1016/j.jvolgeores.2008.02.004.
- **Andronico**, D., Lo Castro, M. D., Sciotto, M., Spina, L. (**2013**). *The 2010 ash emissions at the summit craters of Mt Etna: Relationship with seismo-acoustic signals*. J. Geophys. Res. Solid Earth, 118, 51–70, doi:10.1029/2012JB009895.
- **Arciniega-Ceballos**, A., Dawson, P., Chouet, B.A. (**2012**). *Long period seismic source characterization at Popocatépetl volcano, Mexico*. Geophys. Res. Lett. 39, doi:10.1029/2012GL053494.
- **Arlitt,** R., Kissling E., Ansorge J., TOR working group (**1999**). *3-D crostal structure beneath the TOR array and effects on teleseismic wavefronts*. Tectonophysics 314, 309-319, doi: https://doi.org/10.1016/S0040-1951(99)00250-4.
- **Asten**, M. W., **Henstridge**, J. D. (**1984**). *Array estimators and the use of microseism for reconnaissance of sedimentary basins*. Geophysics 49:1828–1837, doi: https://doi.org/10.1190/1.1441596.

- **Azzaro**, R., Branca, S., Giammanco, S., Gurrieri, S., Rasà, R., Valenza, M. (**1998**). *New evidence for the form and extent of the Pernicana Fault System (Mt. Etna) from structural and soil-gas surveying*. J. Volcanol. Geotherm. Res., 84, 143-152, doi: 10.1016/S0377-0273(98)00036-5.
- **Azzaro**, R., Barbano, M.S., Antichi, B., Rigano, R. (**2000**). *Macroseismic catalogue of Mt. Etna earthquakes from 1832 to 1998*. Acta Vulcanol., 12, 3 - 36.
- **Azzaro**, R., Branca, S., Gwinner, K., Coltelli, M. (**2012**). *The volcano-tectonic map of Etna volcano, 1:100.000 scale: an integrated approach based on a morphotectonic analysis from high-resolution DEM constrained by geologic, active faulting and seismotectonic data*. Boll.Soc.Geol.It.,131, 1, 153-170, doi:10.3301/IJG.2011.29.
- **Azzaro**, R., Bonforte, A., Branca, S., Guglielmino, F. (**2013**). *Geometry and kinematics of the fault systems controlling the unstable flank of Etna volcano (Sicily)*. Journal of volcanology and geothermal research, 251, 5-15, doi:10.1016/j.jvolgeores.2012.10.001.
- **Balmforth**, N.J., Craster, R.V., Rust, C. (**2005**). *Instability in flow through elastic conduits and volcanic tremor*. The Journal of Fluid Mechanics, 527, 353–377. doi: 10.1017/S0022112004002800.
- **Barberi**, G., Cocina, O., Neri, G., Privitera, E., Spampinato, S. (**2000**). *Volcanological inferences from seismic strain tensor computation at Mt. Etna volcano. Sicily*. Bull. Volcanol., 62, 318-330, doi: 10.1007/s004450000101.
- **Bartlett**, M. S. (**1948**). *Smoothing periodograms from time series with continuous spectra*. Nature, 161(4096), 686-687, doi: https://doi.org/10.1038/161686a0.
- **Battaglia**, J., **Aki**, K. (**2003**). *Location of seismic events and eruptive fissures on the Piton de la Fournaise volcano using seismic amplitudes*. J. Geophys. Res., 108, doi:10.1029/2002JB002193.
- **Battaglia**, J., Got, J.L., Okubo, P. (**2003**). *Location of long period events below Kilauea Volcano using seismic amplitudes and accurate relative relocation*. J. Geophys. Res., 108(B12), 2553, doi:10.1029/2003JB002517.
- **Battaglia**, J., Aki, K., and Ferrazzini, V. (**2005**). *Location of tremor sources and estimation of lava output using tremor source amplitude on the Piton de la Fournaise volcano: 1. location of tremor sources*. J. Volcanol. Geoth. Res. 147 (3), 268–290. doi:10.1016/j.jvolgeores.2005.04.005.
- **Bean**, C. J, De Barros, L., Lokmer, I., Metaxian, J-P., O'Brien, G., Murphy, S. (**2014**). *Long-Period seismicity in the shallow volcanic edifice formed from slow-rupture earthquakes*. Nature Geosci, 7, 71-75, doi:10.1038/ngeo2027.
- **Behncke** B., **Neri**, M. (**2003**). *The July-August 2001 eruption of Mt. Etna (Sicily)*. B. Volcanol., 65, 461-476; doi:10.1007/s00445- 003-0274-1
- **Behncke**, B., Branca, S., Corsaro, R. A., De Beni, E., Miraglia, L., Proietti, C., (**2014**). *The 2011–2012 summit activity of Mount Etna: Birth, growth and products of the new SE crater*. Journal of Volcanology and Geothermal Research, 270, 10-21, doi:10.1016/j.jvolgeores.2013.11.012.
- **Benoit**, J.P., **McNutt**, S.R. (**1997**). *New constraints on source processes of volcanic tremor at Arenal Volcano, Costa Rica, using broadband seismic data*. Geophysical Research Letters 24 (4), 449–452, doi: https://doi.org/10.1029/97GL00179.

- **Beroza**, G.C., and **Ide**, S. (**2011**). *Slow earthquakes and nonvolcanic tremor*. Annu. Rev. Earth Planet Sci. 39 (1), 271–296. doi:10.1146/annurev-earth-040809-152531.
- **Beyreuther**, M., Barsch, R., Krischer, L., Megies, T., Behr, Y., Wassermann, J. (**2010**). *ObsPy: a Python toolbox for seismology*. Seismol Res. Lett. 81 (3), 530–533. doi:10.1785/gssrl.81.3.530.
- **Bianca**, M., Monaco, C., Tortorici, L., Cernobori, L. (**1999**). *Quaternary normal faulting in southeastern Sicily (Italy): a seismic source for the 1693 large earthquake*. Geophys. J. Int., 139, 370– 394, doi: https://doi.org/10.1046/j.1365-246x.1999.00942.x.
- **Bonaccorso**, A., Bonforte, A., Guglielmino, F., Palano, M., Puglisi, G. (**2006**). *Composite ground deformation pattern forerunning the 2004–2005 Mount Etna eruption*. Journal of Geophysical Research: Solid Earth, 111(B12), doi: https://doi.org/10.1029/2005JB004206.
- **Bonaccorso**, A., Bonforte, A., Calvari, S., Del Negro, C., Di Grazia, G., Ganci, G., Neri, M., Vicari, A., Boschi, E. (**2011**). *The initial phases of the 2008–2009 Mount Etna eruption: a multidisciplinary approach for hazard assessment*. J. Geophys. Res. 116, B03203, doi: http://dx.doi.org/10.1029/2010JB007906.
- **Bonforte**, A., Guglielmino, F., Coltelli, M., Ferretti, A., Puglisi, G. (**2011**). *Structural assessment of Mount Etna volcano from Permanent Scatterers analysis*. Geochemistry, Geophysics, Geosystems, 12(2), doi: https://doi.org/10.1029/2010GC003213.
- **Bormann**, P. (**2012**). *New Manual of Seismological Observatory Practice*. (NMSOP-2), IASPEI, GFZ German Research Centre for Geosciences, Potsdam, doi: https://doi.org/10.2312/GFZ.NMSOP-2.
- **Bousquet**, J. C., **Lanzafame**, G. (**2004**). *The tectonics and geodynamics of Mt. Etna: synthesis and interpretation of geological and geophysical data. Mt. Etna: volcano laboratory*, 29-47, doi:10.1029/143GM03.
- **Branca**, S., Coltelli, M., and Groppelli, G. (**2004**). *Geological Evolution of Etna volcano. In Etna Volcano Laboratory*. (American Geophysical Union), pp. 49–63, doi:10.1029/143GM04.
- **Branca**, S., Coltelli, M., De Beni, E., and Wijbrans, J. (**2008**). *Geological evolution of Mount Etna volcano (Italy) from earliest products until the first central volcanism (between 500 and 100 ka ago) inferred from geochronological and stratigraphic data.* Int. J. Earth Sci. 97, 135–152, doi:10.1007/s00531-006-0152-0.
- **Branca**, S., Coltelli, M., Groppelli, G., and Lentini, F. (**2011**). *Geological map of Etna volcano, 1:50,000 scale*. Ital. J. Geosci. 130, doi:10.3301/IJG.2011.15.
- **Branca**, S., Ferrara, V. (**2013**). *The morphostructural setting of Mount Etna sedimentary basement (Italy): Implications for the geometry and volume of the volcano and its flank instability*. Tectonophysics. 586, 46-64, doi:10.1016/j.tecto.2012.11.011.
- **Buckingham**, M.J., **Garces**, M.A. (**1996**). *A canonical model of volcano acoustics*. J. Geophys. Res., 101, 8129-8151, doi: https://doi.org/10.1029/95JB01680.
- **Bueno**, A., Benítez, C., De Angelis, S., Díaz-Moreno, A., Ibañez, J.M. (**2019**). *Volcano seismic transfer learning and uncertainty quantification with Bayesian neural networks*. IEEE Trans. Geosci. Remote Sens. (IEEE) 892–902, doi: 10.1109/TGRS.2019.2941494.

- **Bueno**, A., Zuccarello, L., DÃ-az Moreno, A., Woollam, J., Titos, M., Benitez, C., Alvarez, I., Prudencio, J., De Angelis, S. (**2020**). *PICOSS: Python Interface for the Classification of Seismic Signals*. Computers & Geosciences. 142, doi: 0.1016/j.cageo.2020.104531.
- **Calvari**, S., Groppelli, G., and Pasquarè, G. (**1994**). *Preliminary geological data on the south-western wall of the Valle del Bove, Mt Etna, Sicily*. Acta Volcanol. 5, 15–30.
- **Calvari**, S., Tanner, L.H., Groppelli, G., Norini, G. (**2004**). *A comprehensive model for the opening of the Valle del Bove depression and hazard evaluation for the eastern flank of Etna volcano*. In "Mt. Etna Volcano Laboratory" (Bonaccorso, Calvari, Coltelli, Del Negro, Falsaperla Eds.), AGU (Geophysical monograph series), 143, 65–75, doi:10.1029/143GM05.
- **Cannata**, A., Catania, A., Alparone, S., Gresta, S. (**2008**). *Volcanic tremor at Mt. Etna: Inferences on magma dynamics during effusive and explosive activity*. J. Volcanol. Geotherm. Res., doi:10.1016/j.jvolgeores.2007.11.027.
- **Cannata**, A., Hellweg, M., Di Grazia, G., Ford, S., Alparone, S., Gresta, S., Montalto, P., Patanè, D. (**2009a**). *Long period and very long period events at Mt. Etna volcano: Characteristics, variability and causality, and implications for their sources*. J. Volcanol. Geotherm. Res., 187, 227–249, doi:10.1016/j.jvolgeores.2009.09.007.
- **Cannata** A., Carbone, D., Di Grazia, G., Montalto, P., Patanè, D., Zuccarello, L., (**2009b**). *Advances in the study of geophysical signals from Mt. Etna volcano*. Book "The VOLUME Project – VOLcanoes: Understanding subsurface mass moveMEnt", 250-261, Edited by C. J. Bean, A. K. Braiden, I. Lokmer, F. Martini and G. S. O'Brien, ISBN: 978-1-905254-39-2.
- **Cannata**, A., Di Grazia, G., Montalto, P., Ferrari, F., Nunnari, G., Patanè, D., Privitera, E. (**2010**). *New insights into banded tremor from the 2008–2009 Mount Etna eruption*. J. Geophys. Res., 115, B12318, doi:10.1029/2009JB007120.
- **Cannata**, A., Di Grazia, G., Aliotta, M., Cassisi, C., Montalto, P., Patanè, D. (**2013**). *Monitoring seismo-volcanic and infrasonic signals at volcanoes: Mt. Etna case study*, Pure Appl. Geophys., 170, 1751–1771, doi:10.1007/s00024-012-0634 x.
- **Cannata**, A., Spedalieri, G., Behncke, B., Cannavò, F., Di Grazia, G., Gambino, S., Gresta, S., Gurrieri, S., Liuzzo, M. & Palano, M. (**2015**). *Pressurization and depressurization phases inside the plumbing system of Mount Etna volcano: Evidence from a multiparametric approach*. Journal of Geophysical Research: Solid Earth, 120(9), 5965-5982, doi: https://doi.org/10.1002/2015JB012227.
- **Cannata**, A., Iozzia, A., Alparone, S. et al. (**2021**). *Repeating earthquakes and ground deformation reveal the structure and triggering mechanisms of the Pernicana fault, Mt. Etna*. Commun Earth Environ 2, 116 (2021), doi: https://doi.org/10.1038/s43247-021-00188-6.
- **Cannavò**, F., Cannata, A., Cassisi, C., Di Grazia, G., Montalto, P., Prestifilippo, M., Privitera, E., Coltelli, M., Gambino, S. (**2017**). *A multivariate probabilis-tic graphical model for real-time volcano monitor-ing on Mount Etna*, J. Geophys. Res., 122, doi:10.1002/2016JB013512.
- **Capon,** J. (**1969**). *High resolution frequency-wavenumber spectrum analysis*. Proc. IEEE, 57, 1408-1418, doi: 10.1109/PROC.1969.7278.

- **Carbone**, D., Zuccarello, L., Saccorotti, G., Greco, F. (**2006**), *Analysis of simultaneous gravity and tremor anomalies observed during the 2002–2003 Etna eruption*. Earth Planet. Sci. Lett.,245, 616–629, doi:10.1016/j.epsl.2006.03.055.
- **Carbone**, D., Zuccarello, L., Saccorotti, G. (**2008**). *Geophysical indications of magma uprising at Mt Etna during the December 2005 to January 2006 non-eruptive period*. Geophysical Research Letters, 35(6), doi: 10.1029/2008gl033212
- **Catalano**, R., Doglioni, C., Merlini, S. (**2001**). *On the Mesozoic Ionian basin*. Geophys. J. Int., 144, 49-64, doi: https://doi.org/10.1046/j.0956-540X.2000.01287.x.
- **Catalano**, S., **De Guidi**, G. (**2003**). *Late quaternary uplift of northeastern Sicily: relation with the activenormal faulting deformation*. J. Geodyn., 36, 445–467, doi:10.1016/S0264-3707(02)00035-2.
- **Cauchie**, L., **Saccorotti**, G. (**2013**). *Probabilistic inversion of Rayleigh-wave dispersion data: An application to Mt. Etna, Italy*. Journal of Seismology. 17. 335-346, doi:10.1007/s10950-012-9323-6.
- **Cauchie**, L., Saccorotti, G., Bean, C.J. (**2015**). *Amplitude and recurrence time analysis of LP activity at Mt. Etna, Italy*. J. Geophys. Res. Solid Earth n/a – n/a, doi: https://doi.org/10.1002/2015JB011897.
- **Cesca**, S., Braun, T., Tessmer, E., Dahm, T. (**2007**). *Modelling of the April 5, 2003, Stromboli (Italy) paroxysmal eruption from the inversion of broadband seismic data*. Earth and Planetary Science Letters, Volume 261, Issues 1–2, 2007, Pages 164-178, ISSN 0012-821X, doi: https://doi.org/10.1016/j.epsl.2007.06.030.
- **Chávez-García,** F.J., Rodriguez, M., Stephenson, W.R. (**2005**). *An alternative approach to the SPAC analysis of microtremors: exploiting stationarity of noise*. B. Seismol. Soc. Am., 95, 277-293, doi:10.1785/0120030179.
- **Chiou**, S.J., **Bolt,** B.A. (**1993**). *Seismic wave slowness-vector estimation from broad-band array data*. Geophys. J. Int. 114, 234– 248, doi: https://doi.org/10.1111/j.1365-246X.1993.tb03913.x.
- **Chouet**, B. (**1986**). *Dynamics of a fluid-driven crack in three dimensions by the finite difference method*. Journal of Geophysical Research 91, 13,967–13,992, doi:10.1029/JB091iB14p13967.
- **Chouet**, B.A. (**1988**). *Resonance of a fluid-driven crack: radiation properties and implications for the source of long-period events and harmonic tremor.* J. Geophys. Res. 93, 4375– 4400, doi: https://doi.org/10.1029/JB093iB05p04375.
- **Chouet**, B. A. (**1992**). *A seismic model for the source of long-period events and armonic tremor*. IAVCEI Proceed. In Volcanology, III: Volcanic Seismology. P. Gasparini, R. Scarpa, K. Aki (Eds), Springer Verlag, Heidelberg, 133-156, doi: 10.1007/978-3-642-77008-1_11.
- **Chouet**, B., Page, R. A., Stephens, C. D., Lahr, J. C., Power, J. A. (**1994**). *Precursory swarms of long-period events at Redoubt volcano (1989-1990), Alaska: Their origin and use as a forecasting tool*. J. Volcanol. Geotherm. Res., 62, 95-136, doi: https://doi.org/10.1016/0377-0273(94)90030-2.
- **Chouet**, B. (**1996a**). *Long-period volcano seismicity: Its source and use in eruption forecasting*. Nature, 380, 309-316, doi: https://doi.org/10.1038/380309a0
- **Chouet**, B. (**1996b**). *New methods and future trends in seismological volcano monitoring*. In "Monitoring and mitigation of volcano hazards" (Scarpa, Tilling Eds.), Springer, New York, 23–97.

- **Chouet**, B., G. Saccorotti, G. Martini, M. Dawson, P. De Luca, G. Milana, G. Scarpa, R. (**1997**). *Source and path effects in the wavefields of tremor and explosions at Stromboli Volcano, Italy*. J. Geophys. Res. 102, 15129-15150, doi: https://doi.org/10.1029/97JB00953.
- **Chouet**, B. (**2003**). *Volcano seismology*. Pure Appl. Geophys., 160, 739–788, doi:10.1007/PL00012556.
- **Chouet**, B., Dawson, P., Ohminato, T., Martini, M., Saccorotti, G., Giudicepietro, F., De Luca, G., Milana, G., Scarpa, R. (**2003**). *Source mechanism of explosions at Stromboli Volcano, Italy, determined from moment-tensor inversions of verylong-period data*. J. Geophys. Res., 108 (B1), doi:10.1029/20042JB001919.
- **Chouet**, B., Dawson, P., Arciniega-Ceballos, A. (**2005**). *Source mechanism of Vulcanian degassing at Popocatépetl volcano, Mexico, determined from waveform inversions of very long period signals*. J. Geophys. Res., 110, B07301, doi:10.1029/2004JB003524.
- **Chouet**, B., Dawson, P., Martini, M. (**2008**). *Shallow-conduit dynamics at Stromboli Volcano, Italy, imaged from waveform inversions.* In: Lane, S.J., Gilbert, J.S. (Eds.), Fluid Motions in Volcanic Conduits: A Source of Seismic and Acoustic Signals: Geol. Soc., London, Special Publications, 307, pp. 57–84, doi: https://doi.org/10.1144/SP307.5.
- **Chouet**, B., Dawson, P., James, M. R., Lane, S. J. (**2010**). *Seismic source mechanism of degassing bursts at Kilauea Volcano, Hawaii: Results from waveform inversion in the 10–50 s band*. J. Geophys. Res., 115, B09311, doi:10.1029/2009JB006661.
- **Chouet**, B., **Dawson**, P. (**2011**). *Shallow conduit system at Kilauea Volcano, Hawaii, revealed by seismic signals associated with degassing bursts*. Journal of Geophysical Research 116, B12317, doi: http://dx.doi.org/10.1029/2011JB008677.
- **Chouet**, B. A., **Matoza**, R. S. (**2013**). *A multi-decadal view of seismic methods for detecting precursors of magma movement and eruption*. Journal of Volcanology and Geothermal Research, Volume 252, 2013, Pages 108-175, ISSN 0377-0273, doi: https://doi.org/10.1016/j.jvolgeores.2012.11.013.
- **Chunquan**, Y., Yingcai, Z., Xuefeng, S. (**2017**). *Crazyseismic: A MATLAB GUI-based software package for passive seismic data preprocessing*. Seismological Research Letters. 88, doi:10.1785/0220160207.
- **Collier**, L., **Neuberg**, J. (**2006**). *Incorporating seismic observations into 2D conduit flow modeling*. Journal of Volcanology and Geothermal Research 152, 331–346., doi:10.1016/J.JVOLGEORES.2005.11.009.
- **Coltelli**, M., Del Carlo, P., Vezzoli, L. (**2000**). *Stratigraphic constraints for explosive activity in the last 100 kaat Etna volcano, Italy*. Int. J. Earth Sci., 89, pp. 665-677, doi: https://doi.org/10.1007/s005310000117.
- **Coltelli**, M., Patane`, D., Aiuppa, A., Aliotta, M., Aloisi, M., Behncke, B., Cannata, A., Cannavo`, F., DI Grazia, G., Gambino, S., Gurrieri, S., Mattia, M., Montalto, P., Prestifilippo, M., Puglisi, G., Salerno, G., Scandura, D. (**2012**). *Insight into eruptive cyclic behavior of Mount Etna during 2011: geophysical and geochemical constraints*. Geophysical Research Abstracts, EGU2012-1992, bibcode: 2012EGUGA..14.1992C.

- **Cooley,** J. W., **Tukey**, J. W. (**1965**). *An algorithm for the machine calculation of complex Fourier series*. Math. Comput. 19:297-301, doi: https://doi.org/10.1090/S0025-5718-1965-0178586-1.
- **Coombs**, M. L., Wech, A. G., Haney, M. M., Lyons, J. J., Schneider, D. J., Schwaiger, H. F., et al. (**2018**). *Short-term forecasting and detection of explosions during the 2016–2017 eruption of bogoslof volcano, Alaska*. Front. Earth Sci. 6, 122, doi:10.3389/feart.2018.00122.
- **Corsaro**, R.A., **Cristofolini**, R. (**2000**). *Subaqueous volcanism in the Etnean area: evidence for hydro-magmatic activity and regional uplift inferred from the Castle Rock of Acicastello*. Elsevier Oxf. Roy. UNI 1976 Rev. 95, 209–225, doi: doi:10.1016/S0377-0273(99)00130-4.
- **Corsaro**, R.A., **Pompilio**, M. (**2004**). *Buoyancy-controlled eruption of magmas at Mt Etna: Buoyancy-controlled eruption of magmas at Mt Etna*. Terra Nova 16, 16–22, doi: https://doi.org/10.1046/j.1365-3121.2003.00520.x.
- **Cristofolini**, R., Lentini, F., Patanè G., Rasà R. (**1979**). *Integrazione di dati geologici, geofisici e metrologici per la stesura di un profilo crostale in corrispondenza dell'Etna*. Boll. Soc. Geol. It., 98, 239-247.
- **Cristofolini**, R., Gresta, S. Imposa, S. Patanè, G. (**1988**). *Feeding mechanism of eruptive activity at Mt. Etna based on seismological and petrological data*. In "Modelling of Volcanic Process" (King, Scarpa, Eds.), Springer, Berlin, 73–93, doi: doi:10.1007/978-3-322-89414-4_3.
- **Crosson**, D.A., **Bame**, R.S. (**1985**). *A spherical source model for low frequency volcanic earthquakes*. Journal of Geophysical Research, doi: https://doi.org/10.1029/JB090iB12p10237.
- **D'Auria**, L., Giudicepietro, F., Martini, M., Peluso, R. (**2006**). *Seismological insight into the kinematics of the 5 April 2003 vulcanian explosion at Stromboli volcano (southern Italy)*. Geophys. Res. Lett., 33, L08308, doi:10.1029/2006GL026018.
- **Davi**, R., O'Brien, G.S., De Barros, L., Lokmer, I., Bean, C.J., Lesage, P., Mora, M.M., and Soto, G.J., (**2012**). *Seismic source mechanisms of tremor recorded on Arenal volcano, Costa Rica, retrieved by waveform inversion*. J. Volcanol. Geotherm. Res., doi:10.1016/j.jvolgeores.2011.10.008.
- **Dawson**, P. B., Chouet, B., Okubo, P. G., Villaseñor, A., Benz, H. M. (**1999**). *Three-dimensional velocity structure of the Kilauea Caldera, Hawaii*. Geophysical Research Letters, 26(18), 2805-2808, doi:10.1029/1999GL005379.
- **Dawson**, P.B., Chouet, B.A., Power, J. (**2011**). *Determining the seismic source mechanism and location for an explosive eruption with limited observational data: Augustine Volcano, Alaska*. Geophysical Research Letters 38, L03302, doi: http://dx.doi.org/10.1029/2010GL045977.
- **De Angelis**, S., **McNutt**, S.R. (**2007**). *Observations of volcanic tremor during the January–February 2005 eruption of Mt. Veniaminof, Alaska*. Bull Volcanol 69, 927–940, doi: https://doi.org/10.1007/s00445-007-0119-4.
- **De Barros**, L., Bean, C., Lokmer, I., Saccorotti, G., Zuccarello, L., O'Brien, G., Métaxian, J.-P., Patanè, D. (**2009**). *Source geometry from exceptionally high resolution long period event observations at Mt. Etna during the 2008 eruption*. Geophys. Res. Lett., 36, L24305, doi:10.1029/2009GL041273.
- **De Barros**, L., Lokmer, I., Bean, C.J., O'Brien, G.S., Saccorotti, G., Métaxian, J.-P., Zuccarello, L., Patanè, D. (**2011**). *Source mechanism of long-period events*

recorded by a high-density seismic network during the 2008 eruption on Mount Etna. J. Geophys. Res. 116, doi: https://doi.org/10.1029/2010JB007629.

- **De Barros**, L., Lokmer, I., Bean, C.J. **(2013**). *Origin of spurious single forces in the source mechanism of volcanic seismicity*. J. Volcanol. Geotherm. Res. 262, 1-6, doi: 10.1016/j.jvolgeores.2013.06.006.
- **De Beni**, E., Branca, S., Coltelli, M., Groppelli, G., and Wijbrans, J.R. (**2011**). *40Ar/39Ar isotopic dating of Etna volcanic succession*. Ital. J. Geosci. 130, 292–305, doi:10.3301/IJG.2011.14.
- **De Gori**, P., Chiarabba, C., D. Patane`, D. (**2005**), *Qp structure of Mount Etna: Constraints for the physics of the plumbing system*. J. Geophys. Res., 110, B05303, doi:10.1029/2003JB002875.
- **De Meersman**, K., van der Baan, M., Kendall, J. M. (**2006**). *Signal Extraction and Automated Polarization Analysis of Multicomponent Array Data*. Bulletin of the Seismological Society of America. Vol. 96. No.6, 2415-2430, December 2006, doi: 10.1785/0120050235.
- **Del Pezzo**, E., De Martino, S., Gresta, S., Martini, M., Milana, G., Patanè, D., Sabbarese, C. (**1993**). *Velocity and spectral characteristics of the volcanic tremor at Etna deduced by a small seismometer array*. Journal of volcanology and geothermal research, 56(4), 369-378, doi: 10.1016/0377-0273(93)90003-a.
- **Diaz-Moreno**, A. et al. (**2019**). *Volume Flow Rate Estimation for Small Explosions at Mt. Etna, Italy, From Acoustic Waveform Inversion*. Geophys. Res. Lett. 46, 11071–11079, doi: https://doi.org/10.1029/2019GL084598.
- **Di Grazia**, G., Falsaperla, S., & Langer, H. (**2006**). *Volcanic tremor location during the 2004 Mount Etna lava effusion*. Geophysical research letters, 33(4), doi:10.1029/2005GL025177.
- **Di Grazia**, G., Cannata, A., Montalto, P., Patanè, D., Privitera, E., Zuccarello, L., Boschi, E. (**2009**). *A multiparameter approach to volcano monitoring based on 4D analyses of seismo-volcanic and acoustic signals: The 2008 Mt. Etna eruption*. Geophysical Research Letters, 36(18), doi:10.1029/2009GL039567.
- **Di Lieto**, B., Saccorotti, G., Zuccarello, L., Rocca, M. L., and Scarpa, R. (**2007**). *Continuous tracking of volcanic tremor at Mount Etna, Italy*. Geophys. J. Int. 169 (2), 699–705. doi:10.1111/j.1365-246X.2007.03316.x.
- **Dingwell**, D. (**1996**). *Physical properties of magma*. in E. Julius Dasch ed. Encyclopedia of Earth Sciences : MacMillan Reference USA, Simon and Schuster MacMillan, New York, 2:817–820.
- **Doglioni**, C., Innocenti, F., Mariotti, G. (**2001**). *Why Mt Etna?.* Terra Nova 13: 25-31, doi:10.1046/j.1365-3121.2001.00301.x.
- **Douglas** A., Bowers, D., Marshall, P. D., Young, J. B., Porter, D., Wallis, N. J. (**1999**). *Putting nuclear-test monitoring to the test*.Nature, 398, 474–475, doi: https://doi.org/10.1038/19000.
- **Douglas**, A. (**2002**). *Seismometer arrays – their use in earthquake and test ban seismology*. In: Lee, W. H. K., Kanamori, H., Jennings, P. C., and Kisslinger, C. (eds.) : Handbook of Earthquake and Engineering Seismology. Academic Press, ISBN: 9780080489223.
- **Efron**, B. (**1982**). *The Jackknife, the Bootstrap and Other Resampling Plans*. Soc. for Ind. and Appl. Math., Philadelphia, Pa, doi: http://dx.doi.org/10.1137/1.9781611970319.

- **Eibl**, E. P. S., Bean, C. J., Einarsson, B., Pàlsson, F., Vogfjörd, K. S. (**2020**). *Seismic ground vibrations give advanced early-warning of subglacial floods*. Nat. Commun. 11 (1), 2504, doi:10.1038/s41467-020-15744-5Pubmed.
- **Eibl**, E. P. S., Bean, C. J., Vogfjörd, K. S., Ying, Y., Lokmer, I., Möllhoff, M., et al. (**2017b**). *Tremor-rich shallow dyke formation followed by silent magma flow at Bárðarbunga in Iceland*. Nat. Geosci. 10 (4), 299–304, doi:10.1038/ngeo2906.
- **Eibl**, E. P. S., Bean, C. J., Jónsdóttir, I., Höskuldsson, A., Thordarson, T., Coppola, D., et al. (**2017a**). *Multiple coincident eruptive seismic tremor sources during the 2014-2015 eruption at Holuhraun, Iceland*. J. Geophys. Res. Solid Earth. 122 (4), 2972–2987, doi:10.1002/2016jb013892.
- **Falsaperla** S., Privitera, E., Spampinato, S., Cardaci, C. (**1994**). *Seismic activity and volcanic tremor related to the December 14, 1991 Mt. Etna eruption*. Acta Vulcanol.,4, 63-73, doi: https://eurekamag.com/research/019/980/019980250.php.
- **Falsaperla**, S., Lanzafame, G., Longo, V., Spampinato, S. (**1999**). *Regional stress field in the area of Stromboli (Italy): insights into structural data and crustal tectonic earthquakes*. J. Volcanol. Geotherm. Res., 88, 147-166, doi:10.1016/S0377-0273(98)00113-9.
- **Falsaperla**, S., Privitera, E., Chouet, B., Dawson, P. (**2002**). *Analysis of long-period events recorded at Mount Etna (Italy) in 1992, and their relationship to eruptive activity*. Journal of volcanology and geothermal research, 114(3-4), 419-440, doi:10.1016/S0377-0273(01)00299-2.
- **Fehler**, M. (**1983**). Observations of volcanic tremor at Mount St. Helens volcano. J. Geoph. Res., 88, 3476-3484, doi: https://doi.org/10.1029/JB088iB04p03476.
- **Frankel**, A., Hough, S., Friberg, P., Busby, R. (**1991**). *Observations of Loma Prieta aftershocks from a dense array in Sunnywale*. Bull. Seismol. Soc. Am. 80, 1900-1922, doi: https://doi.org/10.1785/BSSA0810051900.
- **Fujita**, E., Ida, Y., Oikawa, J. (**1995**). *Eigen oscillation of a fluid sphere and source mechanism of harmonic volcanic tremor*. J. Volcanol. Geotherm. Res. 69, 365–378, doi: https://doi.org/10.1016/0377-0273(95)00027-5.
- **Fujita**, E. (**2008**). *Banded tremor at Miyakejima volcano, Japan: implication for two-phase flow instability*. J. Geophys. Res., 113, B04207, doi:10.1029/2006JB004829.
- **Furumoto**, M., Kunitomo, T., Inoue, H., Yamada, I., Yamaoka, K., Ikami, A., Fukao, Y. (**1990).** *Twin sources of high-frequency volcanic tremor of izu-oshima, japan*. Geophysical Research Letters, 17:25–27, doi: 10.1029/GL017i001p00025.
- **Garces**, M.A., **McNutt**, S.R. (**1997**). *Theory of the airborne sound field generated in a resonant magma conduit*. J. Volcanol. Geotherm. Res., 78, 155-178, doi: https://doi.org/10.1016/S0377-0273(97)00018-8.
- **García**, L., Álvarez, I., Titos, M., Diáz-Moreno, A., Benítez, C. (**2017**). *Automatic Detection of Long Period Events Based on Subband-Envelope Processing*. IEEE Journal of Selected Topics in Applied Earth Observations and Remote sensing, 10(11), doi: 10.1109/jstars.2017.2739690
- **Goldstein**, P., **Archuleta**, R. J. (**1991**). *Deterministic Frequency-Wavenumber Methods and Direct Measurements of Rupture Propagation During Earthquakes Using a Dense Array: Theory and Methods*. Journal of geophysical research, vol. 96, no.B4, 6173-6185, April 10,1991, doi: https://doi.org/10.1029/90JB02123.

- **Gonnermann**, H.M., **Manga**, M. (**2007**). *The fluid mechanics inside a volcano*. Annual Review of Fluid Mechanics 39, 321–356, doi:10.1146/annurev.fluid.39.050905.110207.
- **Gresta**, S., Lombardo, G., Cristofolini, R. (**1996**). *Characteristic of Volcanic tremor accompanying the September 24th, 1986 explosive eruption of Mt. Etna (Italy)*. Ann. Geofis., 39, 411–420, doi: https://doi.org/10.4401/ag-3976.
- **Gvirtzman**, Z., **Nur**, A. (**1999**). *The formation of Mount Etna as the consequence of slab rollback*. Nature, 401, 782–785, doi: https://doi.org/10.1038/44555.
- **Hagerty**, M.T., Schwartz, S.Y., Garces, M.A., Protti, M. (**2000**). *Analysis of seismic and acoustic observations at Arenal volcano, Costa Rica, 1995-1997*. J. Volcanol. Geotherm. Res. 101, 27-65, doi:10.1016/S0377-0273(00)00162-1.
- **Haldorsen**, J. (**2021**). *Spatial Aliasing and Three-Component Seismic Sensors*. GEOPHYSICS. 86. 1-38, doi: 10.1190/geo2020-0172.1.
- **Hale**, A.J. (**2007**). *Magma flow instabilities in a volcanic conduit: implications for long-period seismicity*. Physics of the Earth and Planetary Interiors 163, 163–178, doi:10.1016/J.PEPI.2007.05.001.
- **Haney**, M.M., Chouet, B.A., Dawson, P.B., Power, J.A. (**2012**). *Source characterization for an explosion during the 2009 eruption of Redoubt Volcano from very-long-period seismic waves*. Journal of Volcanology and Geothermal Research, doi: http://dx.doi.org/10.1016/j.jvolgeores.2012.04.018.
- **Harjes**, H. P., **Henger**, M. (**1973**). *Array-Seismology*. Z. Geophs., 39, 865–905, doi: https://doi.org/10.1007/978-3-642-35344-4_191.
- **Harrington**, R. M., **Brodsky**, E. E. (**2007**). *Volcanic hybrid earthquakes that are brittle-failure events*. Geophysical Research Letters, 34(6), doi: https://doi.org/10.1029/2006GL028714.
- **Harris**, F.J. (**1978**). *On the use of windows for harmonic analysis with the discrete Fourier transform*. Proc. IEEE 66, 51^83, doi:10.1109/PROC.1978.10837.
- **Harris**, A.J.L., Murray, J.B., Aries, S.E., Davies, M.A., Flynn, L.P., Wooster, M.J., Wright, R., Rothery, D.A. (**2000**). *Effusion rate trends at Etna and Krafl a and their implications for eruptive mechanisms*. Journal of Volcanology and Geothermal Research, v. 102, p. 237–269, doi: 10.1016/S0377-0273(00)00190-6.
- **Havskov**, J., Alguacil, G. (**2016**). *Seismic Arrays*. in Instrumentation in Earthquake Seismology, pp. 11–70, Springer, Berlin, Germany, ISBN: 978-3-319-21314-9.
- **Hellweg**, M. (**2000**). *Physical models for the source of Lascar's harmonic tremor*. Journal of Volcanology and Geothermal Research 101, 183–198, doi: https://doi.org/10.1016/S0377-0273(00)00163-3.
- **Hidayat**, D., Voight, B., Langston, C., Ratdomopurbo, A., Ebeling, C. (**2000**). *Broadband seismic experiment at Merapi Volcano, Java, Indonesia: very-long period pulses embedded in multiphase earthquakes*. J. Volcanol. Geotherm. Res., 100, 215-231, doi: 10.1016/s0377-0273(00)00138-4.
- **Ichihara**, M., Rubin, M.B. (**2010**). *Brittleness of fracture in flowing magma.* Journal of Geophysical Research 115, B12202, doi: http://dx.doi.org/10.1029/2010JB007820.
- **Inza**, L., Mars, J.I., Métaxian, J.-P., O'Brien, G.S., Macedo, O. (**2011**). *Seismo-volcano source localization with triaxial broad-band seismic array*. Geophys. J. Int. 187, 371–384, doi: https://doi.org/10.1111/j.1365-246X.2011.05148.x.
- **Inza**, L. A., Métaxian, J.-P., Mars, J. I., C.J., B., O'Brien, G. S., Macedo, O., Zandomeneghi, D. (**2014**). *Analysis of dynamics of vulcanian activity of ubinas*

volcano, using multicomponent seismic antennas. Journal of Volcanogy and Geothermal Research, doi: https://doi.org/10.1016/j.jvolgeores.2013.11.008.

- **Iverson**, R. M., Dzurisin, D., Gardner, C. A., Gerlach, T. M., LaHusen, R. G., Lisowski, M., Major, J. J., Malone, S. D., Messerich, J. A., Moran, S. C., Pallister, J. S., Qamar, A. I., Schilling, S. P., and Vallance, J. W. (**2006**). *Dynamics of seismogenic volcanic extrusion at Mount St. Helens in 2004–05*. Nature, 444, 439–443, doi:10.1038/nature05322.
- **Jellinek**, M., **Bercovici**, D. (**2011**). *Seismic tremors and magma wagging during explosive volcanism*. Nature. 470. 522-5, doi: 10.1038/nature09828.
- **Johnson**, J. B., **Aster**, R. C. (**2005**). *Relative partitioning of acoustic and seismic energy during Strombolian eruptions*. Journal of Volcanology and Geothermal Research, 148(3-4), 334-354, doi:10.1016/j.jvolgeores.2005.05.002
- **Jousset**, P., Dwipa, S., Beauducel, F., Duquesnoy, T., Diament, M. (**2003**). *Temporal gravity at Merapi during the 1993–1995 crisis: an insight into the dynamical behaviour of volcanoes*. J. Volcanol. Geotherm. Res., 100, 289–320, doi: https://doi.org/10.1016/S0377-0273(00)00141-4.
- **Julian**, B.R. (**1994**). *Volcanic tremor: Nonlinear excitation by fluid flow*. J. Geophys. Res. 99, 11859-11877, https://doi.org/10.1029/93JB03129.
- **Jurkevics**, A. (**1988**). *Polarization analysis of three-component array data*. Bull. Seismol. Soc. Am., 78, 1725–1743, 1988, doi: https://doi.org/10.1785/BSSA0780051725.
- **Kanasewich**, E.R., (**1981**). *Time Sequence Analysis in Geophysics*. University of Alberta Press, Edmonton, pp. 1 – 532, doi: https://doi.org/10.2307/3314985-a.
- **Kaneshima**, S., Kawakatsu, H., Matsubayashi, H., Sudo, Y., Tsutsui, T., Ohminato, T., Ito, H., Uhira, K., Yamasato, H., Oikawa, J., Takeo, M., Iidaka, T. (**1996**). *Mechanism of phreatic eruptions at Aso Volcano inferred from near-field broadband seismic observations.* Science. 273, 642-645, doi: DOI: 10.1126/science.273.5275.642.
- **Kawakatsu**, H., Kaneshima, S., Matsubayashi, H., Ohminato, T., Sudo, Y., Tsutsui, T., Uhira, K., Yamasato, H., Ito, H., Legrand, D. (**2000**). *Aso94: Aso seismic observation with broadband instruments*. J. Volcanol. Geotherm. Res. 101, 129–154, doi:10.1016/S0377-0273(00)00166-9.
- **Kendrick**, J., Lavallée, Y., Hess, K.-U., De Angelis, S., Ferk, A., Gaunt, E., Dingwell, D., Leonhardt, R. (**2014**). *Seismogenic frictional melting in the magmatic column*. Solid Earth. 5. 199-208, doi: 10.5194/se-5-199-2014.
- **Kenney**, J. F**., Keeping**, E. S. (1962). *Root Mean Square*. §4.15 in Mathematics of Statistics, Pt. 1, 3rd ed. Princeton, NJ: Van Nostrand, pp. 59-60, 1962.
- **Konstantinou**, K.I., **Sclindwein**, V. (**2002**). *Nature, wavefield properties and source mechanism of volcanic tremor: a review*. J. Volcanol. Geotherm. Res. 119 161–187, doi: https://doi.org/10.1016/S0377-0273(02)00311-6.
- **Kumagai**, H., Chouet, B., Nakano, M. (**2002**). *Temporal evolution of a hydrothermal system in Kusatsu-Shirane Volcano, Japan, inferred from the complex frequencies of long-period events*. J. Geophys. Res., 107, 2236, doi:10.1029/2001JB000653.
- **Kumagai**, H., Miyakawa, K., Negishi, H., Inoue, H., Obara, K., Suetsugu, D. (**2003**). *Magmatic dyke resonances inferred from very-long-period seismic signals*. Science 299, 2058–2061, doi: http://www.jstor.org/stable/3833720.

- **Kumagai**, H. (**2006**). *Temporal evolution of a magmatic dike system inferred from the complex frequencies of very long period seismic signals*. J. Geophys. Res., 111, B06201, doi:10.1029/2005JB003881.
- **Kumagai**, H., Palacios, P., Maeda, T., Castillo, D. B., Nakano, M. (**2009**). *Seismic tracking of lahars using tremor signals*. J. Volcanol. Geotherm. Res. 183 (1), 112–121, doi:10.1016/j.jvolgeores.2009.03.010.
- **Kumagai**, H., Nakano, M., Maeda, T., Yepes, H., Palacios, P., Ruiz, M., Arrais, S., Vaca, M., Molina, I., Yamashima, T. (**2010**). *Broadband seismic monitoring of active volcanoes using deterministic and stochastic approaches*. J. Geophys. Res. 115, B08303, doi:10.1029/2009JB006889.
- **Kumagai**, H., Saito, T., O'Brien, G., Yamashina, T. (**2011**). *Characterization of scattered seismic wavefields simulated in heterogeneous media with topography*. J. Geophys. Res., 116, B03308, doi:10.1029/2010JB007718.
- **La Rocca**, M., Saccorotti, G., Del Pezzo, E., Ibáñez, J. (**2004**). *Probabilistic source location of explosion quakes at stromboli volcano estimated with double array data*. Journal of Volcanology and Geothermal Research, 131:123–142, doi: 10.1016/s0377-0273(03)00321-4.
- **Lahr**, J.C., Chouet, B.A., Stephens, C.D., Power, J.A., Page, R.A. (**1994**). *Earthquake classification, location and error analysis in a volcanic environment: implications for the magmatic system of the 1989–1990 eruptions at Redoubt Volcano, Alaska*. J. Volc. Geotherm. Res., 62, 137–151, doi: https://doi.org/10.1016/0377-0273(94)90031-0.
- **Langer**, H., **Falsaperla**, S. (**1996**). *Long-term observation of volcanic tremor on Stromboli volcano (Italy): a synopsis.* pure and applied geophysics, 147(1), 57-82, doi:10.1007/BF00876436.
- **Lee**, W. H. K., Kanamori, H., Jennings, P. C., Kisslinger, C. (**2002**). *International Handbook of Earthquake and Engineering Seismology*. Part A, Academic Press, , xxiii+933 pp., ISBN: 9780080489223.
- **Leet**, R.C. (**1988**). *Saturated and subcooled hydrothermal boiling in groundwater flow channels as a source of harmonic tremor.* J. Geophys. Res. Solid Earth 93, 4835–4849, doi: https://doi.org/10.1029/JB093iB05p04835.
- **Legrand**, D., Kaneshima, S., Kawakatsu, H. (**2000**). *Moment tensor analysis of near field broadband waveforms observed at Aso volcano*, Japan. J. Volcanol. Geotherm. Res., 101, 155-169, doi:10.1016/S0377-0273(00)00167-0.
- **Lentini**, F., Carbone, S. Guarnieri, P. (**2006**). *Collisional and post collisional tectonics of the Apenninic–Maghrebian orogen (southern Italy)*. In: Dilek, Y., Pavlides, S. (Eds.), Postcollisional tectonics and magmatism in the Mediterranean region and Asia: GSA Special Paper, 409, pp. 57–81, doi: https://doi.org/10.1130/2006.2409(04).
- **Lesage**, P., Glangeaud, F., Mars, J. (**2002**). *Applications of autoregressive and time-frequency analysis to the study of volcanic tremor and LP events*. J. Volcanol. Geotherm. Res., 114, 391-417, doi:10.1016/S0377-0273(01)00298-0.
- **Lesage**, P. (**2009**). *Interactive Matlab software for the analysis of seismic volcanic signals*. Computers & Geosciences. 35. 2137-2144, doi: 10.1016/j.cageo.2009.01.010.
- **Lo Giudice**, E., Patanè, G., Rasà, R., Romano, R. (**1982**). *The structural framework of Mount Etna*. Mem. Soc. Geol. It., 23, 125-158.

- **Lo Giudice**, E., **Rasà**, R. (**1992**). *Very shallow earthquakes and brittle deformation in active volcanic areas: the etnean region as an example*. Tectonophysics 202, 257-268, doi: https://doi.org/10.1016/0040-1951(92)90111-I.
- **Lokmer**, I., Bean, C.J., Saccorotti, G., Patane, D. (**2007**). *Moment-tensor inversion of LP events recorded on Etna in 2004 using constraints obtained from wave simulation tests*. Geophysical Research Letters 34, L22316, doi: http://dx.doi.org/10.1029/2007GL031902.
- **Lokmer**, I., Saccorotti, G., Di Lieto, B., Bean, C.J. (**2008**). *Temporal evolution of long-period seismicity at Etna Volcano, Italy, and its relationships with the 2004–2005 eruption*. Earth and Planetary Science Letters 266, 205–220, doi:10.1016/j.epsl.2007.11.017.
- **Matoza**, R.S., Garcés, M.A., Chouet, B.A., D'Auria, L., Hedlin, M.A.H., De Groot-Hedlin, C., Waite, G.P. (**2009**). *The source of infrasound associated with long-period events at Mount St. Helens*. J. Geophys. Res. 114, doi: https://doi.org/10.1029/2008JB006128.
- **Matoza**, R.S., **Chouet**, B.A. (**2010**). *Subevents of long-period seismicity: Implications for hydrothermal dynamics during the 2004–2008 eruption of Mount St. Helens*. J. Geophys. Res. Solid Earth 115, doi:10.1029/2010JB007839.
- **McNutt**, S. R. (**1992**). *Volcanic tremor*. Encyclopedia of Earth System Science, 4, 417-425.
- **McNutt**, S.R. (**1996**). *Seismic monitoring and eruption forecasting of volcanoes: A review of the state-of-the-art and case histories*. In: Scarpa, Tilling (Eds.), Monitoring and Mitigation of Volcanic Hazards. Springer, Berlin, pp. 100-146, doi: 10.1007/978-3-642-80087-0_3
- **McNutt**, S. R. (**2002**). *Volcano seismology and monitoring for eruptions*. In: Lee et al. (2002), Part A, 383-406, doi: 10.1146/annurev.earth.33.092203.122459.
- **McNutt**, S.R. (**2005**). *Volcanic seismology*. Annual Review of Earth and Planetary Sciences 32, 461 491, doi: 10.1146/annurev.earth.33.092203.122459.
- **McNutt**, S. R. (**2011**). *Volcanic tremor wags on*. Nature 470 (7335), 471–472. doi:10.1038/470471aPubmed, doi: https://doi.org/10.1038/470471a.
- **McNutt**, S. R., Thompson, G., Johnson, J., Angelis, S. D., Fee, D. (**2015**). *Chapter 63—seismic and infrasonic monitoring*, in The encyclopedia of volcanoes. 2nd Edn, Editor H. Sigurdsson (Amsterdam, Netherlands: Academic Press), 1071–1099, doi: https://doi.org/10.1016/B978-0-12-385938-9.00063-8.
- **Messina**, A., Langer, H. (**2011**). *Pattern recognition of volcanic tremor data on Mt. Etna (Italy) with KKAnalysis-A software program for unsupervised classification*. Computers & Geosciences. 37. 953-961, doi: 10.1016/j.cageo.2011.03.015.
- **Métaxian**, J. P., Lesage, P., Dorel, J. (**1997**). *Permanent tremor of masaya volcano, nicaragua: Wave field analysis and source location*. Journal of Geophysical Research, 102:22,529–22,545, doi: https://doi.org/10.1029/97JB01141.
- **Metaxian**, J.P., Lesage, P., Valette, B. (**2002**). *Locating sources of volcanic tremor and emergent events by seismic triangulation: application to Arenal Volcano, Costa Rica*. J. Geophys. Res., 107, doi:10.1029/2001JB000559.
- **Miller**, A. D., Stewart, R. C., White, R. A., Luckett, R., Baptie, B. J., Aspinall, W. P., Voight, B. (**1998**). *Seismicity associated with dome growth and collapse at the*

Soufriere Hills Volcano, Montserrat. Geophysical Research Letters, 25(18), 3401-3404, doi: https://doi.org/10.1029/98GL01778.

- **Monaco**, C., Tapponier, P., Tortorici, L., Gillot, P. Y. (**1997***). Late Quaternary slip rate on the Acireale-Piedimonte normal faults and tectonic origin of Mt. Etna (Sicily)*. Earth Planet. Sci. Lett. 147, 125-139, doi: https://doi.org/10.1016/S0012-821X(97)00005-8.
- **Monaco** C., Catalano S., Cocina O., De Guidi G., Ferlito C., Gresta S., Musumeci C., Tortorici L. (**2005**). *Tectonic control on the eruptive dynamics at Mt. Etna volcano (eastern Sicily) during the 2001 and 2002-2003 eruptions.* J. Volc. Geoterm. Res., 144, 221-233, doi:10.1016/j.jvolgeores.2004.11.024.
- **Montesinos**, B. M., Bean, C. J., Lokmer, I. (**2021**). *Quantifying strong seismic propagation effects in the upper volcanic edifice using sensitivity kernels*. Earth and Planetary Science Letters, Volume 554, 116683, ISSN 0012-821X, doi: https://doi.org/10.1016/j.epsl.2020.116683.
- **Moran**, S. C., Malone, S. D. Qamar, A. I. Thelen, W. A., Wright, A. K., Caplan-Auerbach, J. (**2008**). *Seismicity associated with the renewed dome-building eruption of Mount St. Helens 2004–2005*. in A Volcano Rekindled: The Renewed Eruption of Mount St. Helens, 2004–2006, edited by D. R. Sherrod, W. E. Scott, and P. H. Stauffer, 1750, pp. 27–54, U.S. Geol. Surv. Prof. Pap., doi: https://doi.org/10.3133/pp17502.
- **Morioka**, H., Kumagai, H., Maeda, T. (**2017**). *Theoretical basis of the amplitude source location method for volcano-seismic signals*. J. Geophys. Res. Solid Earth. 122 (8), 6538–6551, doi:10.1002/2017JB013997.
- **Morrissey**, M.M., **Chouet**, B.A. (**1997**). *A numerical investigation of choked flow dynamics and its application to the triggering mechanism of long-period events at Redoubt Volcano, Alaska*. J. Geophys. Res. Solid Earth 102, 7965–7983, doi:10.1029/97JB00023.
- **Morrissey**, M.M., **Chouet**, B. (**2001**). *Trends in long-period seismicity related to magmatic fluid compositions.* J. Volcanol. Geotherm. Res., 108, 265-281, doi:10.1016/S0377-0273(00)00290-0.
- **Moschella**, S., Cannata, A., Di Grazia, G., Gresta, S. (**2018**). *Insights into lava fountain eruptions at Mt. Etna by improved source location of the volcanic tremor*. Annals of geophysics = Annali di geofisica. 61, doi: https://doi.org/10.4401/ag-7552
- **Nakano**, M., Kumagai, H., Chouet, B.A. (**2003**). *Source mechanism of long-period events at Kusatsu-Shirane Volcano, Japan, inferred from waveform inversion of the effective excitation functions*. J. Volcanol. Geotherm. Res., 122, 149-164, doi: https://doi.org/10.1016/S0377-0273(02)00499-7.
- **Nakano**, M. (**2005**). *Waveform inversion of volcano-seismic signals assuming possible source geometries*. Geophys. Res. Lett. 32, doi: https://doi.org/10.1029/2005GL022666.
- **Neidell**, N., **Taner**, M.T. (**1971**). *Semblance and other coherency measures for multichannel data*. Geophysics 36, 482–497, doi: https://doi.org/10.1190/1.1440186.
- **Neri**, M., Acocella, V., Behncke, B. (**2004**). *The role of the Pernicana Fault System in the spreading of Mt. Etna (Italy) during the 2002–2003 eruption*. Bull. Volcanol., 66, 417-430, doi:10.1007/s00445-003-0322-x.

- **Neri**, M., Guglielmino, F., Rust, D. (**2007**). *Flank instability on Mount Etna: radon, radar interferometry and geodetic data from the southern boundary of the unstable sector*. Journal of Geophysical Research 112, doi:10.1029/2006JB004756.
- **Neuberg**, J., Luckett, R., Ripepe, M., Braun, T. (**1994**). *Highlights from a seismic broadband array on Stromboli volcano*. Geophys. Res. Lett., 21, 749-752, doi: https://doi.org/10.1029/94GL00377.
- **Neuberg**, J., **Pointer**, T. (**2000**). *Effects of volcano topography on seismic broad-band waveforms*. Geophys. J. Int., 143, 239–248, doi: https://doi.org/10.1046/j.1365-246x.2000.00251.x
- **Neuberg**, J.W., Tuffen, H., Collier, L., Green, D., Powell, T., Dingwell, D. B. (**2006**). *The trigger mechanism of low-frequency earthquakes on montserrat*. Journal of Volcanology and Geothermal Research, 153:37–50, doi:10.1016/j.jvolgeores.2005.08.008.
- **Nishimura**, T., Nakamichi, H., Tanaka, S., Sato, M., Kobayashi, T., Ueki, S., Hamaguchi, H., Ohtake, M., Sato, H. (**2000**). *Source process of very long period seismic events associated with the 1998 activity of Iwate Volcano, northeastern Japan*. Journal of Geophysical Research 105, 19,135–19,147, doi: 10.1029/2000JB900155.
- **Norini**, G., **Acocella**, V. (**2011**). *Analogue modeling of flank instability at Mount Etna: understanding the driving factors*. Journal of Geophysical Research: Solid Earth, 116(B7), doi:10.1029/2011JB008216.
- **O'Brien**, G. S., **Bean**, C. J. (**2004**). *A 3D discrete numerical elastic lattice method for seismic wave propagation in heterogeneous media with topography*. Geophys. Res. Lett. 31, doi:10.1029/2004GL020069.
- **O'Brien**, G.S., Lokmer, I., De Barros, L., Bean, C.J., Saccoroti, G., Métaxian, J.-P., Patané, D. (**2011**). *Time reverse location of seismic long period events recorded on Mt Etna*. Geophys. J. Int. 184, 452–462, doi: 10.1111/j.1365-246X.2010.04851.x.
- **Ohminato**, T., **Chouet**, B.A. (**1997**). *A free-surface boundary condition for including 3D topography in the finite-difference method*. Bull. Seismol. Soc. Am. 87, 494–515, doi: https://doi.org/10.1785/BSSA0870020494.
- **Ohminato**, T., Chouet, B., Dawson, P., Kedar., S (**1998**). *Waveform inversion of very long period impulsive signals associated with magmatic injection beneath Kilauea Volcano, Hawaii*. J. Geophys. Res., 103, 23839-23862, doi:10.1029/98JB01122.
- **Ohminato**, T., Takeo, M., Kumagai, H., Yamashina, T., Oikawa, J., Koyama, E., Tsuji, H., Urabe, T. (**2006**). *Vulcanian eruptions with dominant single force components observed during the Asama 2004 volcanic activity in Japan*. Earth Planets Space 58, 583–593, doi: https://doi.org/10.1186/BF03351955.
- **Okumura**, S., Nakamura, M., Tsuchiyama, A. (**2006**). *Shear-induced bubble coalescence in rhyolitic melts with low vesicularity*. Geophys. Res. Lett., 33(20), L20316, doi:10.1029/2006GL027347.
- **Okumura**, S., Nakamura, M., Tsuchiyama, A., Nakano, T., Uesugi, K. (**2008**). *Evolution of bubble microstructure in sheared rhyolite: formation of a channel-like bubble network*. J. geophys. Res.: Solid Earth, 113(B7), B07208, doi:10.1029/2007JB005362.

- **Olson,** J. V., **Szuberla**, C. A. L. (**2005**). *Distribution of wave packet sizes in microbarom wave trains observed in Alaska*. J. Acoust. Soc. Am. 117, 1032–1037, doi: 10.1121/1.1854651.
- **Palano**, M., Puglisi, G., Gresta, S. (**2008**). *Ground deformation patterns at Mt. Etna from 1993 to 2000 from joint use of InSAR and GPS techniques*. J. Volcanol. Geotherm. Res., 169(3–4), 99–120, doi:10.1016/j.jvolgeores.2007.08.014.
- **Papale**, P. (**1999**). *Strain-induced magma fragmentation in explosive eruptions*. Nature 397, 425–428, doi: 10.1038/17109.
- **Papouilis**, A. (**1987**). *The Fourier Integral and Its Applications*. McGraw-Hill, Inc., New York, ISBN 13: 9780486823799.
- **Patanè**, D., De Gori, P., Chiarabba, C., Bonaccorso, A. (**2003**). *Magma ascent and the pressurization of Mt. Etna's volcanic system*. Science, 299, 2061–2063, doi: 10.1126/science.1080653.
- **Patanè**, D., Barberi, G., Cocina, O., De Gori, P., Chiarabba, C. (**2006**). *Time-resolved seismic tomography detects magma intrusions at Mount Etna*. Science, 313(5788), 821-823, doi: 10.1126/science.1127724.
- **Patanè**, D., Di Grazia, G., Cannata, A., Montalto, P., Boschi, E. (**2008**). *Shallow magma pathway geometry at Mt. Etna Volcano*. Geochem. Geophys. Geosyst., 9, Q12021, doi:10.1029/2008GC002131.
- **Patanè** D., Aliotta, M., Cannata, A., Cassisi, C., Coltelli, M., Di Grazia, G., Montalto, P., Zuccarello, L. (**2011**). *Interplay between Tectonics and Mount Etna's Volcanism: Insights into the Geometry of the Plumbing System*. Book "New Frontiers in Tectonic Research - At the Midst of Plate Convergence", 73-104, Edited by Uri Schattner, doi:10.5772/23503.
- **Patanè**, D., Aiuppa, A., Aloisi, M., Behncke, B., Cannata, A., Coltelli, M., Di Grazia, G., Gambino, S., Gurrieri, S., Mattia, M., Salerno, G. (**2013**). *Insights into magma and fluid transfer at Mount Etna by a multiparametric approach: A model of the events leading to the 2011 eruptive cycle*. J. Geophys. Res. Solid Earth, 118, 3519–3539, doi:10.1002/jgrb.50248.
- **Pignatelli**, A., Giuntini, A., Consol, R. (**2008**). *Matlab software for the analysis of seismic waves recorded by three-element arrays*. Comput. Geosci. 34, 7 (July, 2008), 792–801, doi: https://doi.org/10.1016/j.cageo.2007.10.003.
- **Prejean**, S., Ellsworth, W., Zoback, M., Waldhauser, F. (**2002**). *Fault structure and kinematics of the Long Valley Caldera region, California, revealed by high-accuracy earthquake hypocenters and focal mechanism stress inversions*. Journal of Geophysical Research: Solid Earth, 107(B12), doi: https://doi.org/10.1029/2001JB001168.
- **Privitera**, E., Sgroi, T., Gresta, S. (**2003**). *Statistical analysis of intermittent volcanic tremor associated with the September 1989 summit explosive eruptions at Mount Etna, Sicily*. Journal of volcanology and geothermal research, 120(3-4), 235-247, doi:10.1016/S0377-0273(02)00400-6.
- **Privitera**, E., Bonanno, A., Gresta, S., Nunnari, G., Puglisi, G. (**2012**). *Triggering mechanisms of static stress on Mount Etna volcano. An application of the boundary element method*. J. Volcanol. Geotherm. Res. 245–246, 149–158, doi:10.1016/j.jvolgeores.2012.08.012.
- **Qin**, L., Vernon, F., Johnson, C., Ben-Zion, Y. (**2019**). *Spectral Characteristics of Daily to Seasonal Ground Motion at the Piñon Flats Observatory from Coherence*

of Seismic Data. Bulletin of the Seismological Society of America. 109, doi: 10.1785/0120190070.

- **Ripepe** M, Coltelli M, Privitera E, Gresta S, Moretti M, Piccinini D (**2001**). *Seismic and infrasonic evidences for an impulsive source of the shallow volcanic tremor at Mt. Etna. Italy*. Geophys Res Lett 28:1071–1074, doi: https://doi.org/10.1029/2000GL011391.
- **Ripperger**, J., Igel, H., Wassermann, J. (**2003**). *Seismic wave simulation in the presence of real volcano topography*. J. Volcanol. Geotherm. Res. 128, 31– 44, doi:10.1016/S0377-0273(03)00245-2.
- **Rittman**, A. (**1973**). *Mount Etna and the 1971 eruption - Structure and evolution of Mount Etna*. Phil. Trans. R. Soc. Lond. A 1973 274 5-16; doi: 10.1098/rsta.1973.0021.
- **Roman**, D.C., **Cashman,** K.V. (**2006**). *The origin of volcano-tectonic earthquake swarms*. Geological Society of America, 34, 6457-6460, doi:10.1130/G222691.
- **Rost**, S., **Thomas**, C. (**2002**). *Array seismology: Method and application*. Rev. Geophysics., 40:1008, 27PP, doi: https://doi.org/10.1029/2000RG000100.
- **Saccorotti**, G., **Del Pezzo**, E. (**2000**). A probabilistic approach to the inversion of data from a seismic array and its application to volcanic signals. Geophysical Journal International, 143:249–261, doi: https://doi.org/10.1046/j.1365-246x.2000.00252.x.
- **Saccorotti**, G. Almendros, J., Carmona, E., Ibáñez, J. M., Del Pezzo, E. (**2001**). *Slowness Anomalies from Two Dense Seismic Arrays at Deception Island Volcano, Antarctica*. Bulletin of the Seismological Society of America 2001; 91 (3): 561–571, doi: https://doi.org/10.1785/0120000073.
- **Saccorotti**, G., Zuccarello, L., Del Pezzo, E., Ibáñez, J. M., Gresta, S. (**2004**). *Quantitative analysis of the tremor wavefiled at Etna volcano, Italy*. J. Volcanol. Geoth. Res., 136, 223-245, doi: https://doi.org/10.1016/j.jvolgeores.2004.04.003.
- **Saccorotti**, G., Lokmer, I., Bean, C. J., Di Grazia, G., Patanè, D. (**2007**). *Analysis of sustained long-period activity at Etna Volcano, Italy*. J. Volcanol. Geotherm. Res., 160, 340-354, doi:10.1016/j.jvolgeores.2006.10.008.
- **Sadeghisorkhani**, H., Gudmundsson, O., Tryggvason, A. (**2017**). *GSpecDisp: a Matlab GUI package for phase-velocity dispersion measurements from ambient-noise correlations*. Computers and Geosciences, doi: https://doi.org/10.1016/j.cageo.2017.09.006.
- **Sanderson**, R.W., Johnson, J.B., Lees, J.M. **(2010**). *Ultra-long period seismic signals and cyclic deflation coincident with eruptions at Santiaguito volcano, Guatemala*. Journal of Volcanology and Geothermal Research, Volume 198, Issues 1–2, 2010, Pages 35-44, ISSN 0377-0273, doi: https://doi.org/10.1016/j.jvolgeores.2010.08.007.
- **Schick** R., **Riuscetti**, M. (**1973**). *An analysis of volcanic tremors at South Italian volcanoes*. Z. Geophysic, 39.
- **Schlindwein**, V., Wassermann, J., Scherbaum, F. (**1995**). *Spectral analysis of harmonic tremor signals at Mt. Semeru volcano, Indonesia*. Geophysical Research Letters, 22(13), 1685-1688, doi: https://doi.org/10.1029/95GL01433.
- **Schmidt**, R.O., (**1986**). *Multiple emitter location and signal parameter estimation*. IEEE Trans. Antennas Propag. 34, 276–280, doi: 10.1109/TAP.1986.1143830.
- **Schweitzer**, J., Fyen, J., Mykkeltveit, S., Gibbons, S. J., Pirli, M., Kühn, D., et al. (**2012**). *Seismic arrays*. in IASPEI New Manual of Seismological Observatory

Practice 2 (NMSOP-2), ed. P. Bormann (Potsdam: IASPEI), doi: 10.2312/GFZ.NMSOP-2_ch9.

- **Sciotto**, M., Cannata, A., Gresta, S., Privitera, E., Spina, L. (2013). *Seismic and infrasound signals at Mt. Etna: Modeling the North-East crater conduit and its relation with the 2008–2009 eruption feeding system*. J. Volcanol. Geotherm. Res. 254, 53–68., doi: 10.1016/j.jvolgeores.2012.12.024.
- **Shyh-Jeng**, C. (**1993**). Estimation of seismic source processes using strong motion array data. Report No. UCBjEERC-91j07 Earthquake Engineering Research Center University of California at Berkeley Berkeley, California.
- **Smith**, P., **Bean**, C. (**2020**). *RETREAT: A REal-Time TREmor Analysis Tool for Seismic Arrays, With Applications for Volcano Monitoring*. Frontiers in Earth Science. 8. 531., doi: https://doi.org/10.3389/feart.2020.586955.
- **Spampinato**, L., M. Sciotto, A. Cannata, F. Cannavo, A. La Spina, M. Palano, G. G. Salerno, E. Privitera, and T. Caltabiano (**2015**). *Multiparametric study of the February–April 2013 paroxysmal phase of Mt. Etna New South-East crater*. Geochem. Geophys. Geosyst., 16, doi:10.1002/2015GC005795.
- **Sparks**, R. (**2000**). *The causes and consequences of eruptions of andesite volcanoes*. Philosophical Transactions of the Royal Society A, 358:1435–1440, doi: https://doi.org/10.1098/rsta.2000.0596.
- **Sparks**, R. S. J., Biggs, J., Neuberg, J. W. (**2012**). *Monitoring volcanoes*. Science 335, 1310–1311, doi:10.1126/science.1219485.
- **Tanguy**, J.C., Kieffer, G., Patanè, G. (**1996**). *Dynamics, lava volume and effusion rate during the 1991-1993 eruption of Mount Etna*. Journal of Volcanology and Geothermal Research 71: 259-265, doi: https://doi.org/10.1016/0377-0273(95)00081-X.
- **Thomas**, M.E., **Neuberg**, J. (**2012**). *What makes a volcano tick — a first explanation of deep multiple seismic sources in ascending magma*. Geology 40 (4), 351–354, doi: https://doi.org/10.1130/G32868.1.
- **Thompson**, G., Reyes, C. (**2018**). *GISMO-A Seismic Data Analysis Toolbox for MATLAB [software package]*, available at http:// geoscience-community-codes.github.io/GISMO/ (last accessed February 2018).
- **Tibaldi** A., **Groppelli**, G., (**2002**). *Volcano-tectonic activity along structures of the unstable NE flank of Mt. Etna (Italy) and their possible origin*. J. Volcanol. Geotherm. Res., 115, 277–302, doi:10.1016/S0377-0273(01)00305-5.
- **Tokimatsu**, K. (**1997**). *Geotechnical site characterization using surface waves*. In: K. Ishihara (ed.), Proc.1st Intl. Conf. Earthquake Geotechnical Engineering, Balkema, 1333-1368.
- **Trovato**, C., Lokmer, I., De Martin, F., Aochi, H. (**2016**). *Long period (LP) events on Mt Etna volcano (Italy): the influence of velocity structures on moment tensor inversion*. Geophysical Journal International, Volume 207, Issue 2, Pages 785–810, doi: https://doi.org/10.1093/gji/ggw285.
- **Uhira**, K., **Takeo**, M. (**1994**). *The source of explosive eruptions of Sakuajima volcano, Japan*. J. Geophys. Res., 99, 17775-17789, doi: https://doi.org/10.1029/94JB00990.
- **Varley**, N. R., Arámbula-Mendoza, R., Reyes-Dávila, G., Stevenson, J., Harwood, R. (**2010**). *Long-period seismicity during magma movement at Volcán de Colima*. Bull. Volcanol., 72(9), 1093–1107, doi:10.1007/s00445-010-0390-7.

- **Vergniolle**, S., **Brandeis**, G. (**1994**). *Origin of the sound generated by Strombolian explosions*. Geophys. Res. Lett., 21, 1959-1962, doi:10.1029/94GL01286.
- **Vergniolle**, S., **Brandeis**, G. (**1996**). *Strombolian explosions: a large bubble breaking at the surface of a lava column as a source of sound*. J. Geophys. Res., 101, 20433-20448, doi:10.1029/96JB01178.
- **Vergniolle**, S., Brandeis, G., Mareschal, J.C. (**1996**). *Strombolian explosions: Eruption dynamics determined from acoustic measurements*. J. Geophys. Res., 101, 20449-20466, doi: 10.1029/96JB01925.
- **Vergniolle**, S., **Caplan-Auerbach**, J**. (2004).** *Acoustic measurements of the 1999 basaltic eruption of Shishaldin volcano, Alaska: 2) Precursor to the Subplinian activity*. J. Volcanol. Geotherm. Res., 137, 135-151, doi:10.1016/j.jvolgeores.2004.05.004.
- **Vergniolle**, S., Boichu, M., Caplan-Auerbach, J. (**2004**). *Acoustic measurements of the 1999 basaltic eruption of Shishaldin volcano, Alaska: 1) Origin of Strombolian activity*. J. Volcanol. Geotherm. Res., 137, 109-134, doi:10.1016/j.jvolgeores.2004.05.003.
- **Viccaro**, M., Garozzo, I., Cannata, A., Di Grazia, G., Gresta, S. (**2014***). Gas burst vs. gas-rich magma recharge: a multidisciplinary study to reveal factors controlling triggering of the recent paroxysmal eruptions at Mt. Etna*. Journal of volcanology and geothermal research, 278, 1-13, doi:10.1016/j.jvolgeores.2014.04.001.
- **Villari**, L., Rasà, R., Caccamo, A., (**1988**). *Volcanic hazard evaluation at Mt. Etna (Sicily, Italy), Some insight from the geostructural pattern constraining flank eruptions*. Proc Kagoshima Int Conf on Volcanoes, pp 491-494.
- **Waite**, G.P., Chouet, B.A., Dawson, P.B. (**2008**). *Eruption dynamics at Mount St. Helens imaged from broadband seismic waveforms: Interaction of the shallow magmatic and hydrothermal systems*. J. Geophys. Res. 113, doi:10.1029/2007JB005259.
- **Waite**, G.P., **Smith**, R.B. (**2004**). *Seismotectonics and stress field of the Yellowstone volcanic plateau from earthquake firstmotions and other indicators*. J. Geophys. Res., 109, doi: 10.1029/2003JB002675.
- **Wang**, H., **Kaveh**, M. (**1985**). *Coherent signal-subspace processing for the detection and estimation of angles of arrival of multiple wide-band sources*. IEEE Trans. ASSP 33, 823– 831, doi: 10.1109/TASSP.1985.1164667.
- **Wassermann**, J. (**2012**). *Volcano Seismology*, IASPEI New Manual of seismological observatory practice 2. Deutsches GeoForschungsZentrum GFZ, Potsdam, doi: https://doi.org/10.2312/GFZ.NMSOP-2_ch13.
- **Webb**, S.L., **Dingwell**, D.B. (**1990**). *Non-Newtonian rheology of igneous melts at high stresses and strain rates: experimental results for rhyolite, andesite, basalt, and nephelinite*. Journal of Geophysical Research 95 (B10), 15,695–15,701, doi: 10.1029/JB095iB10p15695.
- **Weber**, M., **Wicks**, C. W. (**1996**). *Reflections from a distant subduction zone*. Geophysical research letters 23 1996, pp.1453-1456, doi:10.1029/96gl01322.
- **Welch**, P. D. (**1967**). *The Use of Fast Fourier Transform for the Estimation of Power Spectra: A Method Based on Time Averaging Over Short, Modified Periodograms*. IEEE® Transactions on Audio and Electroacoustics. Vol. AU-15, 1967, pp. 70–73, doi: 10.1109/TAU.1967.1161901.

- **Yamamoto**, M., Kawakatsu, H., Kaneshima, S., Mori, T., Tsutsui, T., Sudo, Y., Morita, Y. (**1999**). *Detection of a crack-like conduit beneath the active crater at Aso Volcano, Japan.* Geophysical Research Letters 26, 3677–3680, doi: 10.1029/1999GL005395.
- **Zuccarello**, L., Burton, M. R., Saccorotti, G., Bean, C. J., Patanè, D. (**2013**). *The coupling between very long period seismic events, volcanic tremor, and degassing rates at Mount Etna volcano*. J. Geophys. Res. Solid Earth, 118, doi:10.1002/jgrb.50363.
- **Zuccarello**, L., Paratore M., La Rocca M., Ferrari F., Messina A., Branca S., Contrafatto D., Galluzzo D., Rapisarda S., García L. (**2016**). *Shallow velocity model in the area of Pozzo Pitarrone, Mt. Etna, from single station, array methods and borehole data*. Annals of Geophysics, doi:10.4401/ag-7086.

WEBLIOGRAPHY

- **INGV-SEZIONE DI CATANIA:** https://www.ct.ingv.it
- **IRIS DMCSERVICES:** https://www.iris.edu/hq/
- **MISARA:** https://doi.org/10.5281/zenodo.4642026
- **SEISMO PACKAGE:** http://epsc.wustl.edu/~ggeuler/codes/m/seizmo/